University of Naples Federico II

Polytechnic School and of Basic Sciences

Educational Area: Mathematics, Physics, Natural Sciences

CHEMISTRY SCIENCES DOCTORATE

XXXVI Cycle

Structural and Dynamic Complexity of Advanced Elastomers

Tutors

Prof. Finizia Auriemma

Prof. Odda Ruiz de Ballesteros

Candidate

Giuseppe Femina

Index

Abstract

The aim of this PhD work is to investigate the structure-properties relationships of Hydrogenated Nitrile Butadiene Rubbers (HNBRs). Samples with different chemical composition (ACryloNitrile, ACN, and initial Residual Double Bond, iRDB, content) and different crosslink density were analyzed. The study is focused on the analysis of conformation and dynamics of the chains in both crystalline and amorphous states and the mechanisms inducing Strain-Induced Crystallization (SIC) at room temperature. Additionally, it aims at understanding how SIC is influenced by the degree of crosslinking and the ACN content. The objectives of this project are significant for both the fundamental understanding of polymer physics and rubber elasticity in particular and practical aspects related to rubber processing.

Currently, there are few studies on the behavior of molecular chain orientation during the stretching of HNBR and its relationship with SIC in the literature. Another characteristic of these rubbers is the thermal behavior that some amorphous samples show, when subject to prolonged annealing at temperatures close to the glass transition T_g. In particular, endothermic peaks are generated in DSC heating thermograms at temperatures near T_g. These phenomena are influenced by various factors, such as ACN content, degree of unsaturation, and crosslink density. In the literature, these phenomena are attributed to thermally induced crystallization, but studies related to this aspect are still limited. This behaviour is similar to the behaviour of polystyrene which upon annealing at temperatures below T_g gives endothermic peaks with no melting involved, seems it is atactic.

After a general introduction on rubber elasticity, and the state of the art related to the structure and properties of HNBRs (Chapter I), in the Chapter II the theoretical and experimental background behind the different techniques adopted for the characterization of the samples are

illustrated. In the successive chapters, the results obtained from the different characterization techniques are described and discussed in depth. In particular, the results achieved in this PhD work are divided into three parts. Part 1 focuses on the characterization of chemical, physical, and mechanical properties of vulcanized HNBR samples with sulfur curative packages, along with their non-vulcanized counterparts. Studies have been conducted on the elastomeric network structure, SIC, chain orientation during stretching, and how these aspects depend on the crosslink density for samples with the same chemical composition. The analysis is focused on samples with ACN content of 43 and 44 wt%, with iRDB content of 5.5 and 9 mol%, respectively, and varying crosslink density. Vulcanized samples are amorphous at room temperature, with T_g values that increase as the crosslink density increases. The values of the Young's modulus of vulcanized samples are three times higher than that of the non-vulcanized counterparts. Furthermore, as the crosslink density increases, the tensile strength increases, while the strain at break decreases. SIC is observed in non-vulcanized and weakly to medium crosslinked samples, above a critical strain, while highly crosslinked samples break close to the SIC onset. Crystallinity arises from the presence of a non-negligible population of alternated tetramethylene/ACN (TMAC) sequences, crystallizing in the so-called Form II. The degree of orientation of the amorphous phase gradually increases as the strain increases, reaching a plateau at crystallization onset. The tensile strength of crystallizing HNBRs at high strains is attributed to the alignment of crystals formed by SIC in the stretching direction. The analysis is extended to sulfur vulcanized HNBR samples containing 34 and 36 wt% of ACN. It is shown that these samples are amorphous at room temperature. The glass transition temperature increases as the ACN content and crosslink density increases. They do not exhibit SIC at room temperature. Stretching induces orientation of the amorphous segments along the stretching direction, improving the tensile strength, and toughness while maintaining excellent elastic recovery. These results are detailed in the Chapter III.

Part 2 is focused on the chemical, physical, and mechanical characterization of samples with different ACN content (21, 34, 39, 43, and 50 wt%) and iRDB ≤ 0.9 mol%, as well as on samples with 34 and 43 wt% of ACN and iRDB = 5.5 mol%. Analyses were carried out on non-vulcanized and peroxide vulcanized samples. The vulcanized samples contained also 30 phr of carbon black as a reinforcing filler. The structure of elastomeric network is found to be homogeneous regardless of ACN content. All samples are amorphous at room temperature, except for the non-vulcanized samples with 43 and 50 wt% ACN and iRDB ≤ 0.9 mol%, which are already crystalline at room temperature and in the undeformed state. Vulcanized samples exhibit similar, ACN-independent, mechanical properties, while the non-vulcanized samples show poor mechanical properties. Exceptions occur for the crystalline samples, with 43 and 50 wt% ACN. The possible increase in crystallinity level induced by strain, along with the effect of strain on the orientation of the amorphous chains during stretching of the crystalline samples, was studied in detail. This study highlights that these sample do not exhibit SIC behavior, as the increment of crystallinity level achieved by stretching is due to the nucleation effect exerted by the pre-existing crystals. During release of the tension, the newly formed crystals are partially retained. Furthermore, the crystalline phase and the pinned amorphous chains, in the sample with 50 wt% of ACN, remain partially oriented, probably because the crystals and the amorphous chains remain entrapped in the elastomeric network by effect of local tensions. On the contrary, for the sample with 43 wt% of ACN, the newly formed crystals and the amorphous phase completely lose the orientation. These results are detailed in the Chapter IV:

Part 3 delves into the study of the DSC endothermic peaks generated by annealing treatments at temperatures near T_g, of some amorphous HNBR samples. This study is conducted through thermal analysis and dielectric spectroscopy on a peroxide vulcanized HNBR samples with 21 wt% of ACN and iRDB ≤ 0.9 mol% and on non-vulcanized, sulfur vulcanized and peroxide

vulcanized HNBR samples with 34 wt% of ACN, different iRDB content and different crosslink density. From the analysis it emerges that the DSC endothermic peaks are not due to the formation of thermally induced crystals but are more likely related to physical aging phenomena that generate endothermic relaxation peaks at temperatures above T_g, during DSC heating scans, coupled with occurrence of microphase separation of segments richer of tetramethylene sequences from sequence richer in ACN units. These results are detailed in the Chapter V.

In the conclusion the main results of the PhD thesis are outlined, emphasizing the importance of using complementary techniques and theoretical support to understand the material properties at the molecular level.

Chapter I

Introduction

1.1 From Natural Rubber to Synthetic Rubbers

Although humanity has been aware of its existence for centuries, it is only in the last hundred and fifty years that rubber has become a fundamental component of our civilization. Its very peculiar properties derive from the chemical structure and the way it has been modified. The noun "rubber" is strictly connected to the evolution of Polymer Science and Technology. Automotive industry would probably develop with a great delay, and it is very difficult to predict the evolution of modern human history without rubbers. All started with the paradigmatic discovery that the coagulated products of some latexes extracted from some tropical plants such as Hevea *brasiliensis*, addressed as "natural rubber", had peculiar properties. To date, the rubber properties are stigmatized in those of NR.

Natural rubber (NR) is a polymer of isoprene, specifically 1,4-*cis*-polyisoprene. The initial hypothesis dates back to 1835, when it was demonstrated that isoprene could be obtained by partial degradation of natural rubber. A definitive confirmation came when isoprene was polymerized, resulting in a substance similar to natural rubber. Today, we know that this polymer does not exactly match the constituent molecule of natural rubber but is a mixture of repeating units in *cis* and *trans* configuration. The determination of the chemical formula of natural rubber as a multiple of C_5H_8 building units dates back to 1826 and is credited to Michael Faraday (English, 1791-1867). Natural rubber is obtained in latex form from many trees and tropical shrubs, but the world's largest producer is a tree native to the Amazon region of Brazil, Hevea *brasiliensis*.[1,2]

The initial attempts to utilize NR involved transforming it into a flexible coating for fabrics, making them waterproof. This occurred primarily in England, by a Scottish chemist named Charles MacIntosh, who gave his name to the resulting waterproof clothing (a name still preserved today), and in the United States, starting in the 1830. However, despite achieving good waterproofing, these garments couldn't withstand seasonal variations, becoming stiff and fragile in winter and sticky and malodorous in summer. This led to the perception that the only practical use of natural rubber could be as erasers, as demonstrated by the English chemist Joseph Priestly in 1770.[1,2]

Just as enthusiasm for rubber was waning, around 1834, the American inventor Charles Goodyear began a series of experiments aimed at demonstrating that by mixing an inorganic powder with natural rubber, excess moisture making it sticky on hot days could be absorbed. He tried various substances without success until 1839 when he accidentally dropped some drops of the mixture onto a hot stove, resulting in a product that, after years of further experimentation, proved to be durable, elastic, and stable at both high and low temperatures. His discovery was later named "vulcanization" after the Roman god of fire, Vulcano. Once the properties of vulcanized natural rubber were recognized, the demand for this material grew rapidly, and the “rubber barons”, around a hundred Europeans exploiting the Amazon forests, became extremely wealthy through slavery imposed on the natives tasked with extracting latex from incisions made in the bark. The rubber trees, Hevea *brasiliensis*, accounted for less than 1% of those in the Amazon basin, each producing no more than one and a half kilograms of latex per year. A skilled worker could produce up to eleven kilograms of rubber per day. To increase production in the 1870-1880, many rubber trees were cut down, enabling the extraction of fifty kilograms of latex from each tree. While this increased profits, it deprived them of a source that would have continued to produce.[1,2]

This situation worried England, and in 1876, Henry Alexander Wickam transported 70,000 Hevea *brasiliensis* seeds to the Royal Botanical Gardens laboratories at Kew, just outside London. Some

of these seeds germinated in a specially constructed greenhouse. Shortly after, 1900 rubber tree seedlings were sent to Asia, initiating a second rubber dynasty in Ceylon and Malaysia. In 1907 more than ten million cultivated rubber trees existed, and to meet the necessary workers, thousands of workers were imported. It was also shown that well cared for trees could be tapped daily for their latex and could begin producing after four years, while wild ones required twenty-five years. Rubber production from plantations quickly surpassed that from the Amazon forests: by 1932, 98% of rubber came from Asia. This heavy reliance concerned the United States, which had significant needs for industrialization and transportation, leading to considerations about the possibility of producing synthetic rubber.[1-3]

Attempts to produce synthetic rubber through isoprene polymerization failed initially, as the knowledge at the time didn't allow the creation of a molecule entirely made up of *cis* repeating units, the form capable of endowing the polymer with optimal properties similar to those of natural rubber. Instead, a product constituted by a mixture of double bonds in *cis* and *trans* configurations was obtained. Success in this synthesis awaited until 1953 with the discoveries of Karl Ziegler in Germany and Giulio Natta in Italy. Alternatively, during World War I, when natural rubber supplies to Germany from Southeast Asia were blockaded, German chemical companies developed a variety of products similar to rubber, the best of which was Styrene Butadiene Rubber (SBR), closely mimicking the properties of natural rubber. In 1929, the Standard Oil Company of New Jersey reached an agreement with IG Farben that included access to certain IG Farben patents, including SBR. The Germans believed that this patent lacked sufficient technical details for Americans to produce SBR, but the entire US chemical industry mobilized and soon could manufacture this rubber. By 1945, production had reached 800,000 tons, a significant output for the country's total rubber consumption. In the following decades, other synthetic rubbers like neoprene and butyl

rubber were developed, expanding the term "rubber" to include polymers different from polyisoprene but closely related to its properties.[1,3,4]

During the Korean War in 1951 and the Suez Crisis in 1956, it became evident that even in Europe, relying on regular supplies of natural rubber at stable prices would no longer be feasible. These difficulties, coupled with insufficient natural production, led many European countries to almost simultaneously decide to construct new plants for synthetic elastomer production. Consequently, the rubber industry assumed global dimensions. Since then, growth has been rapid, not just in terms of production capacity but also due to the wide range of types developed to meet diverse market demands.[3,4]

For simplicity, although debatable, synthetic elastomers are commonly categorized into two main families: general-purpose and special purpose. The general-purpose elastomers strike a balance between various physical properties while remaining economical for a broad range of applications, primarily in tire construction. In contrast, special-purpose elastomers sacrifice certain properties for others and generally come at a higher cost, catering to a more sophisticated market where product requirements outweigh economic concerns.[5,6]

Within the realm of general-purpose elastomers, there is a further subdivision into:

- unsaturated elastomers
- predominantly saturated elastomers

Unsaturated elastomers are characterized by the presence, along the polymer chain, of high percentages of (=CH-CH_2-) groups derived from the 1,4 polymerization of conjugated dienes. These groups impart significant flexibility to the macromolecule, resulting in excellent elastic and dynamic properties due to low steric hindrance for rotation around the C-C bonds adjacent to the double bond. Simultaneously, these groups serve as points of chemical crosslinking in these

products. Polymers in this category include polybutadiene, polyisoprene, and butadiene-styrene copolymers.[5]

It's known that saturated hydrocarbon chains can also exhibit good and variable flexibility characteristics, although generally inferior to the aforementioned products, depending on the size and type of substituents on the polymer chain. Therefore, this type of polymer has also found significant applications in the field of elastomers, presenting clear advantages over unsaturated elastomers concerning aging resistance and various chemical agents. In most cases, these polymers contain limited percentages of olefinic unsaturations along the polymer chain or as side groups, enabling crosslinking using standard sulfur-based recipes and accelerants. Polymers in this elastomer class include homopolymers and copolymers of isobutylene and copolymers and terpolymers based on ethylene and propylene.[5]

On the other hand, special-purpose elastomers possess distinct characteristics that set them apart from general rubbers, such as heat and/or oxygen and ozone resistance, solvent and/or lubricant oil resistance, chemical agent resistance, good performance in high and/or low temperatures, air and/or water vapor impermeability, biocompatibility, etc. The first special elastomers, emerging around the 1930s, were initially studied as potential substitutes for natural rubber. The success of styrene-butadiene copolymers during World War II virtually limited the tire market to other synthetic rubbers known at that time but favored their use in specific sectors where their unique properties played a particularly important role. For instance, polychloroprene, unable to compete with SBR in applications such as tires due to its higher rigidity at room temperature and higher cost, found significant use in technical articles like seals, pipes, cables, belts, and fabric waterproofing, owing to its resistance to oils, high temperatures, and atmospheric agents. The intensive research activity in synthetic polymer development during the two decades after World War II significantly enriched the spectrum of special elastomers, adapting their characteristics to the specific requirements of

different application sectors. The development of new elastomers was further facilitated by the high level of knowledge attained in transformation technologies and vulcanization processes, allowing the handling of challenging materials and the production of vulcanized materials suitable for special purposes. The study of elastomer rheology, especially concerning their molecular structure, and the development of new formulations for programmed rate crosslinking significantly advanced transformation techniques. For example, they allowed the use of widely spread and highly productive processes like injection molding, while identifying vulcanization recipes capable of forming particularly stable inter-chain bridges enabled the production of vulcanized materials resistant to high temperatures with minimal compression set.[6]

The importance of special elastomers lies in their unique characteristics that distinguish and differentiate the various materials within this class. Their destiny is linked to increasingly sophisticated and stringent applications rather than the overall volume of use. Some special-purpose elastomers include nitrile rubber, polychloroprene, polyurethanes, fluorinated elastomers, etc.[6]

1.2 Rubber Elasticity

An elastomer is defined as a material capable of undergoing significant deformations due to relatively small forces and reverting to its original dimensions upon the removal of the load. Typically, elastomers exhibit a Young's modulus on the order of 0.1-1 MPa and a deformation at break in the range of 10^3-10^4 %. Even from the earliest studies on the elasticity of natural rubber, it was recognized that the exceptional extensibility of this material stemmed from the ability of individual chains to exist in coiled conformations, that can be greatly stretched by application of a modest tensile force, owing to minute displacements of structural elements.

It was well understood that the segments of macromolecular chains undergo Brownian motion, causing the chains themselves to assume random coil conformations in accordance with the principle of maximum entropy (Fig. 1.1A). Applying a unidirectional force to such a system results in the uncoiling of the chains, a preferential orientation of their axis in the stretching direction hence occurs, leading to a reduction in the number of possible conformations and consequent decrease in entropy (Fig. 1.1B). However, the system evolves over time even without removing the force, as chain segments slip relative to one another, and Brownian motions restore the initial random coil conformations of the chains (Fig. 1.1C). Hence, the macroscopically deformed material is microscopically disordered as in initial state so, upon removing the force, the sample keeps in the plastically deformed state (Fig. 1.1D), since the supplied energy has been entirely dissipated to activate the viscous flow of chains.

For a material to exhibit elasticity, there needs to be some form of impediment to the free movement of segments while still allowing chains to assume random conformations. If macromolecules are linked together by permanent chemical bonds or by different types of physical constraints to form a three-dimensional network (Fig. 1.1 A'), the junction points between chains prevent viscous flow under load, thus hindering the recovery of random conformations (Fig. 1.1 C'). This results in the development of a retractive force within the system, leading to the recovery of the initial state upon removing the applied force. This recovery occurs both at a macroscopic level (dimensions of the sample) and at a microscopic level (structure of macromolecules) (Fig. 1.1 D'). From an experimental standpoint the above behaviour is approached in a quasi-static mechanical tests.[7]

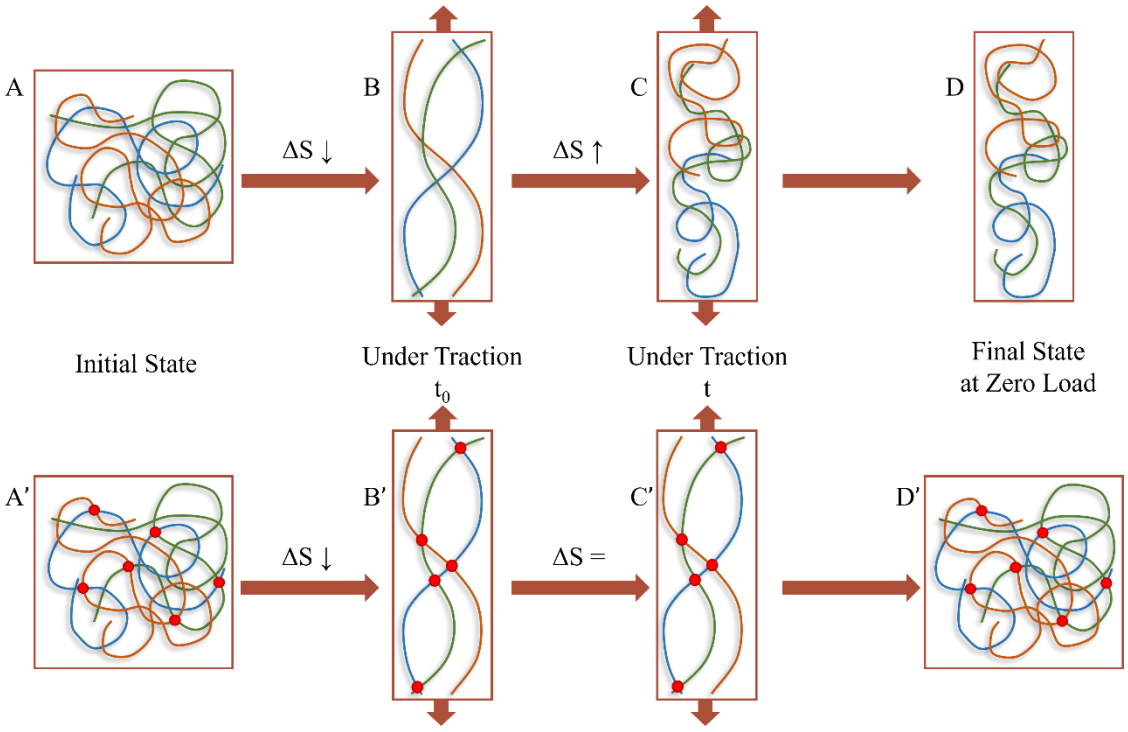

Figure 1.1 Comparison between the structural evolution of a macromolecular system without internal constraints subjected to stretching and the deformation of a sample exhibiting elastomeric characteristics.

The above considerations allow defining the rubbery state as determined by the simultaneous presence of the following items:

1. Flexible chains, consisting of a long sequence of covalent bonds endowed with low rotational barriers, ideally free rotation, around the internal torsion angles.

2. Low intermolecular cohesive forces, similar to those in liquids, allowing extensive movement of chain segments. The polymer must have a glass transition temperature (T_g) much lower than the operating temperature T.

3. Junction points (alias crosslinks) between macromolecular chains, such as permanent chemical bonds or physical nodes, hindering chain slip motion.

It is worth noting that the substantial entropic contribution present in rubber elasticity does not have a counterpart in elasticity of metals or any other type of crystals (ceramics), "frozen" amorphous materials like glasses, regardless of their chemical nature, which is mainly enthalpic in nature.

1.2.1 Simple Elongation

Defining the elastic behavior of a body involves finding the law expressing the total work W expended in the deformation process as a function of the system characteristic parameters. If the final state can be characterized by a single stretch ratio $\lambda = L/L_0$, where L is the final dimension of the sample and L_0 is its initial dimension, generally, the total work W is expressed as: [7,12-19]

$$W = W(T, P, \lambda) \tag{1.1}$$

or

$$W = W(T, V, \lambda). \tag{1.2}$$

T, P and V are the temperature, the pressure and the volume of the system.

Let's consider the simple case of a cubic piece of matter with initial edge dimensions L_0 subjected to homogeneous deformation characterized by three principal loads (Fig. 1.2):

$$p_x = \frac{f_x}{L_0^2} \ldots\ldots\ldots p_y = \frac{f_y}{L_0^2} \ldots\ldots\ldots p_z = \frac{f_z}{L_0^2} \tag{1.3}$$

Along three mutually perpendicular axes the stretch ratios are:

$$\lambda_x = \frac{L_x}{L_0} \ldots\ldots\ldots \lambda_y = \frac{L_y}{L_0} \ldots\ldots\ldots \lambda_z = \frac{L_z}{L_0} \tag{1.4}$$

Under these conditions we have:

$$W = f_x\lambda_x + f_y\lambda_y + f_z\lambda_z \tag{1.5}$$

and we also have:

$$\lambda_x \lambda_y \lambda_z = \frac{V}{V_0} \tag{1.6}$$

For simple elongation, if the force *f* is be applied in the *x*-direction, we instead have:

$$p_x = \frac{f}{L_0^2}; \; p_y = p_z = 0 \tag{1.7}$$

$$\lambda_x = \lambda; \; \lambda_y = \lambda_z = \left(\frac{V}{V_0}\right)^{1/2} \lambda^{-1/2} \tag{1.8}$$

It is often convenient to define the stretch coefficients, which take into account the variation in the shape of the sample (transformation 3 of Fig. 1.2)

$$\Lambda_x = \frac{L_x}{L_1} = \frac{L_x}{L_0 \left(\frac{V_1}{V_0}\right)^{1/3}} = \lambda_x \left(\frac{V_0}{V_1}\right)^{1/3} \tag{1.9}$$

In the case of simple elongation:

$$\Lambda_x = \Lambda = \lambda \left(\frac{V_0}{V}\right)^{1/3}; \; \Lambda_y = \Lambda_z = \Lambda^{-1/2} \tag{1.10}$$

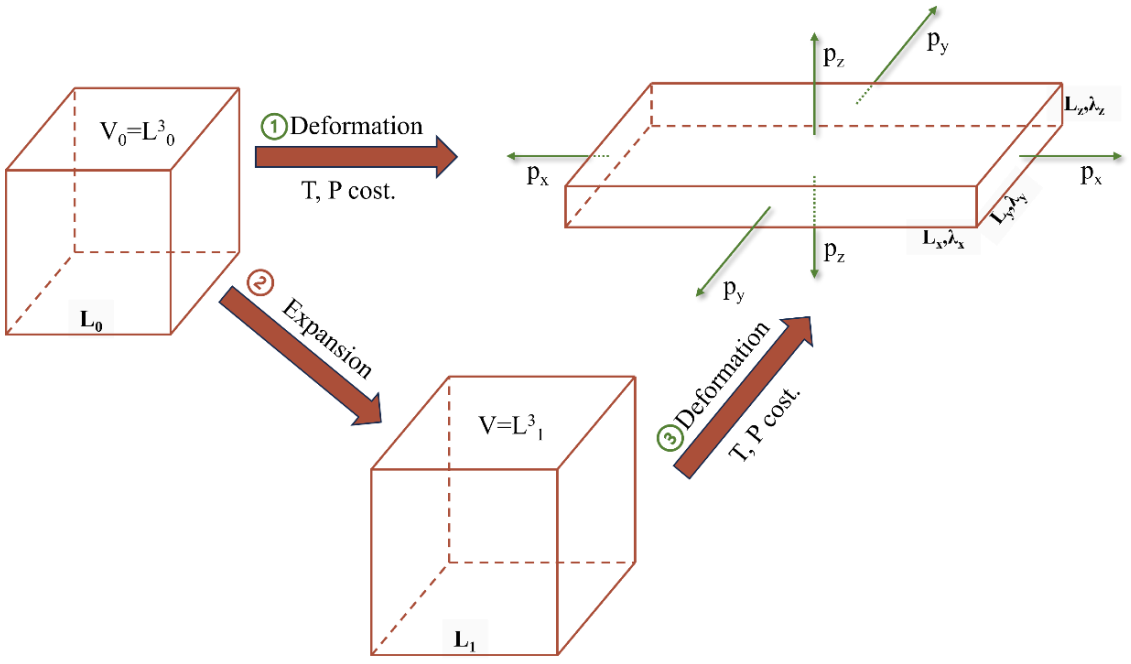

Figure 1.2 Simple deformation; definition of principal loads, stretch ratios, and stretch coefficients.

1.2.2 Thermodynamics of the stretching process

Constant volume state equation

We consider temperature T, volume V, and sample length L as the independent variables of the stretching process. Assuming the process is reversible, the differential change of Helmholtz free energy dA is (at constant T, $dA = dW$):

$$dA = -SdT + fdL \tag{1.11}$$

from which it is possible to obtain:

$$f = \left(\frac{\partial A}{\partial L}\right)_{T,V} = \left(\frac{\partial U}{\partial L}\right)_{T,V} - T\left(\frac{\partial S}{\partial L}\right)_{T,V} = f_e + f_s \tag{1.12}$$

in which U is the internal energy ($\mathrm{d}U = T\mathrm{d}S + \mathrm{d}A$).

This signifies the existence of two contributions, one energetic (f_e) and one entropic (f_s), to the elastic retraction force. Regarding the former, assuming constant volume, since intermolecular interactions are independent of the system shape, f_e depends solely on the intrinsic energetic characteristics of the macromolecular chains. In the case of chains with free rotation around the internal torsion angles, $f_e = 0$, yielding the ideal rubber, the elasticity of which is purely entropic. For chains with partially hindered rotation, $f_e \neq 0$, and its sign depends on the form of the potential barrier. In particular, for C-C bond sequences, if the *trans* conformation is less stable than the *gauche* conformation, stretching may result in increased internal energy of the chain, leading to a positive f_e contribution, and negative otherwise (the polymer P1-C-C-P2 is said to be in a *trans* conformation when the chain ends (P1 and P2) are arranged at 180° relative to each other with respect to the C-C bond axis, and in a *gauche* conformation when P1 and P2 are arranged at 60° relative to each other). From these considerations, it emerges that the energetic contribution to the elastic retraction force basically depends on the barrier type opposing free bond rotation, similar to

the temperature coefficient of the undisturbed dimensions of the macromolecules, including rubbers. As will be shown later, these quantities are simply correlated.[12-19]

Regarding the entropic contribution, from equation 1.11 we have:

$$S = -\left(\frac{\partial A}{\partial T}\right)_{V,L} \tag{1.13}$$

therefore:

$$\left(\frac{\partial S}{\partial L}\right)_{T,V} = -\left(\frac{\partial^2 A}{\partial T \partial L}\right)_V = -\left(\frac{\partial f}{\partial T}\right)_{V,L} \tag{1.14}$$

It has been stated that the entropy of an elastic network decreases as the stretching increases due to transition of the chain conformation from random coil to elongated states. Consequently, the partial derivative of force with respect to the temperature, at constant volume and length, is positive. This entails that to maintain a rubber sample deformed at length L with constant volume, the applied force should increase as the temperature increases. This can be intuitively explained by considering that a sample deformed from L_0 to L due to the application of a force f_1 at temperature T_1 corresponds to a state characterized by chains subjected to elongation in the stretching direction. An increase of the temperature leads to more intense Brownian movements, and hence an increase of the force needed to prevent retraction due to the tendency of the chain to recover more disordered (coiled) conformations.[7,12-19]

This behavior is contrary to metals and arises from the essentially entropic nature of rubber-like elasticity. In the case of crystalline solids, increasing the temperature reduces cohesion forces, allowing the same elongation to be achieved with less effort.

Finally, from equations 1.13 and 1.14, it is found:

$$f = f_e + f_s = \left(\frac{\partial U}{\partial L}\right)_{T,V} + T\left(\frac{\partial f}{\partial T}\right)_{V,L} \tag{1.15}$$

This is the equation of state for elasticity at constant volume. Thermoelastic measurements, involving the study of the force behavior at constant volume V and deformation as a function of temperature, can allow to evaluate the two contributions to the elastic retraction force separately. As shown in Figure 1.3, the tangent at point A on the experimental curve corresponds to the entropy change associated with stretching, while the intercept on the ordinate axis for $T = 0$ K provides the energetic contribution. If the force grows linearly as the temperature increases, f_e and f_s are temperature-independent; if the force is directly proportional to T and *the tangent* at any point passes through the origin, f_e is null, and the elastic force is solely entropic in origin (ideal rubber). [7,12-19]

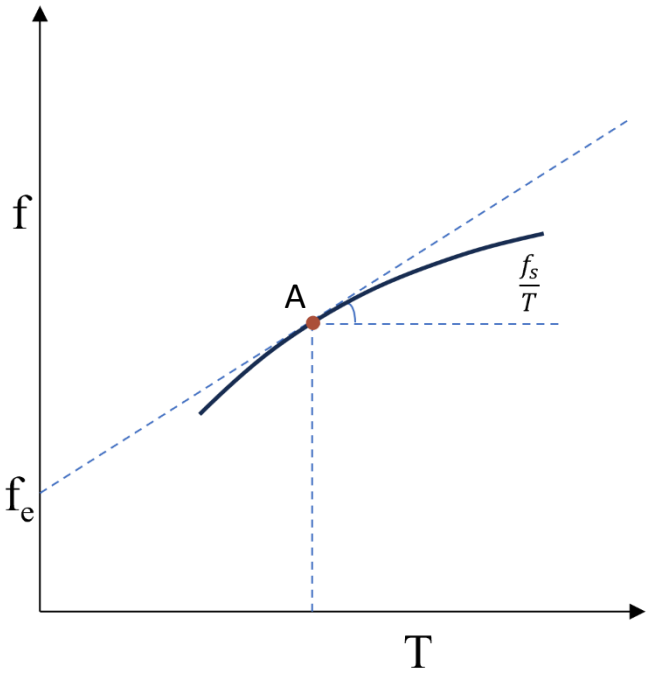

Figure 1.3 Uniaxial elongation. Variation of the elastic retraction force as a function of the temperature, at constant volume and deformation.

The state equation at constant volume, while valuable for outlining the basis of rubber elasticity, is not widely utilized experimentally since maintaining the rubber volume strictly constant during measurements is not easily achievable.

Constant pressure state equation

Given that thermoelastic measurements are typically performed at constant pressure, it is crucial to discuss the state equation of rubber elasticity under these conditions. Considering temperature *T*, pressure *P*, and sample length *L* as independent system variables, assuming a reversible stretching process, the differential change of the Gibbs free energy *dG* is:

$$dG = -VdP - SdT + fdL \tag{1.16}$$

from which it is possible to obtain:

$$f = \left(\frac{\partial G}{\partial L}\right)_{T,P} = \left(\frac{\partial H}{\partial L}\right)_{T,P} - T\left(\frac{\partial S}{\partial L}\right)_{T,P} = f_h + f_s \tag{1.17}$$

and hence we have:

$$f = f_h + f_s = \left(\frac{\partial H}{\partial L}\right)_{T,P} + T\left(\frac{\partial f}{\partial T}\right)_{P,L} \tag{1.18}$$

This represents the state equation for rubber elasticity under constant pressure, in which f_h, and f_s represent the enthalpic and entropic elastic retraction force contributions.

Thus, it is possible to measure the force as a function of temperature while keeping the sample length and pressure constant. Subsequently, one can separate the two contributions to the retraction force, similarly to what shown for constant volume systems. By conducting experiments at various *L* values (Fig. 1.4), the change of f, f_h, and f_s at constant temperature as a function of deformations can be established (Fig. 1.5).[8,9,12-19]

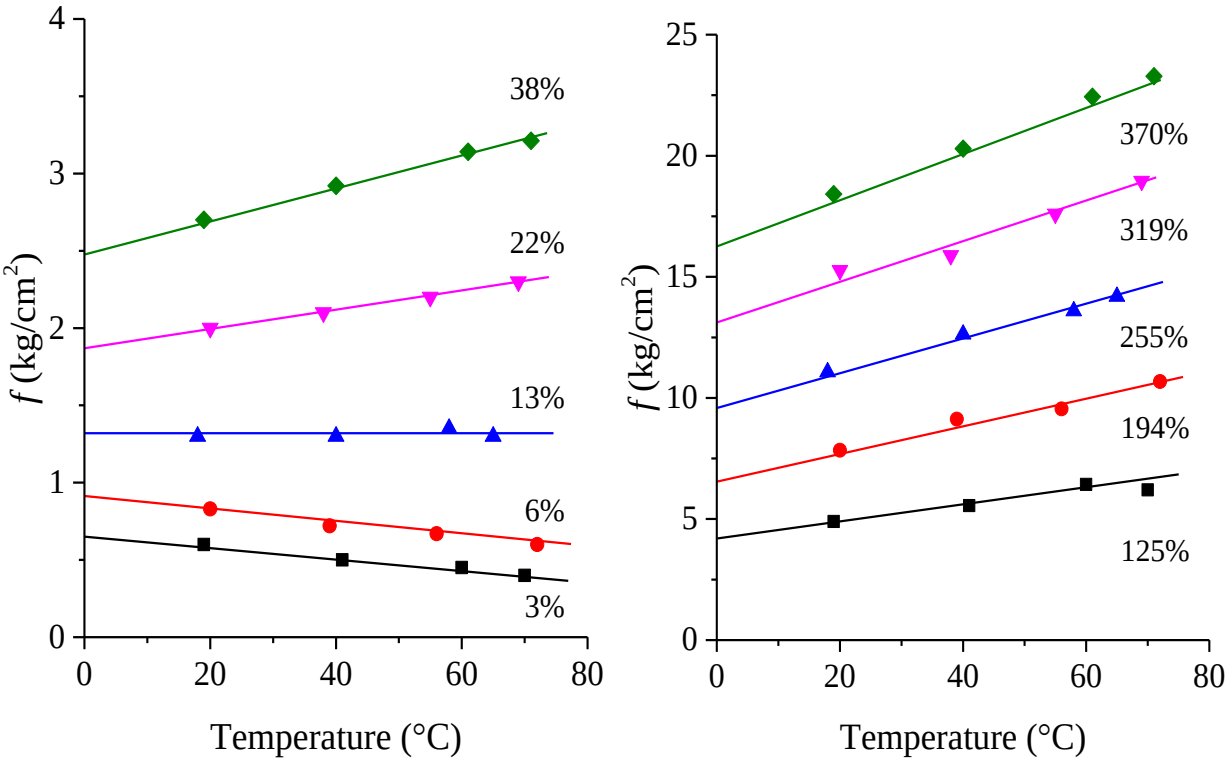

Figure 1.4 Uniaxial elongation. Variation of the elastic retraction force (1 kg/cm^2 = 98.07 kPa) as a function of the temperature, at constant pressure at the indicated values of strain.[8]

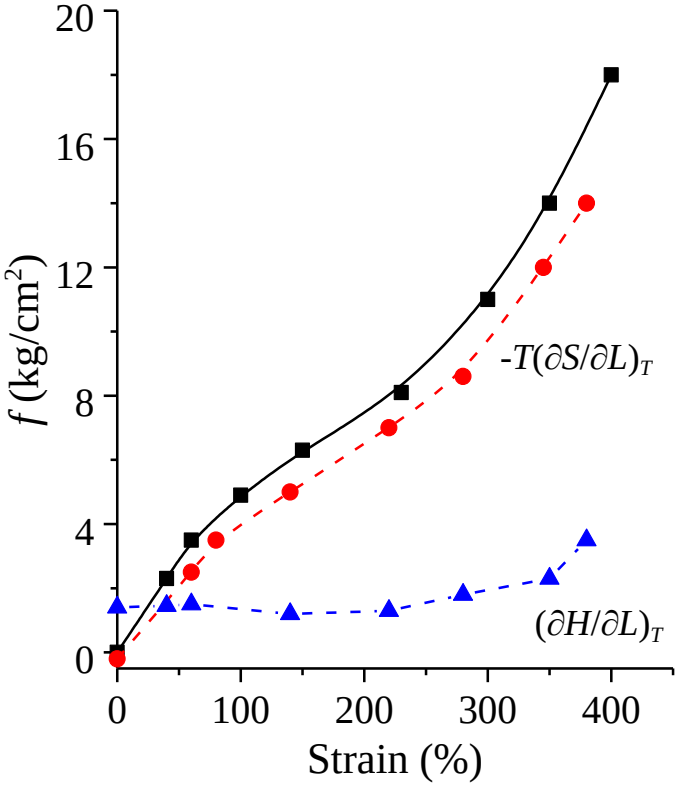

Figure 1.5 Uniaxial elongation. Values of the elastic retraction force (1 kg/cm^2 = 98.07 kPa) and its components as a function of strain from measurements at constant pressure and temperature.[8]

The enthalpic contribution to the retraction force is not straightforward to interpret as it includes, in addition to the term associated with the internal energy of the chains, the contribution arising from the volume variation associated with stretching at constant pressure:

$$\left(\frac{\partial H}{\partial L}\right)_{T,P} = \left(\frac{\partial U}{\partial L}\right)_{T,P} + P\left(\frac{\partial V}{\partial L}\right)_{T,P} = \left(\frac{\partial U}{\partial V}\right)_{T,L}\left(\frac{\partial V}{\partial L}\right)_{T,P} + P\left(\frac{\partial V}{\partial L}\right)_{T,P} \qquad (1.19)$$

The relative volume variation with the sample length is numerically small (Fig. 1.6), but only the term $T\left(\frac{\partial f}{\partial T}\right)_{P,L}$ in Equation 1.18 is negligible, at least for pressures below 100 atm. The term corresponding to the product of the volume change with the sample length at temperature and pressure constant and the pressure, $P\left(\frac{\partial V}{\partial L}\right)_{T,P}$, indeed, is not a priori negligible because P can be very large ($> 10^3$ atm). On the other hand, Figure 1.4 also demonstrates that thermoelasticity measurements at constant pressure and constant sample length lead to negative slopes of the force vs. the temperature for strain below a critical value equal to 100 $(L_i\text{-}L_0)/L_0 \approx 10\%$. This strain corresponds to the strain of thermoelastic inversion. For strain values lower than that of thermoelastic inversion, the force required to keep the sample length constant decreases as the temperature increases. In correspondence of the thermoelastic inversion strain, the force remains constant with the temperature, and only at deformations higher than this critical value, the force increases as the temperature increase. The occurrence of a thermoelastic inversion strain is due to the fact that for small elongations, the effect of the thermal expansion of the sample predominates over the rubber elastic effect. At low deformations, indeed, the thermal expansion experienced by the sample upon heating (enthalpic effect), exceeds the thermally induced disorientation of chains (entropic effect).[8,9,12-19]

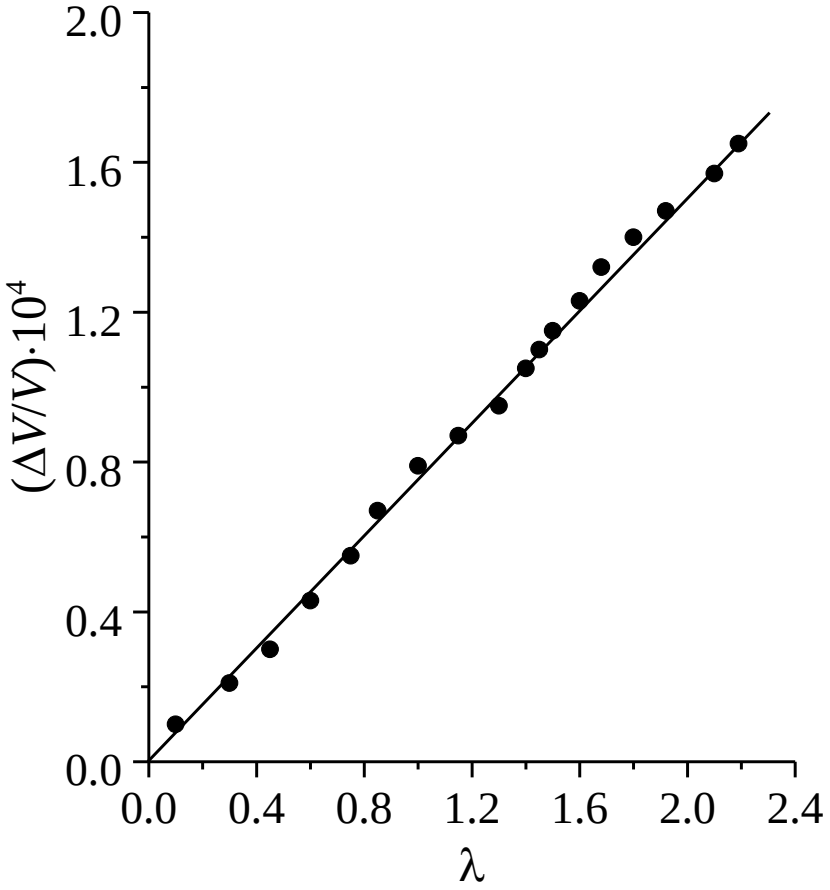

Figure 1.6 Relative volume change as a function of stretch ratio λ.[9]

In order to evaluate the enthalpic contribution to the retraction force, getting rid of the thermoelastic inversion, it is convenient to consider the effect of a constant deformation ratio λ, instead of a constant sample length, on relevant physical quantities, as follows:

$$df = \left(\frac{\partial f}{\partial T}\right)_{P,\lambda} dT + \left(\frac{\partial f}{\partial \lambda}\right)_{P,T} d\lambda \qquad (1.20)$$

$$\left(\frac{\partial f}{\partial T}\right)_{P,L} = \left(\frac{\partial f}{\partial T}\right)_{P,\lambda} + \left(\frac{\partial f}{\partial \lambda}\right)_{P,T} \left(\frac{\partial \lambda}{\partial T}\right)_{P,L} = \left(\frac{\partial f}{\partial T}\right)_{P,\lambda} - \frac{\lambda^3+2}{\lambda^2-1}\frac{\alpha_T f}{3} \qquad (1.21)$$

where α_T is the coefficient of thermal expansion of the undeformed material. In practice, once measured the tensile force as a function of λ at constant temperature, for each λ, one can measure the slope of the force-temperature curve at the selected *T* and constant pressure and can evaluate the quantity $T(\partial f/\partial T)_{P,\lambda}$ (see Fig. 1.7). The curve obtained by subtracting $T(\partial f/\partial T)_{P,\lambda}$ to *f* in Figure

1.7, yields the correct enthalpy contribution at any stretch ratio in the case of a NR sample.[10] This quantity is negative and very small up to stretch ratio of λ = 4, and increases in absolute value, probably by occurrence of strain-induced crystallization (vide infra).

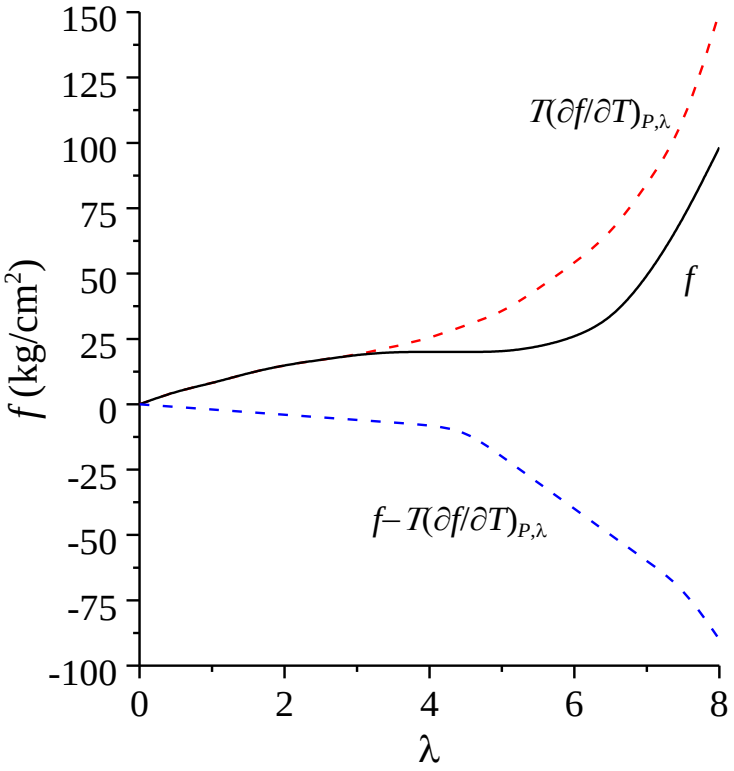

Figure 1.7 Uniaxial elongation. Values of the elastic retraction force (1 kg/cm^2 = 98.07 kPa) measured as a function of stretch ratio λ, and the corrected constants based on eq. 1.9 as functions of the stretch ratio from measurements at constant pressure and length.[10]

1.2.3 Molecular Theory of Rubber Elasticity

The goal of statistical treatment in rubber elasticity is to theoretically derive the expression of retraction force concerning the structural characteristics of the elastomer and the stretch ratio. This treatment can be divided into two parts:

- From the statistical properties of a single chain, a mathematical expression for the chain free energy is derived based on the end-to-end distance between its ends.

- The sum of contributions from individual chains constituting the elastomeric network yields the representation of the elastic properties of the material.

Single Chain

It is important to remember that the molecular description of a polymer single chain is performed resorting to more or less idealized models, where mathematical treatment can be done with varying degrees of approximation, sometimes at the expense of physically significant aspects.

A suitable description of flexible polymer chains in the melt and amorphous state corresponds to chains in the unperturbed state. In the unperturbed state interactions between units along the chain can be neglected in describing the conformational states. A chain for which this is allowed is addressed as phantom. Since the distribution of the size of a phantom chain is a Gaussian function, the chains are also addressed as Gaussian.

Accordingly, the dimensions of the chains in the unperturbed state are described by the probability density $W(r)$, the Gaussian function, that calculates the probability that the distance between two ends of a chain lies in between r and r+dr:

$$W(r)dr = \left(\frac{3}{2\pi<r_0^2>}\right)^{3/2} e^{-\frac{3}{2<r_0^2>}r^2} dr \qquad (1.22)$$

where $< r_0^2 >$ corresponds to the mean square end-to-end distance.

The associated free energy for a single chain based on its dimensions r is then given by:

$$F_{int.} = cost. + kT\frac{3}{2<r_0^2>}r^2 \qquad (1.23)$$

Considering a macromolecule with ends at distance r, the work required to move the second end from r to r + dr is dW = fdr. Hence, we have:

$$f = \frac{dW}{dr} = \left(\frac{\partial F_{int.}}{\partial r}\right)_T = \frac{3kT}{<r_0^2>}r \qquad (1.24)$$

This implies that a macromolecule with ends at distance r is subject to a pulling force f directed along the line joining these ends and is proportional to their distance. Due to the statistical nature of macromolecular size, f represents a value subject to continuous fluctuations. It is evident that the equilibrium state, corresponding to the maximum value of entropy, occurs when the two ends of the macromolecular chain are coincident (phantom chain).[12-19]

Elastic Network

To transfer the concepts pertinent to a single chain to a three-dimensional elastic network, it is necessary to formulate certain assumptions. Firstly, consider the elastic network as a set of chains linked together by a relatively small number of junction points (crosslinks), so that the movements of segments between two consecutive junction points are analogous to those in an isolated chain. The segment of a macromolecule between two consecutive junction points is called an "elastically effective chain". An ideal network is defined if all chains are elastically effective, thus having no defects. If v denotes the number of elastically effective chains contained in a volume V_0 of the material and divides this set into n groups such that the head-to-tail distance r_i is the same (within rather limited limits) for all v_i members of each group, the total free energy is the sum of individual contributions:

$$F(T,V_0) = F^*(T,V_0) + kT\sum_i^n v_i\left(\frac{3}{2<r_{i0}^2>}r_i^2\right) \qquad (1.25)$$

where the term $F^*(T,V_0)$ accounts for intermolecular interactions. The second assumption is to consider the junction points as fixed in the volume occupied by the network. In reality, these points oscillate around their mean positions in line with conformational variations of the elastic chains they are associated with. In a lattice of Gaussian chains, these oscillations can be described by a probability function, which is also Gaussian, and the mean value of fluctuations is independent of the extent of deformation experienced by the lattice. This implies that the part of entropy dependent

on junction point fluctuations does not contribute to the overall value of deformation entropy, thus justifying the assumption made in a first approximation in the theory.[12-19]

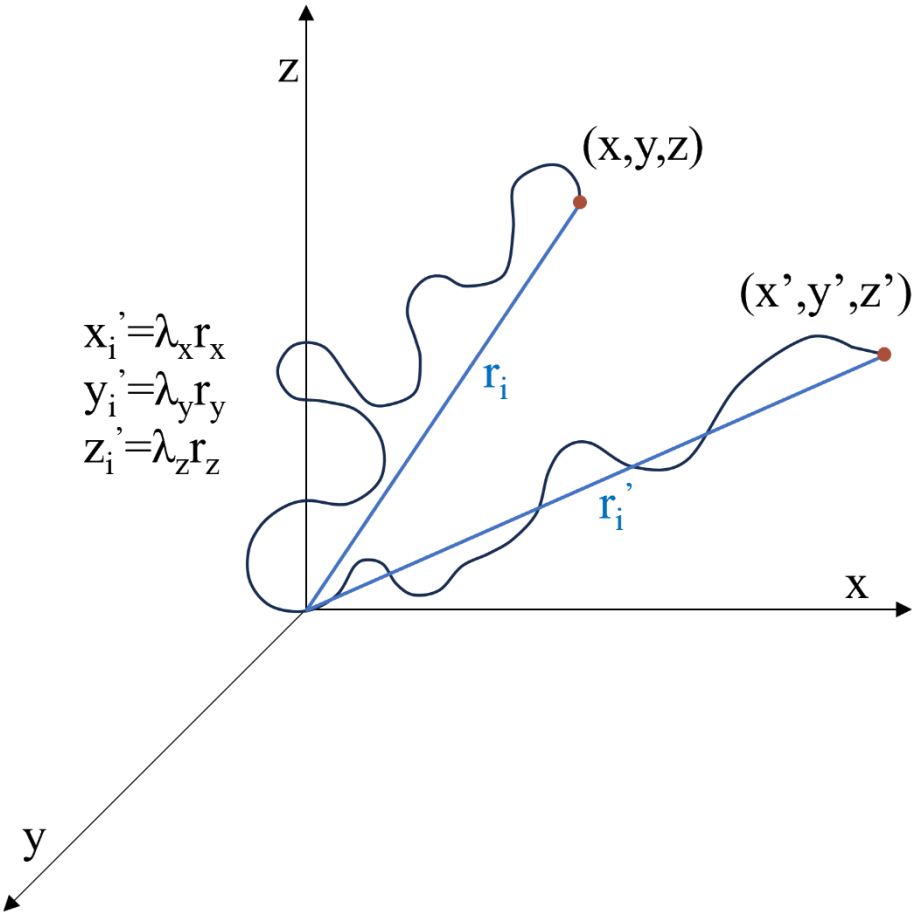

Figure 1.8 Affine elastic deformation of an elastically effective chain in a rubber network with end-to-end distance equal to r_i before deformation, r_i' after deformation.

Thirdly, it's necessary to assume that the deformation of the network is "affine." This means that each elastically effective chain with end-to-end distance equal r_i before deformation (components x_i, y_i, z_i), is subjected to a deformation such that the attained end-to end distance, equal to r_i', have components x_i', y_i', z_i' equal to:

$$x_i' = \lambda_x x_i;\ y_i' = \lambda_y y_i;\ z_i' = \lambda_z z_i \qquad (1.26)$$

where $\lambda_x = \frac{L_x}{L_0}$; $\lambda_y = \frac{L_y}{L_0}$; $\lambda_z = \frac{L_z}{L_0}$ are the *x*, *y* and *z* components of the macroscopic stretch ratios. In the case of simple elongation with the force applied in the *x*-direction, equation 1.8 holds.

A fourth assumption, already considered valid in the thermodynamic treatment of the problem, concerns intermolecular interactions, assumed to depend only on the volume of the sample and not on its shape.[12-19]

If we further assume that the deformation is such that it does not hinder the application of Gaussian statistics to the distribution of dimensions of each elastically effective chain, the free energy of the deformed network can still be written in the form:

$$F(T,V) = F^*(T,V) + kT\sum_i^n v_i\left(\frac{3}{2<r_{i0}^2>}(r_i')^2\right) \qquad (1.27)$$

For uniaxial elongation we have:

$$(r_i')^2 = (x_i')^2 + (y_i')^2 + (z_i')^2 = \lambda^2 x_i^2 + \frac{1}{\lambda}(y_i^2 + z_i^2)\frac{V}{V_0} \qquad (1.28)$$

Additionally, since in the undeformed state all directions of the vector *r* are equivalent:

$$x_i^2 = y_i^2 = z_i^2 = \frac{r_i^2}{3} \qquad (1.29)$$

It follows that:

$$(r_i')^2 = \frac{r_i^2}{3}\left(\lambda^2 + \frac{2}{\lambda}\frac{V}{V_0}\right) \qquad (1.30)$$

Hence, we have:

$$F(T,V) = F^*(T,V) + kT\sum_i^n v_i\frac{r_i^2\left(\lambda^2+\frac{2}{\lambda}\frac{V}{V_0}\right)}{2<r_{i0}^2>} \qquad (1.31)$$

The change in free energy in the system due to stretching is therefore:

$$\Delta F = F^*(T,V) - F^*(T,V_0) + kT\sum_i^n v_i\frac{r_i^2\left(\lambda^2+\frac{2}{\lambda}\frac{V}{V_0}-3\right)}{2<r_{i0}^2>} = \Delta F^* + \frac{vRT}{2}\frac{<r^2>}{<r_0^2>}\left(\lambda^2 + \frac{2}{\lambda}\frac{V}{V_0} - 3\right) \qquad (1.32)$$

using eq. 1.10 it turns out that:

$$\Delta F = \Delta F^* + \frac{vRT}{2}\frac{<r^2>}{<r_0^2>}\left(\frac{V}{V_0}\right)^{\frac{2}{3}}\left(\Lambda^2 + \frac{2}{\Lambda} - 3\left(\frac{V}{V_0}\right)^{-\frac{2}{3}}\right) \quad (1.33)$$

This value is greater than zero since $\Lambda > 1$. In this equation, ΔF^* is the intermolecular contribution associated with the change in volume due to stretching; $<r^2>$ is the mean squared end-to-end distance of the elastically effective chains in an isotropic state at T and V_0, and $<r_0^2>$ is the mean squared end-to-end distance these chains would have if they were free and undisturbed. There are no valid reasons why these two values should, a priori, be numerically coincident. It follows that the elastic retraction force, given by:

$$f = \left(\frac{\partial \Delta F}{\partial L}\right)_{T,V} = \frac{1}{L}\left(\frac{\partial \Delta F}{\partial \Lambda}\right)_{T,V} \quad (1.34)$$

is expressed by the following theoretical equation of state:

$$f = vkT\frac{<r^2>}{<r_0^2>}\frac{V^{1/3}}{{V_0}^{2/3}}\left(\Lambda - \frac{1}{\Lambda^2}\right) \quad (1.35)$$

Based on this, within the limits of the assumptions made, the elastic properties of rubbers are found to be independent of the chemical nature of the macromolecules composing the rubber itself. Instead, they are related to the to the length, number per unit volume and intrinsic properties of elastically effective chains.[12-19]

A very good agreement between experimental results and predictions of molecular theory is observed only for very small values of Λ and in the case of unidirectional compression experiments, with free expansion of the sample in the other two orthogonal directions (Fig. 1.9).[16]

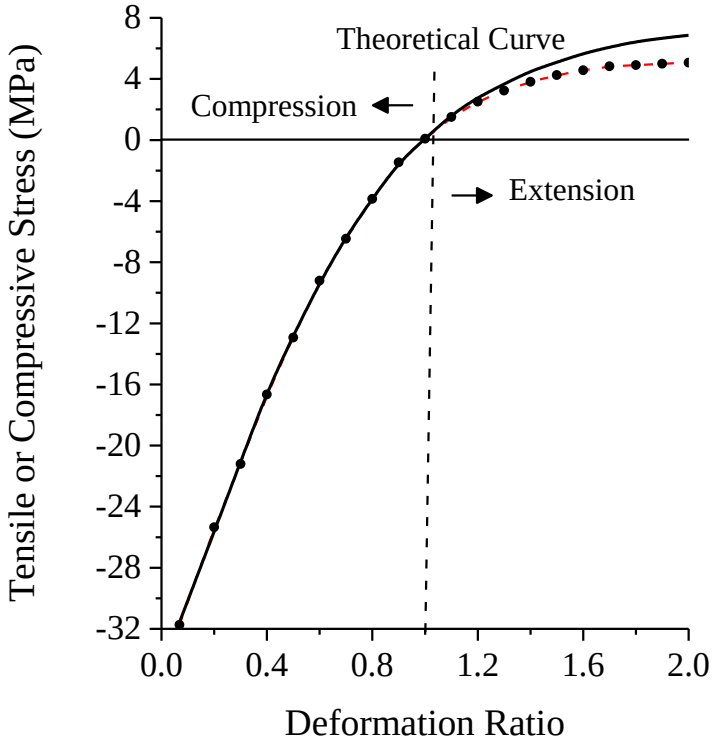

Figure 1.9 Comparison between the experimental curve of compression/extension stress vs. stretch ratio λ measured by applying uniaxial force (dots) and theoretical prediction by eq. 1.35.[16]

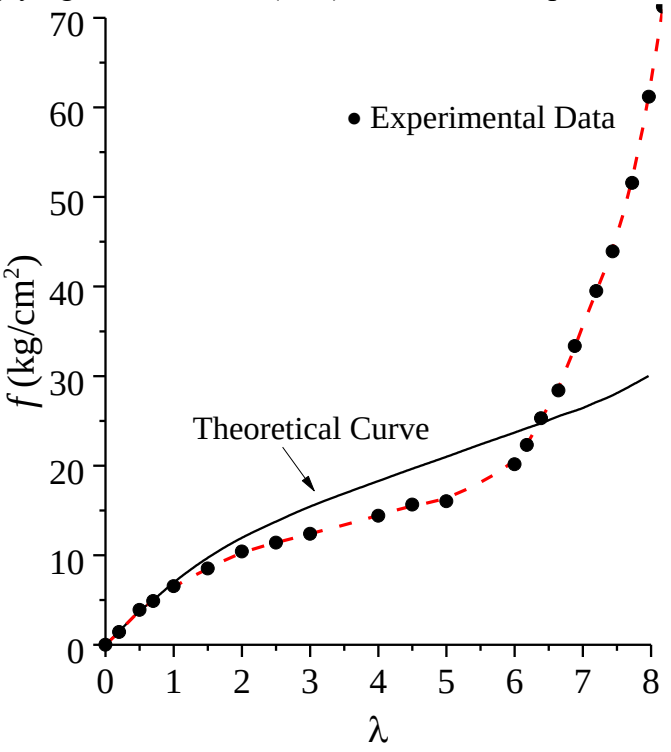

Figure 1.10 Tensile elongation. Comparison between the experimental curve of tensile stress vs. stretch ratio λ measured by applying uniaxial force (dots) and theoretical prediction by eq. 1.35 (1 kg/cm^2 = 98.07 kPa).[14,16]

Significant discrepancies arise for moderately high values of λ (or Λ), where the force observed experimentally is respectively lower and higher than that predicted by equation 1.35 (Fig. 1.10).

At this point, it is of considerable interest to clarify the energetic contribution. Let us select a reference volume V^* such that it corresponds to elastically effective chains with mean square end-to-end distances equal to those of free, undisturbed chains $<r_0^2>$. Then, the equation of state can be modified as follows:

$$\frac{<r^2>}{V_0{}^{2/3}} = \frac{<r_0^2>}{V^{*2/3}} \tag{1.36}$$

$$f = f_e + f_s = vkT\frac{V^{1/3}}{V^{*2/3}}(\Lambda - \frac{1}{\Lambda^2}) \tag{1.37}$$

It is immediately derived that:

$$\left(\frac{\partial lnf/T}{\partial T}\right)_{V,L} = -\frac{dln<r_0^2>}{dT} \tag{1.38}$$

Considering the general relationship:

$$\left(\frac{\partial lnf/T}{\partial T}\right)_{V,L} = \frac{T}{f}\left(\frac{T\left(\frac{\partial f}{\partial T}\right)_{V,L} - f}{T^2}\right) = -\frac{f_e}{fT} \tag{1.39}$$

It is concluded that:

$$\frac{f_e}{fT} = \frac{dln<r_0^2>}{dT} \tag{1.40}$$

This means that by measuring the elastic retraction force as a function of temperature while keeping the volume and length of the sample constant and deriving the energetic contribution f_e to the retraction force from equation 1.20, the coefficient of temperature of the undisturbed chain dimensions constituting the elastomeric network can be evaluated.[12-19]

Given the difficulty encountered in achieving constant volume in experimental realization, most thermoelasticity results have been obtained at constant pressure, resorting to f_e either based on measurements or on the basis of the thermodynamically exact correlation:

$$\frac{f_e}{fT} = -\left(\frac{\partial lnf/T}{\partial T}\right)_{P,L} - \frac{1}{T}\left(\frac{\partial f}{\partial P}\right)_{T,L}\left(\frac{\partial P}{\partial T}\right)_{V,L} \qquad (1.41)$$

From equation 1.41, an approximate relationship between f_e and the thermal expansion coefficient of the undeformed sample, β, can be derived as:

$$\frac{f_e}{fT} = -\left(\frac{\partial lnf/T}{\partial T}\right)_{P,L} - \beta(\Lambda^3 - 1)^{-1} \qquad (1.42)$$

Figure 1.11 compares the results obtained with natural rubber according to equations 1.41 and 1.42. Contrary to predictions, f_e appears to be a function of deformation in the region of low λ values but quickly becomes constant and sufficiently independent of the equation used.[11]

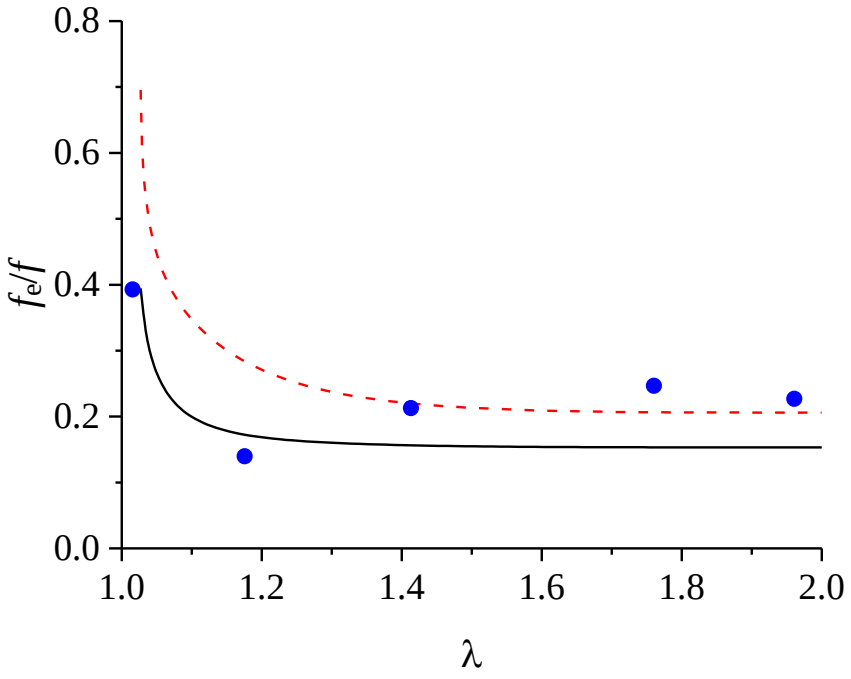

Figure 1.11 Energetic contribution f_e to the retraction force f for natural rubber. Blue dots are experimental values; The solid and dashed lines are data calculated with eq. 1.41 and 1.42, respectively.[11]

On the other hand, comparing the values of the thermal expansion coefficient of unperturbed chain dimensions obtained from thermoelasticity and viscometry measurements reveals a good agreement for some rubbers, alongside significant discrepancies that are due either to solvent effects on the conformational properties of the chains and/or to intermolecular contributions, or to effects that are not easily interpretable for some rubber networks.[7]

1.3 Behavior of elastomers

The mechanical and rheological behavior of bulk polymers is fundamentally different from that of traditional materials, known and used for hundreds or thousands of years. For the latter, the classical theory of elastic solids and the hydrodynamic theory of viscous fluids establish relationships between stresses and small deformations, or deformation rates in the case of fluids, which, with good approximation, hold true in most cases. Both theories enable the analysis of deformation of a finite-sized body under the action of applied forces, starting from the properties of an infinitesimal volume element. The former is based on the assumption of a linear relationship between the stresses applied to a small volume element of solid and the resulting instantaneous, typically small, deformations. The latter develops the hypothesis of a linear relationship between local stresses applied to a small volume element and the gradients of flow velocities. In polymeric materials, behaviors are observed that cannot be explained by classical theories. For instance, elastomers withstand very large deformations, up to ten times their initial length, which cannot be accounted for in a theory limited to small deformations. Moreover, it is generally observed in all polymers that the deformation produced by an applied stress does not establish itself instantaneously but tends to reach an equilibrium value after a possibly lengthy period of time (delayed deformation). There is no longer an immediate relationship between stresses and deformations, as the deformation at a given instant also depends on the stresses applied in previous time periods. These two peculiar

behaviors of polymeric materials, repeatedly measured, have led to the formulation and development of two sophisticated mathematical theories: one regarding large (instantaneous) elastic deformations and another concerning linear viscoelasticity (valid for small deformations). The experimental observation of both large and delayed deformations has further convinced theorists to formulate nonlinear viscoelastic theories.[20-22]

What has been described so far constitutes the 'macroscopic' approach to the study of mechanical properties of polymers, based on the assumption that an elemental volume has mechanical properties depending on constants, as in classical elasticity theory, or on time-dependent functions, as in linear viscoelastic theory, or on functions of deformations and time, as in nonlinear viscoelastic theories. However, as polymer science has progressed and investigation methods have become more refined, it has become increasingly evident that polymeric materials have an extremely complicated internal structure that can be easily altered by applied deformations (typical phenomena being strain-induced crystallization and yielding). This implies that if the results of an experiment can be described by a nonlinear theory using a specific function of time and deformation, this function may not be valid for describing the results of another experiment in which the distribution of applied stresses is altered because the structure of the polymeric material may depend on the distribution of applied stresses.[20-22]

For these reasons, there is a growing emphasis on analyzing the molecular origin of mechanical properties (microscopic approach), allowing, albeit only qualitatively for now, the prediction of the variation direction of mechanical properties based on the material structure. It should be evident from the arguments discussed above that practical problems posed by the technology of processing and using polymeric materials cannot be resolved solely by theoretical studies based on the knowledge of certain fundamental properties. Therefore, in polymer product evaluation laboratories, test methods are employed that subject materials to the same stress distributions

encountered in practical use. In the context of an evolving science of polymeric materials and a phase marked by extreme dispersion of experimental results and theories, elastomers constitute a class of materials that, for a certain uniformity of mechanical properties, can be described uniformly.[20-21]

1.3.1 The Elastomeric Network

Elastomers acquire their most useful and characteristic properties only after crosslinking (vulcanization), a process through which chemical bonds are established between macromolecular chains to form a structure that can be visualized as a three-dimensional network where each intersection point of the network elements is at least three-functional, usually tetrafunctional. The point of junction and intersection is termed a crosslink, from which four branches stand out. The simplest model, known as the ideal network, assumes that the segments are all of equal length and that the network has no defects. In this case, the only parameter characterizing the ideal network is the crosslink density ν_e, that is the moles of elastically effective chains per unit volume. If the segments have uniform length, we have that $\nu_e = 2\rho/fM_c$ where ρ is the density, M_c is the molecular mass of the elastically effective chains and f is the crosslinking functionality. If the elastically effective chains have a length distribution, we have that $\nu_e = 2\rho/f\bar{M}_c$ where $\bar{M}_c$ is the number average molecular mass. A real network differs from the ideal one due to numerous irregularities in the structure, the most important of which are:

- the presence of dangling chain ends, due to the finite molecular weight of the polymer before crosslinking (defect A in Fig. 1.12);
- the presence of chain entanglements that can be permanently or temporarily fixed (B and C respectively in Fig. 1.12) by covalent crosslinks and be considered, in the former case, equivalent to junction points of the network;

- the presence of a sol fraction, molecular species not attached to the network (defect D in Fig. 1.12).

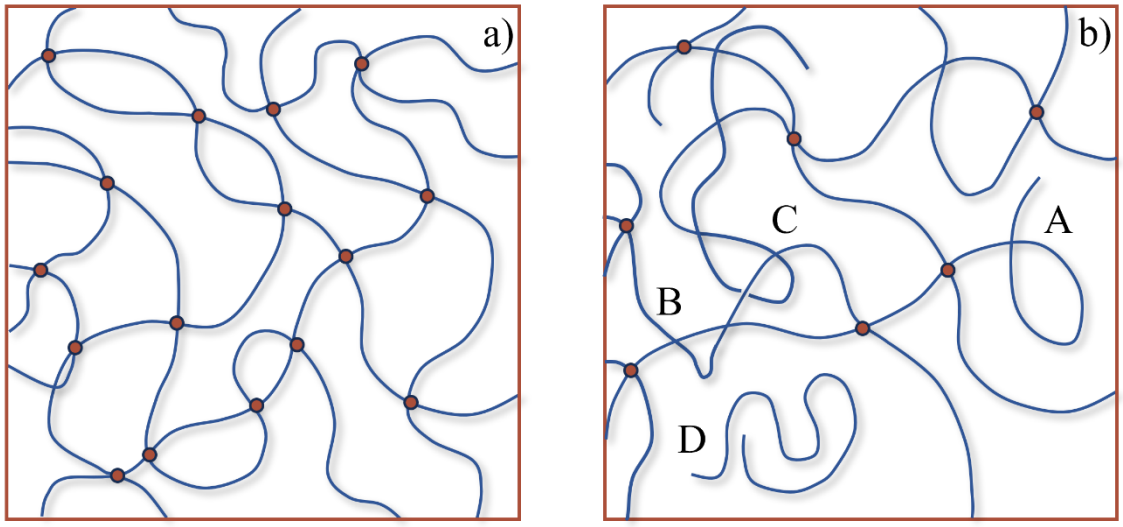

Figure 1.12 Schematic diagram of an ideal network with tetrafunctional nodes (a), and a real network with various types of defects (b). The circles represent the nodes of chemical crosslinking, A represents the dangling chain ends, B and C represent the chain entanglements that can be permanently or temporarily fixed by covalent crosslinks and D represents a sol fraction.

Taking these defects into account, the expression providing the crosslink density becomes:

$$\nu = \left[2\nu_e\left(1 - \frac{b}{2V_e M_n}\right) + 2\omega T_e\right](1 - W_s) \qquad (1.42)$$

where ν_e is the density of crosslinks in moles per unit volume; b is a constant approximately equal to twice the polymer density; M_n is the number average molecular mass of the polymer species before vulcanization; ω is the number of chain entanglements per unit volume; T_e is the probability that the entanglement becomes trapped (point B in Fig. 1.12) between two chemical bonds and therefore becomes an effective junction point of the network; W_s is the weight fraction of sol. For the probability T_e, a general expression has been developed that allows its calculation for any distribution of polymer molecular mass before crosslinking; ω, on the other hand, above a certain molecular mass, assumes a constant and characteristic value for each polymer. The concept of

entanglements between polymer chains is very important and is often invoked to explain certain aspects of polymer mechanical properties. A bulk polymer in the molten state can be considered as a tangled assembly of very long threads; the degree of entanglement, and therefore the number of entanglement points, depends on the intrinsic flexibility of the threads. When subjected to stress distribution, the entanglement state resists deformation and behaves like a network, albeit a labile and temporary one. This 'physical' polymer network explains many properties of polymers both in the molten state, where it is fundamentally important, and in the solid state, where the initial network structure persists even if significant transformations have occurred during the molten-solid transition, such as chemical crosslinking for elastomers and crystallization or vitrification due to cooling for thermoplastic polymers. Several experimental methods are known that allow estimation of the entanglement density, or rather, the average molecular mass of segments between two entanglements, which constitute the physical network, $M_e = M_n / (\omega V)$.[22]

Table 1.1 Molecular mass M_e, and corresponding number of atoms N_e in a polymer chain, comprised between two contiguous entanglements.[22]

Polymer	M_e	N_e
Natural Rubber	5700	340
1,4-Polybutadiene[a]	1900	140
cis-1,4-Polybutadiene[b]	2900	220
1,2-Polybutadiene	3500	130
Styrene-Butadiene Copolymers[c]	3000	180
Polyisobutylene	8900	320
Ethylene-Propylene Copolymers[d]	1600	100
Polydimethylsiloxane	8100	220

a) cis/trans/vinyl = 43/50/7
b) cis/trans/vinyl = 96.5/1.9/1.6
c) Styrene content = 23 wt%
d) Ethylene/Propylene = 46/54

In Table 1.1 some M_e values for the most common elastomers are provided. A typical elastomer before vulcanization generally has a numerical average molecular mass on the order of 10^5 Da,

hence approximately 10 to 30 entanglements/chain. Many entanglements are fixed in position by the crosslinking process, while others remain free to move and potentially disentangle. Their contribution to the mechanical properties of elastomers is certainly significant but has not yet been fully clarified.

1.3.2 Stress-Strain Curve in Tensile Extension (Mooney-Rivlin Equation)

The previously illustrated classical rubber theory, also addressed as rubber kinetic theory, predicts stress-strain curves deviating from experimental data both at intermediate elongations, where the observed stress is lower than the calculated one, and at high elongations, where the observed stress is a higher than the calculated one. These deviations become particularly evident when representing experimental data using the Mooney-Rivlin equation:

$$f^* = \frac{f}{\lambda - \lambda^{-2}} = 2C_1 + \frac{2C_2}{\lambda} \qquad (1.43)$$

where f is the tensile stress, λ is the draw ratio, and $2C_1$ is a constant proportional to the crosslink density, $2C_1 = \rho kT/M_c = \nu kT$. The constant C_2 measures the deviation from the theory in the moderate elongation region. Experimentally, it has been found that in elongation tests, $C_2 = 0$, as predicted by the kinetic theory, only when the polymer has been crosslinked in the presence of large amounts of diluent or when the measurement is performed on a swollen network with solvent. Figure 1.13 schematically depicts typical experimental results in which the values of f^* are reported as a function of the inverse draw ratio λ^{-1}. Deviations of the actual behavior of elastomers from theory are illustrated. Case A, with $C_2 = 0$, corresponds to an ideal elastomer or to a crosslinked elastomer in the presence of a diluent (which is then extracted before the test), or to a crosslinked elastomer in bulk but swollen in a solvent before being subjected to the test; case B is typical of many real elastomers; For cases C and D, there is a rapid rise in stress at high elongations, possibly preceded by a decrease.[20-23] Regarding C_2, two main explanations have been suggested. According

one view, the presence of this deviation from the theoretical behavior is due to intermolecular interactions, favored by a state of local order among the chains. According to a second view, these deviations are instead due to the presence of the entanglements. Deviations at high elongations have been interpreted as being due to the finite extensibility of the network (case C) and strain-induced crystallization in regular polymers, caused by chain alignment when high elongations are reached (case D).[20-23]

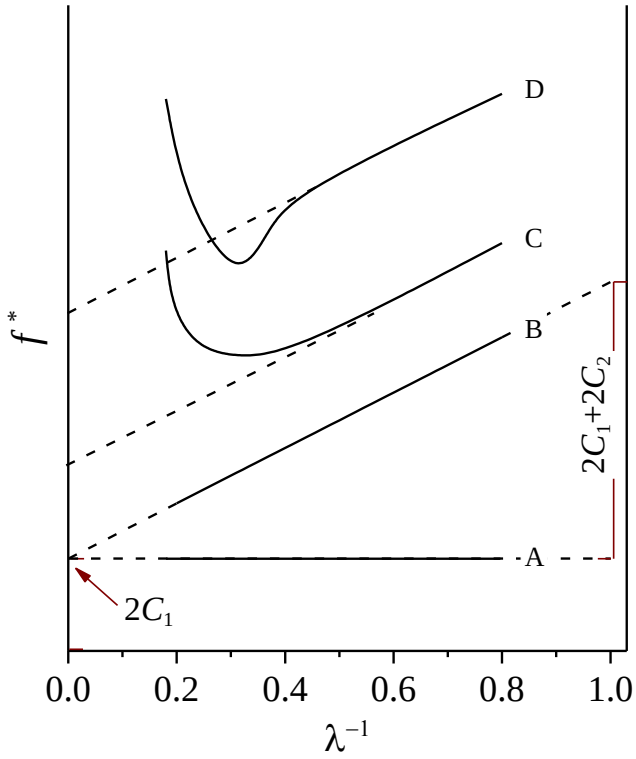

Figure 1.13 Stress-strain curves represented according to the Mooney-Rivlin equation 1.43. Ideal elastomer with $C_2 = 0$, (A); real elastomer, (B); real elastomers with effects due to crystallization or finite extensibility, (C and D).

1.3.3 Fracture Behavior

The simplest test for fracture is uniaxial elongation: one end of the sample is held fixed while the other end is moved away at a constant speed until fracture occurs. A less common test involves hanging a weight at the end of a specimen and waiting for the rupture while measuring the elongation as a function of the elapsed time, as in a creep experiment. By varying the test

conditions: elongation speed, applied load, and temperature, similar results for all elastomers are obtained, as schematically illustrated in Figure 1.14. The load and elongation at rupture as a function of time show a similar behavior to the one of other properties governed by the laws of viscoelasticity. The principle of correspondence between the effects of time and temperature (time-temperature superposition principle, TTS) applies. Accordingly independent measurement of stress (and strain) at break achieved at different temperatures after a time *t*, within an equal time interval (in tests at constant elongation speed, the inverse of the elongation speed is considered as the elapsed time) can be horizontally shifted in a graph featuring the logarithm of the rupture time, forming a single curve known as the master curve, which demonstrates the dependence of strain at break, at a selected reference temperature, across an extensive time interval that is difficult to experimentally cover directly. The figure illustrates, in its essential features, the common behavior of all elastomers: the elongation reaches a maximum (usually on the order of λ = 8-10) at a given temperature while the rupture load steadily decreases, (in general from values of 30-40 MPa, characteristic for shorter test times or lower temperatures). At long times or high temperatures, both rupture load and elongation at rupture assume extremely low values.[20-23]

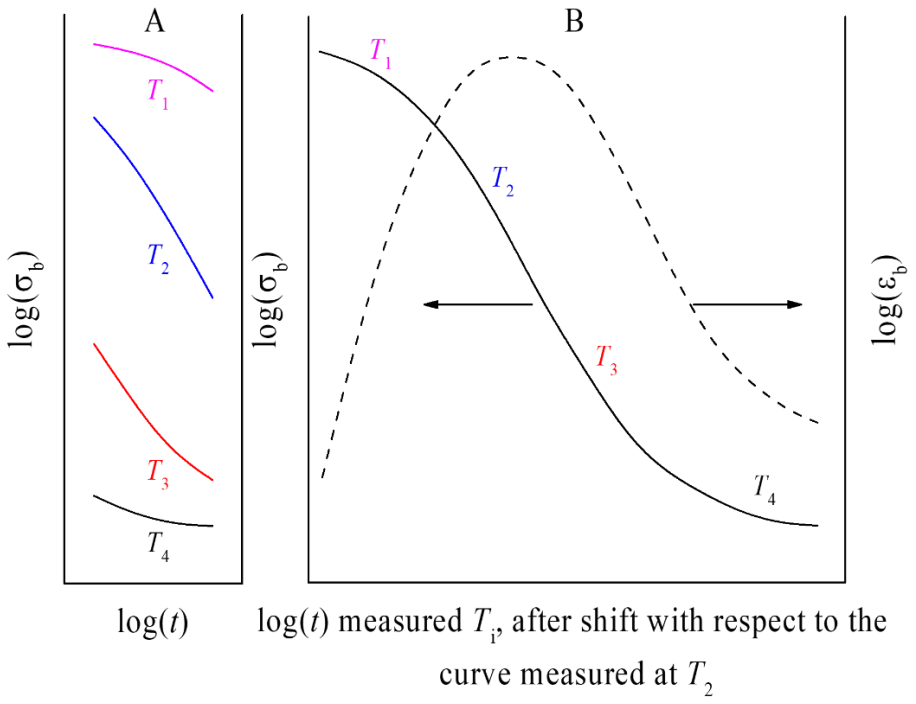

Figure 1.14 Rupture load as a function of time at four temperatures, T_1, T_2, T_3, and T_4 (A). The same data have been horizontally shifted on the log(t) scale to form a single curve, keeping the curve measured at T_2 (reference temperature) fixed. The result is a curve representing the material behavior at temperature T_2 over a very broad time interval (master curve) (B). The master curve representing elongations at rupture over long time at the reference temperature T_2 is also shown in B (dashed line).

According to the model underlying the kinetic theory of rubber elasticity, the polymer is a body where the only impediment to deformation is the existence of a three-dimensional network. Fracture can only occur when the chains composing the network reach their maximum extensibility, i.e., when the elongation ratio equals the average square root of the number of segments included the elastically effective chains. Since in a practically relevant elastomer, the number of flexible segments constituting the network element is on the order of 100 or more, fracture should only occur when the draw ratio is on the order of 10. Experimentally, if tests are conducted under equilibrium conditions between force and deformation, i.e., for very long times, significantly lower values are found, as mentioned earlier. The causes of this are likely attributable to the non-uniformity of the network, which contains various types of defects, such as non-uniform length of

the elastically effective chains composing it, the presence of chain ends, small voids, or microscopic particles of foreign substances. Near these defects, deformation can be much larger than the average in the sample and exceed the extensibility of the chains at that point. The rupture of these chains transfers a portion of the applied forces onto adjacent chains, which can then surpass the extensibility limit in turn. This initiates a catastrophic process leading to total, practically instantaneous rupture of the specimen.[20-23]

Fortunately, elastomers only partially correspond to the model discussed earlier, as they involve mechanisms of viscous resistance to deformation internally. This internal viscosity of elastomers is a function of time and temperature and decreases, tending to zero, at long times and high temperatures. Its effect is to prevent the formation of excessively high instantaneous local stress concentrations and to dissipate the energy, made available by the random rupture of some chains, into anelastic movements, thus not transferring the stress immediately onto the adjacent chains but redistributing it through rearrangement over a larger volume of material. The combined effect of elasticity and viscosity is manifested through stress relaxation processes characterized by an average time constant. If the deformation duration is shorter or longer than the time constant, the relaxation processes do not intervene in the local stress distribution, leading to rupture at low elongations. When the deformation duration is on the same order of magnitude as the time constant, there is a maximum reinforcement effect and hence a maximum elongation at rupture. The rupture load, on the other hand, depends on the number of chains that must break when the sample separates into two parts; at short times, the entire network is involved simultaneously, whereas at long times, fracture propagates instant by instant through the most stressed fraction of macromolecular chains.[20-23]

The viscoelastic behavior of elastomers is quite regular: for all, the curve representing a property, such as elongation at rupture or the viscoelastic modulus, as a function of the logarithm of time,

assumes the same shape. The main difference lies in the fact that the curves for each polymer are shifted along the time axis, and their position is essentially determined by the value of the glass transition temperature of that elastomer T_g. If, instead of the absolute temperature, the difference between the temperature and T_g (T - T_g) is used as a variable, a master curve representing the properties of many elastomers can be constructed, regardless of their chemical structure. Partially deviating from this regular behavior are crystallizable rubbers. For these rubbers, a second mechanism operates, alongside the viscoelastic one, which has a significant effect on rupture properties. At points where, due to the presence of network defects, large deformations occur, the chains crystallize, forming very strong and tenacious structures that prevent rupture. The reinforcement mechanisms due to crystallization operate at temperatures different from those of the viscoelastic type. An example is shown in Fig. 1.15. For styrene-butadiene copolymers with T_g ≈ -55 °C, the elongation at rupture λ is greater than 5 only in the range between -40 and 2 °C, where, at the test speed of 500 mm/min, the viscoelastic reinforcement mechanisms are active.[20-23]

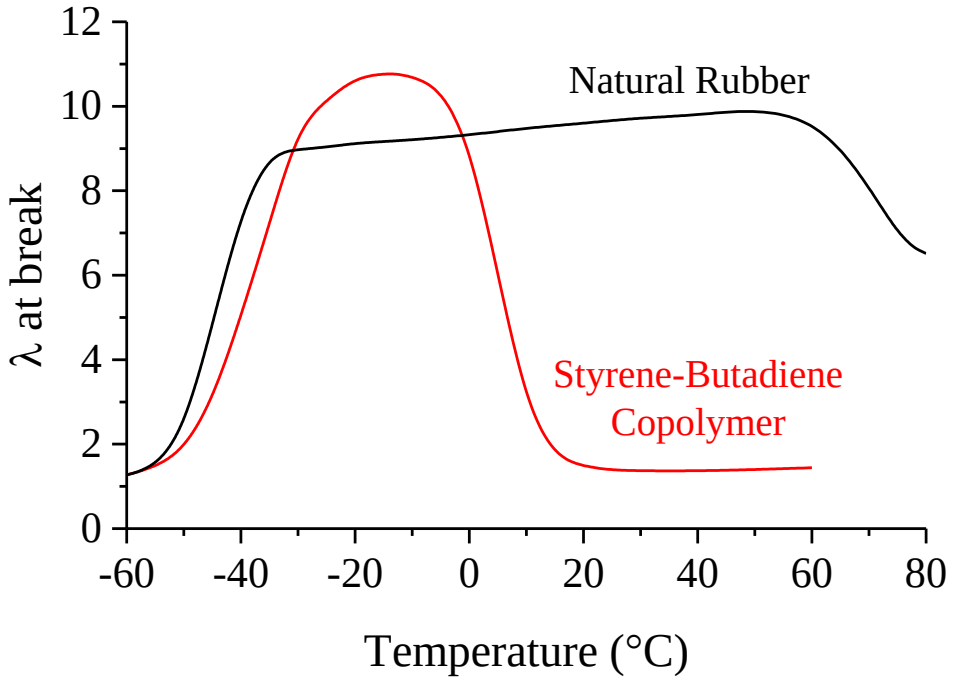

Figure 1.15 Fracture elongation as a function of temperature for a butadiene-styrene copolymer and natural rubber.

Natural rubber, instead, with a T_g of ≈ -70 °C, exhibits draw ratio at rupture greater than 5 from -45 to 85 °C because, in this temperature range, premature rupture is hindered by crystallization. This simple example highlights the significant practical importance of crystallizable rubbers. Non-crystallizable rubbers like styrene-butadiene copolymers generally have very poor fracture properties at room temperature. Consequently, they are never used alone but rather blended with carbon black or other reinforcing fillers. The primary effect of these fillers appears to provide the polymer with viscoelastic dissipation mechanisms, operating even at room temperature, thereby delaying fracture. In a blend with 20-40% carbon black, the fracture load of this rubber can increase by an order of magnitude, going from a few MPa to 25-30 MPa.[21-23]

Beyond the previously described tensile fracture, more complex fracture types, such as laceration, growth of micro fissures under repeated stresses, and abrasion, hold practical importance. External forces applied in these fracture types are consistently very low, well below the tensile fracture load. However, fractures occur due to the creation of stress distributions with very high peaks near impurities or small cuts. The growth of these cuts, also encouraged by degradative chemical reactions with atmospheric oxygen or ozone, starts slowly but tends to accelerate autonomously and can lead, depending on test conditions, to either pronounced ruptures or the ablation of small pieces of rubber. For these fractures, the previously expressed concepts remain valid, summarized as follows: elastomers are never perfectly elastic bodies; a portion of the energy expended in deforming them is dissipated in overcoming viscous resistance to the movement of macromolecular chains or in local structural rearrangements due to crystallization or the presence of fillers like carbon black. This dissipated energy governs the resistance of elastomers to various types of fractures.[21-23]

1.3.4 Effect of Fillers on Rubber Properties

The blending of rubbers with fillers consisting of finely divided inorganic material particles is an ancient practice in the rubber industry. The initial purpose was to increase the hardness and elastic modulus of blends while reducing costs by diluting the elastomer with inexpensive components. However, it was soon realized that specific types of fillers greatly enhanced fracture properties, particularly abrasion resistance, cut formation, and fatigue resistance. Presently, fillers have an importance almost equal to that of the elastomer in imparting the required properties to the product. The most important filler is carbon black, primarily composed of carbon in the form of particles with a variable diameter, ranging from 10 to 100 nm, depending on the used production process. The most commonly employed types have an average diameter between 10 and 60 nm and a highly complex morphology because each particle consists of an aggregate of particles with a diameter around 0.1 nm.[21-23]

The most easily measurable effect resulting from the incorporation of carbon black is an increase in the elastic modulus and hardness. This effect is well described by the Guth equation:

$$E = E_0(1 + 0.67gV_f + 1.62g^2{V_f}^2) \qquad (1.44)$$

where E_0 and E are the moduli of the unfilled and filled elastomeric species, respectively, measured under small deformations, V_f is the volume fraction of the filler, and g is a factor accounting for the effect of particle shape. For larger deformations, the Mooney-Rivlin equation can be used, introducing an effective deformation of the elastomeric phase, greater than the overall deformation. Since the filled elastomer consists of a practically inextensible component, carbon black, embedded in an easily extendible matrix, the local deformation on the latter is greater than that imposed at the ends of the specimen. The effective deformation can be calculated with an equation similar to that of Guth:

$$\lambda' = \lambda(1 + 0.67gV_f + 1.62g^2{V_f}^2) \quad (1.46)$$

Another significant effect of carbon black is an increase of the hysteresis in stress-strain curves and the Mullins effect. When a constant-rate deformation cycle is applied to the specimen, comprising elongation to a specified value of λ followed by a return to initial dimensions (λ = 1), it is observed that the stress-strain curve in the first half of the cycle is higher than that in the second half, and the load applied to the specimen returns to zero when the deformation is still present (λ > 1). In a subsequent deformation cycle, the forward and reverse stress-strain curves are always lower than those corresponding to measurements during the first cycle. The first phenomenon, usually referred to as hysteresis, and the second Mullins effect or softening under stress, occur because after the initial application of stress, the material has a lower elastic modulus. These phenomena have been the subject of intensive research. The possible explanation of this behavior may be envisaged in three fundamental mechanisms:

- The presence of complex-shaped particles may render deformation non-affine, with particle displacements that are hardly reversible.
- Various interactions are established between macromolecular chains and the surface of carbon black particles, which can be considered as additional transversal bonds, either strong (almost permanent) or weak (labile). Due to the applied stress, these bonds break, making the material more extensible in the subsequent deformation cycle. Weak bonds reform easily, contributing to maintenance of the applied stress while redistributing the stress equally among the different chains. This results in a reinforcing effect.
- The fraction of elastomer in contact with the surface of carbon black is physically adsorbed; the physical properties of the physiosorbed part differ from normal ones due to the restricted mobility of adsorbed segments. This can explain the high value of hysteresis.

In any case, it has been ascertained through numerous experiments that the mechanisms operating during the extensional deformation of a specimen, leading to hysteresis and the Mullins effect, are the same mechanisms that confer high fracture resistance to the filled elastomer. Hence, it is confirmed that an enhancement in the fracture resistance of elastomers can only be achieved by introducing stress relaxation mechanisms, in this case, through the filler-polymer interaction, at the expense of greater dissipation of elastic energy.[21-23]

1.3.5 Dissipation of deformation energy

As previously observed, rubbers exhibit good fracture properties and high coefficients of friction only when the processes of relaxation are active, i.e., viscous dissipative mechanisms that convert part of the energy expended in deformation into heat. This results in a temperature increase depending on the thermal capacity of the system. In the case of large rolling tires, each volume of material undergoes deformation at a frequency corresponding to the tire rotation frequency, approximately 10 cycles per second. The heat generated during each deformation cycle accumulates due to the low thermal conductivity of rubbers, leading to extremely high temperatures at certain points, risking thermo-oxidative degradation of the material and catastrophic ruptures.[21-23]

To avoid this issue in the points most thermally isolated and subjected to deformation on the tire, polymers with low dissipation are used. In this, as in other cases, it is necessary to find the best compromise between fracture properties, coefficient of friction, and dissipation of mechanical energy into heat, which generally presents as a negative characteristic. The best results are obtained by using crystallizable elastomers under strain and, more generally, by blending different elastomers together with various types of fillers such as carbon black, silica, and mineral oils.[21-23]

1.4 Viscoelastic behavior

Unlike ideal elastic solids, the behavior of viscoelastic substances under stress can be described in terms of a response that possesses both an elastic and a viscous (dissipative) component. Poorly or non-vulcanized rubber samples are affected by viscous chain sliding. The application of mechanical stresses causes both a change in the conformation of the polymer chains and interchain sliding, i.e., a modification in the positions of the center of mass of the polymer chains.[20,23]

Removing the stress allows the polymer chains to return to their original coiled conformation with elastic recovery of part of the deformation, while the viscous sliding of the chains leads to irreversible deformation. At a macroscopic level, the sample does not recover its initial shape and size once the load causing the deformation is removed. The residual deformation achieved upon stress removal depends on the residual tension remaining inside generated by segmental movements. The relative slippage of the chains tends to decrease (or even cancel out) the tension but, for this to occur, a certain time is required, defined as the relaxation time. The relative importance of elastic (reversible) and viscous (irreversible) deformations is also time and rate-dependent: slow and/or sustained deformations favor the viscous sliding of polymer chains. In highly crosslinked elastomers, viscous sliding is limited due to the presence of crosslinks between chains that prevent relative motion, which would otherwise decrease the residual tension. The connection points between chains inhibit the relative sliding between chains, and the presence of crosslinking imparts a memory effect. In higher molecular weight or vulcanized polymers, the resistance to viscous sliding and the presence of a pronounced elastic component allows for high extensions, mostly reversible, over a wide temperature range above the T_g. Consequently, the material exhibits elastomeric behavior.[20,23]

It is worth noting that filled elastomers show peculiar viscoelastic properties and in particular the so-called Payne effect. This effect is observed under cyclic loading conditions and corresponds to a dependence of the viscoelastic storage modulus on the applied strain amplitude. Indeed, at strain amplitude greater than ≈ 0.1%, the storage modulus decreases rapidly as the strain amplitude increases until achieving a lower bound with further increase of strain amplitude, around to 20%. In the same strain amplitude region the loss modulus presents a maximum.[7]

1.5 Strain-induced crystallization (SIC)

Some elastomers with a regular constitution and configuration of the monomeric units, although entirely amorphous at room temperature, can crystallize due to extensive deformation. The most well-known examples are natural rubber, synthetic polyisoprene, 1,4-*cis*-polybutadiene, polyisobutene, and nitrile rubbers. Crystallization, which can occur even at temperatures higher than the melting temperature of the polymer species in its undeformed state, is a consequence of the reduction in entropy of the network due to deformation. The effects on mechanical properties are significant and depend on the distribution of deformations and test conditions.[24]

If a polymer network is deformed at a very high temperature, sufficient to prevent crystallization under strain, and then, while maintaining a constant deformation, cooled to room temperature, crystallization occurs, resulting in a reduction in the stress required to maintain the lattice extended; the stress may reach zero and may also become negative. It is assumed that since crystallization occurs for the polymer chains that are oriented along the stretching direction, the amorphous segments covalently linked to the crystalline stems relax, causing a reduction of the tension exerted by the applied forces.[24] This is schematically illustrated in Fig. 1.16A. The kinetic theory establishes that for an ideal elastomer, the restoring force should be proportional to the absolute

temperature, and hence the ratio f/T should be constant as the temperature varies; However, if the polymer crystallizes below a certain temperature T_m, the quantity f/T ratio should decrease.[24-27]

On the other hand, as illustrated in Fig. 1.16B, if one considers a tensile test where the specimen is elongated by holding one end fixed and moving the other at a constant deformation rate, the crystals formed as the deformation increases should induce an increase of the applied force because the crystalline regions are practically inextensible compared to the amorphous matrix in which they are embedded (reinforcement).[24-27]

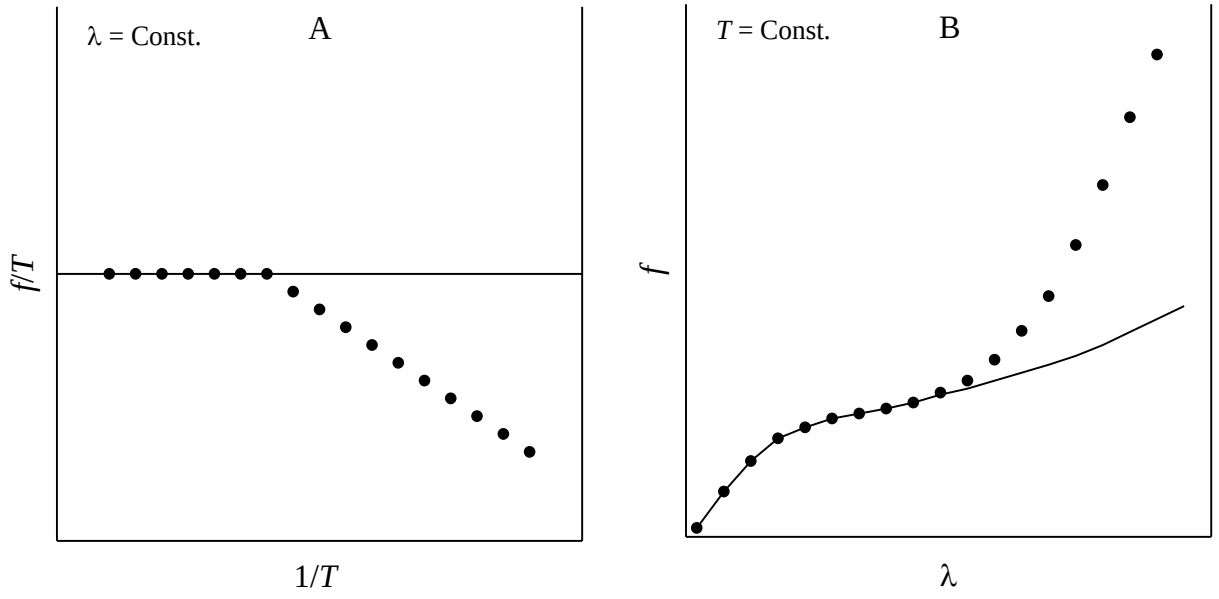

Figure 1.16 Effect of strain-induced crystallization (SIC) on the tensile force of elastomers, in experiments carried out at constant stretch ratio, as a function of the inverse of the temperature (A), and at constant temperature as a function of stretch ratio (B). Solid curves are theoretical curves of an amorphous rubber used for comparison.

Theoretical treatments of the phenomenon, initiated by Flory,[27] are still under development, and the results qualitatively agree with experimental data. According to theory:[24-27]

$$\frac{1}{T_m} \cong \frac{1}{T_m^0} - \frac{R(6s-1)}{2N\Delta H_u}\lambda^2 \qquad (1.45)$$

Here, T_m is the temperature of incipient crystallization at stretch ratio λ (it was assumed $T_m = T_c$, melting and crystallization temperature respectively), T_m^0 is the corresponding temperature in the absence of deformation, N is the number of segments comprised in an average elastically active chain, ΔH_u is the enthalpy of fusion per mole, and s is the number of segments forming the initial crystallization nucleus. Furthermore, the theoretical results indicate that the f/T ratio decreases as the temperature decreases and for $T < T_m$, the decrease is proportional to $1/T$. This scheme applies at high elongations ($\lambda > 3$) and for modest crystallinity development.[24] The stress-strain curve case is far more complex because the specimen, instant by instant, is far from thermodynamic equilibrium conditions, and kinetic factors need to be introduced into the equations. Moreover, as soon as the first crystals form, the polymer becomes a composite material that no longer follows the laws of rubber elasticity. What is important to highlight is that the phenomenon of strain-induced crystallization holds significant practical importance as it increases the rupture resistance of crystallizable rubbers, making their use possible even under severe conditions.[24]

The phenomenon of strain-induced crystallization (SIC) can be described in polymer physics through the Landau-Ginzburg model, which provides a theoretical explanation of how mechanical deformation can induce crystallization in an amorphous polymer. The Landau-Ginzburg model, originally developed to describe phase transitions in materials, has also been applied to the phenomenon of deformation-induced crystallization. In this context, the key concept is the free energy of deformation, which considers the interactions between polymer chains, their mobility, and their ability to form crystals.[25,26]

When an amorphous polymer undergoes mechanical deformation, its molecular structure undergoes changes that favor the formation of crystalline nuclei. These changes are described by the Landau-Ginzburg model through the free energy of deformation. In particular, the model indicates that deformation induces a change in the polymer free energy, facilitating the formation

of ordered or crystalline regions within the material. The free energy of deformation accounts for interactions between polymer chains and the constraints imposed by the deformation itself. When the polymer undergoes deformation, the chains can align in a more ordered manner, increasing the probability of forming crystalline regions. This process is influenced by various factors such as temperature, deformation rate, and the chemical nature of the polymer. In the context of SIC, the Landau-Ginzburg model describes how mechanical deformation can reduce the free energy of the system, favoring the transition towards a more ordered or crystalline structure. The theory thus provides an explanation of the mechanism through which deformation can promote crystallization in amorphous polymers.[20,23]

Among various polymers capable of undergoing SIC, crosslinked natural rubber has been extensively studied. These studies have revealed that during stretching, before crystallization, the amorphous phase tends to orient itself along the stretching direction, resulting in a loss of conformational entropy (Fig. 1.17A). In fact, uniaxial stretching induces a significant decrease in the conformational entropy of the chains in the amorphous state, causing a decrease in the fusion entropy ΔS_m. Therefore, crystallization under strain at room temperature occurs because at this temperature, the crystals are more stable than the deformed amorphous phase since the product $T\Delta S_m$ is smaller than the enthalpy of fusion ΔH_m. When the amorphous chains crystallize, they form crystalline segments already oriented along the stretching direction (Fig. 1.17B). The transition from the rubbery to crystalline state leads to a local volume decrease with consequent partial recovery of conformational entropy due to the partial relaxation of the oriented amorphous chains near the crystallized segments. Macroscopically, this phenomenon is evident in the constant stress region of stress-strain curves because during stretching in this range, three phenomena occur: orientation of the amorphous phase, crystallization, and subsequent relaxation of the amorphous phase itself. Only when all crystallizable segments are in the crystalline state does the stress

increase due to the orientation of the amorphous phase and the presence of the crystalline phase. In a stress-strain graph, this range is defined as strain-hardening (Fig. 1.17C).[27,28]

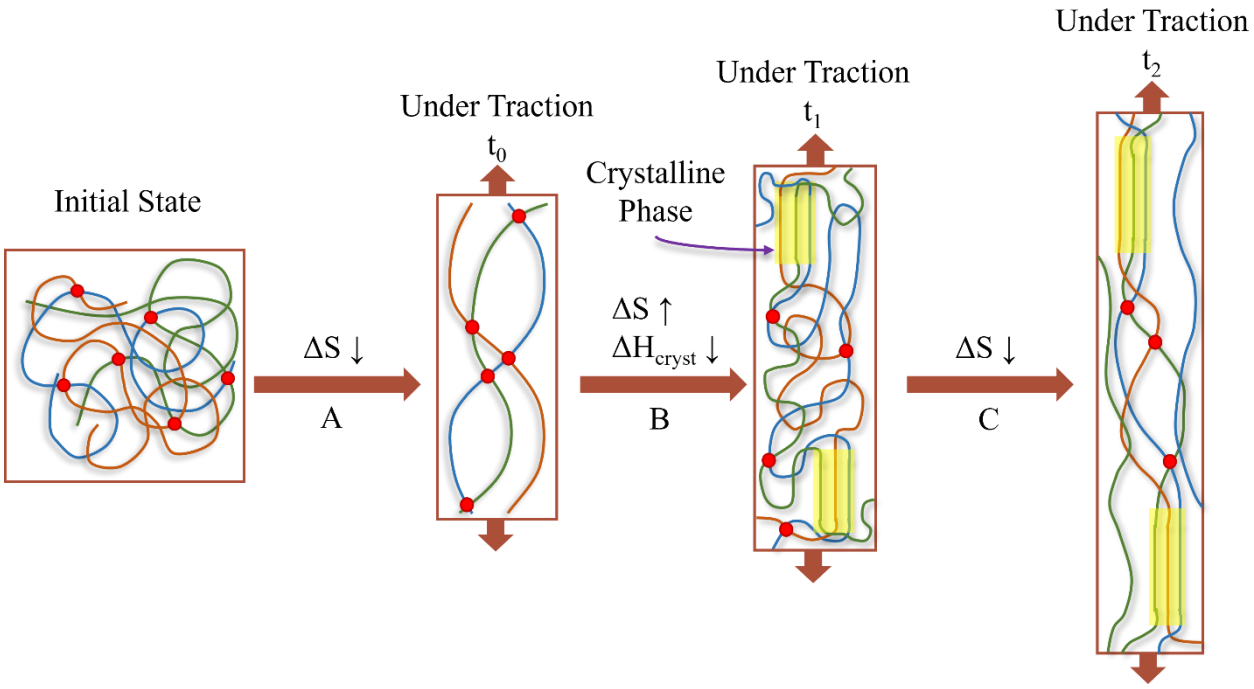

Figure 1.17 Representation of the SIC phenomenon.

An anisotropy in the orientation of segments belonging to crystalline and amorphous phases induced by stretching generates X-ray fiber diffraction patterns characterized by an anisotropic intensity distribution in the two-dimensional patterns from both phases.[29]

The anisotropy in the diffraction halo originating from amorphous chains has been interpreted according to distinct views.[30–44] On one hand, it is suggested that this anisotropy is due to a contribution from an oriented amorphous phase overlaid with a contribution from a non-oriented amorphous phase.[30–37] On the other hand, it has been hypothesized that there exists only a type of weakly oriented amorphous phase, whose orientation steadily increases with increasing deformation before crystallization, reaching a plateau due to relaxation at deformations higher than those at the beginning of crystallization.[38–44]

All these considerations agree on the key role played by the orientation of amorphous chains on the SIC. The segmental orientation and SIC of crosslinked NR are strongly influenced by the crosslink density.[30,31,38,45–47]

In-depth studies conducted on NR have shown that for sulfur vulcanized NR, the deformation marking the onset of crystallization is nearly constant, regardless of the crosslink density.[17,18,25,32,33] For peroxide crosslinked NR, instead, the deformation marking the onset of crystallization decreases as the crosslink density increase. The reasons of these differences are unclear and may not be attributed to crosslink heterogeneity in sulfur vulcanized NR.[30,31,38,45–47]

It is noteworthy that this latter behavior aligns with predictions from the classical theory of rubber elasticity for homogeneous networks.[27,48] Therefore, a constant value of deformation at the onset of SIC has been interpreted as being due to a heterogeneous distribution of the crosslinks,[30,31,38,45–47,49] even though direct investigations have demonstrated that the distribution of crosslinks in sulfur vulcanized NR is homogeneous.[50]

1.6 Transformation and Vulcanization of Elastomers

A polymer that exhibits good elastomeric behavior satisfies some general conditions:

1. The glass transition temperature is below room temperature (typically, elastomers of practical interest have T_g < -20 °C). This condition is achieved when the macromolecular chains are characterized by numerous backbone bonds with low internal rotation barrier, thereby imparting flexibility to the chains.
2. Absence of strong intermolecular interactions.
3. The polymers should be amorphous or poorly crystallinity at room temperature and in the resting state.

For a polymer to be of industrial interest as elastomer, it must not only meet these conditions but also possess high molecular mass, a prerequisite for exhibiting good mechanical properties and acceptable processing conditions, as greater molecular masses entail a greater number of entanglements/chain. Synthetic elastomers have molecular mass on the order of 10^5 Da, natural rubber (in its raw state) has molecular mass of about 10^6 Da.

An elastomer obtained either through synthesis or latex coagulation in the case of natural rubber is termed 'raw'. It behaves as an incompressible viscoelastic fluid. As such, it responds to solicitations in ways that depend on time or the frequency of solicitation and temperature, more precisely, on the difference between the test temperature and the T_g. Raw elastomers, like all viscoelastic materials, can exhibit three behavior regions (Scheme 1.1):

- Glassy solid: modulus = 10^3 MPa. This situation holds at low temperatures and/or high frequencies and/or for very short time.
- Viscous liquid: modulus = 10^{-1} MPa (tending to zero). This situation holds at high temperatures and/or low frequencies and/or for rather long time.
- Rubbery material: modulus ~ 0.5 MPa. This situation holds at intermediate temperatures and/or frequencies and/or for intermediate time.

Scheme 1.1: Values of modulus as a function of temperature.

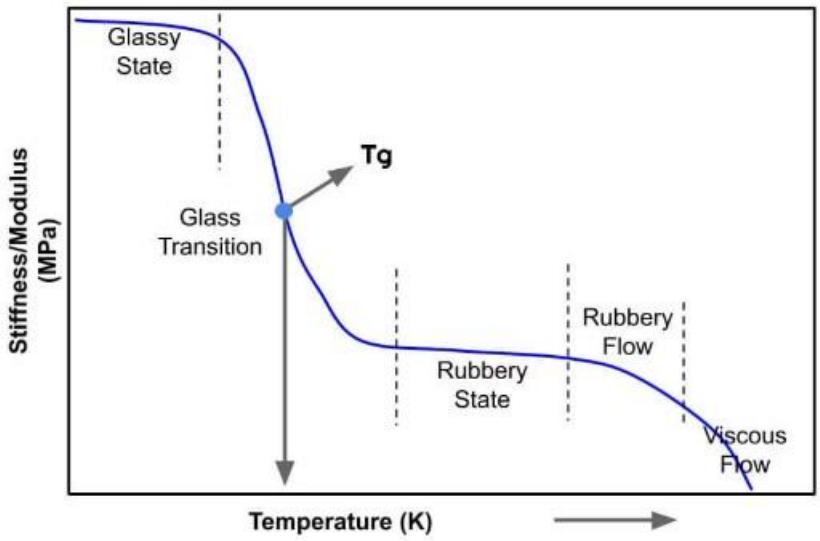

The fact that the elastomer can cross from the rubbery region to that of the viscous fluid is exploited for all transformation operations to confer the desired shape to the material. However, the time dependent properties may inherently result in some instability over time. This is because the macromolecular chains undergo relative translational movements, responsible for viscous flow. Only by binding the chains to each other can the viscous flow zone be removed, practically extending the rubbery behavior region to near-zero frequency. The system thus gains dimensional stability, insolubility, and the ability to manifest, in a practically reversible manner, its long-range elasticity properties. In traditional elastomers, this is achieved by creating crosslinks between macromolecules (crosslinking), subjecting the polymers to the so-called vulcanization.[51,55]

1.6.1 Vulcanization

The chemical process that transforms the soluble tangle of macromolecules constituting the raw elastomer into an insoluble three-dimensional network is called crosslinking or vulcanization. The formation of junctions between individual macromolecules (crosslinks) occurs randomly; therefore, the resulting network consists of macromolecular segments of varying lengths

(elastically active chains) originating from these junction points. Inactively elastic chains, such as chains involved in a single crosslink point, intramolecular rings, dangling ends and labile entanglements are also formed. Entanglements that end up trapped within the crosslinked network, instead, become permanent so that they may easily act as additional crosslinks. While the average length of elastically active chains (hence the number of junction points) influences the elastic properties of the network, the remaining ineffectively elastic chains contribute to increasing the hysteresis of the network. The type of chemical reaction employed for vulcanization depends on the chemical nature of the elastomer and, in particular, on the presence of reactive sites such as double bonds (or rather, allylic hydrogen atoms) and/or appropriate functional groups such as allylic chlorine atoms and ester groups. In all cases if the elastomer contains allylic hydrogens (unsaturated rubbers), and thus in the majority of cases, it is possible to vulcanize with either elemental sulfur, and/or sulfur provided by organic compounds called sulfur donors.[51,52,55]

Vulcanization based on elemental sulfur

The crosslinking of natural rubber with only sulfur at high temperature was historically the first vulcanization process (Goodyear, 1839). The chemistry of this reaction is similar to an oxidation of methylene groups at the α-double bonds with the formation of mono and polysulfide crosslinks and H_2S. The slowness of the reaction led to the search for faster, hence more practical systems, resulting in the today accelerated systems. A modern accelerated vulcanizing system based on sulfur consists of sulfur, an organic compound acting as an accelerator, and so-called co-agents consisting of a metal oxide (usually ZnO) and a higher fatty acid (usually stearic acid), or, in their place, the soap (zinc stearate). The fundamental types of accelerators on the market are classified based on their chemical structure and activity (semi-fast, fast, ultra-fast accelerators). A possible reaction mechanism admits that the active species is a zinc perthiomercapturo complex, which is soluble in the elastomeric phase. This complex, formed by the reaction between sulfur, accelerator,

ZnO, and fatty acid (see Fig. 1.18), interacts with allylic hydrogens (AH) along the chains, creating polysulfide pendant groups terminated by an accelerator fragment (precursors to the crosslinks). The polysulfide pendant group can interact with another hydrocarbon chain (RH), leading to a polysulfide bridge or undergo desulfurization processes catalyzed by the active perthiomercapturo complex. The reaction of polysulfide pendant group with a functional group belonging to the same chain to which it is linked lead to formation cycles, which are elastically inefficient. The active perthiomercapturo complex has the ability to interact with preformed polysulfide bridges, capturing sulfur, to start a new sulfurization reaction. In this way, bridges with a lower sulfur content are formed. The polysulfide bridges can break, either by interacting with the perthiomercapturo complex or by pure thermal action, leading to the formation of sulfured side groups ($R\text{-}S_x\text{-}AH$), which are inefficient for network formation. Desulfurization reactions can also lead to further chain cyclization reactions. The prevalence of desulfurization reactions ultimately leading to monosulfide bridges and thus to an efficient sulfur utilization, depends on the used sulfur/accelerator ratio. If the concentration of the active complex is low (sulfur/accelerator ratio greater than about 2.5), the desulfurization process is slow, and reactions leading to the breakdown of polysulfide bridges responsible primarily for the reversion phenomenon prevail. Conversely, if the complex concentration is high (sulfur/accelerator ratio less than about 0.6), rapid desulfurization occurs, leading to the final formation of mono- and disulfide bridges. Vulcanization systems of the first type (sulfur/accelerator > 2.5) are called conventional, while those of the second type efficient.[51-53,55]

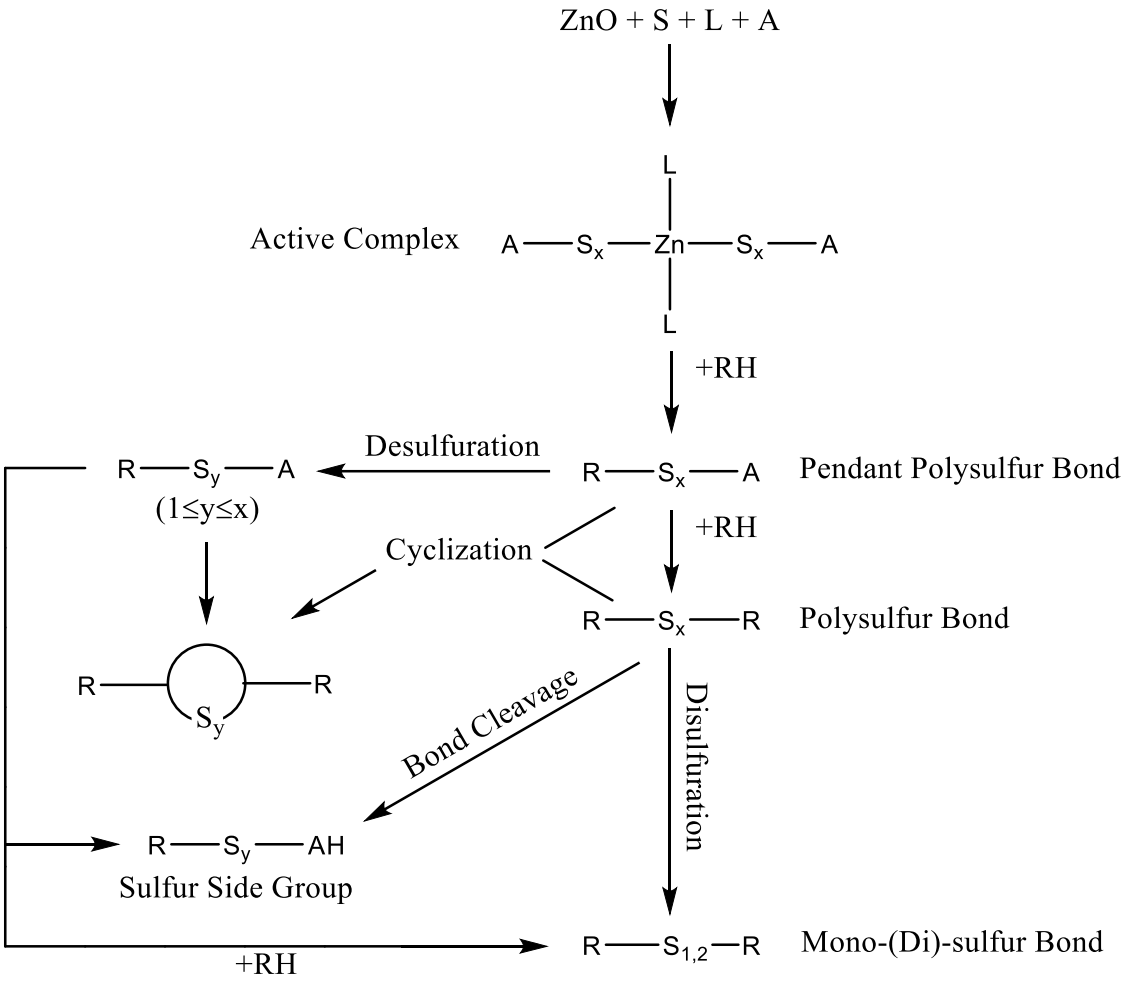

Figure 1.18 Schematic of the sulfur vulcanization mechanism with accelerant (derivatives of mercaptobenzothiazole). A = accelerant fragment; L = ligand (fatty acid anion); AH = allylic hydrogens; R = elastomeric chain.

Vulcanization based on sulfur donors

There are various compounds that allow the vulcanization of unsaturated elastomers without the need of using elemental sulfur. These compounds are called sulfur donors: the most commonly used are morpholine disulfide and tetraalkylthiuram disulfides (Fig. 1.19):

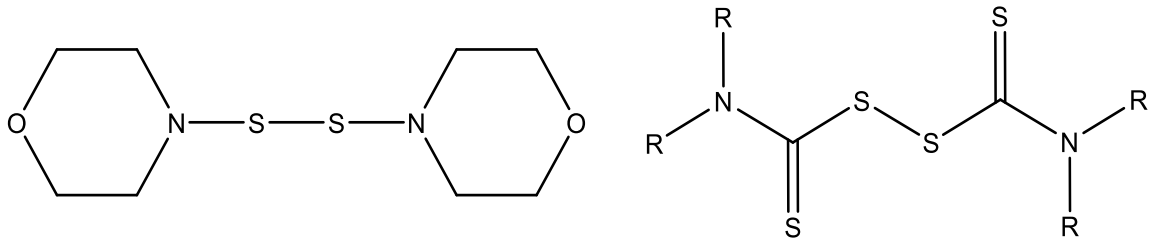

Figure 1.19 Disulfide species commonly used for vulcanization of rubbers based on sulfur donors: 4,4-dithiomorpholine (left) and tetraalkylthiuram disulfide (right).

This type of vulcanization leads to the formation of essentially mono- and disulfide bridges as well as carbon-carbon ones. The absence of polysulfide bridges ensures a low incidence of the reversion phenomenon. In the case of thiurams, the vulcanization mechanism occurs through the following stages:

- Decomposition of the thiuram with the formation of various types of radicals: R_2N-C(S)·, R_2N-C(S)-S·, R_2NC(S)-SS·, ·S-S·, S·.
- Formation of polymeric radicals by interactions of the thiuram radicals with the macromolecules (sum of radicals to double bonds; extraction of allylic hydrogens).
- Recombination of the polymeric radicals among themselves or with the sulfuric radicals (-S·, S-S·) with the formation of C-C, C-S-C, C-S-S-C bridges.

Vulcanization based on peroxides

The use of peroxides theoretically allows the crosslinking of any elastomer. In practice, their use is limited to the vulcanization of saturated rubbers, particularly ethylene-propylene copolymers and silicone rubbers. The most commonly used peroxides are shown in Figure 1.20:

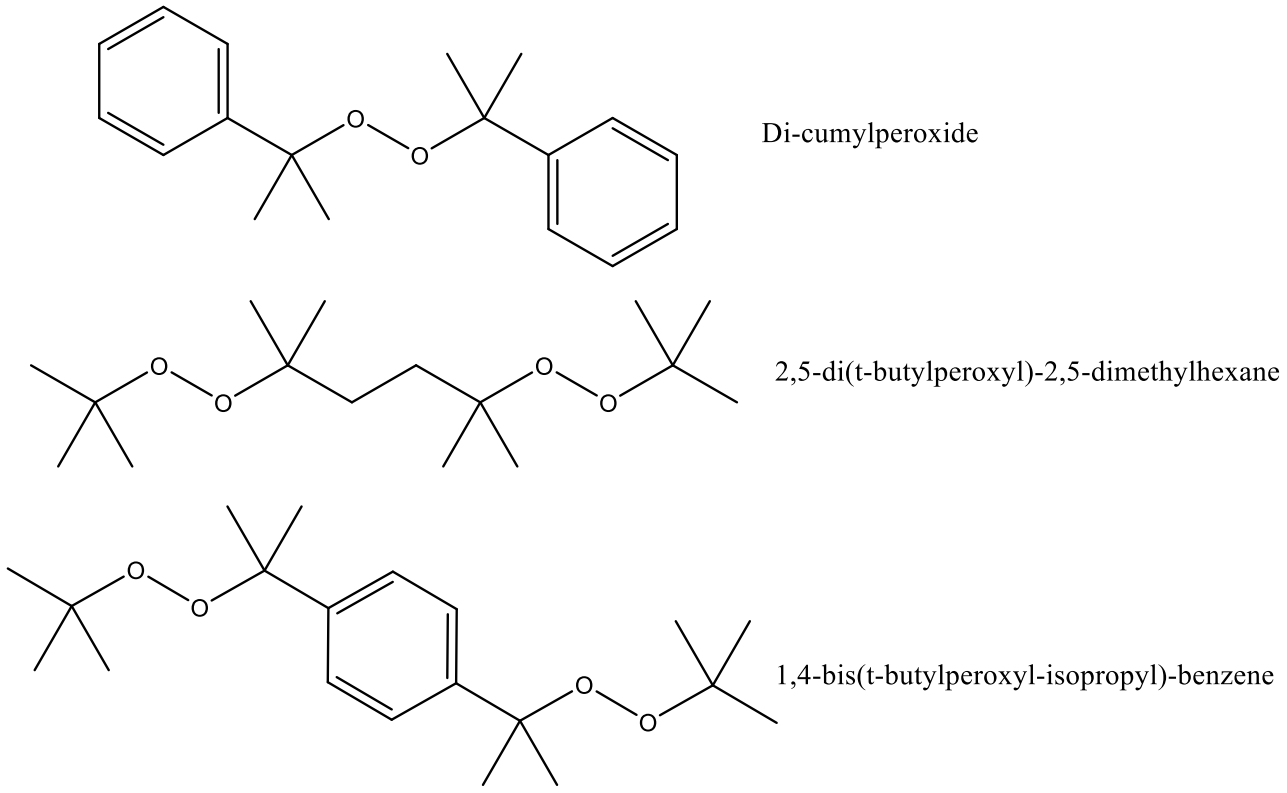

Figure 1.20 Peroxide species commonly used for the crosslinking of saturated elastomers.

At the vulcanization temperature, the peroxide undergoes homolytic fission, forming alkoxyl radicals (R-O·), which generally stabilize by extracting a hydrogen atom from a macromolecular chain, forming a polymeric radical. Coupling of polymeric radicals forms C-C bridges. In the case of saturated elastomers, this is the only mechanism that leads to the formation of crosslinks. In the case of unsaturated rubbers, radicals can stabilize, in addition to coupling, by addition to a double bond, forming another radical; this reaction can proceed through a mechanism similar to radical polyaddition, forming polymeric C-C bridges (as in the case of *cis*-1,4-polybutadienes). Side

reactions are possible, such as the combination of alkoxyl and polymeric radicals (formation of pendant groups) and the dismutation of polymeric radicals with chain scission. This reaction is typical for polyisobutylene, butyl rubber, and atactic polypropylene, which consequently depolymerize instead of undergoing crosslinking. In ethylene-propylene copolymers, the scission reaction becomes increasingly prevalent as the propylene content increases. A proposed mechanism involves a β-scission that affects potentially radicalized methyl groups (Fig. 1.21):[52-53,55]

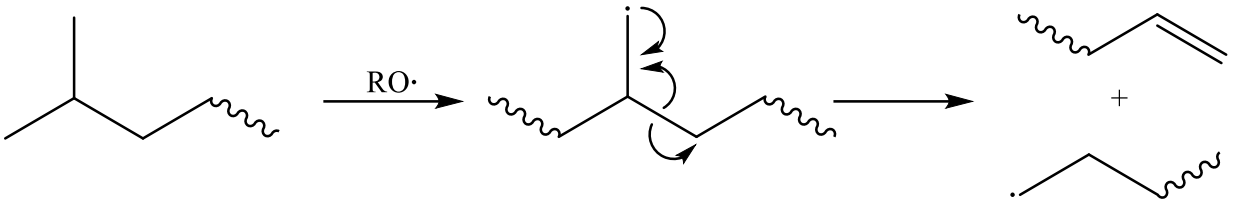

Figure 1.21 Possible side reactions involved in crosslinking with peroxides.

To reduce the incidence of this reaction, crosslinking coagents are used to stabilize polymeric radicals, such as sulfur, quinoid dioxide, triallyl cyanurate, and diallyl phthalate.

1.6.2 Kinetic Aspects of Vulcanization

The study of crosslink formation kinetics is of practical and theoretical interest. Since vulcanization involves the system's reagent becoming insoluble, the kinetics of crosslinking cannot be carried out using classical chemical-physical approaches based on the separation of reaction products from the reactants, and thus intrinsically involving the solubility of analytes. The relationship between time and the number of crosslinks per unit volume, or the degree of crosslinking (ν), can only be tracked using indirect methods. The value of ν can be determined, with appropriate samples, by resorting to the existing relationship between ν and the force of elastic retraction, according to the theory of rubber elasticity:

$$\sigma = \nu RT\,(\lambda - \lambda^{-2}) \qquad (1.47)$$

where λ is the stretch ratio and σ is the retraction stress at equilibrium.

Alternatively, one can use the measurement of the equilibrium swelling degree of vulcanizates in a solvent with a known polymer-solvent interaction parameter χ, using the Flory-Rehner equation:

$$\nu_e = \frac{\rho_r}{2M_c} = -\frac{1}{V_s}\frac{[In(1-V_r)+V_r+\chi V_r^2]}{V_r^{1/3}+\frac{V_r}{2}} \quad (1.48)$$

In equation 1.48, V_r is the volume fraction of elastomer in the swollen state, V_s is the molar volume of the solvent, ρ_r is the polymer density, M_c is the average molecular weight between two crosslink points, and ν_e is the crosslink density expressed in moles of crosslinks per rubber volume. The crosslink density expressed in millimoles of crosslinks per gram of rubber, ν, is:

$$\nu = \frac{1}{2M_c} = \frac{\nu_e}{\rho_r} \quad (1.49)$$

These methods are not only lengthy and tedious but, in principle, require the examined system to be biphasic (polymer and solvent). In practice, another approach is used based on the fact that the elastic modulus increases with the degree of crosslinking and is therefore an indirect measure.[51] For this purpose, so-called rheometers are used, whose sensors generally consist of oscillating rotors in a thermostated chamber (at the vulcanization temperature) filled with the material to be vulcanized. As the degree of crosslinking increases, the modulus of the material increases, requiring greater torque to maintain rotor oscillation. Continuous recording of the torque (τ) over time provides a graphical description of the crosslinking kinetics, called a rheogram or rheometric curve (Fig.1.22).[51,55]

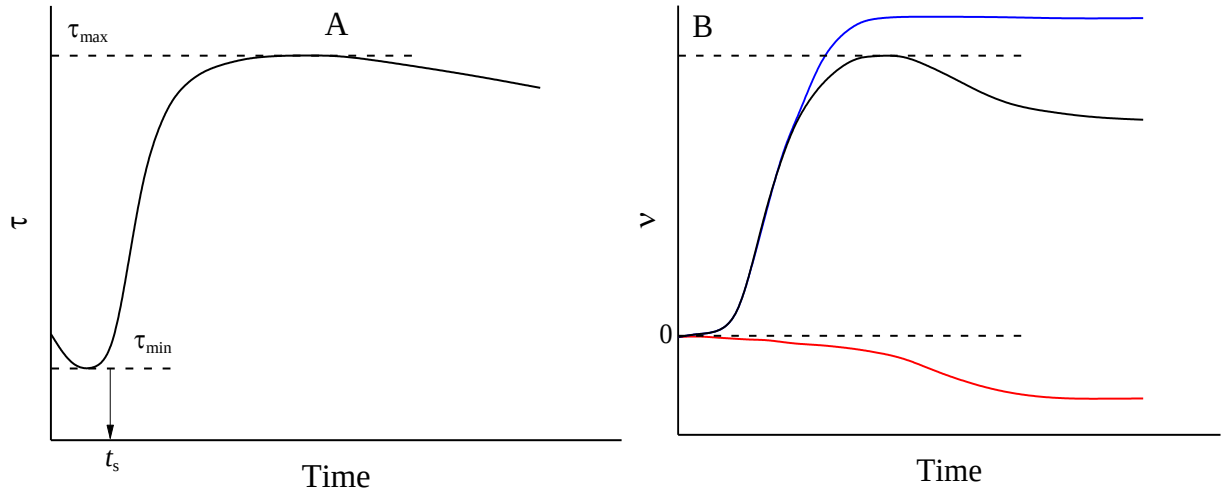

Figure 1.22 A) Typical rheometric curve of a system exhibiting reversion. B) Component reactions of the vulcanization kinetics: blue curve represents crosslink formation reaction; red curve represents crosslink destruction reaction (reversion) and black curve represents the overall reaction.

A classical rheometric curve (Fig. 1.22A) consists of a sigmoid in which the different segments originate from the prevalence of various phenomena. The initial minimum of torque results from the fluidization of the material at the vulcanization temperature, countered by the incipient crosslinking, which leads, after a certain induction time, called the scorch time (t_s), to a rapid rise in the torque. Conventionally, t_s is assumed to be the time at which the torque increases by 0.225 Nm after the minimum value (τ_{min}). The curve then stabilizes at a constant value, τ_{max} (vulcanization plateau), and eventually may decrease (reversion), a common case in conventional sulfur vulcanizations. This behavior is the result of two concurrent reactions: the formation of primary crosslinks and the destruction of the same (Fig. 1.22B). The reversed trend of the destruction reaction of the bonds is explained by considering the possibility that the breaking of the bonds increases with the increase in their number while decreases with the increase in their bond energy (decreasing in the order C-C, C-S-C, C-S_2-C, C-S_x-C with x > 2). The polysulfide bonds evolve over time to thermally more stable species (monosulfide bonds). The phenomenon of reversion, although typical of polysulfide bonding, is only noticeably present in some elastomers, particularly

in polyisoprenes. The fact that the demolition reaction of the preformed bonds occurs concurrently with their formation prevents the attainment of the theoretical level of crosslinking (the actual vulcanization plateau is positioned at lower levels, Fig. 1.22B), resulting in a loss of crosslinking efficiency. The lower the vulcanization temperature, the lower the crosslinking efficiency (Fig. 1.23). The decrease in efficiency can only be compensated by increasing the doses of vulcanizing agents. Conversely, reversion can be overcome by using low sulfur/accelerant ratio formulations (efficient systems, also called EV: efficient vulcanization) or sulfur donors; or by using peroxides or phenolic resins that provide thermally stable C-C bonds. These systems currently represent the best approximation to the ideal crosslinking system, i.e., free from reversion phenomena and efficiency loss with temperature.[51-53,55]

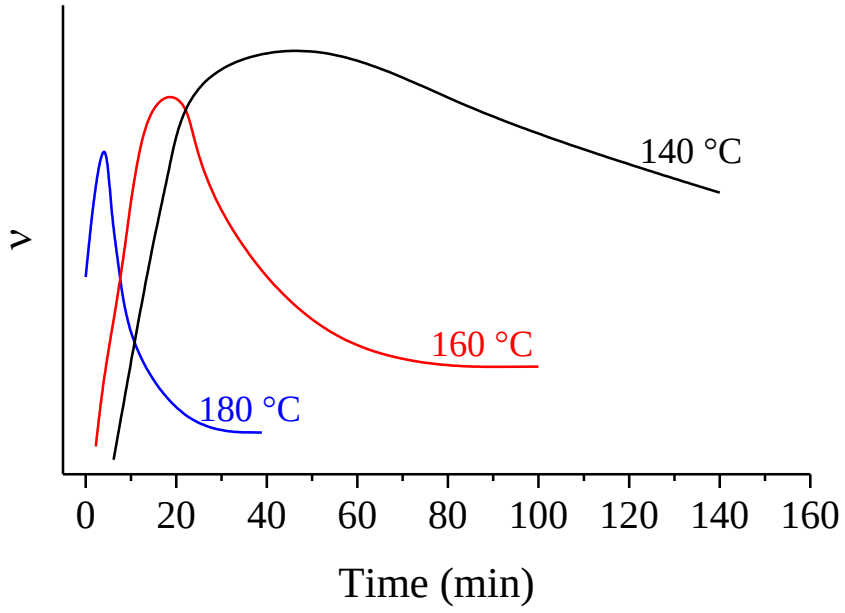

Figure 1.23 Relationship between the crosslink density and vulcanization time of a NR sample vulcanized with sulfur and sulfenamide at different temperatures.[51]

1.6.3 Physical properties of vulcanizates

The stress-strain curves of a vulcanized elastomer obtained in practice deviate from those predicted by both the theory of Gaussian and non-Gaussian statistical networks. For the latter, the theory predicts a steep rise in the curve at high deformations, as observed experimentally (Fig. 1.10). However, the predicted steep rise in the stress-strain curve does not quantitatively represent the actual rubber elasticity. In fact, the theory does not consider the complex factors of a real network such as excluded volume effects, entanglements, energetic contributions, non-affinity of deformation, all sources of deviation in general. A theory that takes into account all these contributions, still to be developed entirely, would fall short for the fundamental reason that in practice, deformation occurs under non-equilibrium conditions. This inevitably entails a contribution from the viscosity of the system, which is more pronounced at higher draw speeds or lower test temperatures. Consequently, the measured stress (under dynamic conditions) exceeds the theoretical stress (at equilibrium) and decreases with increasing temperature (contrary to what the theory predicts). Another consequence of the viscous contribution to stress is the appearance of hysteresis cycles when a specimen is cyclically deformed (Fig. 1.24).[51,52]

Figure 1.24 schematically illustrates the phenomenon for the hysteresis cycle for a pristine vulcanized elastomer. In the case of crystallizable elastomers under strain, the enthalpy of crystallite formation leads to an increase in the hysteresis. Hysteresis phenomena are responsible for the good fracture behavior of vulcanizates deformed under non-equilibrium conditions. In fact, as already discussed, the dissipative mechanisms of viscoelastic relaxation, dependent on time and temperature, contribute to making the stress distribution more uniform within the material and delaying their concentration at singular points constituted by various defects in the vulcanized system, where the microfractures responsible for the macroscopic fracture process initiate.[51,52,55]

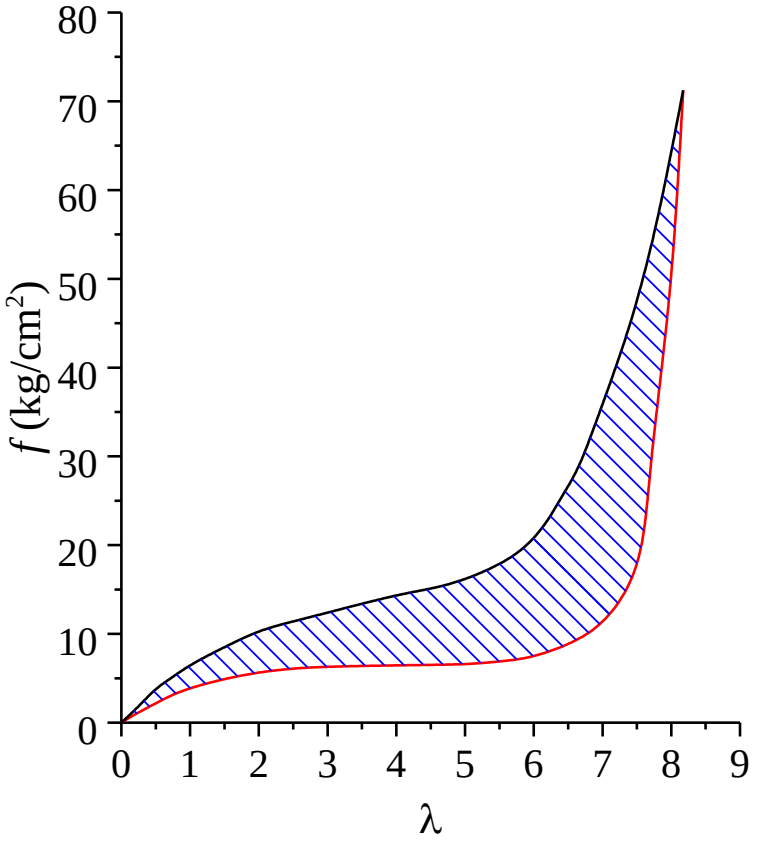

Figure 1.24 Schematic representation of a hysteresis cycle (1 kg/cm^2 = 98.07 kPa).

Since these mechanisms manifest as hysteresis in cyclic deformations, it is immediate that a vulcanizate exhibits good fracture properties under conditions of temperature and deformation velocity where dissipative processes are active. This behavior is obviously undesirable in applications that require both low hysteresis and excellent fracture resistance simultaneously. Crystallizable elastomers allow overcoming this problem because the crystallization induced by large deformations has the same effect on the fracture of the above-mentioned viscoelastic dissipative processes, but with a crucial difference. While the kinetics of viscoelastic relaxations in elastomers are practically independent of deformation, crystallization is a function of deformation. Many practical fracture phenomena (e.g., abrasion, tearing) stem from the establishment of large deformations in small domains of the material, whereas other properties of primary practical importance, such as elastic modulus and hysteresis, depend on the entire mass, which, in contrast,

typically experiences small deformations. Natural rubber owes its great utility to low hysteresis combined with its ease of crystallization under strain, even at temperatures higher than room temperature, resulting in high elongations at break (Fig. 1.15). Amorphous rubbers exhibit good elongation at break at temperatures 20-30 °C higher than the glass transition temperature (T_g) while break at low elongations at room temperature (Fig. 1.15). As we will see, the use of appropriate ingredients, called reinforcing fillers (together with appropriate compatibilizing agents), which lead to a clear increase in hysteresis, allows overcoming the phenomenon of breaking at low elongations of amorphous elastomers.[51,52,55]

Dependence of properties on the degree of crosslinking

The main modifications brought about by vulcanization are schematically represented in Figure 1.25. In the range of crosslinking degrees of practical interest ($0.3\ 10^{-4} – 1.5\ 10^{-4}$ mol/cm^3), as ν increases, the modulus, hardness, and resilience increase, while elongation at break and hysteresis decrease. On the other hand, breaking load and tear resistance reach a maximum.

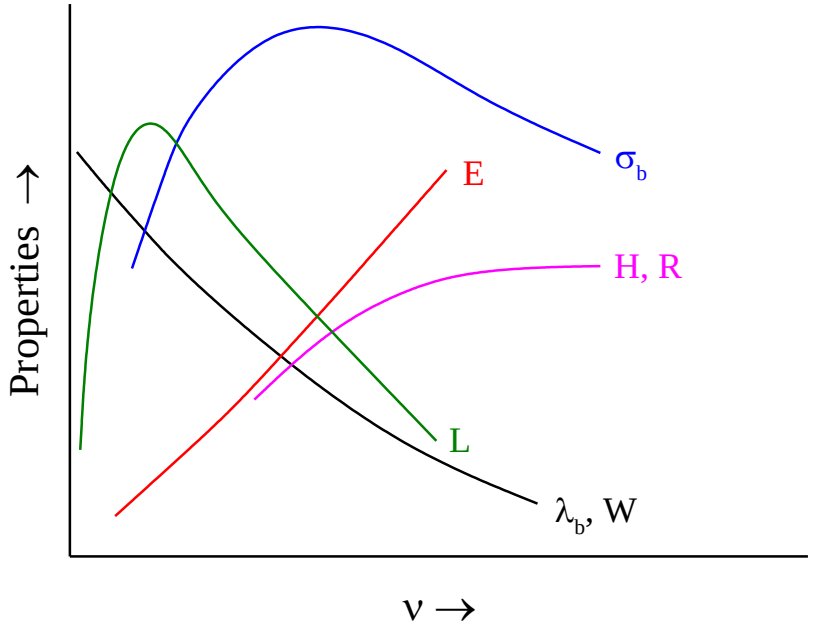

Figure 1.25 Variation of the physical properties of vulcanizates as a function of the degree of crosslinking, ν. *L*: tear resistance; *E*: modulus; *H*: hardness; *R*: resilience; *W*: hysteresis; λ_b: strain at break and σ_b: stress at break.[51]

The existence of these maxima is not predicted by theories of elastic networks, according to which the rupture resistance increases with the increase of the modulus and therefore ν. As already mentioned, in real networks and for non-equilibrium deformations, hysteresis leads to an increase in rupture resistance. The fact that hysteresis decreases as ν increases justifies these maxima from a phenomenological point of view.

1.6.4 Blends

The properties of vulcanized elastomers as such (gum stocks) are generally insufficient to meet the technological requirements of high mechanical properties, good dynamic properties, durability, workability, and cost containment. These requirements are achieved by adding specific ingredients to the elastomer. The dispersion of these in the raw elastomer provides blends. The main ingredients can be divided into the following families: vulcanizing agents; fillers; plasticizers; and antioxidants.

Fillers

To increase the hardness of vulcanizates, improve mechanical properties, and also reduce production costs, it is common practice to add high amounts of solid substances in powdered form.

Based on their effect on mechanical properties, they are divided into:

- Reinforcing fillers: they enhance rupture properties and hardness. The main ones are carbon black, silica, and synthetic silicates.
- Inert fillers: they act as pure fillers (cost reduction) with little influence on properties. Among the best-known are calcium carbonate, talc, coarse particle kaolins and barites.
- Semi-reinforcing fillers: they have intermediate characteristics. Fine particle kaolins are generally used.

Carbon black is a highly surface/volume ratio pseudographitic carbon. It is obtained by incomplete and controlled combustion of hydrocarbons and/or gases, and its properties vary significantly depending on the combustion process. The most used process is the furnace process, which operates with a reducing flame, at around 1700 °C, abruptly quenched with water. The molecular fragments formed in this way quickly recombine into high molecular weight structures similar to those of graphite. These structures weld to each other forming particles called aggregates. These aggregates condense, giving rise to disordered structures (or agglomerates), rich in vacuoles, with a very high surface/volume ratio (primary structure of carbon black).[54,55]

Carbon black particles also contain oxygenated chemical functions, such as hydroxyls, carboxyls, and/or lactones, quinonic groups, which condition the surface properties of carbon black. Since the size of the aggregates and the structure of carbon black condition the properties of blends and vulcanizates, carbon black is classified based on these parameters. A practical measure of aggregate sizes (diameters in the range of 10-500 nm) is provided by the surface area, determined by nitrogen adsorption. The structure is estimated based on oil absorption measurements (dibutyl phthalate). Oil absorption increases with the volume of vacuoles (typical values are 60-120 cm^3/100 g of carbon black).[54,55]

The reinforcing action (increase in modulus, hardness, and rupture properties) generally increases as the specific surface of carbon black increases and decreases as the aggregate diameter increases. During mixing, macromolecules penetrate the vacuoles of the primary structure, wetting the surfaces of the particles they interact with strongly through adsorption. Between carbon black and elastomer, in addition to these physical bonds, chemical bonds can form through interaction between oxygenated groups and radicals that form due to chain scission of the elastomeric chains due to the intense shear forces during mixing. The carbon black-elastomer interaction is so strong

that it renders a part of the rubber insoluble in solvents. This inseparable part from the filler is called bound rubber.[51,54,55]

The first consequence of this phenomenon is the creation of a pseudo-network in raw blends (non-vulcanized), hence a significant increase in the viscosity of the system (hardening of the blend). The second consequence is reinforcement in vulcanizates. Reinforcement is accomplished through different mechanisms depending on the magnitude of the imposed deformation. For small deformations, such those involved in the measure of hardness, the material responds as if it were composed of a network of carbon black particles. Hence, the modulus is very high. This is the reason for the increase in hardness caused by carbon black or more generally by reinforcing fillers. As the deformation increases, this pseudo-network is rapidly destroyed, and the filler acts through multiple mechanisms. The rigid carbon black particles embedded in the rubbery network limit its extensibility, amplifying the effect of stretching, purely due to volume, resulting in increased stress. Rubber-filler interactions also act as additional crosslinks to those imparted by vulcanization, contributing to further stress increase.[51,54,55]

The increase in rupture resistance is instead hysteresis-induced. The increase in hysteresis is partly due to the increase in system viscosity, partly due to the sliding of adsorbed chains on the particle surface, and partly due to their desorption. Sliding and desorption of polymer segments are irreversible and therefore dissipative phenomena. The use of reinforcing fillers is inevitable in the case of elastomers not crystallizing under strain which, at room temperature (away from the T_g), are less hysteresis-prone, and hence lacking in rupture properties. Their use in crystallizable elastomers is required to increase moduli and hardness. The effect of reinforcing fillers on elastomers under strain is illustrated in Figure 1.26. It should also be noted that reinforcing fillers drastically increase abrasion resistance to the point of making them indispensable. [51,54,55]

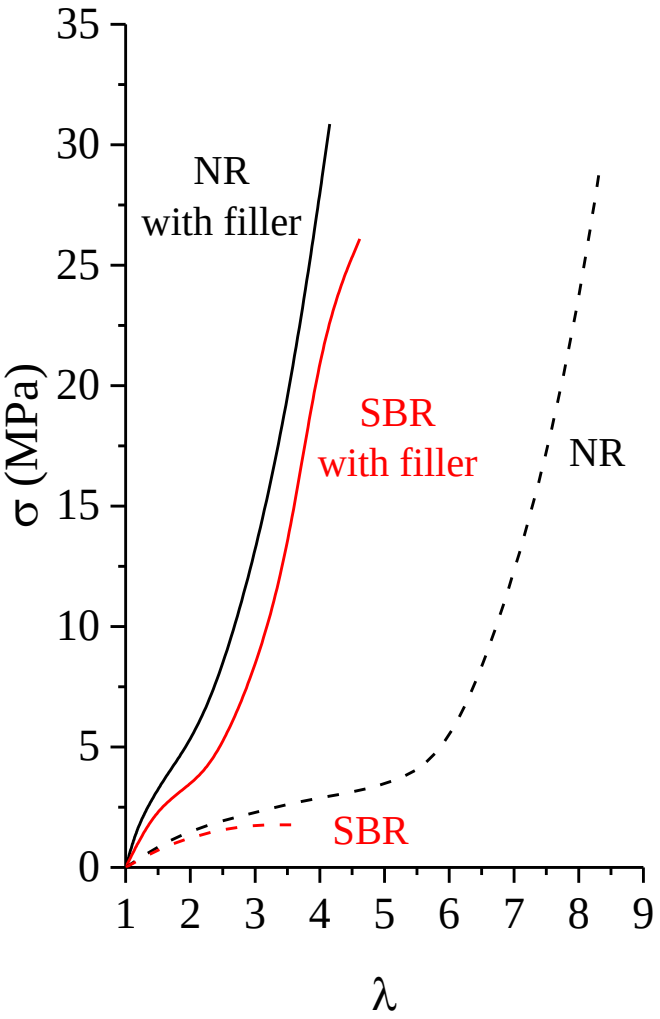

Figure 1.26 Comparison of stress-strain curves of an amorphous elastomer (SBR) and a crystallizable one (NR): dashed curves represent unreinforced samples and solid curves represent samples reinforced with carbon black.

Plasticizers

The need to reduce the viscosity of polymers and blends to facilitate processing involves the use of plasticizing substances, generally made up of mineral or synthetic oils (e.g., phthalates, adipates) compatible with the elastomer. Their use is often dictated by cost reasons because they allow the use of high rates of fillers without compromising the fluidity of blends and the hardness of vulcanizates. Some types of commercial rubbers already contain substantial quantities of plasticizers, called extenders, added to the elastomer by the manufacturers. Factors governing the

choice of plasticizer type include cost, compatibility, low-temperature properties, volatility, staining power. The staining power refers to the ability to cause color changes in the manufactured item or introduce such changes on surfaces of items in contact with the vulcanizate containing the staining product. Compatibility is related to the chemical affinity of materials, in other words, to the reciprocal values of solubility parameters and polarity. Poor compatibility leads to the exudation of plasticizers to the surface of the vulcanizate or blends over time, resulting in obvious drawbacks. Since the plasticizer acts as a solvent, it has the effect of increasing the flexibility of the vulcanizate at low temperatures, provided that its freezing point is lower than the polymer T_g.[55]

Antioxidants

Over time, elastomers undergo oxidative attacks that cause a progressive deterioration of properties (aging). This occurs through radical-type reactions whose reaction mechanism consists of three main phases: initiation, propagation, and termination. The formation of the macroradical R-O· with the formation of peroxides ROOR and the dismutation reaction of the macroradical with the formation of carbonyl groups and new free radicals can occur. In the case of unsaturated rubbers, additional reactions of radicals to double bonds should also be considered. The occurrence of this type of reaction for long time leads to an increase in crosslink density. Simultaneously, rearrangement reactions of hydroperoxide macroradicals that cause chain breaks and hence destruction of the network become active. Depending on the prevalence of one of these reactions, the overall effect will be an increase in crosslinking over time (as in homo- and copolymers of butadiene) or a decrease (as in polyisoprenes). The propagation stage is drastically influenced by the presence of heavy metal ions (e.g., Fe, Co, Cu, V, etc.) that accelerate the decomposition of hydroperoxides by acting as a redox couple. In the case of sulfur vulcanization, during aging, reactions leading to the destruction of crosslinks by oxidation of the sulfur link operated by peroxy radicals are possible. To counteract these reactions, substances capable of inhibiting or delaying

radical reactions, called antioxidants, are used. These can be classified into two categories, according to their action mechanisms:

1. Preventive action antioxidants. They counteract radical formation. The class includes substances that decompose hydroperoxides into inactive compounds, such as phosphites and dithioesters (e.g., dilaurildithiopropionates). Their activity is modest.
2. Propagation inhibitors. They interact with radicals ROO· giving rise to inactive products. Aromatic amines (diarylamines, aryl-alkyl-amines) and phenols, usually substituted in the ortho position with bulky alkyl groups (e.g., t-butyl), belong to this class.

From a technological point of view, antioxidants are classified into staining and non-staining. Aromatic amines constitute the staining class, characterized by the highest protective power; unfortunately, they are toxic. A particular type of aging of unsaturated rubbers is caused by ozone, which is always present in the atmosphere (approx. 0.1 ppm). Ozone adds to a double bond forming an ozonide, the decomposition of which leads to chain breakage and the formation of carbonyl and peroxide compounds. The destructive attack of ozone is particularly evident when the vulcanizate is subjected to deformation, resulting in the formation of cracks that propagate over time. The only stabilizers capable of counteracting ozone (antiozonants) belong to the class of p-phenylenediamines. It is common practice to use paraffinic waxes as protectors as well. These are poorly soluble in rubber and slowly rise to the surface, forming a film that is impermeable to ozone, acting as a barrier. [55]

1.7 Nitrile and Hydrogenated Nitrile Elastomers

The present thesis work is related to an in depth study of the structure-properties relationships of hydrogenated butadiene/acrylonitrile rubbers (nitrile rubbers) characterized by different amounts of:

1) residual double bonds;

2) acrylonitrile content;

3) crosslink density.

In the following paragraphs the general properties of nitrile rubbers, and of the hydrogenate counterparts are discussed.

1.7.1 Nitrile rubbers

The term nitrile rubbers refers to copolymers of an unsaturated nitrile with a diene, particularly those of acrylonitrile with butadiene. Copolymers of acrylonitrile and butadiene, also known as NBR, are synthetic elastomers resistant to organic solvents and flexible at low temperatures. These copolymers were discovered in Germany in 1930 and later industrially developed, both in Germany in 1935 under the name "Buna-N" and in the United States as "GR-A" (Government Rubber-Acrylonitrile) in the early 1940s. They are an important industrial product, covering about 4% of the rubber market.[56,57]

The starting monomers are acrylonitrile (ACN) and butadiene. Butadiene (1,3-butadiene) is the raw monomer used for various types of synthetic rubber and thermoplastic polymers. It can be obtained through the dehydrogenation of *n*-butane (found in natural gas), 1- or 2-butylene (found in cracking gas). Polymerization of butadiene using organometallic or lithium alkyl catalysts or

cobalt-based catalysts produces *cis*-1,4-polybutadiene, a widely used synthetic rubber (Fig. 1.27).[56,57]

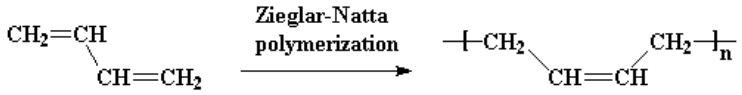

Figure 1.27 Polymerization of butadiene to *cis*-1,4-polybutadiene

Polybutadiene is a polymer characterized by a glass transition temperature T_g that varies based on its constituent units. For instance, polybutadiene with a high 1,4-cis unit content (approximately 98 %) has a $T_g \approx$ -106 °C. It is primarily used in tire manufacturing, in the production of impact-resistant polystyrene, ABS resins, and other automotive parts.[56,57]

Acrylonitrile (ACN) is a polar chemical compound produced by the oxidation of propylene in the presence of ammonia (ammonoxidation reaction) at a temperature of 400-500 °C and has a T_g of ≈ 95 °C. Nitrile rubbers (Fig. 1.28) are prepared through the copolymerization of acrylonitrile and butadiene.[56,57]

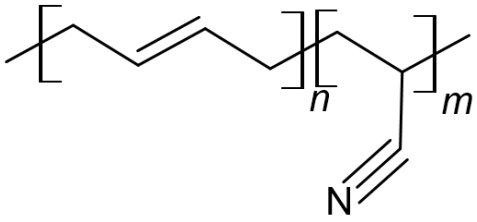

Figure 1.28 Structure of NBR

The starting monomers are widely available on the market: acrylonitrile, usually obtained by ammonoxidation of propylene on heterogeneous catalysts in fluidized bed reactors, is a highly polar monomer that readily copolymerizes with butadiene. The copolymerization is conducted in emulsion at a temperature between 5 and 30 °C, utilizing an anionic-type emulsifier, a molecular weight regulator (preferably an aliphatic mercaptan), and an electrolyte to reduce emulsion

viscosity and potentially act as a buffer. Sodium, potassium, or ammonium salts of C_{12}-C_{18} fatty acids, alkyl- aryl sulfonates, alkyl sulfates, etc., either alone or in combination, are used as emulsifiers. The choice of aliphatic mercaptan as a molecular weight regulator depends on polymerization conditions. For high conversion or low acrylonitrile percentages, a high molecular weight mercaptan like *tert*-tetradecyl mercaptan is used, while for around 60% conversion and high acrylonitrile content, a more reactive mercaptan like *tert*-nonyl mercaptan is preferred. The quantity of mercaptan used depends on the desired molecular weight, typically ranging from 0.25 to 0.75 wt% of the monomer weight. Organic hydroperoxide systems, such as cumene hydroperoxide, diisopropylbenzene hydroperoxide, etc., in the presence of ferrous sulfate, formaldehyde, sodium sulfite, and sodium salt of ethylenediaminetetraacetic acid as a chelating agent, are commonly employed.[56,57]

The reaction environment comprises an aqueous phase (also acting as a heat sink capable of absorbing reaction heat) and the monomers forming the discontinuous phase, along with radical initiators and a surfactant (Fig. 1.29). Surfactants have hydrophilic (head) and hydrophobic (tail, non-polar) ends. Due to electrostatic interactions with water molecules, they arrange themselves to minimize surface tension by forming micelles, with the head facing the aqueous environment and the tail in the inner hydrocarbon-rich core of the micelle. The monomer is mainly solubilized within the micelles due to their hydrophobic environment, while a small portion dissolves in water. The radical initiator (primarily peroxides) dissolves in water and reacts with the monomers. The growing radical is absorbed into the micelle containing the monomer, where it reacts within the relatively small volume of the micelle itself. Polymerization occurs in a limited number of micelles due to continuous monomer diffusion towards active micelles and continues until a radical diffuses inside, terminating the reaction through combination.[56,57]

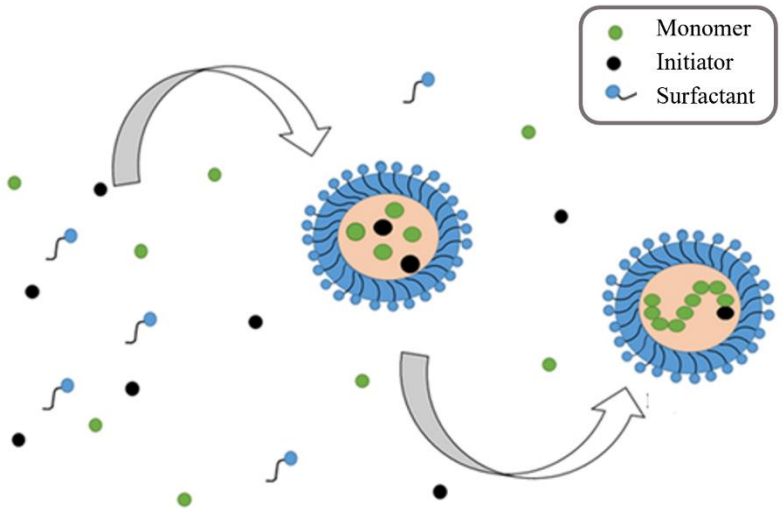

Figure 1.29 Representation of radical emulsion polymerization

In current practice, both monomers are loaded into an autoclave at the beginning of the process. Due to differing reactivities, the copolymer composition varies with conversion. Polymerization is stopped at a conversion between 60 % and 95 %, depending on the desired product, by adding an inhibitor, and unreacted monomers are recovered and recycled.[56,57]

The latex, typically containing 25 % polymer and 1.5% emulsifiers and electrolytes, suitably supplemented with an antioxidant, is further diluted with water, and coagulated, for example, using concentrated solutions of an electrolyte, controlling coagulant choice, agitation, and temperature, given their influence on particle size and morphology. The polymer is filtered, washed multiple times with water to remove impurities, and then dried. Polymerization temperature particularly influences processability characteristics. At the same composition, lower-temperature polymerization results in better behavior during mixing, calendering, and extrusion. The butadiene units in the copolymer are mainly 1,4-*trans*, although 1,4-*cis* and 1,2 units are also present. The percentage of 1,2 units decreases with increasing acrylonitrile content in the copolymer, while higher polymerization temperatures promote the formation of 1,4-*cis* units at the expense of 1,4-

trans units. The best tensile characteristics of nitrile rubber compared to SBR are attributed to the highest content of 1,4-*trans* units and the polarity of the nitrile group.[56,57]

The reactivity ratios of the two monomers, R_B for the butadiene and R_{ACN} for the acrylonitrile, (shown in Table 1.2), are both below 1 and this indicates that both monomers present on the chain terminals prefer cross-propagation over homopropagation.[59]

Table 1.2 Reactivity ratio at 5 and 50 °C for acrylonitrile and butadiene.[59]

T **(°C)**	R_B	R_{ACN}
5	0.25 – 0.28	0.02
50	0.35 – 0.42	0.04 – 0.05

The elastomer is classified based on the percentage of acrylonitrile, generally ranging between 18 and 50 wt%. This percentage is crucial, as increasing acrylonitrile content enhances density, workability, vulcanization speed, oil resistance, compatibility with polar solvents, while reducing elastic characteristics and gas permeability. For instance, the glass transition temperature of the plasticized and vulcanized products varies between -56 and -16 °C, and the brittleness temperature ranges between -55 and -16.6 °C depending on the acrylonitrile content between 20 and 52 %.[58,60] Nitrile rubbers are generally formulated and vulcanized similarly to natural rubber and SBR. They possess good resistance properties against oils, fats, and solvents, along with good elasticity, even at low temperatures. Consequently, common applications include gasket construction, gloves, belts, and flexible tubing. However, NBR also presents disadvantages. The presence of carbon-carbon unsaturated bonds in the polymer structure makes it reactive to thermal and oxidative degradation, compromising material integrity under specific operating conditions.[56-58,60]

1.7.2 Hydrogenated NBR Rubber

The drawbacks associated with the reactivity of double bonds can be addressed through the hydrogenation of carbon-carbon unsaturated bonds, resulting in hydrogenated butadiene/nitrile rubbers (HNBR). The partial or complete hydrogenation of NBR rubber (Fig. 1.30) is carried out in the presence of the Wilkinson catalyst. It is a rhodium-based catalyst [$RhCl(PPh_3)_3$] that allows selective hydrogenation by targeting only the -C=C- double bonds of butadiene, responsible for thermo-oxidative degradation phenomena. This process reduces the reactivity of butadiene significantly, resulting in tetramethylene sequences, while leaving the -C≡N bond unchanged.[59-63]

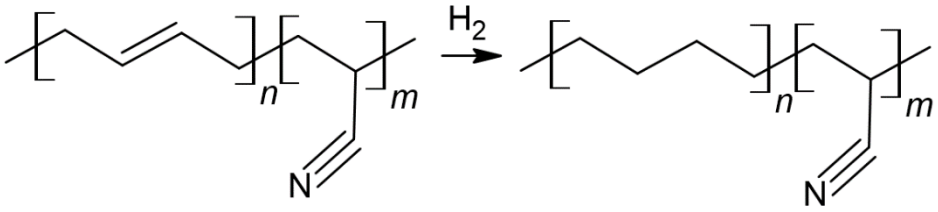

Figure 1.30 Selective catalytic hydrogenation of NBR to form HNBR.

The skeleton of HNBR mainly consists of acrylonitrile (ACN) and tetramethylene (TM) sequences. The TM sequences are chemically equivalent to polyethylene sequences (Fig. 1.31).[63]

To a lesser extent, there are residual double bonds and pendant ethylenic groups resulting from 1-2 addition of butadiene units; most of the butadiene segments in the chain (from 90 to 99%) are hydrogenated, while the remainder (from 1 to 10 %) remains unsaturated, contributing to branching.[63]

HNBR rubber retains the elastic properties of NBR but exhibits remarkable resistance to thermo-oxidative degradation and significant enhancement in mechanical properties. However, due to its expensive process, it is avoided when working temperatures are not notably high.[58]

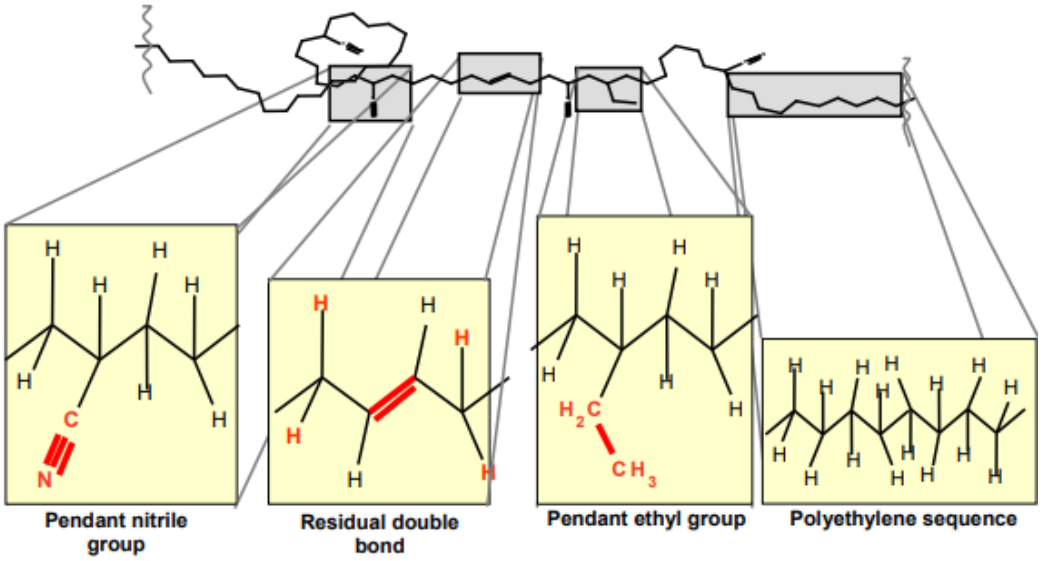

Figure 1.31 Structural elements of HNBR.

In 1980, Bayer AG leveraged its extensive experience with nitrile rubbers, introducing Therban, hydrogenated nitrile rubbers, to meet the increasing demands of advanced automotive technology. Therban offers the following characteristics:

1. High resistance to oils and fats
2. Capability to operate from -40 to 165 °C
3. Superior performance in aggressive fluids such as power steering fluids, automatic transmission fluids, engine oils, diesel, and brake fluids
4. A unique range of thermally stable samples with both partial and complete saturation, with acrylonitrile (ACN) contents ranging from 17 % to 44 %
5. Excellent abrasion resistance
6. Outstanding ozone resistance for saturated samples

The hydrogenation of unsaturated bonds is never 100% complete, and based on the content of residual double bonds, HNBR rubbers can be divided into two classes:

- Almost completely saturated rubbers containing a residual double bond percentage below 0.9%, cross-linkable with peroxides to obtain materials with superior resistance to thermal aging, ozone, and acidic gases.
- Unsaturated HNBR rubbers with a residual double bond content between 3 and 10 %, cross-linkable with peroxides or sulfur-based systems.

1.7.3 Dependence of T_g on ACN content

In general, the temperature range within which an elastomer can be used is a crucial factor for employing that specific elastomer for a particular application. The lower extreme of this temperature range corresponds to the polymer glass transition temperature (T_g). Figure 1.32 shows the values of T_g for two sets of HNBR and NBR samples as a function of ACN content.[58]

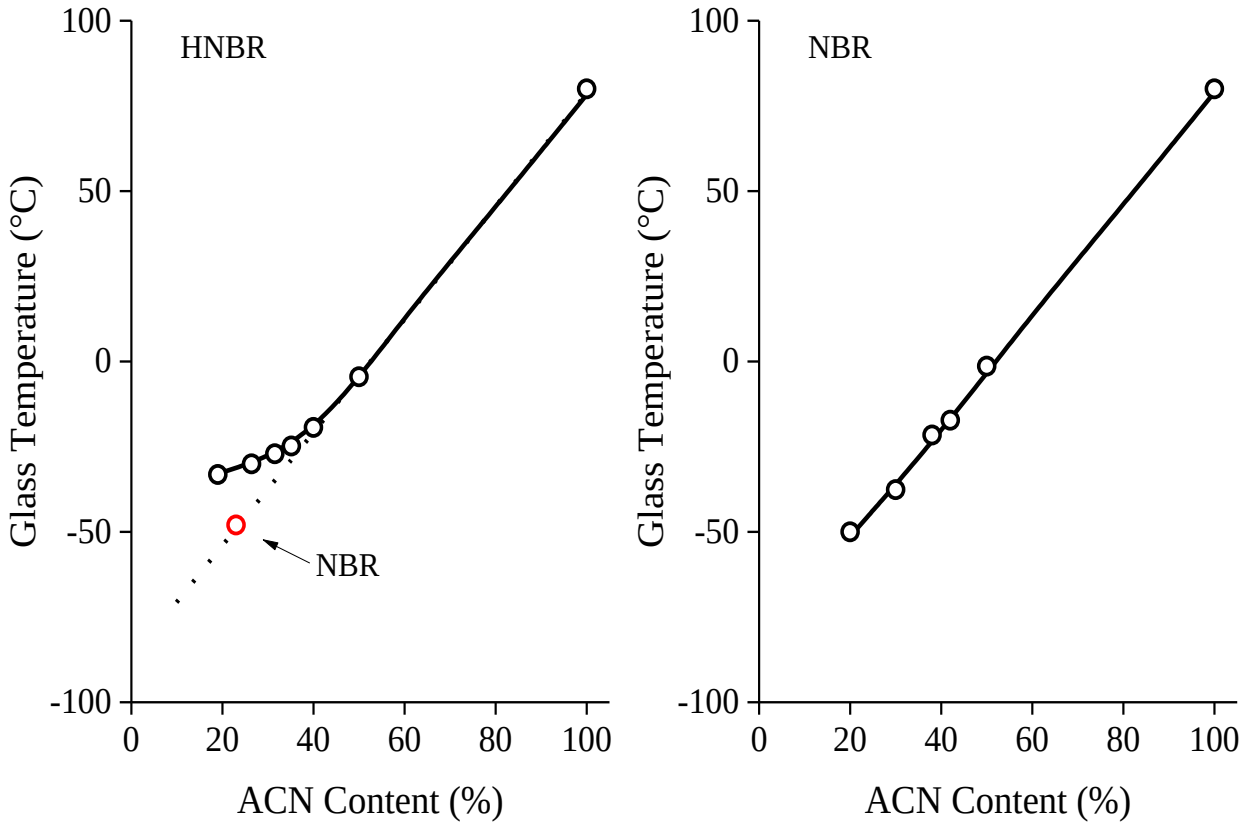

Figure 1.32 Correlation between the glass transition temperature and acrylonitrile content for NBR and HNBR (Therban).[58] (Reprinted with permission from ref. 58).

It is apparent that the T_g values increase linearly as the ACN content increases (Fig. 1.32). However, for the HNBR samples, there is a deviation from linearity for ACN content below 30 wt%. This is due to the crystallization of long tetramethylene sequences in the orthorhombic form of polyethylene (PE).[58]

The presence of polar groups, increasing the intensity of intermolecular forces between adjacent chains, reduces mobility and raises the value of T_g.[58] Hydrogenation of NBR, on the other hand, leads to a decrease of intrinsic chain flexibility at low temperatures and an increase in the glass transition temperature. The adjacent bond to unsaturation present in NBR, indeed, are almost free to rotate due to the low torsion barrier. In general, the T_g value of HNBR samples is never lower

than -38 °C for any ACN content. Compared with NBR, this indicates that HNBR rubbers show a lower flexibility at low temperatures.[58]

1.7.4 Strain-induced crystallization of HNBR

Although HNBR are a copolymers composed of at least five different comonomeric units (1,2 and 1,4 non-hydrogenated butadiene units, 1,2 and 1,4 (tetramethylene) hydrogenated butadiene units, and ACN units), they are able to crystallize by effect of strain even at room temperature. However, the statistical concatenation of the different units can significantly disturb the constitutional regularity of regular sequences, hindering their crystallization. Therefore, the ability of HNBR to crystallize depends not only on the ACN content but also on the degree of hydrogenation and the statistical distribution of such units in the chain.[58,64]

HNBR exhibits two different crystalline forms depending on the ACN content. The X-ray fiber diffraction images obtained by stretching at room temperature HNBR samples with ACN content of 18 mol% and 45 mol% are shown in Figure 1.33. These crystalline forms are respectively indicated as Form I and Form II. [64]

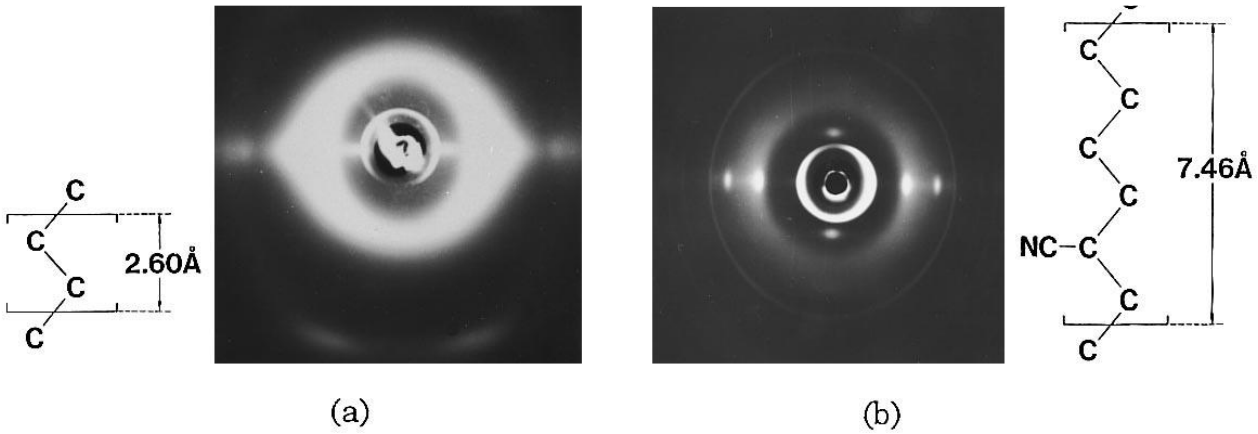

Figure 1.33 X-ray fiber diffraction patterns obtained of HNBR samples with HNBR with ACN content of 19 wt% (a) and 45 wt% (b), deformed at room temperature at strain near 400 %.[64] (Reprinted with permission from ref. 64).

The X-ray fiber diffraction image in Figure 1.33a of Form I obtained from HNBR samples with low ACN content (18 mol%) indicates a chain periodicity c = 2.6 Å, similar to the c-axis of the orthorhombic crystalline form of polyethylene (= 2.54 Å). This indicates crystallization of the HNBR sample in a crystalline form similar to that of polyethylene. The constitutional repetition unit -CH_2-CH_2-, is shown in Figure 1.33a. The crystallization of this form is due to the presence of long tetramethylene sequences in HNBR samples with ACN content lower than 34 wt%.[64]

The X-ray fiber diffraction image of Figure 1.33b shows that the sample with 45wt% ACN content crystallizes in a different form (Form II). Form II occurs in HNBR samples with ACN contents greater than 37 wt%. It corresponds to a chain periodicity c = 7.46 Å and it compatible with the crystallization of long alternate sequences of ACN and tetramethylene units (TMAC) in a trans-planar conformation as sketched in Figure 1.33b.[64]

It has been shown that HNBR samples with low ACN content crystallize in the Form I already in the undeformed state at low temperatures. For these samples the crystallinity degree increases during stretching. In particular, at -30 °C, the degree of crystallinity increases until reaching a plateau at 100% strain (Fig. 1.34). HNBR samples with high ACN content, instead, are generally amorphous in the undeformed state, and do not experience cold crystallization. However, they crystallize in Form II by effect of stretching. For these samples, at -30 °C, crystallization starts at strains greater than 100 % and crystallinity keeps increasing until reaching the rupture (Fig. 1.34).[64]

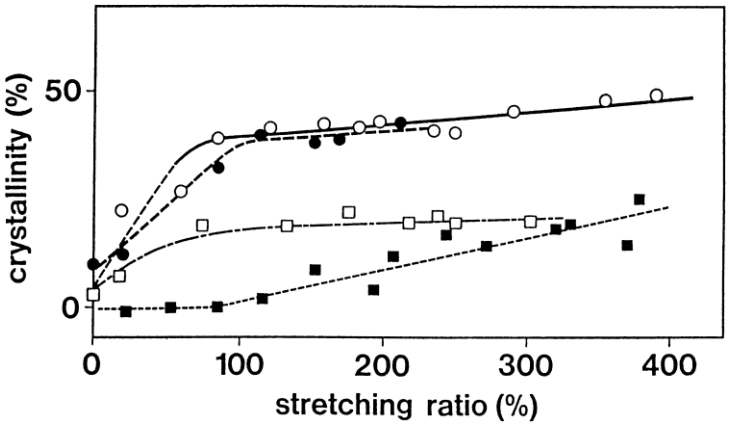

Figure 1.34 Values of crystallinity index at -30°C as a function of draw ratio in HNBR samples with different acrylonitrile content. ■ ACN = 18 mol%; ● ACN = 28 mol%; □ ACN = 37 mol%; ○ ACN = 45 mol%.[64] (Reprinted with permission from ref. 64).

These results indicates that rubbers with lower ACN content crystallize during stretching more easily compared to samples with high ACN content, because crystallization occurs already in the undeformed state by cold crystallization. The ease of crystallization is responsible for the lower flexibility at low temperatures (measured at elongation ratios below 50 %) of these samples. HNBR samples with an ACN content between 34 and 37 wt% do not tend crystallizing. At these intermediate ACN content values, crystallization is hindered due to the constitutional irregularity of the chains, as the tetramethylene sequences and/or the alternate tetramethylene/ACN sequences are too short.[58,64] Finally, it has been argued that HNBR samples with high ACN content (ACN > 37 wt%) and low residual double bond content (< 0.9%) have the potential to crystallize in Form II even in the undeformed state, and that this crystallization does not occur because of the crystallization low kinetics.[58,64] The melting temperature of Form II has been estimated to be approximately equal to 42 °C.[58,64]

X-ray diffraction images of HNBR samples with different ACN content collected for different strains at 25 °C, are shown in Figure 1.35. The samples are amorphous in the unstretched state and crystallize by stretching. In particular, for the samples with 19, 41, and 44 wt% ACN, the crystalline

reflections start appearing at strains of 200 %, 400 %, and 300 %, respectively. The sample with 19 wt% ACN crystallizes in Form I, whereas the samples with 41 and 44 wt% ACN crystallize in Form II. The sample with 33% ACN, instead, does not crystallize by stretching at room temperature even at large strains, and only the polarization of the amorphous halo on the equator occurs.[70]

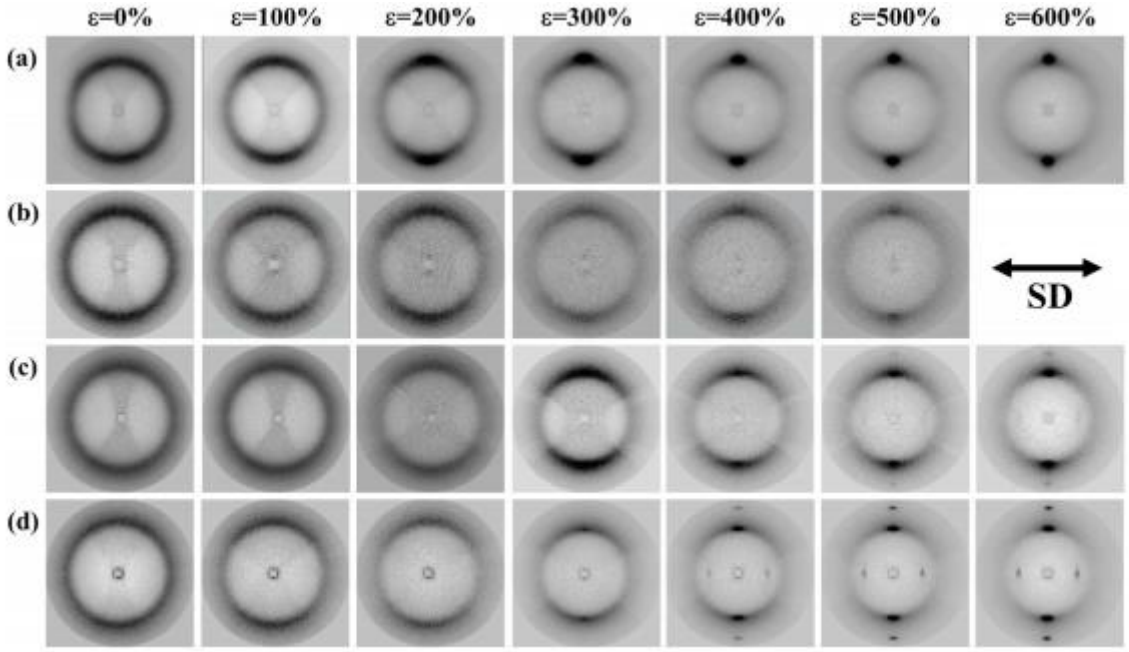

Figure 1.35 X-ray fiber diffraction images collected at 25 °C while stretching at the indicated strains, HNBR samples with ACN content of (a) 19 %, (b) 33 %, (c) 41 %, and (d) 44 %.[70] (Reprinted with permission from ref. 70).

1.7.5 Crystallization at low temperature of HNBR rubbers

The low temperature crystallization of unstretched HNBR samples has been also studied. As an example, the DSC thermograms collected for a HNBR sample with ACN and residual double content of 36 wt% and 4 mol%, respectively, are shown in Figure 1.36.[65]

The protocol used in this study includes cooling the sample from 20 °C to a variable temperature of -50, -40, -30, -20, -10, and 0 °C, isotherm at that temperature (annealing) for a defined time between 1.5 and 96 hours, successive cooling to a temperature of -75 °C, and final heating to 50 °C. The study was conducted operating at a scanning rate of 20 °C/min. The DSC thermograms recorded in the last heating step from -75 to 50 °C, after a 24 h isotherm at various annealing temperatures, are shown Figure 1.36. It is observed that the sample shows remarkable endothermic peaks ascribable to the annealing protocol.[65] These peaks occur close to the glass transition temperature and have area and position that depend on the temperature adopted for the annealing. We argue that these peaks are only in part due to the melting of the crystals formed by cold crystallization during the thermal protocol, as relaxation phenomena of amorphous segments by effect of physical ageing in the glassy state may also occur.[71,72] Physical aging of polymers in the glassy state indeed, may be generally enhanced through annealing treatments at temperatures 10-30 °C lower than the glass transition temperature.[71,72] Since the glass transition of the HNBR sample of ref. 65 occurs at about -20 °C, we believe that the large endothermic peaks of Figure 1.36, occurring for the sample annealed at -40 and -30 °C are essentially due to relaxation phenomena of amorphous segments in the glassy state, coupled with possible occurrence of microphase separation of segments richer of tetramethylene sequences from sequence richer in ACN units. These endotherms are centered at temperature lower than T_g. The large endothermic peaks of Figure 1.36, occurring for the sample annealed at -20 and -10 °C, instead, are likely due

to the melting of the crystals formed in the annealing protocol. These peaks are centered at temperatures higher than T_g.

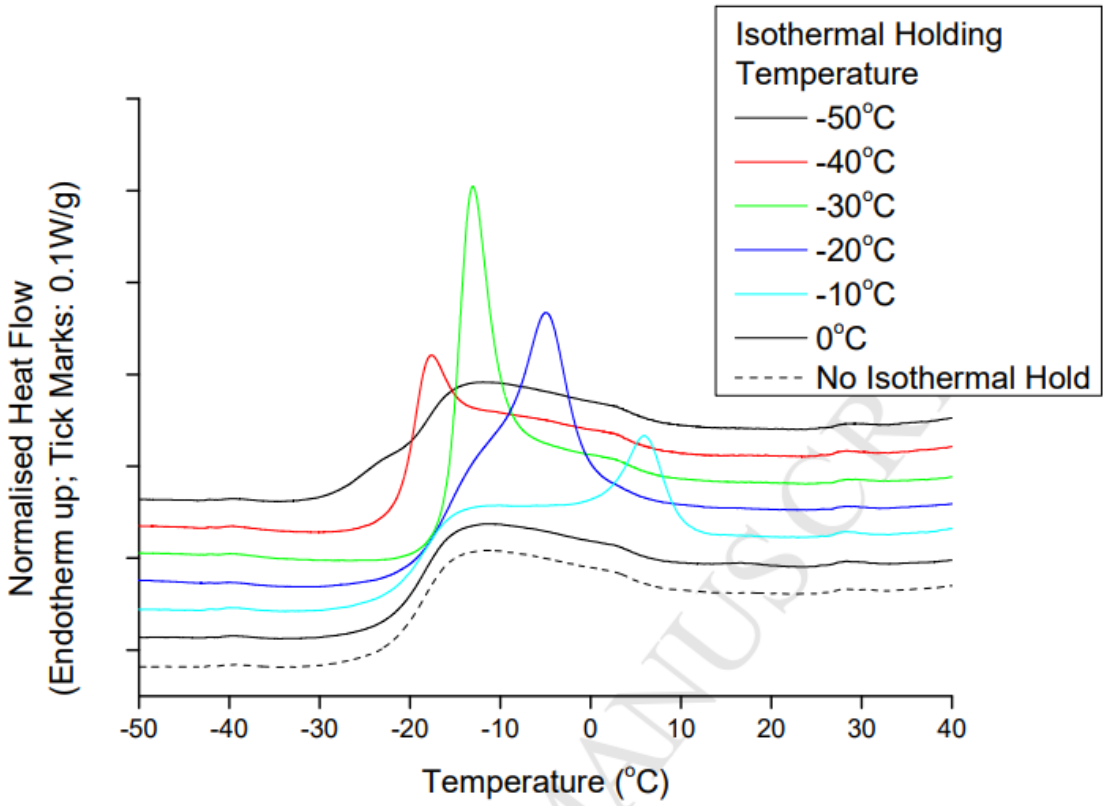

Figure 1.36 DSC heating thermograms of an HNBR sample with ACN content of 36 wt% and residual double bond percentage of 4 mol%, recorded from -75 to 50 °C after a 24-hour isotherm at the indicated temperatures.[65](Reprinted with permission from ref. 65).

For this same sample, the kinetics of cold crystallization/relaxation at -20 °C has also been indirectly probed. The DSC thermograms relative to the sample annealed at -20 °C for different times, recorded in the last heating step, are shown in Figure 1.37. An endothermic peak is clearly apparent, at temperatures higher than the T_g at -20°C. The higher the annealing time, the higher the enthalpy and melting temperature related to this peak. [65]

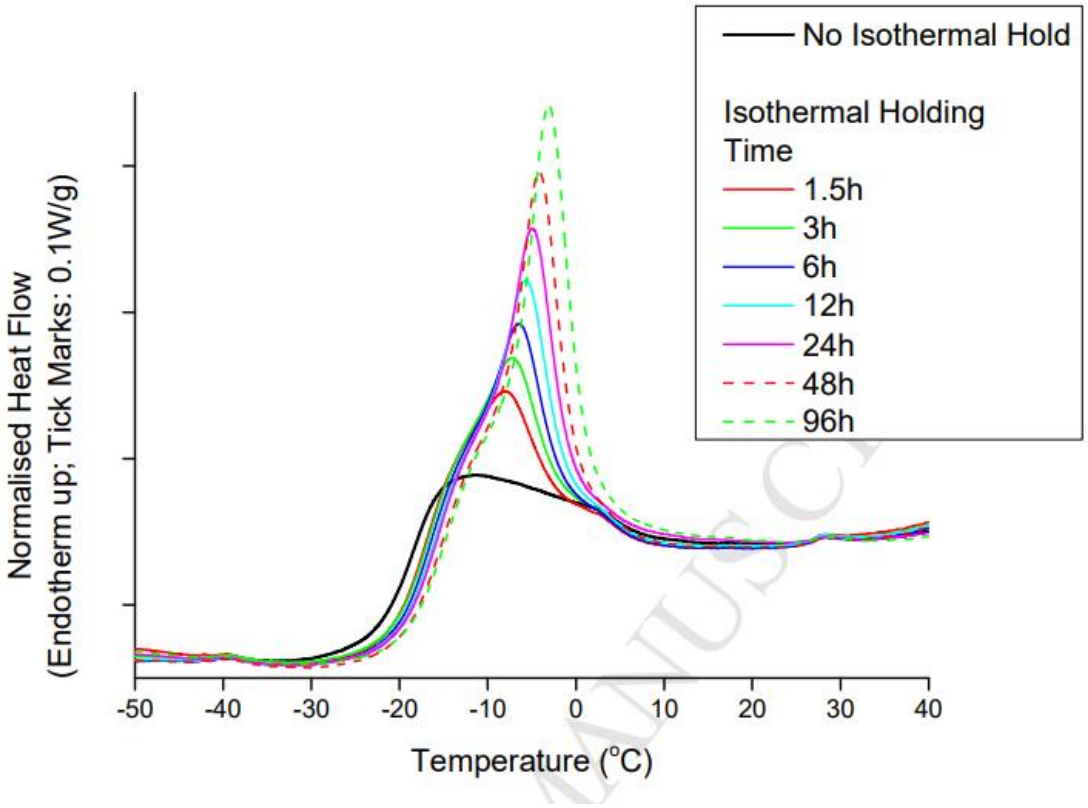

Figure 1.37 DSC heating thermograms relative to an HNBR sample with an ACN content of 36 wt% and a residual double bond of 4 mol%, recorded from -75 to 50 °C, after an isotherm at -20 °C for the indicated annealing times.[65](Reprinted with permission from ref. 65).

The cold crystallization results from Figures 1.36 and 1.37 are interpreted by postulating that the HNBR sample with ACN content of 36 wt% and residual double bond of 4 mol% is characterized by the presence of tetramethylene sequences long enough to crystallize. Although the degree of crystallinity due to annealing is estimated to be rather low, a significant increase in hardness has been observed after 24 hours of exposure.[65]

Schawe et al. in ref. 66, have analyzed the thermal behavior of a HNBR sample with ACN content of 34 wt% through low-temperature annealing experiments performed using a differential scanning calorimeter operating at high heating and cooling rates (FDSC). Also in this case, endothermic peaks emerged at temperature close to T_g, after annealing. The authors have interpreted the presence of these endothermic peaks as due to the melting of crystals formed during the low-temperature

isotherms. The relative amount of such crystals increases with prolonged annealing time until reaching a plateau value due to the formation of a rigid amorphous phase (RAF). It has been shown that the relaxation kinetics of the rigid amorphous phase and the crystallization kinetics are identical. It has been argued that the low-temperature crystallization of the HNBR sample is not controlled by nucleation but by diffusion.[66]

The above results indicate that the study of cold crystallization of HNBR samples of industrial interest may be complicated by occurrence of relaxation phenomena of amorphous segments caused by annealing treatments at temperatures below T_g.

1.7.6 Applications of HNBR

HNBR rubbers have found widespread use across various industrial sectors, such as in the oil, petroleum, and automotive industries, where this specific type of rubber has seen increasing applications in the manufacturing of seals, particularly O-rings and transmission belts. Due to their excellent abrasion resistance properties, HNBR rubbers also find extensive use in the construction of pump seals and drilling systems. Figure 1.38 shows some applications of HNBR rubbers.[58]

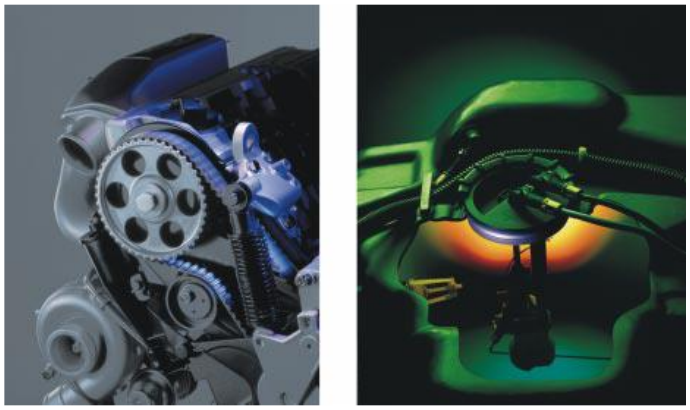

Figure 1.38 Applications of Therban rubber: a distribution belt in a typical engine compartment (left); as a component of tank gaskets (right).[58] (Reprinted with permission from ref. 65).

Chapter II

Experimental Section

2.1 Materials

The HNBR samples were supplied by Arlanxeo (Maastricht, The Netherlands) as square sheets with a size of (100 × 100) mm and a thickness of 1.2 – 1.4 mm. Two different sets of HNBR samples were analyzed, a first set including samples that were crosslinked with a sulfur-based curative system, and a second set including samples that were crosslinked with a peroxide-based curative system.

Sulfur vulcanized HNBR samples

The set of sulfur vulcanized HNBR samples consists of four subsets, each subset including HNBR samples with identical content of ACN units and initial residual double bonds (iRDBs), but different crosslink density. For each subset, the corresponding non vulcanized samples were also analyzed. The main characteristics of these samples are shown in Table 2.1. The initial, non-vulcanized samples were Therban® 3446 and Therban® 3627, Therban® 4367 and Therban® 4498VP, respectively, characterized by content of ACN units equal to 34, 36 , 43 and 44 wt%, respectively and iRDBs equal to 4, 2, 5.5 and 9 %. The non vulcanized samples have comparable molecular mass, as indicated by the Mooney viscosity of 61, 66, 61 and 78 MU, respectively. They were vulcanized with a sulfur system and the amount of sulfur added was varied between 0.38 and 3.01 phr (parts per hundred parts of rubber) to cover a wide range of crosslink density (Table 2.1). The curative package includes sulfur, stearic acid, mercaptobenzothiazole (MBT) and tetramethylthiuram disulfide (TMTD) as primary and secondary accelerants, respectively, and zinc oxide as activator (Table 2.2). For all HNBR samples, the content of sulfur (S) and accelerants

(MBT and TMTD) varies while keeping constant the ratio S/MBT and S/TMTD equal to 2.98 and 1.31, respectively. This implies an increase in the crosslinking density as the sulfur content increases from 0.38 to 3.01 phr, but similar network structures and types of sulfur bonds for all the vulcanized rubbers. The components of the curative package used for vulcanization with different S contents are shown in Table 2.2. Here following, the non-vulcanized samples are denoted as HNBRX-NV, where X is the weight percentage of ACN, whereas the corresponding vulcanized ones are denoted as HNBRX-Y, where Y is the amount (in phr) of the added sulfur.

Table 2.1 Content of ACN and initial amount of initial residual double bonds (iRDB), Mooney viscosity (ML), sulfur content and bulk density (ρ).

HNBR	Samples	ACN (wt%)	iRDB (mol%)	ML(1+4) @100°C (MU)[a]	Sulfur (phr)[b]	ρ (g/cm³)[c]
Therban® 3446	HNBR34-NV	34	4	61	0	0.950
	HNBR34-0.38				0.38	0.991
	HNBR34-0.75				0.75	0.994
	HNBR34-1.1				1.13	0.997
	HNBR34-1.5				1.50	0.999
	HNBR34-1.9				1.88	1.002
	HNBR34-2.3				2.26	1.005
	HNBR34-3.0				3.01	1.010
Therban® 3627	HNBR36-NV	36	2	66	0	0.950
	HNBR36-0.38				0.38	1.002
	HNBR36-0.75				0.75	1.004
	HNBR36-1.1				1.13	1.007
	HNBR36-1.5				1.50	1.010
	HNBR36-1.9				1.88	1.012
	HNBR36-2.3				2.26	1.015
	HNBR36-3.0				3.01	1.020
Therban® 4367	HNBR43-NV	43	5.5	61	0	0.980
	HNBR43-0.75				0.75	1.024
	HNBR43-1.1				1.13	1.027
	HNBR43-1.5				1.50	1.029
	HNBR43-2.3				2.26	1.034
	HNBR43-3.0				3.01	1.039
Therban® 4498VP	HNBR44-NV	44	9	78	0	0.980
	HNBR44-0.38				0.38	1.022
	HNBR44-0.75				0.75	1.025
	HNBR44-1.1				1.13	1.027
	HNBR44-1.5				1.50	1.030
	HNBR44-1.9				1.88	1.032
	HNBR44-2.3				2.26	1.035
	HNBR44-3.0				3.01	1.039

[a)]The Mooney viscosity, referred to the non-vulcanized sample, corresponds to the final torque measured after 4 min of testing, determined with use of a large rotor at 125 °C, after 1 min of preheating. [b)]The sulfur content corresponds to the 80% of RHENOGRAN S-80 content (shown in table 2.2).[c)]Data supplied by Arlanxeo. The bulk density is measured after curing.

Table 2.2 Curative package components used for vulcanization with different S phr.

Curative package component[a]		HNBR 0.38	HNBR 0.75	HNBR 1.1	HNBR 1.5	HNBR 1.9	HNBR 2.3	HNBR 3.0
PALMERA A9818	Stearic Acid (98%)	1	1	1	1	1	1	1
RHENOGRAN S-80	Sulphur/EPDM (80/20)[b]	0.47	0.94	1.41	1.88	2.35	2.82	3.76
RHENOGRAN MBT-80	2-mercaptobenzothiazole/ EPDM (80/20)[b]	0.158	0.315	0.473	0.63	0.788	0.945	1.26
RHENOGRAN TMTD-70	Tetramethylthiuram disulphide/EPDM (80/20)[b]	0.358	0.715	1.073	1.43	1.788	2.145	2.86
ZINKOXYD AKTIV	ZnO[c]	0	5	5	5	5	5	5

[a]) The components of the rubber compounds are in parts per hundred of rubber (phr). [b]) elastomer binder and dispersing agents (EPDM). [c]) Fine particles of precipitated zinc oxide.

Epoxide vulcanized HNBR samples

The set of peroxide vulcanized HNBR samples consists of seven subsets. Each subset includes two samples with identical content of ACN units and iRDBs, that is a non-vulcanized HNBR sample and sample crosslinked with a peroxide-based curative package in the presence of 30 phr of carbon black (CB) as reinforcing filler. The main characteristics of these samples are shown in Table 2.3. Samples with content of ACN equal to 21 (Therban® LT 2007), 34 (Therban® 3407), 39 (Therban® 3907), 43 (Therban® 4307), and 50 (Therban® 5008 VP) wt% and iRDB $\leq$ 0.9 mol% were considered, along with samples with content of ACN equal to 34 (Therban® 3467) and 43 (Therban® AT 4364 VP) wt% and iRDB $\approx$ 5.5 mol%. The samples are denoted as HNBRX-YNV, where X is the weight percentage of ACN and Y is the percentage of iRDB, for the non-vulcanized (NV) samples and HNBRX-YPC for peroxide vulcanized with CB (PC) samples.

The composition of the curative package is the same for all crosslinked samples, and the amount of CB used for the reinforced networks was in all cases 30 phr. As shown in Table 2.4, the curative package contains 4,4'-bis-(1,1-dimethylbenzyl)-diphenylamine, magnesium oxide, di(*tert*)-butylperoxyisopropylbenzene and triallylisocyanurate.

Table 2.3 Content of ACN initial residual double bonds (iRDB), Mooney viscosity (ML), sulfur content and bulk density (ρ).

HNBR	Samples	ACN (wt%)	iRDB (mol%)	ML(1+4) @100°C (MU)[a]	ρ (g/cm³)[b]
Therban® LT 2007	HNBR21-0.9NV	21	Max 0.9	74	0.960
	HNBR21-0.9PC				1.110
Therban® 3407	HNBR34-0.9NV	34	Max 0.9	70	0.950
	HNBR34-0.9PC				1.101
Therban® 3907	HNBR39-0.9NV	39	Max 0.9	70	0.960
	HNBR39-0.9PC				1.110
Therban® 4307	HNBR43-0.9NV	43	Max 0.9	63	0.960
	HNBR43-0.9PC				1.129
Therban® 5008 VP	HNBR50-0.9	50	Max 0.9	80	0.980
	HNBR50-0.9PC				1.129
Therban® 3467	HNBR34-5.5NV	34	5.5	68	0.950
	HNBR34-5.5PC				1.101
Therban® AT 4364 VP	HNBR43-5.5NV	43	5.5	69	0.980
	HNBR21-0.9PC				1.129

[a)]The Mooney viscosity, referred to the non-vulcanized sample, corresponds to the final torque measured after 4 min of testing, determined with use of a large rotor at 125 °C, after 1 min of preheating. [b)]Data supplied by Arlanxeo. The bulk density is measured after curing.

Table 2.4 Curative package components.

Curing package content		Quantity(phr)	Properties
Corax N 330	Carbon black	30	Reinforcer
Luvomaxx CDPA	4,4'-bis-(1,1-dimethylbenzyl)-diphenylamine	1.5	Antioxidant
Maglite DE	Magnesium oxide	3	Acid neutralizer, anti-aging agent
Perkadox 14-40 B-PD-S	di(*tert*)-butylperoxyisopropylbenzene	6	Bifunctional peroxide crosslinker
Kettlitz-TAIC	triallylisocyanurate	1.5	Co-activator for peroxide crosslinking

2.2 Techniques and tools

2.2.1 Swelling Test

The swelling of polymer network is a chemical-physical phenomenon involving an increase in the volume of the samples when it comes into contact with a specific solvent. Upon swelling, the mutual forces established between the polymer chain segments are different from those occurring in the absence of the solvent (Fig. 2.1).

In principle, indeed, considering the expansion coefficient of the coils α due to the effect of the solvent, three different cases can occur:

1. $\alpha < 1$: poor solvent condition; the polymer has difficulty dissolving in the solvent, causing the representative statistical coil of the polymer to have more compact size than that in theta condition, meaning the mean square end-to-end distance decreases.
2. $\alpha = 1$: theta condition, in which polymer coils act like ideal chains, assuming them as an isolated chains in an amorphous bulk at equilibrium.
3. $\alpha > 1$: good solvent condition; the polymer dissolves easily in the solvent, causing the representative statistical coil of the polymer to have a larger size than that in the theta condition, meaning the mean square end-to-end distance increases.

In equilibrium swelling experiments of polymer networks, since the selected solvent is a good solvent, there is an increase in the end-to-end distance of the network strands, which will vary depending on:

1. Nature of the polymer
2. Nature of the solvent
3. Nature of the network
4. Filler content
5. Temperature

The Flory-Rehner theory of swelling is commonly used to explain and predict the swelling behavior of crosslinked polymer networks immersed in a good solvent.[73]

At its core, the Flory-Rehner theory combines principles from thermodynamics and polymer science to describe the equilibrium state of swollen elastomers.[73] It considers the balance between the elastic energy of the polymer network and the thermodynamic interactions between the polymer chains and the solvent, on the basis of the following concepts:

1. Elastic Energy: The theory accounts for the elastic energy stored within the crosslinked polymer network. This energy opposes the expansion of the network caused by the solvent.
2. Thermodynamic Interactions: The polymer-polymer, solvent-solvent and polymer-solvent interactions and are taken into account to evaluate the change of interaction energy upon mixing. The Flory-Huggins interaction parameter (χ) is generally used to quantify these interactions. It is crucial in determining the extent of mixing and the overall swelling behavior. These interactions influence the degree of swelling at equilibrium.
3. Free Energy of Mixing and Elastic Contribution: The total free energy change by effect of swelling (ΔG_{tot}) is calculated as the sum of the free energy of mixing (ΔG_{mix}) and the free

energy change associated with the elastic contribution (ΔG_{elas}), as the Flory-Rehner theory postulates that these components are additive and separable.[73]

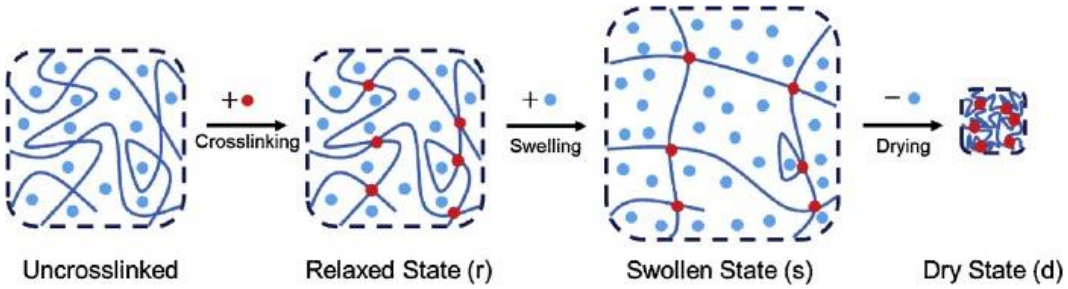

Figure 2.1 Representation of the swelling effect induced by solvent on a crosslinked network.

Within this framework, it is assumed that at equilibrium, the elastic forces within the polymer network balance the forces involved in the swelling caused by the change in polymer/solvent mixing free energy. In this way it is possible to establish how factors like polymer-solvent compatibility, crosslink density, and temperature influence the extent of swelling in elastomers.

Based on condition 3, we have that $\Delta G_{tot} = \Delta G_{mix} + \Delta G_{elas}$. This can be further articulated in terms of changes in the chemical potential of the solvent, $\Delta\mu_s^{tot}$, by differentiation with respect to the solvent moles:

$$\frac{\Delta\mu_s^{tot}}{RT} = \frac{\Delta\mu_s^{mix}}{RT} + \frac{\Delta\mu_s^{elas}}{RT} \qquad (2.1)$$

Here, R and T represent the ideal gas constant and temperature, respectively.

As stated above, at equilibrium, the elastic forces counteract the expansion of the network caused by the mixing contribution, so that the total change in the chemical potential becomes zero:

$$\frac{\Delta\mu_s^{mix}}{RT} = -\frac{\Delta\mu_s^{elas}}{RT} \qquad (2.2)$$

The Flory-Huggins expression is widely accepted as the most suitable approach to define the mixing term:

$$\frac{\Delta\mu_s^{mix}}{RT} = \ln(1 - V_r) + (1 - \frac{V_s}{V_r^0})V_r + \chi V_r^2 \qquad (2.3)$$

where χ represents the Flory-Huggins polymer-solvent interaction parameter, V_r is the volume fraction of rubber at swelling equilibrium, V_r^0 and V_s are the molar volume of the polymer and the solvent.

For a crosslinked polymer where V_r^0 tends to infinity, equation 2.3 may be simplified to:

$$\frac{\Delta\mu_s^{mix}}{RT} = \ln(1 - V_r) + V_r + \chi V_r^2 \qquad (2.4)$$

As for the elastic contribution to the total free energy change ΔG_{elas}, this term may be expressed using any molecular theory for rubber networks. The Flory-Rehner theory initially assumed the affine deformation model to describe the behavior of swollen polymer networks:[74-75]

$$\Delta G_{elas} = \frac{RT}{2M_c}\left(\lambda_x^2 + \lambda_y^2 + \lambda_z^2 - 3\right) - \frac{2RT\frac{V}{V_0}}{fM_c} \qquad (2.5)$$

The ΔG_{elas} term was expressed by equation 2.5, considering the elongation of the network in three dimensions λ_x, λ_y, λ_z, the volume of polymer-solvent system V, the volume of pure polymer V_0, the crosslinking functionality f, and the number average molecular mass of network strands M_c.

Considering the equilibrium requirements given by equation 2.2 and the mixing term in equation 2.4, the crosslink density $\nu_e (= \frac{2\rho_r}{fM_c}$ with ρ_r the density of the crosslinked rubber) is calculated by the classical Flory-Rehner equation (equation 2.6) as.[74-75]

$$\nu_e = -\frac{1}{V_s}\frac{ln(1-V_r)+V_r+\chi V_r^2}{\sqrt[3]{V_r}-\frac{2V_r}{f}} \qquad (2.6)$$

It is worth noting that the determination of the average molecular weight between crosslinks (M_c) from swelling experiments is subjected to numerous uncertainties due to the choice of the model for the evaluation of the elastic contribution to the free energy (equation 2.5) and the adopted values of V_r, χ, or f in equation 2.6. The value of the Flory-Huggins interaction parameter χ is crucial. It is generally assumed constant for a given polymer-solvent pair. However, experimental and

theoretical works revealed its (generally weak) dependence on the volume fraction of polymer V_r. Additionally, the V_r dependence of M_c for crosslinked star and linear polymers is different, so that the values of M_c evaluated from equilibrium swelling experiments are affected by uncertainties also depending on the topology of the polymers network. Determination of the rubber volume fraction V_r in a swollen network at equilibrium is another source of ambiguity. While earlier works measured the volume of swollen samples, current gravimetric methods are more popular despite requiring corrections for factors like insoluble ingredients, "real" rubber density, and time-dependent solvent imbibition during swelling. These corrections introduce considerable uncertainty. However, in spite the numerous sources of errors, equilibrium swelling experiments represent a standard tool in rubber science and technology for the determination of ν_e. [74-75]

Experimental Procedure

The values of ν_e were determined by equilibrium swelling tests according to the ASTM D297-21. The plates of the vulcanized samples are cut in squared pieces of approximately 2.5 mg (≈ 0.5 cm X 0.5 cm). The pieces are weighed and then immersed in methyl ethyl ketone (MEK, Alpha Aesar, molar volume V_s = 90.2 cm^3/mol; density ρ_S = 0.8054 g/cm^3) at room temperature. The solvent is renewed every 24 h. The swelled samples are removed from the solvent, kindly blotted with an adsorbing paper to remove the excess of MEK at the surface and weighed every 10-12 h, reaching a constant weight (w_{rw}) in approximately 72 h. Finally, the samples are dried in a vacuum oven at 72 °C achieving a constant weight (w_{rd}) in ~24 h. The volume fraction of the crosslinked rubbers at swelling equilibrium (V_r) is deduced as:

$$V_r = \frac{\frac{W_{rd}}{\rho_{rd}}}{\frac{W_{rd}}{\rho_{rd}} + \frac{W_{rw} - W_{rd}}{\rho_s}} \qquad (2.7)$$

In equation 2.7, w_{rd} represents the weight of the dry rubber, w_{rw} denotes the weight of the swollen rubber with solvent at equilibrium, ρ_{rd} and ρ_s respectively represent the density of the dry rubber and the solvent respectively, and (w_{rw} - w_{rd}) corresponds to the quantity of adsorbed solvent at equilibrium.

The crosslink density ν_e is calculated by equation 2.6, in the assumption that the functionality of the crosslinks is $f = 4$:

$$\nu_e = -\frac{1}{V_s}\frac{ln(1-V_r)+V_r+\chi V_r^2}{\sqrt[3]{V_r}-\frac{V_r}{2}} \qquad (2.8)$$

In Equation 2.8 χ is the Flory-Huggins interaction parameter between MEK and HNBR, fixed at 0.453.[76,77]

The values of ν_e are obtained as average over the results of 5 independent measurements. It has been checked that the weight loss (sol fraction) in swelling test for all the samples is below 7 wt%, and it is around 2-3 wt% for the highly vulcanized samples.

2.2.2 Spectroscopic techniques

Double Quantum Low Field NMR

Since the crosslink density obtained via swelling test is not very accurate, there are other techniques capable of determining this property. Several combined studies have utilized NMR (Nuclear Magnetic Resonance) in conjunction with swelling experiments. A well-established linear relationship between network parameters obtained from equilibrium swelling and NMR data exists. This correlation suggests that the models linking the actual NMR observables (such as averaged residual dipolar coupling, D_{res}) with crosslink density are reliable.

In literature, proton multiple-quantum NMR (MQ NMR) has been identified as a more quantitative and robust method for measuring residual dipolar couplings. The NMR is based on magnetic properties of atomic nuclei with non-zero nuclear spin *I*. These nuclei possess an angular

momentum of spin, μ. When a nucleus is placed in a magnetic field characterized by the magnetic flux density $\boldsymbol{B}_0$ oriented along the *z*-direction, the nucleus oscillates like a spinning top, as the μ vector undergoes precession around the *z*, describing a conical surface (Fig. 2.2). In this condition, the quantum number m_I may assume values ranging from - *I* to + *I* in increments of one unit, encompassing 2*I* + 1 distinct states. For ^{1}H and ^{13}C nuclei, *I* = 1/2, allowing two possible orientations: parallel and antiparallel compared to B_0.[78-79]

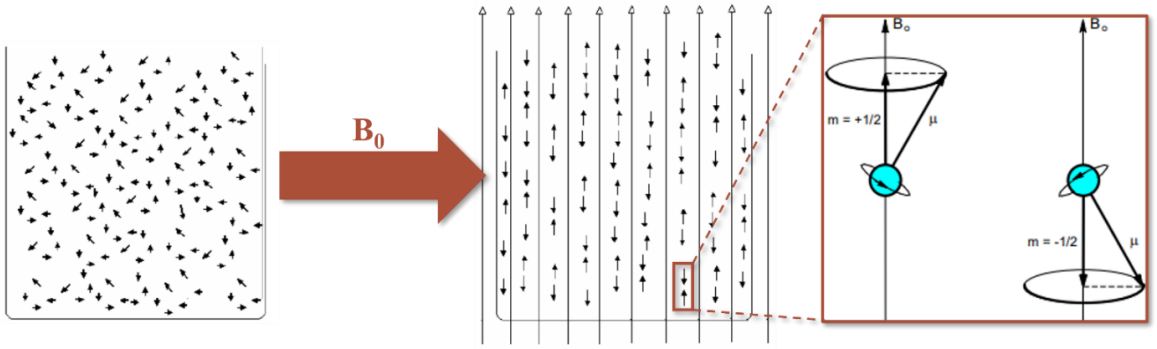

Figure 2.2 Representation of spin angular moments arranged randomly in the absence of $\boldsymbol{B}_0$ and arranged with the *z*-component either parallel or antiparallel to the applied magnetic field $\boldsymbol{B}_0$, oriented along the vertical axis. In the presence of $\boldsymbol{B}_0$, the angular magnetic moment begins a precession movement around the orientation axis of $\boldsymbol{B}_0$.

These orientations correspond to two energetic states. The energy difference between these states increases as the applied magnetic field increases. The precession motion of nuclear magnetic moments occurs at a frequency ω proportional to the energy difference between the two levels and is known as the Larmor frequency, the population of spins in the lowest energy level being slightly more abundant. The resultant of all magnetic moments is referred to as the macroscopic magnetization vector $\boldsymbol{M}_0$ (Fig. 2.3).[78-79]

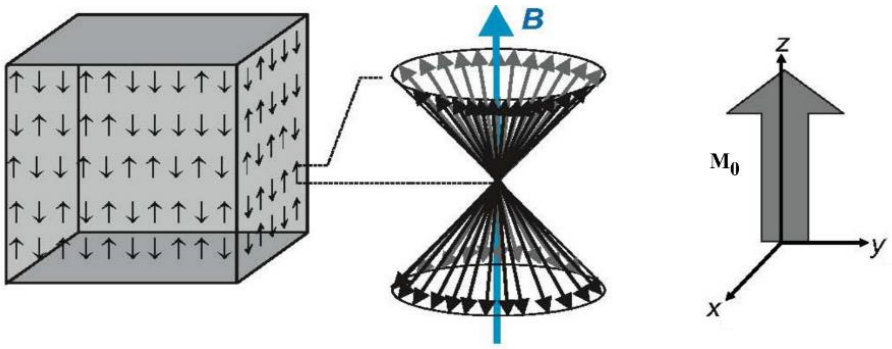

Figure 2.3 Representation of the macroscopic transverse magnetization vector, given by the sum of all spin magnetic moments of the nuclei in the system.

When applying a radiofrequency (RF) to the system, the effect is to deviate by an angle θ the magnetization vector $\boldsymbol{M}_o$ from its initial direction along the $\boldsymbol{B}_0$ field, the magnitude of which depends on the magnitude of the $\boldsymbol{B}_1$ magnetic field induced by the radiofrequency generator. Consequently, the magnetization has a longitudinal component M_z different from the equilibrium value, and a transverse component M_{xy} in the *xy*-plane (Fig. 2.4a). As soon as the action of the $\boldsymbol{B}_1$ field ceases, the rotated macroscopic magnetization $\boldsymbol{M}$ vector returns to equilibrium, corresponding to the restoration of $\boldsymbol{M}_0$ along z, following a spiral path with precession at the Larmor frequency ω (Fig 2.4b-c and Fig. 2.5).[78-79]

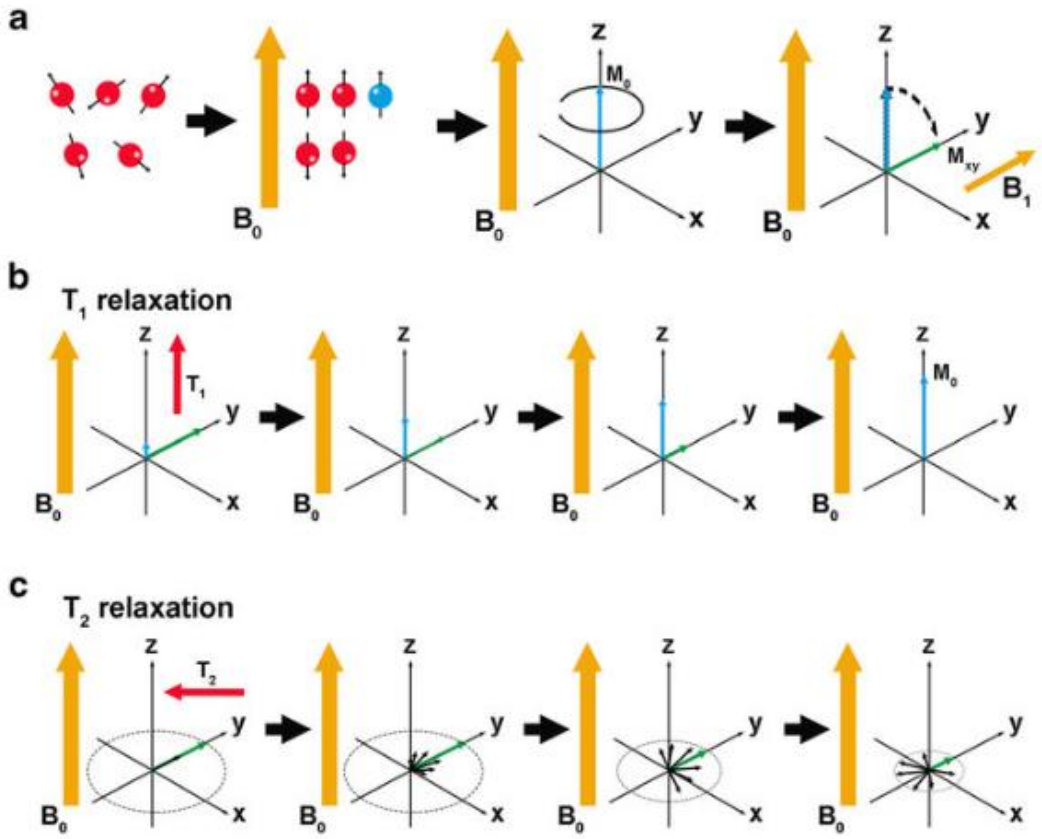

Figure 2.4 a) Rotation of M_0 from the equilibrium position, aligned with the z-axis, into the *xy*-plane following the application of the radiofrequency pulse generating a magnetic field $\boldsymbol{B}_1$, orthogonal to $\boldsymbol{B}_0$. b) Relaxation of the longitudinal component of the macroscopic magnetization vector, which occurs with the characteristic time T_1. c) Relaxation of the transverse component of the macroscopic magnetization vector, which occurs with the characteristic time T_2.

The process occurs via two exponential relaxation mechanisms: transverse relaxation or spin-spin relaxation, and longitudinal relaxation or spin-lattice relaxation.

1. Spin-spin interaction causes the damping of the transverse component of $\boldsymbol{M}$ with a time constant T_2, known as the transverse relaxation time (Fig. 2.5). Different local magnetic fields resulting from individual spins on nearby spins, actual field inhomogeneity, and system nonuniformity result in each spin experiencing a slightly different field. Consequently, each spin has a different precession frequency, causing the M_{xy} component to decay to zero due to phase coherence loss.

$$M_{xy} = M_0 e^{-\frac{\tau}{T_2}} \qquad (2.9)$$

For example, liquids have the longest T_2 on the order of seconds for protons, amorphous solids have T_2 in the range of milliseconds, while the transverse magnetization of crystalline samples decays in around 1/20 ms.[78-79]

2. The restoration of $\boldsymbol{M}$ along z happens with a characteristic time T_1, referred to as the longitudinal relaxation time (Fig. 2.5). This process involves an energy exchange with the lattice and is due to the spin-lattice interaction. The lattice comprises atoms and molecules in motion, including spins. T_1 depends on molecular mobility, with efficient energy exchange occurring when molecules and spins precess at the same frequency, i.e., the Larmor frequency.

$$M_z = M_0 \left(1 - e^{-\frac{\tau}{T_1}}\right) \qquad (2.10)$$

Low values of T_1 are typical for liquids, gases, or solutions, while they are high for solids. For liquids, $T_1 = 10^{-2}$-10^2 s, whereas for solids T_1 can be on the order of hours.[78-79]

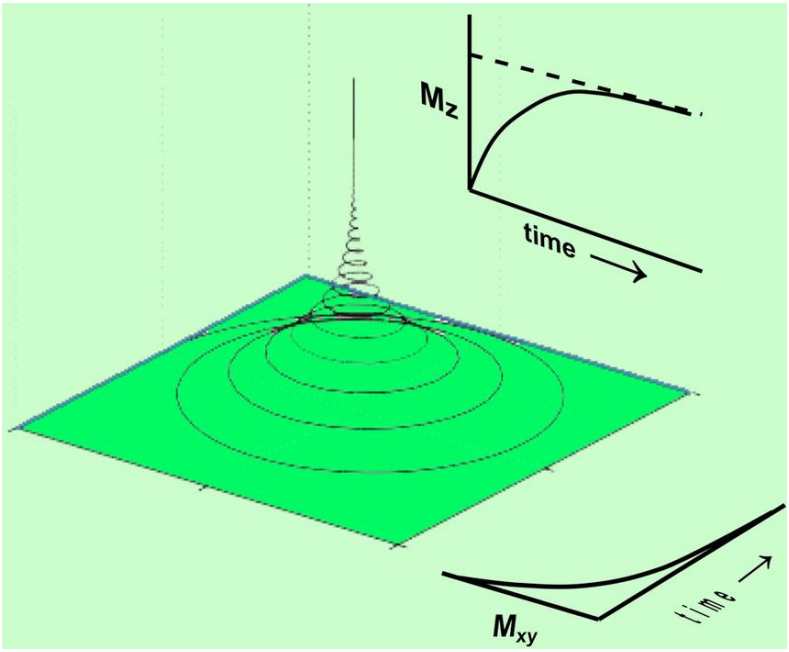

Figure 2.5 Representation of the relaxation of the ***M*** vector from the excited state to the equilibrium state. The vector restores the equilibrium state through a precession motion. The transverse (M_{xy}) and longitudinal (M_z) relaxation trends over time are represented.

Placing a receiving coil in the *xy* plane, the motion of the ***M*** vector induces an electromotive force across it, following Faraday-Neumann's law, representing the NMR signal. This signal, termed Free Induction Decay (FID), over time exhibits damped oscillations at the ω frequency, with a decay constant equal to T_2 and intensity proportional to the magnitude of transverse magnetization.[78-79]

The NMR signal depends on parameters T_1, T_2, and the total number of nuclei per unit volume (proton density). The decay time of FID intensity is directly correlated with proton density through its amplitude and T_2. However, the measurement of T_1 is indirect and relies on the acquisition techniques. By appropriately choosing the RF pulse sequence, it is possible to impart a chosen spin system dynamic, subsequently obtaining the desired physical information from the NMR signal over time.

NMR techniques is generally based on Fourier transform of the FID to glean information about spectral chemical shifts and the chemical connectivity. However, Time Domain NMR (TD-NMR)

directly analyzes the FID. While TD-NMR may disregard details about the chemical environment of individual nuclei, it offers insights into molecular mobility. The characteristic signal features of this technique offer valuable information on the morphology, topology, and dynamics of diverse polymer matrices, particularly in elastomeric materials.[80-82]

TD-NMR is a versatile tool capable of providing extensive information about polymeric materials, ranging from simple Bloch Decay experiments to complex multiple-quantum experiments. Remarkably, even when employed at low magnetic fields, TD-NMR yields robust data, proving effective even in sensitive contexts like forensics, detecting variations in the same commercial products across different batches.[80-82]

In the Bloch Decay (BD) experiment, a single pulse is used to rotate proton magnetization ($\boldsymbol{M}_0$) by 90°, maximizing the measured signal immediately post-pulse. By assessing the intensity of the signal at a fixed temperature, this method evaluates the number of protons in a sample, a standard technique for measuring hydrogen content in distillate petroleum products. Experiments such as Hahn echo, solid echo, and CPMG sequences provide T_2 relaxation times, reflecting system dynamics and structure. The choice of pulse sequence depends on the material's nature, whether it is soft, hard, or liquid. T_1 measurements are essential for setting appropriate recycle delays (must set to $\geq 5T_1$), aid in studying polymer side chains and segmental motions.[80-85]

1. Solid Echo Sequence (T_2)

The solid echo sequence refocuses strong dipolar interactions in highly constrained polymer chains, providing T_2 relaxation times. This sequence can isolate magnetization from softer phases by appropriate adjustments in echo times. It is generated by a 90° pulse applied at a time τ after the first 90° excitation pulse. The two 90° pulses must be 90° out of phase. The echo maximum is at a time τ after the second pulse.[84]

2. CPMG Sequence (T_2)

The Carr Purcell Meiboom Gill (CPMG) pulse sequence measures T_2 relaxation time by analyzing the decay curve. This sequence consists of a first 90° pulse followed by a train of equally spaced 180° pulses, as shown in Figure 2.6. The signal is measured in the midpoint between each pair of 180° pulses and the obtained decaying curve is fitted against equation 2.9. This method is based on total FID intensity rather than single-frequency domain peaks.[85]

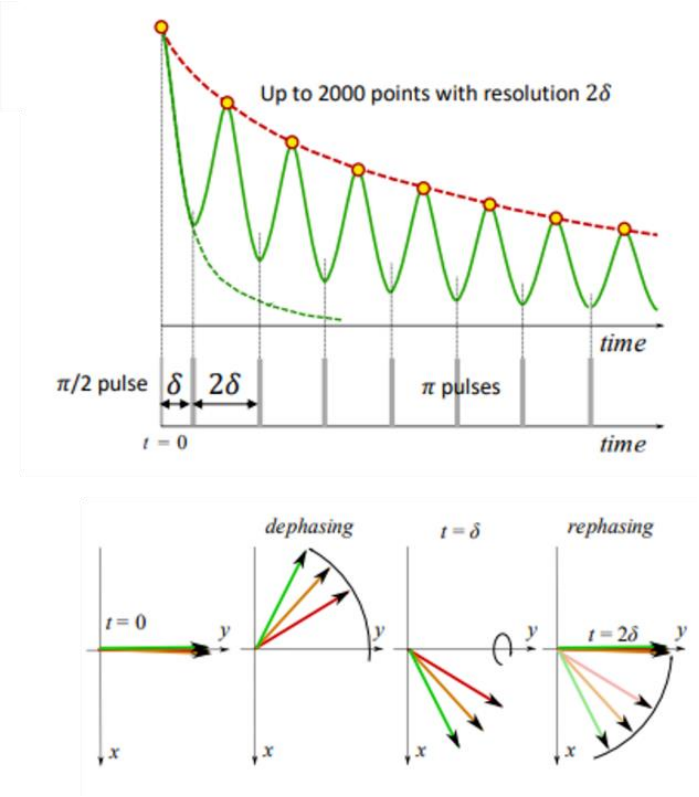

Figure 2.6 Representation of CPMG pulse sequence. After a 90°-pulse, the M_{xy} component is aligned with the y-axis (time $t = 0$). After a delay time $t = \delta$, a 180°- pulse is applied, which repeats every $t = 2\delta$.

3. Hahn Echo Sequence (T_2)

The Hahn echo sequence efficiently measures T_2 by suppressing magnetic field inhomogeneities and chemical shift effects, contributing to a clearer signal. The Hahn echo pulse sequence consist of a 90° pulse and 180° refocusing pulse. A 90° pulse flips the magnetization in the *XY*-plane, and during the first τ delay, the magnetization evolves according to its chemical shift (and field

inhomogeneities). Then a 180° pulse will be applied to invert the magnetization (Fig. 2.7). Following the inversion pulse, another τ delay will apply. During this delay, the magnetization refocuses. At the end of this second delay, the echo will be lined up.[85]

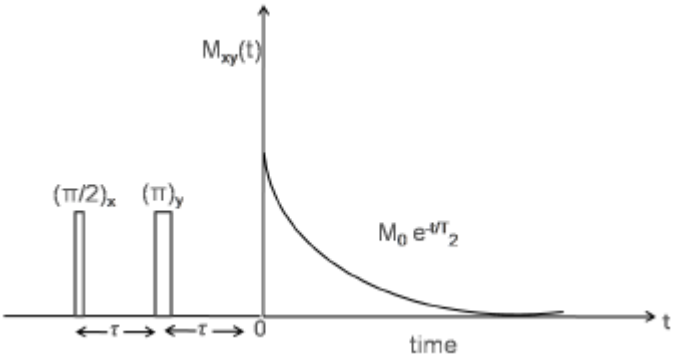

Figure 2.7 Hahn echo pulse sequence and obtained signal intensity fitted with exponential function to obtain T_2.

Multiple-Quantum NMR (MQ NMR) is a versatile technique for studying networked polymer structures and dynamics. This method exploits orientation-dependent interactions between dipolar spins, providing insights into dipolar couplings and network crosslink density. MQ NMR offers a distinctive advantage compared to equilibrium swelling. It not only provides the crosslink density and distribution but also operates swiftly without the need for solvents. An additional benefit is its compatibility with low-cost, low-resolution instruments, bypassing the necessity for high chemical shift resolution without compromising data quality. Furthermore, various NMR pulse sequences are accessible for characterizing different polymer properties, including bound rubber fraction in filled networks, polymer dynamics, and segmental motions.[83] The MQ-NMR methods leverage direct dipole-dipole interactions to generate high-order coherences. Researchers have made significant improvements in this field since the initial experimental detection of MQ phenomena, recognizing its robustness and importance in elucidating molecular-scale structures. Since the early ‘00s, K. Saalwachter has focused on developing MQ NMR techniques, particularly for characterizing vulcanized elastomer networks.[83,87] The technique not only provides the value of the

dipolar coupling constant but also allows for the determination of its distribution. The following sections will provide a brief overview of the fundamentals of MQ NMR.

The dipolar interaction between two spins may be quantified by a direct spin-spin interaction Hamiltonian ($\widehat{H}_D$) and the expression for the dipolar coupling constant (D_{ij}) between spins i and j, which are separated by a distance r_{ij} and an angle θ_{ij} relative to the magnetic field direction ($\boldsymbol{B}_0$), as given by equation 2.11 and 2.12. A diagram illustrating the orientation of magnetic dipoles in an external static field ($\boldsymbol{B}_0$) is depicted in Figure 2.8.

$$\widehat{H}_D = \frac{\hbar^2\mu_0}{4\pi}\frac{\gamma_i\gamma_j}{r_{ij}^3}\frac{1}{2}(3cos^2\theta_{ij} - 1)(3\hat{I}_{iz}\hat{I}_{yz} - \widehat{I_\iota} \cdot \widehat{I_\iota}) \qquad (2.11)$$

$$D_{ij} = \frac{\hbar^2\mu_0}{4\pi}\frac{\gamma_i\gamma_j}{r_{ij}^3}\frac{1}{2}(3 < cos^2\theta_{ij} > -1) \qquad (2.12)$$

Under the effect of molecular motions, the angular factor $\frac{1}{2}(3\langle cos^2\theta_{ij}\rangle - 1)$ fluctuates and it is equal to zero for isotropic motions and non-zero, yet small, for anisotropic motions.

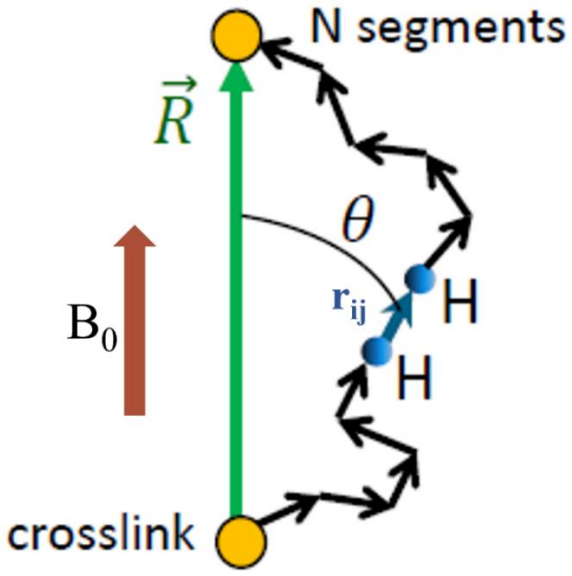

Figure 2.8 Schematic depicting the dependency of dipole-dipole interaction on the orientation and separation (r_{ij}) of two dipoles in a static magnetic field ($\boldsymbol{B}_0$).

In the case of homonuclear dipolar interactions (where the gyromagnetic ratios of two spins are equal), equation 2.12 is replaced by equation 2.13. Residual dipolar interactions due to local anisotropy motion in a system can be measured using NMR experimental spectra. They are due to incomplete averaging to zero of internuclear dipolar coupling.

$$D_{ij} = \frac{\hbar^2 \mu_0}{4\pi} \frac{\gamma^2}{r_{ij}^3} \frac{1}{2} (3 < cos^2 \theta_{ij} > -1) \qquad (2.13)$$

These measurements yield significant information about molecular structure and dynamics. Early experiments conducted by A. Pines' group in the 80's demonstrated this phenomenon using a benzene molecule oriented in a liquid crystal and simulated spectra for symmetric six-carbon systems.

MQ coherences, unlike single-quantum coherences, are not directly observable using NMR coils. They follow different selection rules ($\Delta m \neq \pm 1$) and are detected indirectly using coherence transfer through multi-dimensional spectroscopic methods. Sequences of RF pulses are designed to indirectly create these spin-forbidden MQ coherences. Observing MQ transitions is valuable due to the information they provide about the energy level diagram of a spin system, especially in cases featuring multiple coupled spins (Fig. 2.9).[88-90]

The theory involves the use of unitary transformations called propagators to simplify the analysis of complex time-dependent processes caused by RF pulses. By using cyclic pulse sequences and averaging over the effects of the applied RF, the average Hamiltonian theory simplifies the understanding and calculation of the system's behavior during NMR experiments.

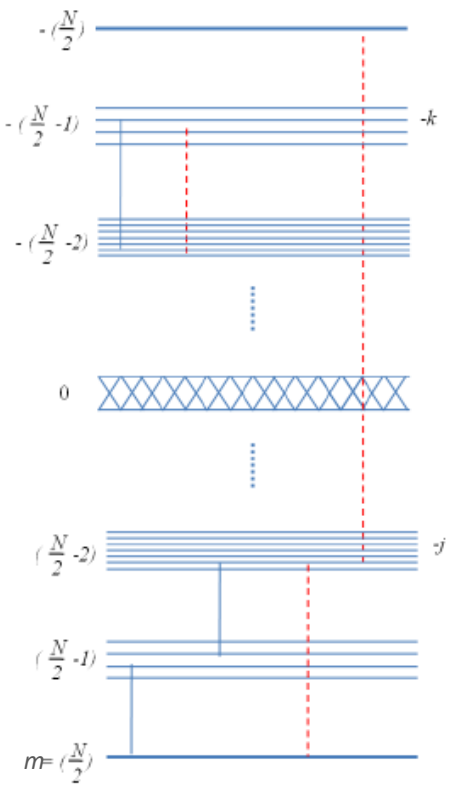

Figure 2.9 The energy level diagram of *N* coupled **12** spins in a magnetic field. The groups of energy levels are characterized by the magnetic Zeeman quantum number *m*. The splitting in each group are due to chemical shifts and couplings between the spins. The solid vertical lines indicate allowed (Δm = ±**1**) one-quantum transitions and the red colored dashed vertical lines indicate forbidden multiple-quantum ($\Delta m = \pm \boldsymbol{n}$, $\boldsymbol{n}$ = **2**,…$\boldsymbol{N}$) transitions.[90]

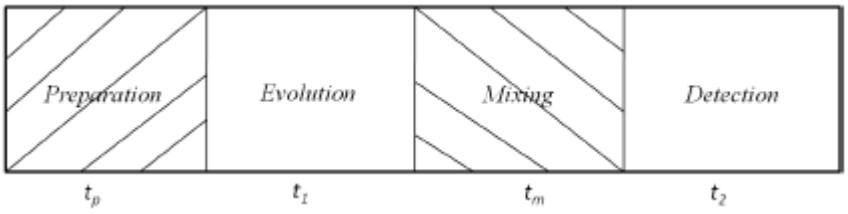

Figure 2.10 General Schematic of 2-D NMR experiments to detect multiple-quantum coherences.

Pulse sequences are designed to prepare, evolve, mix, and detect multiple-quantum coherences. These sequences involve specific periods (e.g., preparation, evolution, mixing, and detection) and use various pulse configurations and delays to create desired interactions and suppress unwanted contributions (Fig. 2.10). As stated above, techniques like MQ NMR focus on analyzing network

structures by exploiting the anisotropy of segmental motions in polymeric systems. This method allows the measurement of residual interactions due to incomplete averaging of hydrogen dipolar (or quadrupolar) interactions. However, challenges arise from practical limitations like RF inhomogeneities, pulse imperfections, and signal losses, which necessitate modifications in pulse sequences to improve stability and reliability in data acquisition.[83] Modifications in pulse sequences, like introducing specific pulse configurations and delays, aim to mitigate issues related to field inhomogeneities and maintain stability in signal acquisition. The original double quantum (DQ) pulse sequence designed to obtain such a desired interaction is shown in Figure 2.11. The total excitation (t_{exe}) and reconversion (t_{rec}) times are expressed as $t_{DQ} = t_{exe} = t_{rec} = n_c t_c$. Here, t_c and n_c denote the time for one cycle and number of cycles respectively. When applied for longer times, the stability of this sequence has been proved to be challenged by flip-angle deviation caused by weak $\boldsymbol{B}_1$ field heterogeneities in combination with considerable shift dispersion caused by shimming problem due to irregular sample shape in high field. With low field instruments, there are strong field inhomogeneities, pulse imperfections etc. that causes losses in the signal.[86]

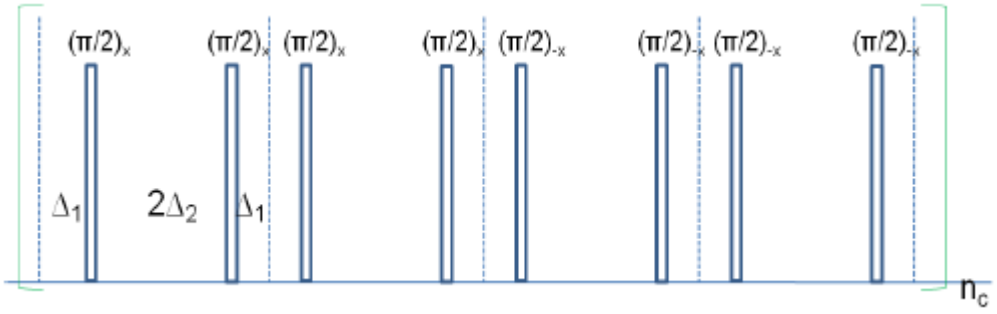

Figure 2.11 Multiple-quantum pulse sequence with appropriate delays between 90º pulses and phases.

To avoid such effects Saalwachter found that four 180º pulses in between every two 90º pulses is enough to achieve desired stability and also keep the duty cycle at the minimum.[83] Such a pulse sequence is shown in Figure 2.12. The appropriate delays between the pulses are $\Delta_1 = t_c/24 - t_p/2$

and $\Delta_2=t_c/12-t_p/2$, where t_p is 90º pulse length. The pulse sequence could be applied using different t_c and n_c. The DQ selection was performed using four-step phase cycle for the carrier phase (Φ_0) in the reconversion period ($\Delta\Phi$ = 0º, 90º, 180º, 270º) while inverting the receiver phase for alternating scans. This yields an overall 16-step phase cycle. Due to this reason, in DQ experiments, minimum 16 scans should be used for data acquisition for completion of phase cycling. [83,88]

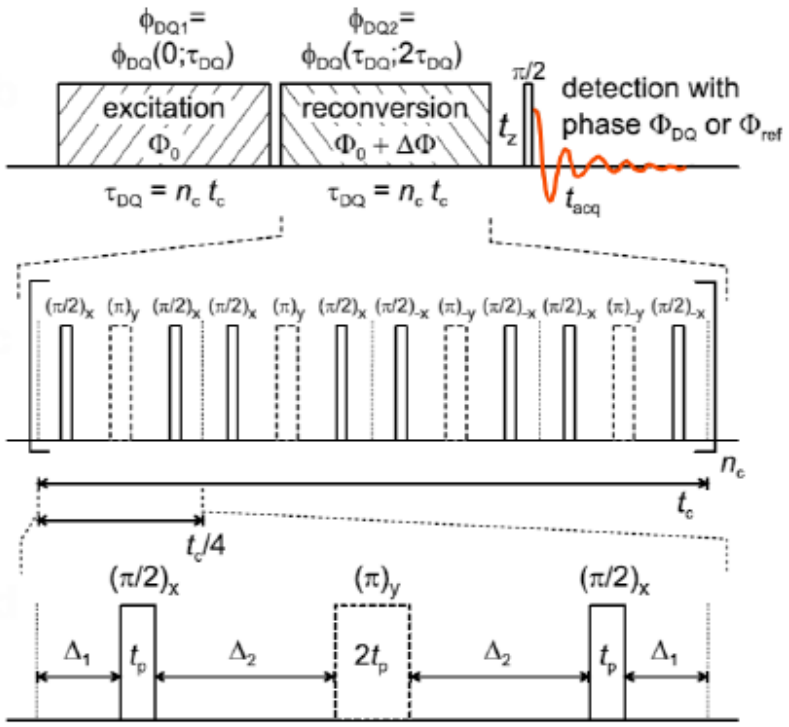

Figure 2.12 Stages of a typical multiple-quantum experimental scheme with 180º phase cycling in between 90º pulses.[83]

The relaxation of M_{xy} component of the magnetization vector is expressed as a function of phase pulse (Φ) as:

$$M_{xy}(\tau) = \int_0^{\tau} \cos\Phi e^{-\frac{\Phi^2}{\Phi^2(\tau)}} d\Phi = e^{-\frac{\Phi^2(\tau)}{2}} = M_0 e^{-\frac{\tau}{T_2}} \quad (2.14)$$

Considering that:

$$\langle \Phi^2(\tau) \rangle = \frac{\tau}{\tau_c} \omega_d^2 \tau_c^2 = \omega_d^2 \frac{\tau}{\tau_c} \omega_d^2 \tau_c \tau \quad (2.15)$$

and that

$$\langle \Phi(\tau) \rangle = 0 \quad (2.16)$$

it follows that:

$$\frac{1}{T_2} \approx \omega_d^2 \tau_c \quad (2.17)$$

Imperfect motional averaging of chain segments in polymers, fluctuating rapidly between topological constraints like crosslinks or chain entanglements, results in residual NMR interactions such as ^{1}H dipolar (or ^{2}H quadrupolar) interactions. These interactions can be significant, reaching magnitudes of several percent of the corresponding static interactions.

The orientation autocorrelation function $C(|t_a - t_b|)$ is a fundamental descriptor of polymer chain dynamics (equation 2.18). It represents the probability that a chain segment that assumes a particular orientation at time t_a is in the same orientation after the time lapse $t = |t_a - t_b|$.

$$C(|t_a - t_b|) = \langle \omega(0)\, \omega(t) \rangle = \omega_d^2 e^{-\frac{\tau}{\tau_c}} = \langle P_2(\cos\theta_{t_a})\, P_2(\cos\theta_{t_b}) \rangle \quad (2.18)$$

with $P_2(\cos\theta)$ the second Legendre polynomial:

$$P_2(\cos\theta) = \frac{1}{2}(3 < cos^2\theta > -1) \quad (2.19)$$

The orientation autocorrelation function exhibits a characteristic behavior in crosslinked polymers or entangled polymer melts. It shows a fast decay due to segmental motions (Rouse-like dynamics) with a typical time scale of ns to μs, along with a more or less pronounced plateau region that

reflects residual correlations due to crosslinks and/or topological constraints such as entanglements. The latter cause a slower decay, over a time scale from ms to s, as slow, cooperative modes are involved. Such a behavior is schematically depicted in Figure 2.13.[83]

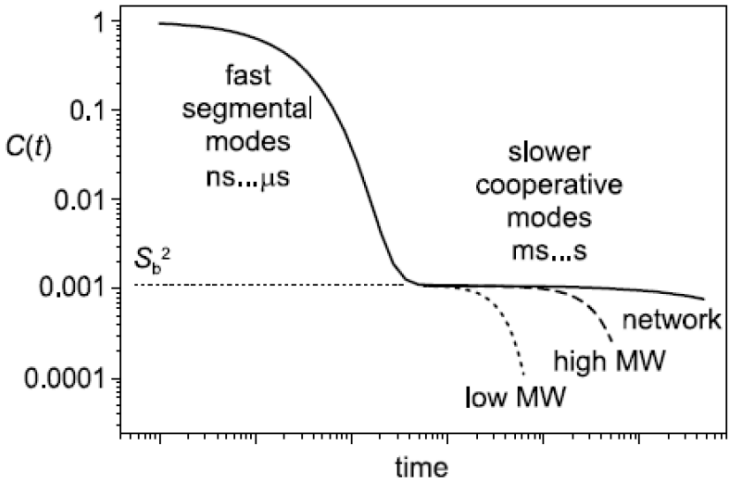

Figure 2.13 Orientation autocorrelation function for various chain dynamics in polymer melts above the glass transition temperature.[83]

The following couple of assumptions or hypotheses are the basis to detect through MQ NMR measurements the separation of the different time scales in the orientation autocorrelation function:

1. The topological constraints are constant during the time scale of the NMR experiment.
2. All local segmental motions (Rouse dynamics) are fast.

In these hypotheses, it is convenient to consider the dipolar coupling constant given by equation 2.13:

$$D_{ij} = \frac{\hbar^2 \mu_0}{4\pi} \frac{\gamma^2}{r_{ij}^3} \frac{1}{2} (3 < cos^2 \theta_{ij} > -1) \qquad (2.13)$$

as due to the product of two factors:

1. The static limit dipolar coupling, D_{stat} that would be obtained by assuming no motion.

$$D_{stat} = \frac{\hbar^2 \mu_0}{4\pi} \frac{\gamma^2}{r_{ij}^3} = \hbar \omega_d = h\nu \approx 25kHz \qquad (2.20)$$

2. The angular factor $\left(3 < cos^2\theta_{ij} > -1\right) = P_2(\cos\theta)$ that reflects the effect of molecular motion of chain ends or chain segments between two crosslinks.

If the average of angular factor is different from zero (anisotropic motion), the time average of the dipolar coupling constant (equation 2.13) over the time in the plateau region defines the residual dipolar coupling D_{res}, that is:

$$D_{stat}\langle P_2(\cos\theta)\rangle = D_{res} \qquad (2.21)$$

The corresponding relaxation signal is:

$$M(\tau) = e^{-\frac{\tau}{T_2}}\langle\cos(D_{res}t)\rangle_{chains} \qquad (2.22)$$

For isotropic motions $P_2(\cos\theta) = 0$ and the corresponding relaxation signal is:

$$M(\tau) = e^{-\frac{\tau}{T_2}} \qquad (2.23)$$

The heigh of the plateau in the orientation autocorrelation function (Fig. 2.13) is by definition the square of the order parameter S_b^2, with S_b given by:

$$S_b = k\frac{D_{res}}{D_{stat}} \qquad (2.24)$$

where k accounts for the averaging over the very fast intra-segmental motions (pre-averaging).[92]

In the assumption of Gaussian statistics for the polymer chains, S_b can be also evaluated as:

$$S_b = \frac{3}{5}\frac{r^2}{N} \qquad (2.25)$$

where $r^2 = \boldsymbol{r}^2/\boldsymbol{r}_0^2$, $\boldsymbol{r}$ is the end-to-end vector of chain segments between constraints (crosslinks, entanglements), $\boldsymbol{r}_0$ is the corresponding value in the unperturbed state, whereas N is the number of Kuhn segments between constraints. Chains can take up different conformations, but on average, they are oriented parallel to the direction that connects the two adjacent crosslinks or entanglements and hence the lower limit for the value of the dynamic order parameter S_b of a polymer chain between two spatially fixed points depends only on the number of Kuhn segments N between them and hence S_b is defined by Equation (2.18).[91]

$$S_b = \frac{3}{5}\frac{1}{N} \quad (2.26)$$

that is, it corresponds at assuming $r^2 = 1$ in equation 2.25.

Substitution of equation 2.26 in equation 2.24, provides the link between D_{res} and the crosslink density ν, that is:

$$D_{res} \approx kD_{stat}\frac{1}{N} \approx \frac{1}{M_c} \approx \nu \quad (2.27)$$

where M_c is the molar mass between crosslinks or entanglements, proportional to N.[83]

Experimental Procedure

Solid-state ^{1}H MQ TD-NMR experiments were carried out on a Bruker minispec mq20 spectrometer operating at a resonance frequency of 20 MHz with a 90° pulse length of 2-2.2 μs, a 180° pulse length of 2 times the 90° pulse length, and a dead time of 14 μs, according to the pulse sequence of Figure 2.12. The acquisition was done with 256 scans. The recycle delay was set equal to 5 times the relaxation time T_1 that was measured for each sample. Values of T_1 in the range 40-50 ms for the non-vulcanized samples, and 50-70 ms for the vulcanized sample were obtained.

Several (5-10) discs of rubber samples, with thickness 1.2-1.4 mm and diameter of 7 mm, were piled in a standard minispec tube (a glass tube with an inner diameter of 8 mm) so as to occupy a tube height of 8 mm. The sample were set inside the instrument and kept at the measuring temperature of 363 K for at least 10 min before starting the experiment.

This technique is used to investigate the network structure through the analysis of nuclear spin dipolar interactions between protons. The measured quantity is the non-zero residual value D_{res} of these nuclear spin dipolar interactions, due to incomplete motional averaging of chain segments attached to the network strands.[83] Local reorientation motions are anisotropic due to topological constraints, even though the system is overall isotropic in the relaxed state.

In addition to I_{DQ} the so-called reference signal intensity (I_{ref}) is obtained with the same pulse sequence (just changing the phase of the last pulse). The reference (I_{ref}) and DQ (I_{DQ}) intensities of a typical DQ experiment are shown in Figure 2.14. Generic expressions for I_{ref} and I_{DQ} may be written as:

$$I_{ref}(t) = e^{-\frac{t}{T_2}}(cos^2(D_{res}t))_{all\ chains} \quad (2.28)$$

$$I_{DQ}(t) = e^{-\frac{t}{T_2}}(sin^2(D_{res}t))_{all\ chains} \quad (2.29)$$

The sum of these two signal intensities is defined as total intensity, I_{tot}:

$$I_{tot}(t) = I_{ref}(t) + I_{DQ}(t) = e^{-\frac{t}{T_2}} \quad (2.30)$$

In networks the relaxation contributions to I_{DQ} and I_{tot} are nearly equal, such that the effect of molecular motions (dynamical information) on I_{DQ} can be removed through point-by-point division to give the normalized double-quantum intensity, $I_{nDQ} = I_{DQ} / I_{tot}$ (equation 2.31):[75]

$$I_{nDQ}(t) = \frac{I_{DQ}(t)}{I_{tot}(t)} \approx (sin^2(D_{res}t))_{all\ chains} \quad (2.31)$$

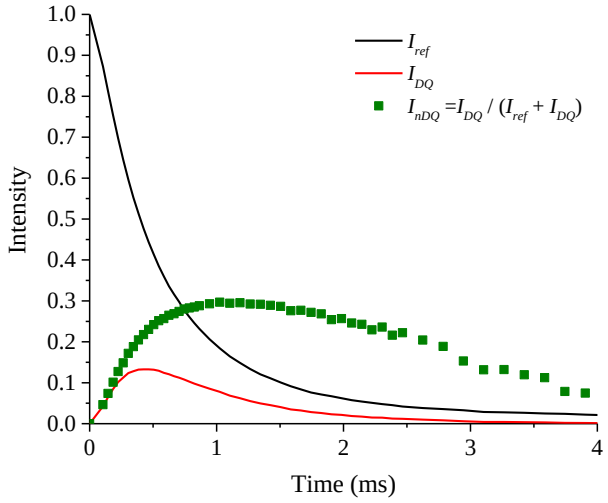

Figure 2.14 Representation of the data recorded by DQ-NMR experiment. The black line represents the reference signal, and the red line is the DQ signal. The green squares are the normalized DQ signal obtained by the ratio between DQ signal and the total signal (the total signal is the sum of DQ signal and reference signal).

The I_{nDQ} signal is a function of the excitation plus reconversion time τ_{DQ}:

$$\tau_{DQ} = bn_c t_c \qquad (2.32)$$

where $b = 1 - 12\frac{t_p}{t_c}$, is a scaling factor, t_p is 90° pulse length, t_c is the cycle time and n_c is the number of cycles.

I_{nDQ} has to attain a long-time intensity plateau at 50% (because I_{DQ} only contains half of the excited quantum orders) if the investigated material consists of only elastically active network chains. However, in real networks, additional components such as short dangling chains, defect of chains, sol or some solvent (defects) may be present. They contribute to the I_{ref} signal, not to I_{DQ} because the corresponding residual coupling is zero. It results that I_{tot} slowly decays (Fig. 2.14).

It is therefore necessary to remove this slowly relaxing contribution. The intensity function of these defects (I_{def}) was calculated by the fitting of the tail of I_{ref} - I_{DQ} function. Normally the fitting function used to determine I_{def} is an exponential decay function. For all the samples we used a double exponential function in such a way that I_{nDQ} reaches a plateau corresponding to 0.5 (Fig. 2.15).

The I_{def} fitting function used to determine the defect of the system is:

$$I_{def}(t) = A_1 e^{-\frac{t}{\tau_1}} + A_2 e^{-\frac{t}{\tau_2}} \qquad (2.33)$$

where A_1 +A_2 represents the total fraction of defects.

After subtraction of slowly decaying components, we reach stable plateau at a network relevant time scales according to:

$$I_{nDQ}(t) = \frac{I_{DQ}(t)}{I_{tot}(t) - I_{def}(t)} \qquad (2.34)$$

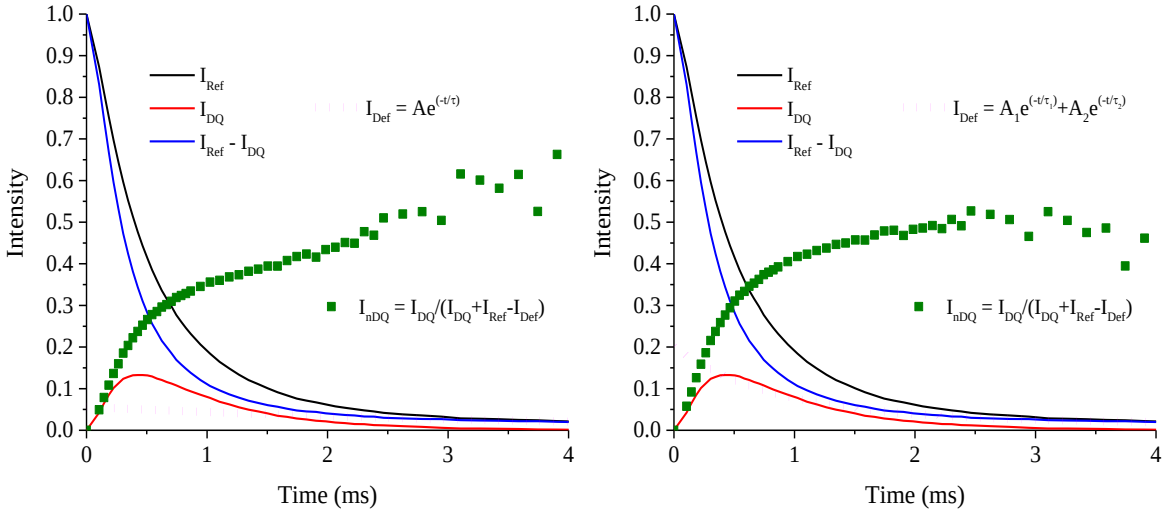

Figure 2.15 The intensity of the defects are determined by fitting the difference of the reference and DQ signals (blue curve). The blue curve exhibits a more defined tail compared to the reference signal. In ~~the~~ figure a) the defect curve (magenta dots) is obtained using a single exponential decay fitting function, whereas in figure b) it is obtained using a double exponential fitting function. In the latter case the fitting function better represents the defect content, and the normalized DQ signal (green squares) better reaches the plateau at 0.5.

In inhomogeneous polymer networks with broad or even multimodal distribution of D_{res}, such as spatially separated bimodal or multimodal chain length distributions, the I_{nDQ} can be fitted by a Fredholm distribution integral Equation 2.27: [95,96]

$$I_{nDQ}(t) = \int_{D_{min}}^{D_{max}} P(D_{res})K(t, D_{res})dD_{res} \qquad (2.35)$$

where $K(t, D_{res})$ is the so-called Kernel function and would correspond to a perfectly homogeneous sample. It is determined empirically.

The kernel function that we used is:

$$K(t, D_{res}) = \frac{1}{2}\left[1 - e^{-(0.8378D_{res}t)^{\frac{3}{2}}}\cos(0.583D_{res}t)\right] \qquad (2.36)$$

$P(D_{res})$ is a distribution function not directly obtained from the experimental data, but it is associated with experimentally obtained I_{nDQ} and may be obtained with a complex mathematical

method called Tikhonov regularization. Instead, we used a log normal distribution or a double log normal distribution:

$$P(D) = \frac{1}{D\sigma\sqrt{2\pi}} e^{-\frac{(\ln(D)-\mu)^2}{2\sigma^2}} \tag{2.37}$$

or

$$P(D) = F_1 \left(\frac{1}{D\sigma\sqrt{2\pi}} e^{-\frac{(\ln(D)-\mu_1)^2}{2\sigma^2}} \right) + F_2 \left(\frac{1}{D\sigma\sqrt{2\pi}} e^{-\frac{(\ln(D)-\mu_2)^2}{2\sigma^2}} \right) \tag{2.38}$$

with F_1+F_2 = 1, μ = ln(D_{max}) and D_{max} is the D_{res} value of the maximum of the distribution. The D_{res} average (D_{av}) correspond to:

$$D_{av} = e^{\mu+\frac{\sigma^2}{2}} \tag{2.39}$$

D_{av} is the used parameter, proportional to crosslink density (see equation 2.27).

Magic-Sandwich Echo (MSE) NMR

As previously discussed, DQ-NMR measurements provide information about the mobile phase of a polymer, characterized by slow relaxation times T_2 (time is of the magnitude order of milliseconds up to seconds). Through TD-NMR techniques, it is also possible to obtain insights into the rigid part of a polymeric system. This rigid portion, which can be a crystalline phase or a polymer segment stiffened by the presence of fillers, exhibits very fast T_2 relaxation times ($t \approx 50$ μs). During the FID acquisition, the initial 15 μs (dead time) of the signal, containing the rapid initial decay and therefore the response of the rigid polymer fraction, are not acquired due to the rather long receiver dead time. To acquire information about the entire FID shape, a "magic-sandwich echo" (MSE) pulse sequence is employed. This sequence is much more efficient than the conventionally used solid-echo, which cannot properly refocus multispin dipolar interactions. The pulse sequence

utilized is outlined in Figure 2.16 and was specifically designed to accommodate the finite phase switching time t_ϕ of an instrument.[97-99]

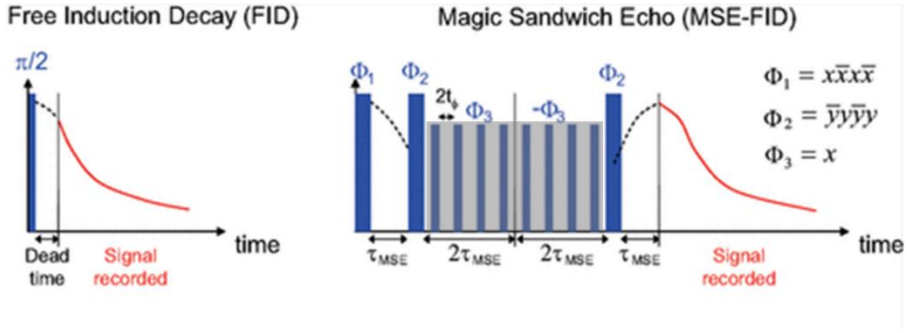

Figure 2.16 Pulse sequences for Magic-Sandwich Echo (MSE). Solid bars denote 90° pulses, and the gray-shaded lines represent groups of pulses. Initial part of the FID is missing due the dead time of the receiver. That is why we use the MSE to refocus the signal and thus measure the entire shape of the decay. This sequence is typically used to study the polymer mobility in the semicrystalline samples.[97]

Following the application of the MSE sequence, the obtained FID signal can be described by the combination of modified exponential functions, valid for a bicomponent materials including rigid and mobile phases:

$$FID(t) = f \cdot e^{-(t/\tau)^{b_1}} + (1-f) \cdot e^{-(t/\tau)^{b_2}} \qquad (2.40)$$

In equation 2.40, $b_1 = 2$ corresponds to a Gaussian decay, which can describe the behavior of a rigid polymer, whereas $b_2 \approx 1$ describes a more mobile elastomer. The weight (f) of each fitting component provides the amount of mobile/less mobile polymer in a sample. Generally, only MSE/FID data up to 0.25 ms is fitted, as longer-term decay is dominated by field inhomogeneities. Yet, the initial part is typically well-described by a simple modified exponential.[97,99]

Experimental MSE Procedure

Solid-state MSE NMR experiments were carried out on a Bruker minispec mq20 spectrometer operating at a resonance frequency of 20 MHz with a 90° pulse length of 2.2 μs and a dead time of 14 μs, according to the pulse sequence of Figure 2.16. The acquisition was done with 256 scans. The recycle delay was set equal to 5 times the relaxation time T_1 of the sample, equal to 41.2 ms. Several (5-10) discs of the rubber with thickness 0.8-1.6 mm and diameter of 7 mm, were piled in a standard minispec tube (a glass tube with an inner diameter of 8 mm), so as to occupy a tube height of 8mm. The sample were set inside the instrument and kept at the measuring temperature for at least 10 min before starting each experiment. Measurements were carried out for the non-vulcanized HNBR sample with 50 wt% of ACN, since it is the sole HNBR sample that shows some crystallinity at room temperature and in the undeformed state. As indicated by thermal analysis and X-ray powder diffraction, this sample is characterized by crystallization of long alternating tetramethylene-acrylonitrile (TMAC) sequences in the form II (see Chapter 1).[64] Since the melting temperature T_m occurs at 315 K (42 °C), MSE NMR measurements were carried out at 303 K (T = 30 °C, that is at $T < T_m$) to detect the rigid crystalline fraction expected to show fast T_2 relaxation times, and at 321 K (T = 48 °C, that is at $T > T_m$) where the FID is not expected to contain information regarding the crystalline fraction, since the polymer is in the melt state. Successively, measurements were repeated at 303 K, in order to compare the obtained FID with that of the first experiment, relative to the pristine sample.

The degree of crystallinity x_c was calculated using two approaches:

1. Since Form II exhibits slow crystallization kinetics, x_c was calculated as the ratio between the difference in areas of the FID at T = 303 K relative to the pristine sample (A_{30}) and at T = 303 K, after the melting of the crystals and successive cooling (A_{30AM}), and the A_{30} value:

$$x_c = 100 \frac{A_{30} - A_{30AM}}{A_{30}} \quad (2.41)$$

2. By determining the ratio between the difference in the maximum intensity of the FID at T = 303 K relative to the pristine sample (I^{max}_{30}) and at T = 303 K after the melting of the crystals and successive cooling (I^{max}_{30AM}), and the I^{max}_{30} value.

$$x_c = 100 \frac{I_{30}^{max} - I_{30AM}^{max}}{I_{30}^{max}} \quad (2.42)$$

Dielectric Spectroscopy

In a dielectric material subjected to an external electric field E, charges redistribute creating polarization within it. The polarization P is determined by various contributions, resulting from atomic polarization, caused by the modification of the charge distribution of molecules, ions, or the crystalline phase of the material, and electronic polarization, resulting from the distortion of the electronic charge distribution around the atomic nuclei. Added to these is the orientational polarization contribution, arising from the molecular dipole moments orienting themselves in line with the applied electric field. When subjected to a time-varying electric field, each material develops these diverse polarization contributions over a characteristic time, allowing the distinction of the three phenomena on a temporal scale. Characteristic times for electronic polarization are typically on the order of 10^{-17} s, while for atomic polarization, they are around 10^{-14} s. On the other hand, orientational polarization exhibits characteristic times greater than 10^{-12} s.[100]

When an electric field $E(t)$ varies over a much longer time scale compared to the characteristic times of the system, the delay effects in the material response become negligible, and its polarization can be considered in phase with the applied field (quasi-static assumption). For a dielectric, linear, isotropic material, under the quasi-static assumption, the polarization is described by:

$$\boldsymbol{P}(t) = \varepsilon_0 \chi_s \boldsymbol{E}(t) \quad (2.43)$$

Here χ_s represents the (static) dielectric susceptibility, and ε_0 is the vacuum permittivity.

It is noteworthy that the linearity assumption holds in experiments, since typical electric fields present in the material are on the order of 10^9 V/m, while those typically applied experimentally rarely exceed 10^5 V/m.

If, however, the quasi-static assumption is not satisfied, the polarization will exhibit delay effects due to the material's response time, and equation 2.43 will no longer be valid.

If the system satisfies the assumptions of causality, linearity, and isotropy, the polarization can be described using the following relationship:

$$\boldsymbol{P}(t) = \varepsilon_0 \int \chi(t - t')\boldsymbol{E}(t')dt' \qquad (2.44)$$

Here $\chi(t-t') = \chi_s f(t-t')$, with $\chi_s = \varepsilon_s - 1$ representing the static susceptibility, and $f(t-t')$ is the system response function.

The total polarization of the system can be expressed as $\boldsymbol{P} = \boldsymbol{P}_{in} + \boldsymbol{P}_{or}$, which is the sum of an induced and orientational polarization contribution. For the $\boldsymbol{P}_{in}$ term, the quasi-static assumption can be applied in all experimental conditions relevant to dielectric relaxation dynamics measurements, where electric fields vary with characteristic times ranging from fractions of nanoseconds to tens of thousands of seconds. In these cases, the electric field frequencies typically used in dielectric relaxation process studies range from fractions of mHz to tens of GHz. Consequently, $\boldsymbol{P}_{in}$ can be expressed as:

$$\boldsymbol{P_{in}}(t) = \varepsilon_0 \chi_\infty \boldsymbol{E}(t) \qquad (2.45)$$

Here, $\chi_\infty = \varepsilon_\infty - 1$ denotes the electric susceptibility for frequencies much higher than the applied field frequency. To describe the orientational contribution, it is necessary to employ the linear response theory introduced earlier, thus:

$$\boldsymbol{P_{or}}(t) = \varepsilon_0(\varepsilon_s - \varepsilon_\infty) \int f_{or}(t - t')\boldsymbol{E}(t')dt' \qquad (2.46)$$

Here, $f_{or}(t–t')$ represents the response function solely due to orientational contributions. By utilizing the results obtained for $\boldsymbol{P}_{in}$ and $\boldsymbol{P}_{or}$, the total polarization can be expressed as:

$$\boldsymbol{P}(t) = \varepsilon_\infty \boldsymbol{E}(t) + \varepsilon_0(\varepsilon_s - \varepsilon_\infty) \int f_{or}(t - t')\boldsymbol{E}(t')dt' \qquad (2.47)$$

As most experiments are conducted in the frequency domain, it is advantageous to have a description of polarization in such a domain. Performing the Laplace transform calculated at $i\omega$ for equation 2.47 yields the frequency dependence of the material's polarization, given by:

$$\boldsymbol{P}(\omega) = \varepsilon_\infty + \varepsilon_0(\varepsilon_s - \varepsilon_\infty) f_{or}(\omega)\boldsymbol{E}(\omega) \qquad (2.48)$$

Here, $f_{or}(\omega)$ and $\boldsymbol{E}(\omega)$ represent the Laplace transform of $f_{or}(t)$ and $\boldsymbol{E}(t)$, respectively. Equation 2.48 indicates that in the frequency domain, the polarization is expressed by a complex function. Indeed, the material's dielectric function is given by:

$$\varepsilon'(\omega) + i\varepsilon''(\omega) = \varepsilon_\infty + (\varepsilon_s - \varepsilon_\infty) \int f_{or}(t) e^{-i\omega t} dt \qquad (2.49)$$

Where ε' and ε'' represent the real and imaginary parts of the dielectric permittivity and correspond to the in phase and out of phase responses of a material, respectively. In particular, ε' is associated with the energy exchanged between the electric field and the material, while ε" is related to the energy dissipated within the material.

For an isotropic medium, containing N equivalent polar molecules in a spherical volume V, the static dielectric constant associated with orientational polarization can be described by:[101]

$$\varepsilon_s - \varepsilon_\infty = \left[\frac{4\pi}{3k_B T} \frac{3\varepsilon_s(2\varepsilon_s - \varepsilon_\infty)}{(2\varepsilon_s + 1)^2}\right] \frac{\langle m(0)m(0)\rangle}{V} \qquad (2.50)$$

Where k_B is the Boltzmann constant, T is the temperature, $m(0)$ is the instantaneous dipole moment of a macroscopic sphere of material within the sample at an arbitrary time $t = 0$.

For polymeric solutions or amorphous state above the glass transition temperature, constituted by flexible chains containing only one type of dipole μ, equation 2.50 can be rewritten as:[101]

$$\varepsilon_s - \varepsilon_\infty = \left[c_r \frac{4\pi}{3k_B T} \frac{3\varepsilon_s}{(2\varepsilon_s - \varepsilon_\infty)} \left(\frac{\varepsilon_\infty + 2}{3}\right)^2\right] g(0)\mu^2 \qquad (2.51)$$

Here, c_r is the number of dipole groups per unit volume, and $g(0)$ is the Kirkwood correlation factor, which differs from 1 if the interaction between different polar groups results in a statistical correlation between their orientations.

Dielectric relaxation is described through the permittivity (or dielectric function) measured in both the time and frequency domains since it reflects the motions of polar molecules or groups present in the dielectric material (Fig. 2.17).

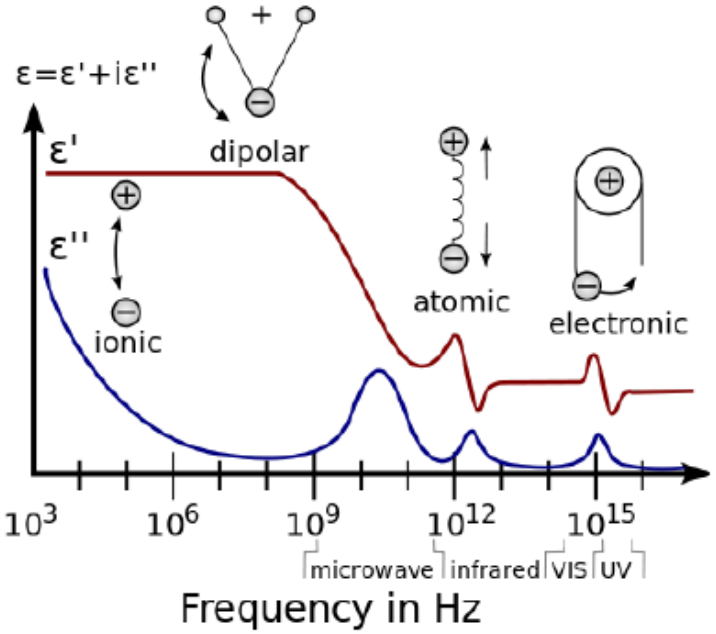

Figure 2.17: Schematic diagram illustrating the contributions of different natures of electric polarization in a material. The figure also displays the typical conductivity contribution at low frequencies.

Due to the structural complexity characterizing polymer chains, different segments of the chain can initiate distinct dielectric relaxation processes, exhibiting significantly different characteristic times among themselves. The motion of functional groups or small chain segments results in what is denoted as secondary relaxation processes, or β and γ relaxation. Additional non-cooperative rotations of large chain portions may also occurred, leading to the Johari-Goldstein relaxation.[102] Additionally, the complexity of relaxation processes is augmented by the presence of cooperative mechanisms involving segments of chains belonging to different polymeric molecules, giving rise to the structural relaxation process of the system, or α process, related to the T_g of the material.[102,103] On the other hand, for symmetric polymers, the global rotational motions of the chains give rise to very slow processes known as normal modes. Considering these different processes, a typical dielectric relaxation spectrum in frequency and isothermal conditions takes the form shown in Figure 2.18, where each process gives rise to a peak in ε'' and a step in ε'.[101] These processes are temperature dependent, as the frequency marking relaxation phenomena decreases as temperature decreases.

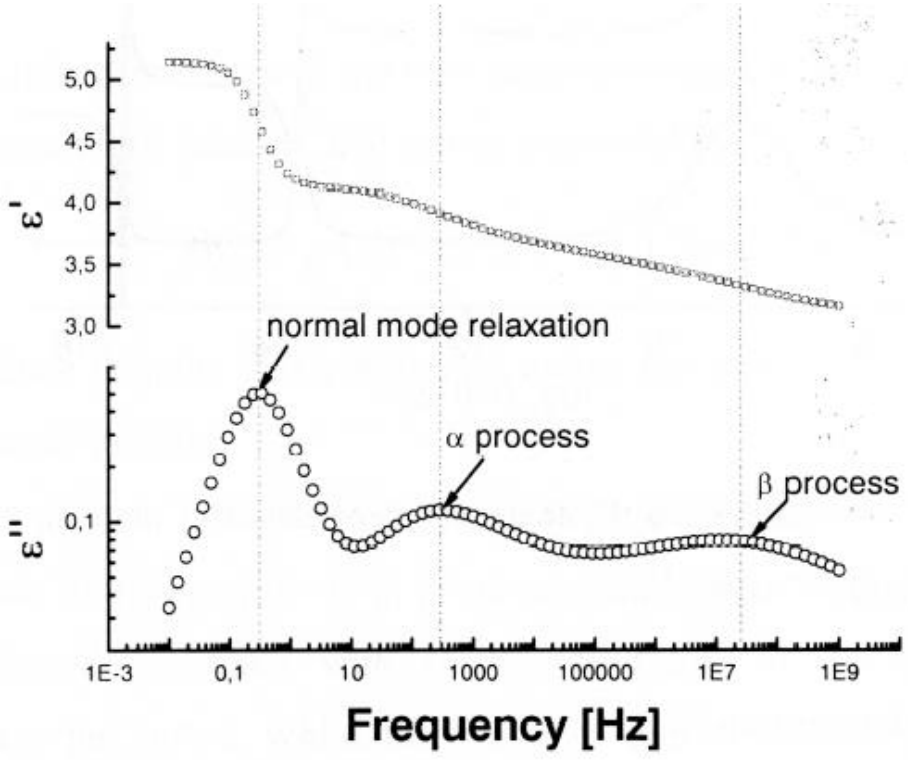

Figure 2.18: Diagram of the real part ε' and imaginary part ε'' of the dielectric function as a function of frequency.[101]

One of the most crucial properties of amorphous polymeric substances is the glass transition, strongly associated with the material structural relaxation process. The variation in material viscosity is closely linked to the ability of molecules or molecular segments to reorient in space according to the external electric field they are subjected to, and thus, to the characteristic relaxation times. In fact, according to the Maxwell model for viscoelasticity, the characteristic relaxation time and material viscosity are related by the relation $\eta = G\tau$, where G represents the shear stress. Consistent with dielectric relaxation, the definition used for T_g is the temperature at which $\tau = 100$ s.[101]

Several phenomenological functions have been proposed to describe relaxation processes, capable of delineating the typical shapes of observed relaxation processes in ε. These functions are associated with a relaxation time distribution function, described using an appropriate weight

function. Among the most frequently used are the Cole-Cole function, Cole-Davidson function, Fuoss-Kirkwood function, and the Kohlrausch-Williams-Watts function. The most general of these functions is the Havriliak-Negami (HN) function:[100,104-106]

$$\varepsilon_{HN}(\omega) = \varepsilon_{\infty} + \frac{\Delta\varepsilon}{\left[1+(i\omega\tau_{HN})^{\alpha'}\right]^{\beta'}} \qquad (2.52)$$

Here, ε_{∞} is the dielectric constant of complete relaxation concerning the considered process, $\Delta\varepsilon = \varepsilon_s - \varepsilon_{\infty}$ is the dielectric strength of the process, τ_{HN} is the characteristic relaxation time, while α and β are two parameters describing the width and symmetry of the peaks of ε'', respectively. Another frequently used relaxation function, derived from physical considerations, is the Debye function, obtained from the assumption that all molecules involved in the relaxation process share the same characteristic time.[106] By appropriately varying the values of the parameters α' and β', the HN function can be reduced to each of the functions introduced so far. Specifically, the Debye function (α' = 1, β' = 1), the Cole-Cole function (β' = 1), and the Cole-Davidson function (α' = 1) can be obtained. Thus, the complete description of a relaxation process includes the calculation of four parameters: relaxation strength, relaxation time and two shape parameters. Usually, this is performed by use of a least squares fit of the HN function to the experimental loss function. This so-called HN analysis is particularly useful for separating two superimposing relaxation processes as well as for separating a conductivity term from the low-frequency end of the overall spectrum. If frequency scans are performed at different temperatures, using the HN function, it is possible to derive the characteristic relaxation times for each temperature.[106]

Polymers are generally characterized by the presence of various dipolar units in different environments. This leads to a broad distribution of relaxation times. The corresponding loss peaks are usually extended over several frequency decades. Starting isothermally at low frequencies, generally the α relaxation is found which accompanies the glass transition in the amorphous part

of the material, that is the onset of segmental movements of the polymer chains. The loss peak of the α relaxation has an asymmetric shape. Its temperature dependence obeys the Vogel-Fulcher-Tammann law (VFT law) which can be derived from the theory of the glass transition:[106]

$$\tau_{HN}(T) = \tau_0 e^{\frac{DT_V}{(T-T_V)}} \quad (2.53)$$

In equation 2.53 τ_0 is the high temperature limit of the dielectric relaxation time, D is a measure of fragility parameter, and T_V is the Vogel temperature which is related to the dynamic glass transition temperature, with zero free volume. Sometimes T_V is also called ideal glass transition temperature. The asymmetric shape and the VFT behavior are typical features of a co-operative process. Generally, the α relaxation has the highest strength, therefore it is often called the primary or main relaxation. At higher frequencies the β relaxation may be present which involves local intra-molecular movements. It is sometimes followed by the γ relaxation of even smaller molecular units. Consequently, they are called secondary relaxations. Finally, a δ relaxation due to isolated molecules of impurities can be present at the high-frequency end of the spectrum. The loss peaks of these processes are symmetric, and they show an Arrhenius temperature dependence $\tau_{HN}(T) = \tau_0 e^{\frac{E_a}{k_B T}}$, where k_B is Boltzmann constant and E_a is the activation energy. These are typical features of a non-cooperative process.[106]

Experimental Procedure

The samples were cut in the shape of discs with a diameter of 40 mm and were metallized with gold, both on the upper and lower sides, forming a metallic circular surface on the sample with a diameter of 36 mm. The metallic surface is used to allow the flow of current between the capacitor electrodes into which the sample has been inserted for dielectric spectroscopy measurements. These measurements were carried out with a broadband dielectric spectrometer Novocontrol Alpha analyzer. It was used over a frequency range from $1 \cdot 10^6$ Hz to $4 \cdot 10^{-2}$ Hz and over a temperature

range from -100 °C (173K) to 50 °C (313 K). The temperature ramps were carried out with a rate of 2 K/min and a voltage of 3 V was applied. The dielectric dissipative part ε'' which is the imaginary part of the complex dielectric permittivity, was measured as a function of temperature. Annealing experiments were also conducted on HNBR sample 34 wt% of ACN to assess the cold crystallization phenomenon. Initially, the samples were heated to 50 °C and then held at a specific annealing temperature, T_a (close to T_g), for various durations (annealing times, t_a). Subsequently, for each t_a (at constant T), frequency scans were conducted within a range from $1 \cdot 10^6$ Hz to $4 \cdot 10^{-2}$ Hz. The selected T_a values for the sample with ACN content of 34 wt% were -20 and -10 °C. For both T_a, frequency scans were performed after annealing for the following times: 600, 1800, 3600, 7200, 14400 s. A typical fit to alpha relaxation peak emerging from the measure of ε'' to the HN function is illustrated in Fig. 2.19.[106] The following fitting function was used:

$$\varepsilon'' = \left[\Delta\varepsilon'' \, r(\omega) \sin\left(\alpha' \varphi(\omega)\right)\right] + \left(\frac{\sigma}{\omega^s}\right) \tag{2.54}$$

where:

$$r(\omega) = \left(1 + 2(\omega\tau_{HN})^{\beta'} \cos\left(\frac{\beta'\pi}{2}\right) + (\omega\tau_{HN})^{2\beta'}\right)^{-\frac{\alpha'}{2}} \tag{2.55}$$

and

$$\varphi(\omega) = \arctan\left[\frac{\sin(\beta'\pi/2)}{(\omega\tau_{HN})^{-\beta'} + \cos(\beta'\pi/2)}\right] \tag{2.56}$$

In eq. 2.54 σ/ω^s is the conductivity contribution which consists in the conductivity σ and the exponent s ($0 \leq s \leq 1$).

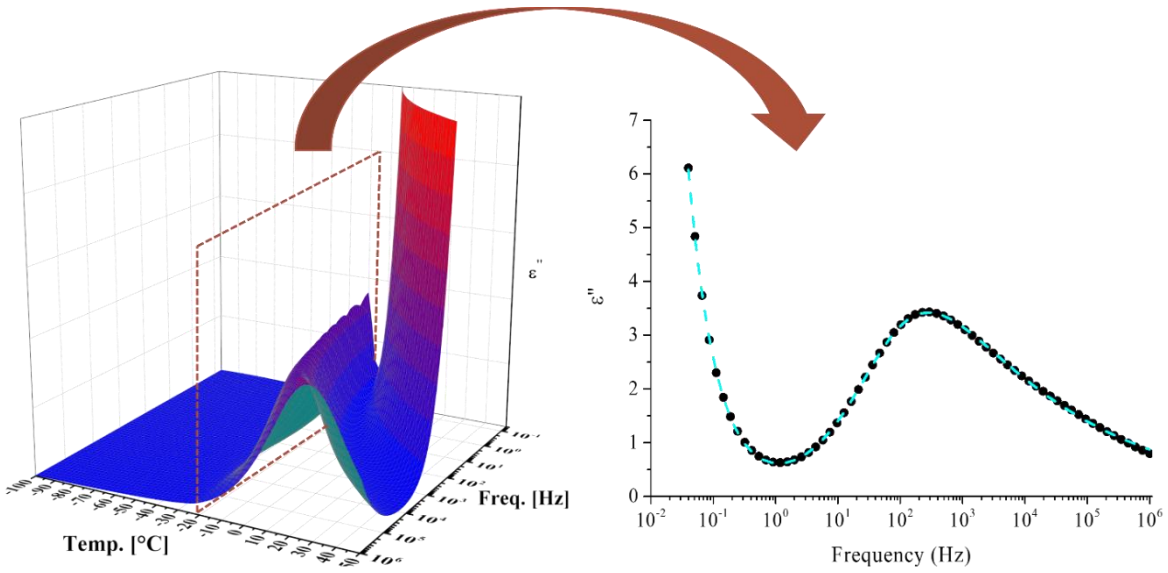

Figure 2.19 Dielectric spectroscopy experiments yield the frequency-dependent behavior of ε" at different temperatures. From this dataset, within the temperature range exhibiting the α relaxation, the trend of ε" as a function of frequency is extrapolated at a specific temperature (black dots). This dataset is then fitted using the HN equation (dashed curve).

The relaxation times obtained at different *T*, through the fitting with the HN function, are plotted as a function of temperature. Then the data were fitted using the VFT fitting function to determine the fragility parameter (*D*) of the α relaxation process:

$$\ln(\tau_{HN}) = \ln(\tau_0) + \frac{DT_V}{(T-T_V)} \qquad (2.57)$$

2.2.3 Differential Scanning Calorimetry

Differential Scanning Calorimetry (DSC) is a thermal analysis technique used for studying the physicochemical properties of the material under investigation, highlighting endothermic and exothermic phenomena as temperature changes, without degrading the sample.

In the case of a calorimetric scan performed at a constant heating rate, in the absence of transitions, the DSC curve varies monotonically with temperature. However, when processes occur involving heat absorption or release, the signal exhibits endo- or exothermic peaks. The extent of these

variations depends on the quantity of material involved in the process. The area under a peak represents the energy released (exo) or absorbed (endo) during the transformation.[107,108]

Differential scanning calorimetry is a widely used and versatile technique for characterizing the thermal behavior of polymers. Its common investigative fields involve the study of physical phenomena (glass transition, melting, crystallization) and chemical processes (dehydration, oxidation, polymerization). Specifically, DSC analysis in the realm of polymeric materials is employed to assess:

- The melting of a pure product (endothermic transition).
- Crystallization (exothermic transition).
- The degree of crystallinity of a material.
- The glass transition and/or second-order transitions associated with a change in specific heat Δc_p between the glassy and rubbery states.
- Chemical reactions (crosslinking, vulcanization).
- The presence of polymorphism.

It is termed differential because it measures the difference in thermal flux between the sample under examination and a reference one (the empty sample pan) as a function of temperature (often also as a function of time), following a controlled temperature program. This results in a thermogram, that is a graph of the heat flow dq/dt as a function of temperature.[107,108]

An example of a thermogram is shown in Figure 2.20.

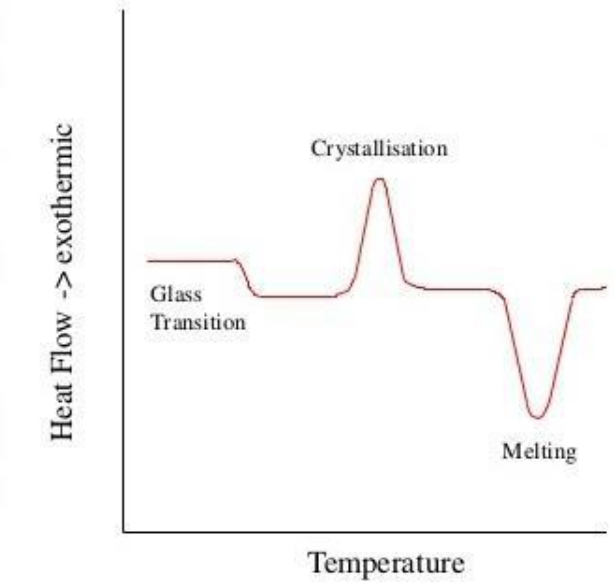

Figure 2.20 Typical DCS thermogram.

The operating principle of DSC is based on the requirement for equality between the temperatures of the reference and the sample. Initially, the difference in thermal flux remains constant as the sample undergoes no phase changes. When the sample subsequently melts, absorbing heat, the instrument must provide a higher thermal flux to the sample compared to the reference, allowing them to reach the same temperature, thus displaying an endothermic peak in the thermogram. Conversely, when the sample crystallizes, releasing heat, the instrument must deliver a lower thermal flux to the sample compared to the reference, enabling them to reach the same temperature, resulting in an exothermic peak in the thermogram. In the thermogram, the area under a peak is proportional to the mass and the enthalpy of fusion-crystallization, which in turn is proportional to the sample's degree of crystallinity.[107,108]

Thermal analysis using DSC was performed for each HNBR sample. The instruments used for the analysis were the DSC 822 and DSC 3+ by Mettler Toledo, which were both equipped with an intracooler system. A polymer sample weighing 2-7 mg was placed inside a perforated and sealed

aluminum pan. The perforation allows nitrogen to enter during the analysis, ensuring an inert environment and eliminating traces of solvents or moisture that could condense during the cooling phase.

For preliminary thermal analyses, the starting temperature was set at -90 °C, and the final temperature was 100 °C with a scanning rate of 10 °C/min. The thermogram represents the differential thermal flux as a function of temperature. Through these preliminary analyses, the T_g values of the samples where measured and the possible presence of crystalline phases were probed. The low temperature induced crystallization phenomena possibly involved for some selected HNBR samples are also studied by performing annealing experiments at various temperatures and for different duration times. These experiments were carried out on non-vulcanized HNBR samples with ACN content of 21 and 34 wt%. The temperature used for the annealing experiments were selected close to the glass transition temperatures, as those giving the highest enthalpy in the DSC heating scan recorded after 60 min isotherm of the samples at temperatures of -50, -40, -35, -30, -25, -20, and -10 °C. The annealing temperatures of -30 and -20 °C were thus selected for the samples with 21 and 34 wt% of ACN. The annealing at these temperatures was carried out for 3.75, 7.5, 15, 30, 60, 120, 240, 360, 480, and 960 min.

2.2.4 Mechanical Properties

The instrument used for the measurement of the stress-strain curves until reaching the rupture and the hysteresis cycles was an “Instron 5566” dynamometer with a load cell of 1000 N whereas for the determination of the Young’s moduli a “Zwicky” electromechanical machine by ZwickRoell with a load cell of 100N was used. Measurements were conducted at room temperature, on dumbbell specimens (Fig. 2.21) cut from the squared sheets by means of a pressure die-cutting machine, with thickness, width, and gauge length equal to 0.8-1.5, 3 and 15 mm, respectively. The specimen is placed between two grips and stretched at fixed stain rate. The initial length of the sample (L_0) and displacement ($\Delta L = L - L_0$) are measured as the grip-to-grip distance.

For the determination of the stress-strain curves and Young's modulus the international standards ASTM D638-22 were used, while for the measurement of the hysteresis cycles the international standards used are ASTM D412-16.

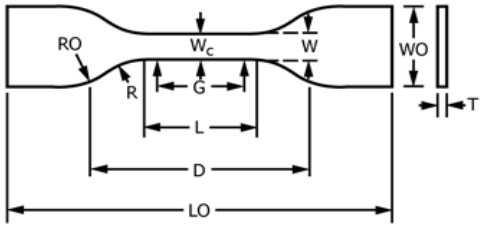

WO = 1 cm

$W = W_c = 3$ mm

L = 15 mm

LO = 6.5 cm

Figure 2.21 Geometry of the dumbbell-shaped specimens used for the determination of the mechanical parameters.

This geometry of the specimens allows to have a contact area between the material and the grips higher than the area exposed to air along the gauge length. This guarantees a uniform stretching and to maximize the applied stress in correspondence of the central part of the specimens, in such a way that breaking occurs in regions not too close to the grips.

Each test was performed at least on 5 independent specimens. The stress-strain curves, the curves recorded during the hysteresis cycles and the mechanical parameters extracted from them represent an average over at least 5 independent measurements.

Stress-Strain Curves

The sample, placed between the grips of the electromechanical machine, is subjected to a deformation at a constant strain rate r/L_0, where L_0 is gauge length. According to the ASTM standard, the ratio r/L_0 is set equal to ten (i.e. $r/L_0 = 10 \frac{\text{mm}}{\text{min mm}}$). The specimen is deformed until it breaks. This technique allows to obtain a curve known as the "stress-strain curve" where the applied engineering stress σ in MPa, equal to the tensile force F divided by the initial cross section A_0, is reported as a function of the engineering strain (ε [%]), defined as:

$$\sigma = \frac{F}{A_0} \tag{2.58}$$

and

$$\varepsilon = 100\left[\frac{L-L_0}{L_0}\right] = 100\left[\frac{\Delta L}{L_0}\right] \tag{2.59}$$

where L and L_0 are the length of the deformed specimen and the initial one, respectively, measured as the distance between the clamps (free or gauge length).

The tension set at break (t_b) was determined by bringing the two broken pieces close together, so that they were in good contact over the full area of the break and measuring the final distance L_0' between two benchmarks, initially drawn on the specimens at distance L_0, after 10 minutes. The tension set at break was calculated as:

$$t_b = \left[\frac{L_0' - L_0}{L_0}\right] 100 \tag{2.60}$$

Estimation of the Young's modulus

The rubbers are highly nonlinear elastic materials but at very low strains, the stress/strain is a constant (Young's modulus). Therefore Hooke's law may be considered valid at low strains. However, as the strain increases, this linearity ceases, and Hooke's law is no longer valid.

The Young's modulus was calculated as the slope of the initial, linear interval, of the stress-strain curves. It was determined by conducting the tests (ASTM D638) at a constant stain rate such as to have $r/L_0 = 0.1 \frac{\text{mm}}{\text{min}}$.

The Young's modulus is a parameter directly correlated with the stiffness of a rubber and is influenced by the degree of crosslinking.

$$E = \frac{\sigma}{\varepsilon} \qquad (2.61)$$

Hysteresis cycles

Hysteresis cycles were recorded for all the samples in order to quantify the degree of elasticity of the materials.-The specimens were stretched to a maximum strain ε_{max} = [(70-80 %)·ε_b] at a constant strain rate of 30 min^{-1} and subsequently unload at the same rate. The length of the specimen after the release of the tension L_r^i was measured after 10 min at the end of each cycle (i indicates the number of the cycle), along with the tension set t_s^i defined by:

$$t_s^i = \left[\frac{L_r^i - L_r^{i-1}}{L_r^{i-1}}\right] 100 \qquad (2.62)$$

Notice that L_r^{i-1}represents the initial length of the specimen at cycle i, and it is numerically coincident with the length of the specimen measured 10 min after the end of cycle i-1. When i = 1, $L_r^{i-1} = L_0$.

The value of hysteresis W_{diss}^{i} representing the relative amount of dissipated energy for each cycle, was calculated through the following equation:

$$W_{diss}^{i} = 100\frac{A_1^i - A_2^i}{A_1^i} \quad (2.63)$$

where A_1 and A_2 represent the area under the stress strain curve recorded during the loading step until reaching the strain ε_{max} and the successive unloading step until reaching stress equal zero at the same strain rate.

2.2.5 Wide Angle X-ray Diffraction

The X-ray scattering techniques applied to polymers are very useful because they can provide information about structure, polymorphism, crystallinity, and proportions of different crystalline phases present in the sample. Depending on the diffraction angle, analysis techniques can be divided into SAXS (Small Angle X-ray Scattering) and WAXS (Wide Angle X-ray Scattering). The WAXS technique provides information about molecular structure, packing of chains in the crystalline phase, crystallinity, orientation, and dimensions of crystalline domains.

The WAXS technique of a polycrystalline materials (powders) involves the diffraction of a monochromatic beam by powdered specimens and/or unoriented films. Since the axes of individual crystals and/or the chain segments in the amorphous phase are randomly oriented, the diffraction pattern is a combination of diffraction patterns from all possible orientations of the (crystalline and amorphous) structural elements constituting the sample.[109]

The phenomenon of X-ray diffraction from crystalline materials can be explained through the Bragg's law. When X-ray radiation is incident, a Bragg peak occurs when the scattered rays from various planes interfere constructively. Constructive interference happens when the phase difference between the scattered X-ray in a given direction and at the same time is a multiple of

2π.[109] In practice, Bragg diffraction occurs when a radiation of wavelength λ comparable to the interplanar distances of a crystal is specularly scattered by those planes and experiences constructive interference. Hence, the angle of incidence formed by an X-ray beam with the planes θ equals the angle that the scattered beam form with the same planes. Powder diffraction apparatuses working in reflection geometry entail that the detector for scattered rays must be positioned at an angle 2θ with respect to the direction of incident beam (Scheme 2.1A).[109] The angle θ, the wavelength λ of incident X-ray radiation and the interplanar distance *d* are connected by the relation corresponding to the Bragg's law:

$$2d\ sin\ \theta = n\lambda \qquad (2.64)$$

where *n* is an integer representing the order of the diffraction.[109]

Scheme 2.1 Scheme of reflection (A) and transmission (B) diffraction geometries for WAXS data collections.

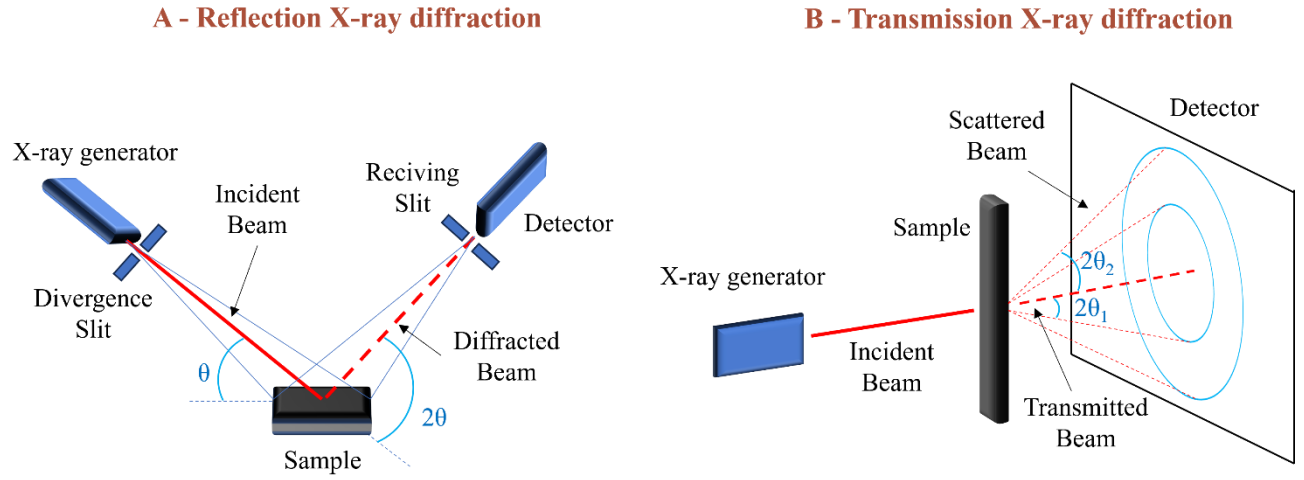

The diffraction profile of a semicrystalline polymer consists of relatively sharp peaks originating from the ordered part of the material and a halo due to the radiation scattered by the amorphous regions. Therefore, another interesting application of the WAXS technique is the measure of the degree of crystallinity, i.e., the fraction of crystalline phase present in a polymer sample. The degree

of crystallinity is a technologically important parameter as it significantly influences the properties of the polymer material, such as mechanical properties.[109]

The evaluation of the crystallinity index using powder diffraction of polycrystalline (unoriented) samples can be performed either using a standard (generally an external standard), or evaluating a crystallinity index in assumption that the diffraction intensities of amorphous and crystalline regions in the sample are additive. The following relationship maybe used:

$$x_c = 100\left(\frac{I_c}{I_c+I_a}\right) \qquad (2.65)$$

Where x_c is the crystallinity index and I_c and I_a are the area under the X-ray diffraction profiles of the crystalline and amorphous contributions, evaluated after background subtraction.

In alternative, if the polymer can be obtained in a perfectly amorphous state, a possible procedure may involve comparing the intensity I_a of the maximum in the profile scattered by the amorphous component of the sample under examination with the corresponding I_a^0 value of a completely disordered sample. The degree of crystallinity is then given by[109]:

$$1 - x_c = \frac{I_a}{I_a^0} \qquad (2.66)$$

If the polymer cannot be obtained in a completely amorphous form, which is the case for many polymeric materials, more complicated procedures are necessary.

External standard techniques are based on comparing diffraction intensities in the profile of the polymer under examination with those of a standard. These are relative methods.

Experimental Procedure 1 - X-ray Powder Diffraction

Wide angle X-ray diffraction (WAXS) profiles were recorded at room temperature (*RT*) with an Empyrean diffractometer (Malvern Panalytical) using CuKα radiation (λ =1.5418 Å) at a scanning rate of 0.0705 deg/s in a 2θ range of 5°-60°.

Some HNBR samples with ACN content > 40 wt% are found to be semicrystalline at *RT* and in the undeformed state. The crystalline phase is attributed to the crystallization of the alternating tetramethylene-ACN (TMAC) sequences. For these samples, the crystallinity index was evaluated through the ratio between the areas of the profile of the semi-crystalline sample ($A_{tot} = A_{cr} + A_{am}$) and the profile of the same sample but completely in the amorphous state (A_{am}).

$$x_c = 100\left(1 - \frac{A_{am}}{A_{tot}}\right) \qquad (2.67)$$

Given the slow crystallization kinetics of these samples, it was possible to obtain the completely amorphous sample through a simple thermal treatment, implying the heating of the sample at a temperature above the melting temperature of 42 °C, i.e. 70 °C, and successive cooling to *RT* after 10 min isotherm at that temperature.

Experimental Procedure 2 - X-ray fiber diffraction

As mentioned earlier, during the stretching of an elastomer, the polymer chains begin to align along the stretching direction, and in certain cases, SIC can occur. To assess the degree of chain orientation in both the amorphous and crystalline phases during stretching, the fiber diffraction technique has been employed, which makes use of diffraction transmission geometry (Scheme 2.1B). Bidimensional (2D) WAXS patterns were recorded with a Bruker-Nonius KappaCCD diffractometer (MoKα radiation, wavelength = 0.71073 Å) on fibers obtained by gradually stretching rubber specimens at different strains, while keeping the samples in tension, using a home-made tensile apparatus (estimated average loading rate = 30 mm min^{-1}) with a detector-sample distance of 70 mm. Additional measurements were performed on the non-vulcanized sample, by stretching independent specimens at loading rate of 150 mm min^{-1} at various strains. For each imposed strain value, 5 images of 1 min/image were recorded and then added together. Radial, equatorial, meridional and azimuthal one-dimensional (1D) profiles were extracted from

the 2D WAXS patterns by using the freeware software Fit2D,[110] as shown in Figure 2.22. In particular, azimuthal profiles spanning a narrow 2θ range centered around the equatorial reflection at 2θ (MoKα) ≈ 8.4° (i.e. 7.4° ≤ 2θ ≤ 9.4°) corresponding to the interplanar distance *d* of ≈ 0.48 nm (Fig. 2.22D) and a wider 2θ region encompassing the whole amorphous halo (i.e. 6.8° ≤ 2θ ≤ 13.2°) (Fig. 2.22E) were extracted from the 2D WAXS images.

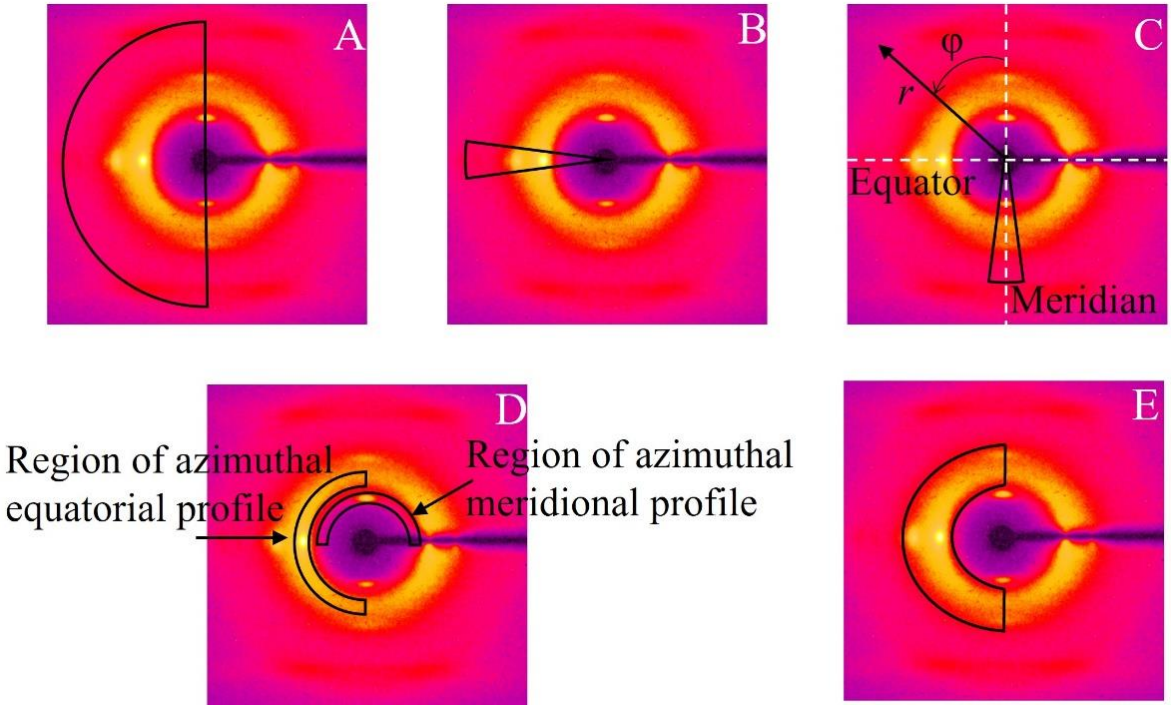

Figure 2.22 Regions of 2D X-ray fiber diffraction images used to extract the radial (A), equatorial (B), meridional (C) and azimuthal profiles (D, E). The equatorial and meridional lines, the radial vector *r* and the azimuthal angle φ are defined in C, where φ =0 on the meridian and φ=90° on the equator. The azimuthal profiles in D are extracted using a narrow 2θ region surrounding the equatorial reflection at 2θ(MoKα) ≈ 8.4° (7.4 ≤ 2θ (MoKα) ≤ 9.4°), and the meridional reflection at 2θ (MoKα) = 5.7° (i.e. 4.7 ≤ 2θ ≤ 6.7°). Additional azimuthal profiles are extracted over a wider 2θ region encompassing the whole amorphous halo (E) (6.8 ≤ 2θ (MoKα) ≤ 13.2°). The azimuthal and equatorial slices span a φ range comprised between 85 and 95°, and -5 and +5°, respectively.

For each strain, the degree of orientation of the crystalline and amorphous phase of the HNBR fibers was estimated from the azimuthal profile (Fig. 2.23). The fitting function $I_{am}(t)$ for the amorphous contribution to the azimuthal intensity distribution, where *t* is equal to $t=\cos\varphi$ with φ the azimuthal angle (Fig. 2.22C), was approximated by a linear combination of even order

Legendre polynomial, truncated to the 4th order.[111,112] Considering that the zero, second and fourth order Legendre polynomials are $P_0 = 1$, $P_2 = (3t^2-1)/2$ and $P_4 = (35t^4-30t^2+2)/8$, respectively, the fitting function for the amorphous contribution $I_{am}(t)$ is given by equation:

$$I_{am}(t) = A + Bt^2 + CBt^4 \quad (2.68)$$

The crystalline contribution to the azimuthal intensity distribution $I_{cr}(t)$ instead, is approximated by a Gaussian function centered at φ = 90°. The degree of orientation (order parameter) $P_2^{\text{WAXS-x}}$ for the amorphous (x = am) and crystalline (x = cr) phases is measured by the coefficient associated to the second Legendre polynomial as:

$$P_2^{\text{WAXS}-\text{x}} = \frac{1}{2}(3\langle cos^2\,\varphi\rangle_{\text{x}} - 1) \quad (2.69)$$

where $\langle\cos^2\varphi\rangle_x$ is the mean square of cos φ and it is calculated by equation 2.70:

$$\langle cos^2\,\varphi\rangle_{\text{x}} = \frac{\int_0^{\pi/2} I_x(cos\,\varphi)cos^2\,\varphi\,sin\,\varphi d\varphi}{\int_0^{\pi/2} I_x(cos\,\varphi)\,sin\,\varphi d\varphi} \quad (2.70)$$

In equation 2.70 I_x corresponds to the contribution to the WAXS intensity from the amorphous phase I_{am} (equation 2.68), for the calculation of $\langle cos^2\varphi\rangle_{am}$, to the contribution to the WAXS intensity from the crystalline phase I_{cr}, for the calculation of $\langle cos^2\varphi\rangle_{cr}$. Equation 2.69 entails that the order parameter $P_2^{\text{WAXS-x}}$ would be 1 for a perfect orientation of the correlation distance vectors parallel to the stretching direction, -0.5 for a perfect orientation perpendicular to the stretching direction and 0 for isotropic orientation. Since the polarization of the amorphous halo and of the strongest reflection due to the crystallization of the alternating TMAC sequences occurs on the equator, the values of the order parameter marking the orientation of the amorphous and crystalline segments would be negative.

Based on equations 2.68 – 2.70, the order parameter for the amorphous phase is calculated as:

$$P_2^{\text{WAXS}-\text{am}} = \frac{14B+12C}{105A+35B+21C} \quad (2.71)$$

From the azimuthal profiles of the kind shown in Fig. 2.23C', an approximate index of crystallinity x_c was also evaluated from the relative intensity of the reflection at $2\theta(\text{MoK}\alpha) \approx 8.4$, that is $x_{cr} = 100 \times A_{cr} / A_{tot}$, with A_{cr} the area of the crystalline peaks at $2\theta \approx 8°$ and A_{tot} the area subtending the whole profile, in the narrow 2θ region comprised between 7.4° and 9.4°, as indicated in Figure 2.22D.

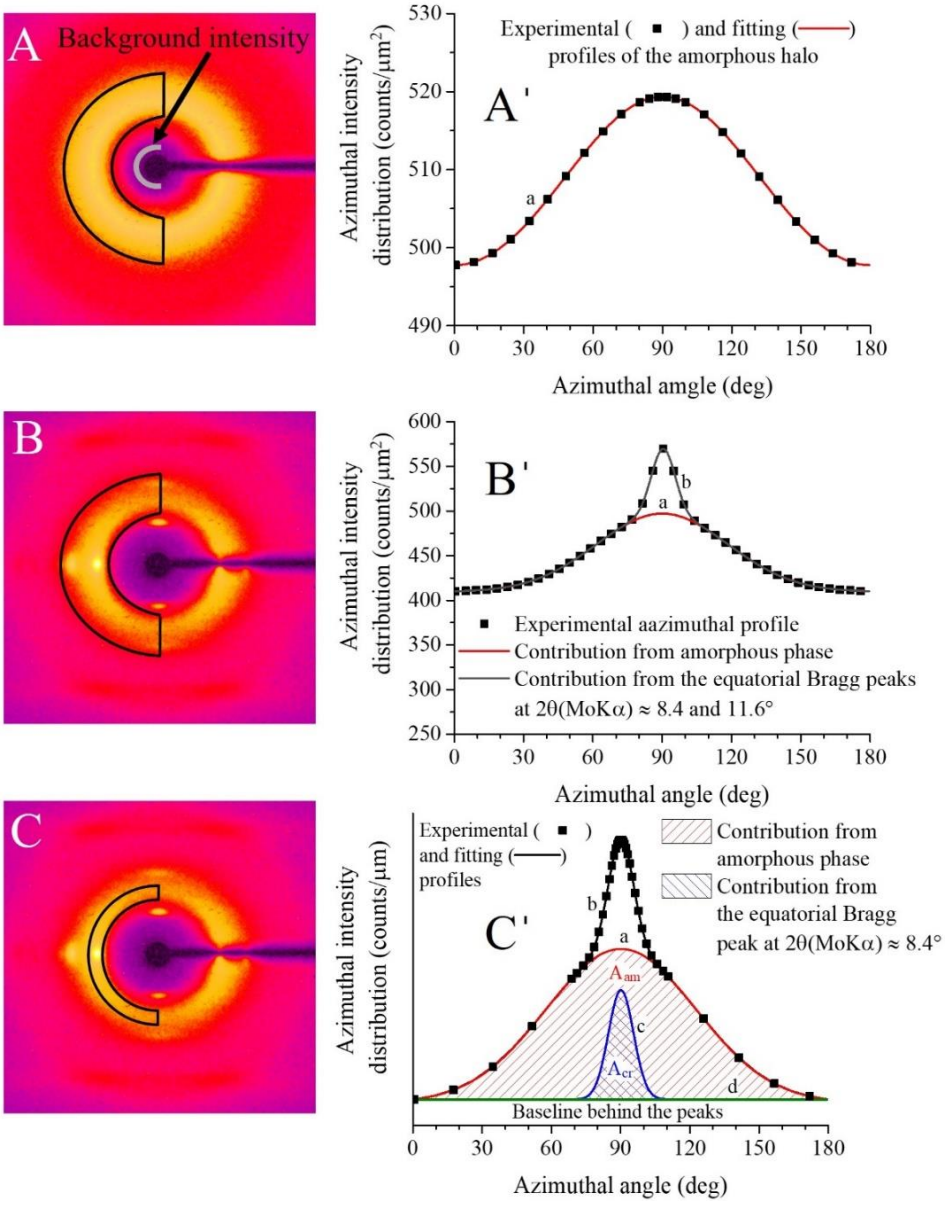

Figure 2.23 2D WAXS fiber images relative to a HNBR sample at strains lower (A) and higher (B,C) than that of incipient crystallization and corresponding azimuthal profiles (A'-C'). The background contribution subtracted to the azimuthal profiles is approximated by the intensity in the region indicated in A. In A, A' the sample is completely amorphous, in B,B',C,C' the samples are semicrystalline. The fit to the data (square) as a sum of amorphous and crystalline contributions (b) are indicated. The contribution from the amorphous phase, modelled as a sum of Legendre polynomials of even order truncated to the 4th term (equation 2.68) is indicated in A'-C' (a). The contribution from the crystalline phase modelled as a Gaussian function is indicated in B' and C' (c). The crystalline contribution is the overlay of the equatorial reflections at 2θ(MoKα) ≈8.4 and 11.6° in B', and of the sole reflection at 2θ(MoKα) ≈8.4 in C'. The equatorial crystallinity index x_c is calculated from profiles of the kind shown in C' as the ratio between the intensity of the equatorial reflection at 2θ(MoKα) ≈8.4° A_{cr} and the total area subtending the azimuthal profile A_{tot}, after subtraction of the baseline d (C'). A_{cr} is evaluated as the difference between A_{tot} and the contribution from the amorphous phase A_{am} ($A_{cr}=A_{tot}-A_{am}$).

Experimental Procedure 3 - In-Situ X-ray fiber diffraction

Conventional X-ray sources are generally not well suited to resolve structural transitions occurring during stretching at seconds or sub-second time scales. The acquisition process, indeed, requires image acquisition with a good signal-to-noise ratio over times on the order of minutes, so it is not possible to carry out X-ray fiber diffraction measurements during dynamic stretching of an elastomer at high strain rates. In general, synchrotron radiation offers numerous advantages in terms of intensity, spatial, and temporal coherence.

The main features that differentiate the X-ray radiation generated at synchrotron light sources from that produced by conventional sources are:

1. Radiation Intensity: Synchrotron facilities provide X-ray fluxes of very high intensity, enabling rapid acquisitions without compromising data quality. The increased intensity allows for reduced exposure times, facilitating more frequent acquisitions.[113]
2. Spatial and Temporal Coherence: Synchrotron radiation exhibits superior spatial and temporal coherence compared to conventional sources. This results in higher measurement precision and in the ability to detect transient phenomena. In a synchrotron, electrons travel in temporally and spatially separated 'bunches.' There is a time interval on the order of nanoseconds between one bunch of electrons and the next.[113]
3. Wide Range of Energies: The ability to tune the wavelength of synchrotron radiation allows for adaptation to the specific needs of the material under study, enhancing the resolution and sensitivity of the analysis.[113]

Time resolved X-ray fiber WAXS analysis was carried out at the ESRF BM26 beam line in Grenoble. 2D WAXS patterns were recorded in situ at *RT* with a Pilatus-300K-W detector using X-ray radiation with wavelength λ = 0.10332 Å, during stretching and retraction experiments at controlled stain rates of rectangular specimens of HNBR samples with width of 5 mm, thickness

of 0.8-1.4 mm, and initial gauge length of 15 mm. The sample to detector distance, equal to 154.2 mm, was calibrated with alpha-Al_2O_3 (alumina). The tensile stage was a Linkam TST350 apparatus, with a load cell of 200 N and a maximum distance accessible between the grips of 80 mm. The maximum strain achieved in the experiments was 400%. Using the tensile stage, 2D WAXS patterns were recorded in situ to follow the structural evolutions of the HNBR samples during two consecutive hysteresis cycles. The Linksys32 control software was utilized to set up the tensile experiment.

Measurements were carried out at different loading/unloading rates equal to 2, 20, 30 and 60 mm/min (i.e. stain rates equal to 0.13, 1.33, 2 and 4 min^{-1}, respectively, considering that the initial gauge length is 15 mm). The acquisition frequency of diffraction patterns was set at 1 frame every 30, 3, 2 and 1s for the loading/unloading rates of 2, 20, 30 and 60 mm/min, respectively. It was checked that all samples experience uniform deformation.

Data reduction of 2D patterns along with the extraction of 1D radial, equatorial and azimuthal profiles was carried out using BUBBLE software,[114] available at ESRF website. Raw data were processed after subtraction of air scattering and normalization for the transmission factor.

The azimuthal profiles were extracted using a narrow q ($Å^{-1}$) region surrounding the equatorial reflection at ≈ 1.35 $Å^{-1}$ (1.1 $Å^{-1} \leq q \leq 1.6$ $Å^{-1}$), and the meridional reflection at $q \approx 0.85$ $Å^{-1}$ (0.72 $Å^{-1} \leq q \leq 0.98$ $Å^{-1}$). Additional azimuthal profiles are extracted over a wider q region encompassing the whole amorphous halo (1.1 $Å^{-1} \leq q \leq 1.9$ $Å^{-1}$). Equatorial and meridional profiles were also extracted by integrating the intensity as a function of the radial vector over slices spanning a φ range comprised between 85 and 95°, and -5 and +5°, respectively.

The degree of orientation of the crystalline and amorphous phases and the approximate crystallinity index were calculated using the same procedure as employed for the analysis of the 2D WAXS patterns recorded ex-situ, illustrated in the preceding paragraph.

Chapter III

Sulfur vulcanized HNBR samples

This chapter is focused on the characterization of chemical, physical and mechanical properties of a set of vulcanized HNBR samples with sulfur curative packages, and of the corresponding non-vulcanized counterpart. Different subsets are considered, featuring different content of ACN units and initial residual double bonds (iRDB). The sample details are reported in Table 2.1 of Chapter II.

3.1 Crosslink density Characterization

In elastomer science the characterization of the network topology resulting from vulcanization is a crucial factor because macroscopic properties depend on crosslink density and degree of heterogeneity of the network. One of the most common methods for the determination crosslink density relies on the equilibrium swelling theory proposed by Flory and Rehner.[73] The method consists in the evaluation of the change of the Gibbs free energy reached by vulcanizates immersed in a good solvent, upon swelling. According to the theory, the equilibrium swelling ratio is related to the balance between the entropy gain resulting from polymer/solvent mixing and the heat of mixing, which can be positive or negative depending on the Flory interaction parameter, on one hand, and the loss of entropy of polymer chains subjected to extension and hence to a decrease of the number of accessible conformations, on the other hand.[115] However, the crosslink density obtained via equilibrium swelling tests does not account for the possible presence of heterogeneities, and the obtained results are critically dependent on the adopted thermodynamical models that describe the mixing free energy and the elastic response of the network.[73] As discussed in the Chapter II, the average value of crosslink density of a network may be directly probed through proton DQ-NMR experiments, with the advantages that the obtained results do not depend

on any thermodynamic argument, and additional relevant information concerning the spatial heterogeneity of the network, concentration of entanglement along with the amount of inelastic defects may be also obtained.[73] In the first part of this chapter, the values of crosslink density measured through equilibrium swelling and DQ-NMR experiments are compared. This allows to gain information not only related to the crosslink density value and topology of the network as a function of added sulfur content, but also to validate the thermodynamic models adopted in the Flory-Rehner approach.

Swelling Tests characterization

The crosslink density obtained through swelling tests (ν_e) takes into account chemical crosslinking and any trapped entanglements. During the swelling of the rubber by the solvent, physical entanglements tend to relax, and the sol phase dissolves. The Flory-Rehner relationship that describes the swelling phenomenon is based on the affine model of rubber elasticity. This model assumes that the deformation experienced by the network strands at micro-scale, leading to a chain in the average position of crosslinks, is the same as the macroscopic deformation applied to the entire network.[115]

As shown in Chapter II (equation 2.6), assuming a crosslink functionality $f = 4$, the Flory-Rehner equation is as it follows:

$$\nu_e = -\frac{1}{V_s}\frac{ln(1-V_r)+V_r+\chi V_r^2}{(V_r)^{\frac{1}{3}}-\frac{V_r}{2}} \qquad (3.1)$$

The Flory-Rehner approach can be extended also assuming different models to describe rubber elasticity, such as the so-called phantom model for instance, adopting the phantom model, we obtain:[116]

$$\nu_e = -\frac{1}{V_s}\frac{ln(1-V_r)+V_r+\chi V_r^2}{(1-\frac{2}{f})(V_r)^{\frac{1}{3}}} \qquad (3.2)$$

which for $f = 4$ equation 3.2 becomes:

$$\nu_e = -\frac{2}{V_s}\frac{ln(1-V_r)+V_r+\chi V_r^2}{(V_r)^{\frac{1}{3}}} \quad (3.3)$$

According to the phantom model, the position of the crosslinks is not fixed in space, but fluctuates; therefore, the deformation of the network strand is partly suppressed by the fluctuating crosslink node. Due to these simple differences, for a given measured V_r value, the estimated crosslink density is higher for the phantom network model.[115]

The evaluated values of ν_e for HNBR samples using the two models are listed in Table 3.1 and reported in Figure 3.1 as a function of sulfur content.

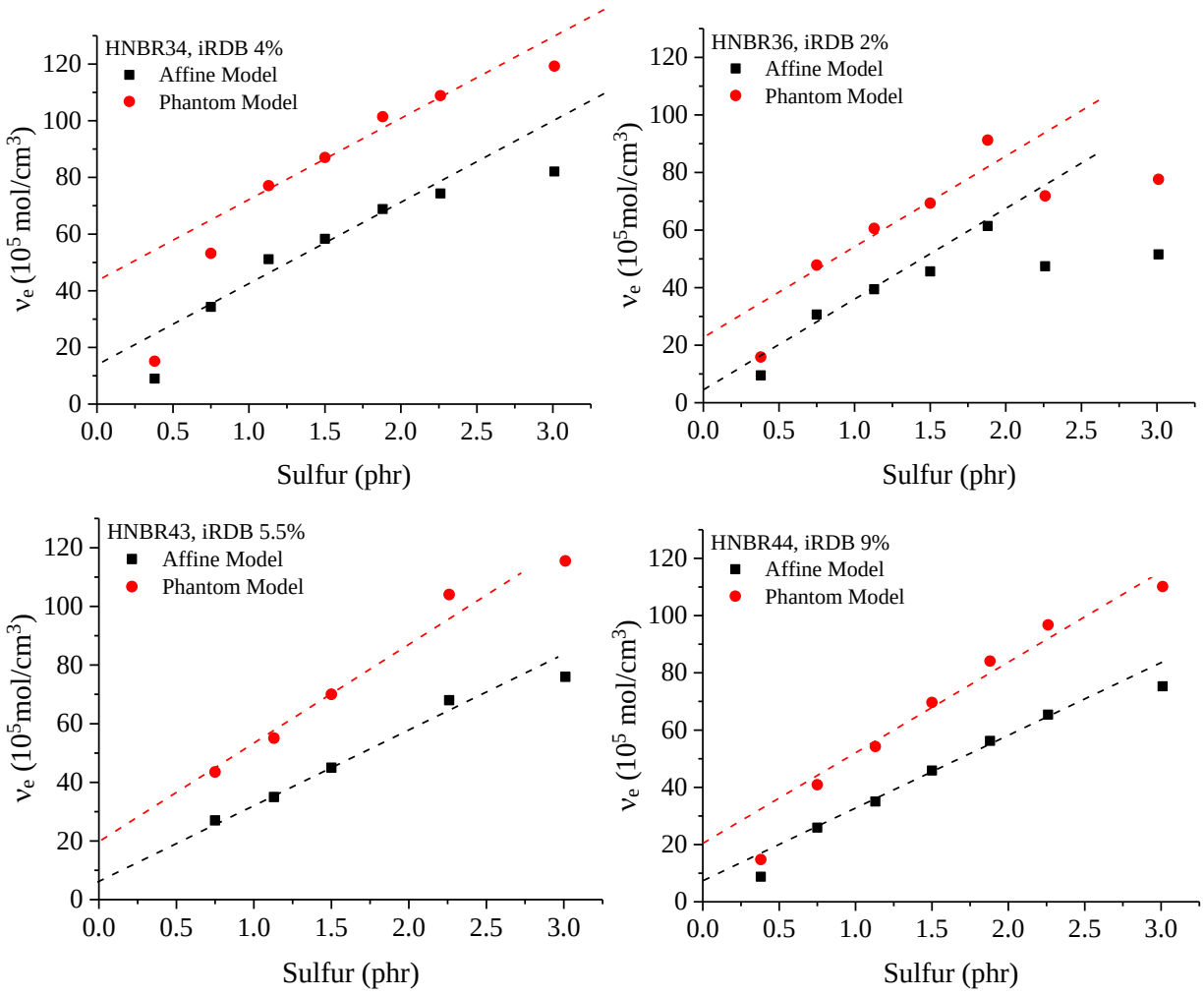

Figure 3.1 Degree of crosslinking ν_e as a function of the added sulfur content in the curative package, for different HNBR samples. The black squares and red dots represent the data obtained assuming the affine model (equation 3.1), and the phantom model (equation 3.3), respectively. The added sulfur content is in phr (parts per hundreds of rubbers) units. The linear interpolation of data for added sulfur content comprised between 0.8 and 2 phr are indicated by the dashed lines.

Table 3.1 Values of crosslink density estimated from equilibrium swelling experiments ν_e on the basis of affine and phantom model, average number of monomeric units/network strand N_N, residual dipolar coupling constant D_{res}, fraction of defects and overall relative distribution width of D_{res}, σ/Dres, for the different subsets of sulfur vulcanized HNBR samples and the corresponding non-vulcanized ones.

Samples	ACN (wt%)	iRDB (mol%)	$\nu_e\,10^5$ (mol/cm^3)[a]	N_N	$\nu_e\,10^5$ (mol/cm^3)[a]	N_N	D_{res} (kHz)	Defect Fraction	σ/D_{res}
			Affine Model		Phantom Model				
HNBR34-NV	34	4	-	-	-	-	0.59	0.39	0.22
HNBR34-0.38			9.0	100	15	60	0.74	0.23	0.17
HNBR34-0.75			34	26	53	17	0.88	0.16	0.16
HNBR34-1.1			51	18	77	12	0.98	0.17	0.15
HNBR34-1.5			58	46	87	10	1.02	0.14	0.13
HNBR34-1.9			69	13	101	9	1.01	0.17	0.13
HNBR34-2.3			74	12	109	8	1.16	0.10	0.13
HNBR34-3.0			82	11	119	8	1.32	0.09	0.13
HNBR36-NV	36	2	-	-	-		0.62	0.38	0.23
HNBR36-0.38			9.5	96	16	58	0.75	0.22	0.19
HNBR36-0.75			31	30	48	19	0.87	0.20	0.15
HNBR36-1.1			39	23	61	15	0.98	0.14	0.15
HNBR36-1.5			46	20	69	13	1.05	0.07	0.15
HNBR36-1.9			61	15	91	10	1.02	0.13	0.14
HNBR36-2.3			47	19	72	13	1.09	0.09	0.12
HNBR36-3.0			51	18	78	12	1.11	0.05	0.12
HNBR43-NV	43	5.5	-	-	-	-	0.64	0.32	0.22
HNBR43-0.75			27	35	44	22	0.84	0.18	0.17
HNBR43-1.1			35	27	55	17	0.90	0.15	0.16
HNBR43-1.5			45	21	70	14	0.96	0.10	0.16
HNBR43-2.3			68	14	104	9	1.17	0.08	0.15
HNBR43-3.0			76	13	116	8	1.28	0.08	0.13
HNBR44-NV	44	9		-	-	-	0.60	0.31	0.21
HNBR44-0.38			8.8	108	15	64	0.76	0.20	0.20
HNBR44-0.75			26	37	41	23	0.84	0.14	0.17
HNBR44-1.1			35	27	54	18	0.92	0.13	0.16
HNBR44-1.5			46	21	70	14	0.99	0.10	0.15
HNBR44-1.9			56	17	84	11	1.02	0.10	0.15
HNBR44-2.3			65	15	97	10	1.13	0.09	0.14
HNBR44-3.0			75	13	110	9	1.21	0.07	0.14

[a] Obtained by swelling test

[b] Data are affected by 10% relative error

Regardless of the adopted model (eq. 3.1 and eq. 3.3), the ν_e values increase as the added sulfur content increases. For the sample with ACN = 36 wt% and the lowest initial content of residual double bonds (2 mol%), the crosslink density increases for added sulfur content lower than 2 phr, then decreases by addition of sulfur greater than 2 phr, while approaching a quasi-plateau (Fig. 3.1). This may be attributed to the low content of iRDB, leading to a gradual saturation of functionalities and subsequent formation of polysulfur instead of monosulfur bridges by addition of quantities of sulfur higher than 2 phr (see Appendix (A) Table A1). In no case the overall increase of ν_e is linear. However, discarding the data at high content of added sulfur, due to saturation effect, and those at low content of added sulfur, the linear interpolation of data does not extrapolate to zero at 0 phr of sulfur (Fig. 3.1). The resultant extrapolated values correspond to the amount of trapped entanglements, generated at high crosslink density. This entails that for values of added sulfur content lower than a threshold, the network created by chemical crosslinking fails to trap physical entanglements that can contribute to elastic potential and causes a deviation from linearity.[49,116]

From the crosslink density, it is possible to determine the average molecular mass of a network strand $\langle M_N \rangle$:

$$\frac{\rho_r}{2\nu_e} = \langle M_N \rangle \tag{3.4}$$

and, hence, the average number of monomeric units/network strands (N_N) can be obtained as:

$$\frac{\langle M_N \rangle}{\langle M_M \rangle} = N_N \tag{3.5}$$

where $\langle M_M \rangle$ is the molecular mass of the average monomeric unit. Considering that for HNBR:

$$\langle M_M \rangle = M_{\mathrm{ACN}} x_{\mathrm{ACN}} + M_{\mathrm{TM}}(1 - x_{\mathrm{ACN}} - x_{\mathrm{B}}) + M_{\mathrm{B}} x_{\mathrm{B}} \tag{3.6}$$

where M_{ACN}, M_{TM}, and M_B correspond to the molecular mass of acrylonitrile, tetramethylene, and butylene units, respectively and x_{ACN} and x_B are the molar fraction of acrylonitrile and butylene groups (equal to the degree of unsaturation), respectively. The values of N_N calculated for HNBR samples are reported in Figure 3.2 as a function of sulfur content.

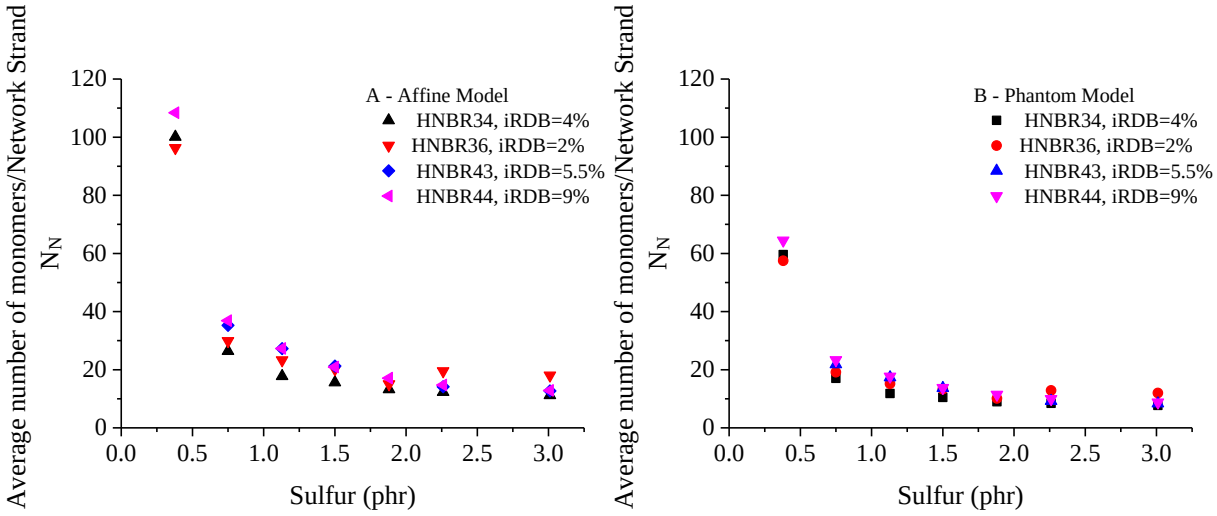

Figure 3.2 Calculated values of the average number of monomers/network strand (N_N) as a function of the added sulfur content in the curative package for HNBR samples, for the affine model (A), and the phantom model (B). The added sulfur content is in phr (parts per hundreds of rubbers) units.

The N_N values decrease steeply in samples that are vulcanized by addition of a curative package with low sulfur content, until to approach a quasi-plateau for added sulfur content of 1.5 phr corresponding to 20-12 units/network strand for the affine model and 18-8 units/ network strand for the phantom model.

DQ-NMR characterization

Through DQ-NMR experiments, it was possible to measure the value of the residual dipolar coupling constant (D_{res}) (obtained by the fitting parameter of I_{nDQ} showed in Fig. A19), which is proportional to the crosslink density. It takes into account not only the network formed by the chemical crosslinks but also the total concentration of physical entanglements, including temporary

entanglements that not end up trapped upon vulcanization. Moreover, it is possible to extract the content of defects present in the network (sol phase or dangling chains) by analyzing the decay of the normalized DQ signal at high time values, as defects exhibit very slow relaxation times. Since temporary entanglements relax or dissolve in the swelling tests, the values of D_{res} should be considered more accurate than the crosslink density values measured through swelling experiments or other methods in general. The challenge lies in the existence of an unknown proportionality factor that links the values of D_{res} to those of ν_e (see Chapter II for details):

$$D_{res} \approx \langle P_2(\cos\theta)\rangle D_{stat}\frac{1}{k} \approx D_{stat}\frac{1}{Nk} \approx \frac{1}{M_c} \approx \nu \qquad (3.8)$$

The measured values of residual dipolar coupling constant D_{res} represent an average over a distribution of the $\widetilde{D}_{res}$ values in the macroscopic network, which, as discussed in the Chapter II, was modelled with a lognormal distribution function.

The values of D_{res} of the sulfur vulcanized HNBR samples are reported in Figure 3.3A as a function of the added sulfur content. It is apparent that for all the HNBR samples, the values of D_{res} increase almost linearly as the added sulfur content increases (Fig. 3.3A). Only the sample with 36 wt% of ACN and lowest content of initial residual double bonds content, equal to 2 seems to approach a nearly constant value of $D_{res} \approx 1.05$ (kHz) %, at added sulfur content greater than 1.88 phr. A similar trend was observed for ν_e vs. S in Figure 3.1.

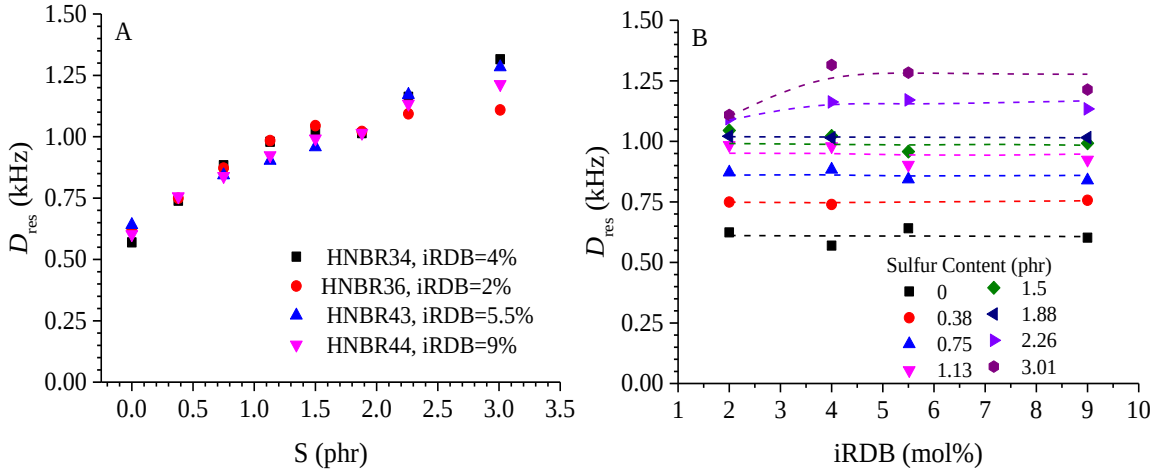

Figure 3.3 A): Values of the D_{res} as a function of the added sulfur content for different type of HNBR samples. B): Values of D_{res} as a function of the iRDB content.

Figure 3.3B highlights that, in the adopted curing conditions, the values of D_{res} achieved by adding the same quantity of sulfur does not depend on the iRDB content, and only for the HBBR sample with iRDB content equal to 2 mol% (and 36 wt% of ACN), at added sulfur content greater than 1.88 phr, the values of D_{res} are lower than the plateau. As mentioned earlier, these deviations occur because for the HNBR36-2 sample, the addition of sulfur in the curative package higher than a threshold (1.88 phr) leads to the low content of iRDB (2 mol%), and hence to almost complete saturation of functionalities.

The DQ-NMR analysis also highlights that all HNBR samples contain a non-negligible faction of slowly relaxing protons included in defective portions of chain (defects) in the network, that produce a long tail at long times of the NMR signals. These defects consist of sol phase (less than 7 wt%, as a results of swelling tests), dangling chain ends, closed loops and other imperfections that relax slowly over time. The estimated values of defect fraction are reported as a function of the value of D_{res} in the Figure 3.4A. It is observed that for low values of D_{res} the defect content is high. The highest values occur for the non-vulcanized samples. At high values of D_{res}, although the defect fraction values are rather scattered, all samples exhibit a defect fraction comprised between 0.05 and 0.15. This behavior may be ascribed to the effect that an increase in crosslink density may

have on some defects, such as the reduction of sol fraction and/or the length the terminal chains (dangling ends). In particular, as the chain terminals tend to become short at high crosslink density, the corresponding relaxion time tends to increase, so their contribution to the tail of relevant DQ-NMR signals tends to vanish.

The lognormal distribution functions of the $\widetilde{D}_{res}$ values obtained by fitting the normalized DQ signals of the HNBR samples with equation 2.27 (Chapter II) are shown in Figure 3.5. The values of the ratio between the standard deviation of $\widetilde{D}_{res}$ distribution σ and the average value of $\widetilde{D}_{res}$ (i.e. overall relative distribution width σ/D_{res}) are reported in Figure 3.4B as a function of the added sulfur content. Generally, low values of the σ/D_{res} ratio indicate a homogeneous distribution of crosslink density.[49] It is apparent that the sulfur vulcanized HNBR samples exhibit homogeneous crosslinking with σ/D_{res} values close or lower than 0.2 and that the non-vulcanized samples and those crosslinked with the minimum sulfur content have the least homogeneous distribution of crosslinks compared to the other samples.

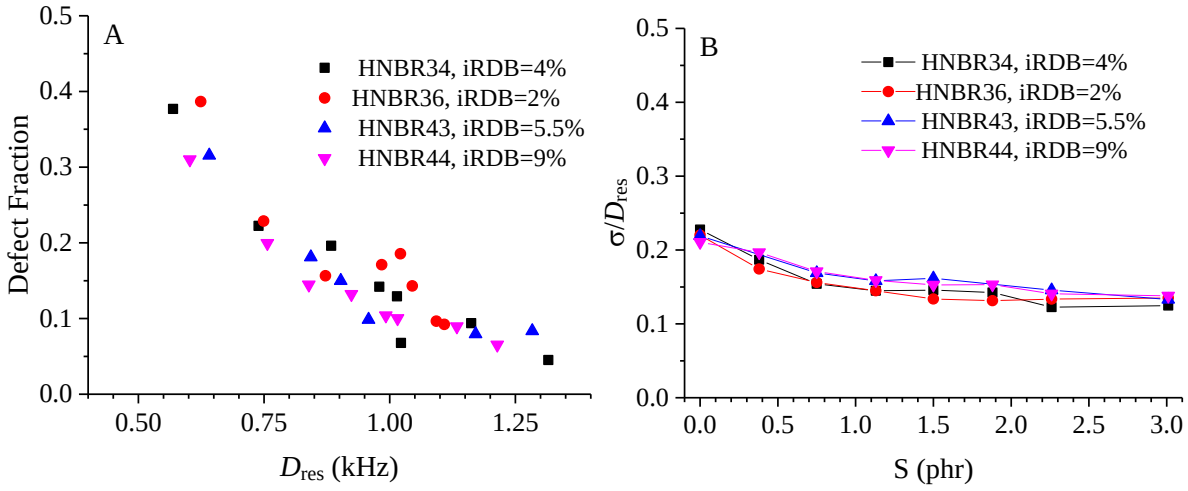

Figure 3.4. A): Values of defects fraction as a function of D_{res}. B): Ratio between the standard deviation of $\widetilde{D}_{res}$ distribution σ and the average value of $\widetilde{D}_{res}$ (i.e. overall relative distribution width σ/D_{res} as a function of added sulfur content.

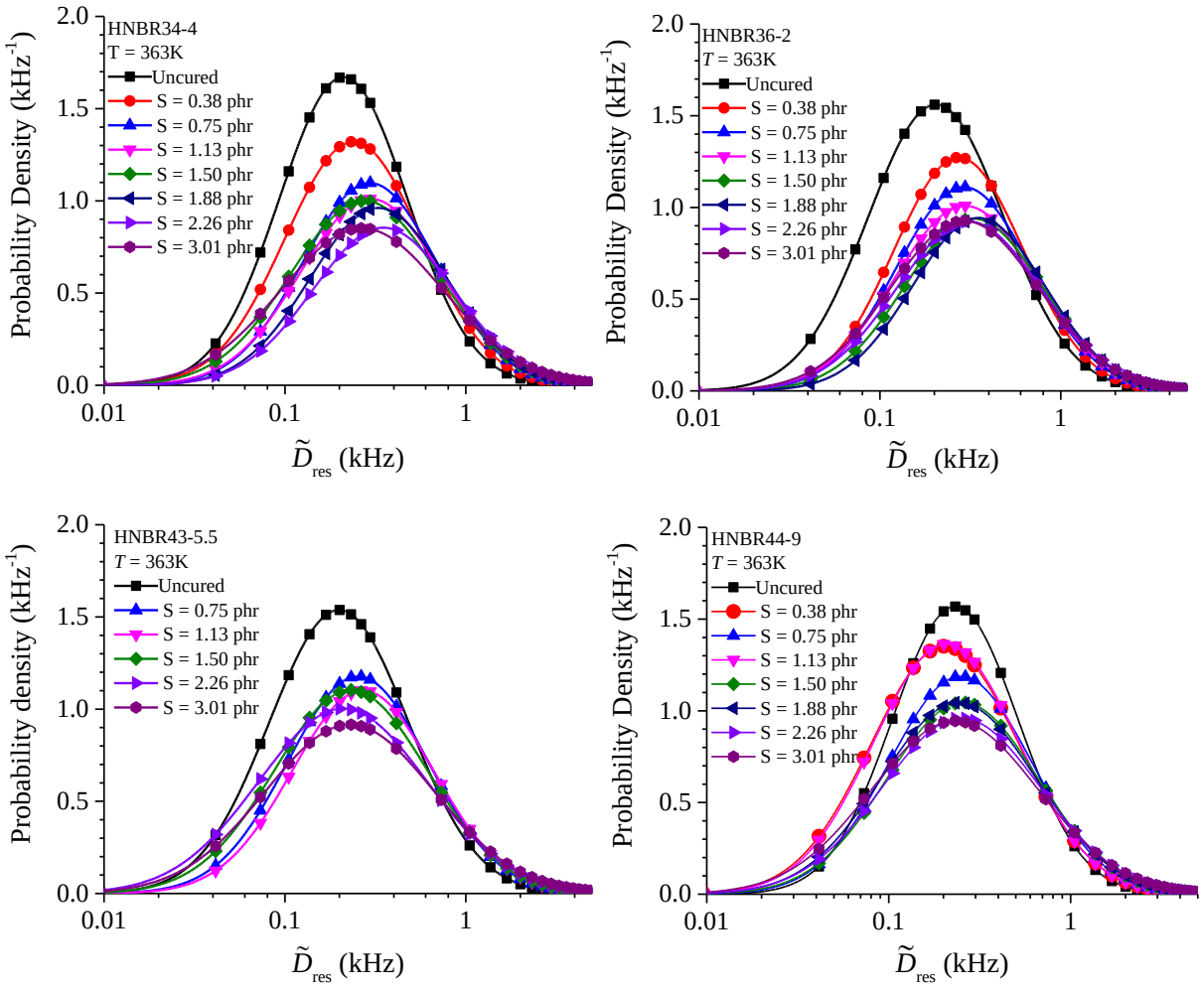

Figure 3.5 The lognormal distribution functions of $\widetilde{D}_{res}$ values for HNBR samples with different sulfur contents.

Comparative study of crosslink density obtained by Swelling test and DQ-NMR

The values of D_{res} are reported as a function of the values of crosslink density obtained through swelling tests in Figure 3.6. All samples show that D_{res} increases linearly with ν_e.[83] Considering that the swelling tests account for chemical crosslinks and trapped entanglements only, while D_{res} accounts for both chemical crosslinks and total entanglements (temporary entanglements and trapped entanglements), the data are interpolated to equation:

$$\rho_r D_{res} = \rho_r D_{res}^0 + u\nu_e \qquad (3.9)$$

where D^0_{res} represents the value of residual coupling constant due to non-trapped entanglements, ρ_r is the density of the samples, while u is a scaling constant, with dimensions kHz g/mol.

From Figure 3.6, the extrapolated values at $v_e = 0$ give the value of the residual coupling constant due to non-trapped entanglements D^0_{res}. As shown in Table 3.2, the values of D^0_{res} are, within the experimental error, not dissimilar from those of D_{res} relative to the non-crosslinked samples. This agreement holds for all samples, especially for the values of D^0_{res} obtained using the phantom model.[75,117]

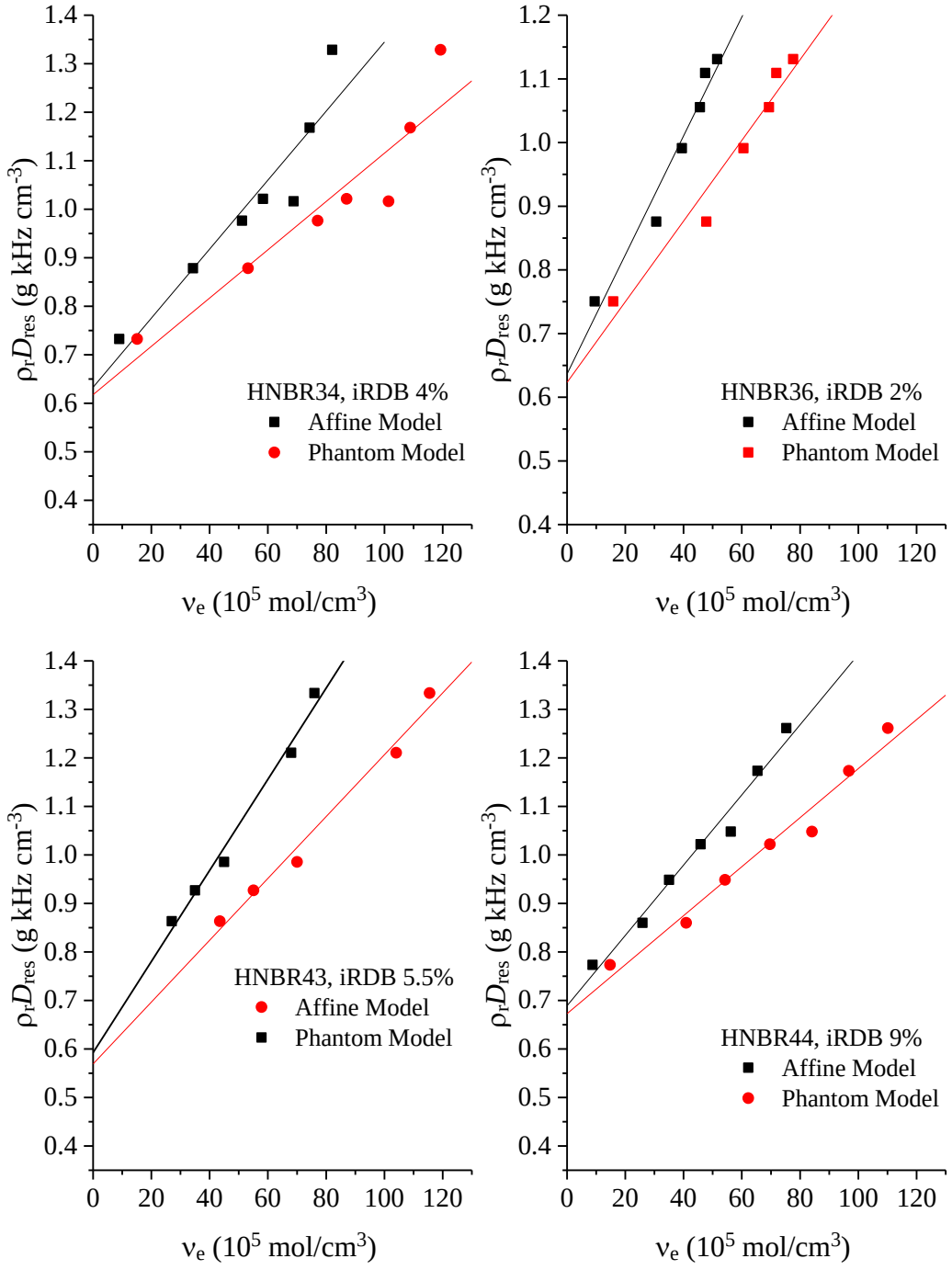

Figure 3.6 Values of D_{res} times density ρ_r as a function of ν_e extracted from swelling experiments. The black squares are the ν_e data obtained using the affine model and the red dots are those obtained using the phantom model.

Table 3.2 Values of residual dipolar coupling constant D_{res} measured for the non-vulcanized samples, of D^0_{res} obtained by linear extrapolation of data in Figure 3.6 to ν_e=0, using values of equilibrium crosslink density estimated from swelling experiments on the basis of the affine and phantom models.[a]

HNBR		**Affine Model**		**Phantom Model**	
ACN (wt%), iRDB (mol%)	D_{res} (kHz) Non-Vulcanized Sample	D^0_{res} (kHz)	Slope (kHz g/mol)	D^0_{res} (kHz)	Slope (kHz g/mol)
34, 4	0.60	0.63	0.0071	0.62	0.0050
36, 2	0.60	0.64	0.0093	0.62	0.0063
43, 5.5	0.64	0.59	0.0072	0.60	0.0050
44, 9	0.62	0.69	0.0072	0.68	0.0051

[a] Data are affected by 10% relative error.

3.2 Thermal and structural analysis

The WAXS profiles and the DSC heating scans of the sulfur vulcanized HNBR samples with different content of ACN units and iRDBs are shown in Figure 3.7 and 3.8, respectively. Data relative to the corresponding non-vulcanized samples are also reported. With exception of the crystalline peaks due to the crystalline additive zinc oxide, talc and clinochlore, the WAXS profiles of Figure 3.7 show the presence of a halo centered at $2\theta \approx 19°$, indicating that the HNBR samples are amorphous at room temperature. This is also confirmed by the results of thermal analysis. The DSC thermograms of Figure 3.8, indeed, do not present any endothermic peak, but only an inflection point below *RT*, due to the glass transition. These samples do not experience thermally induced crystallization at low temperatures, even by subjecting them to annealing for long time at temperatures comprised in between the T_g and 25 °C (data not shown), probably because of a slow kinetics.

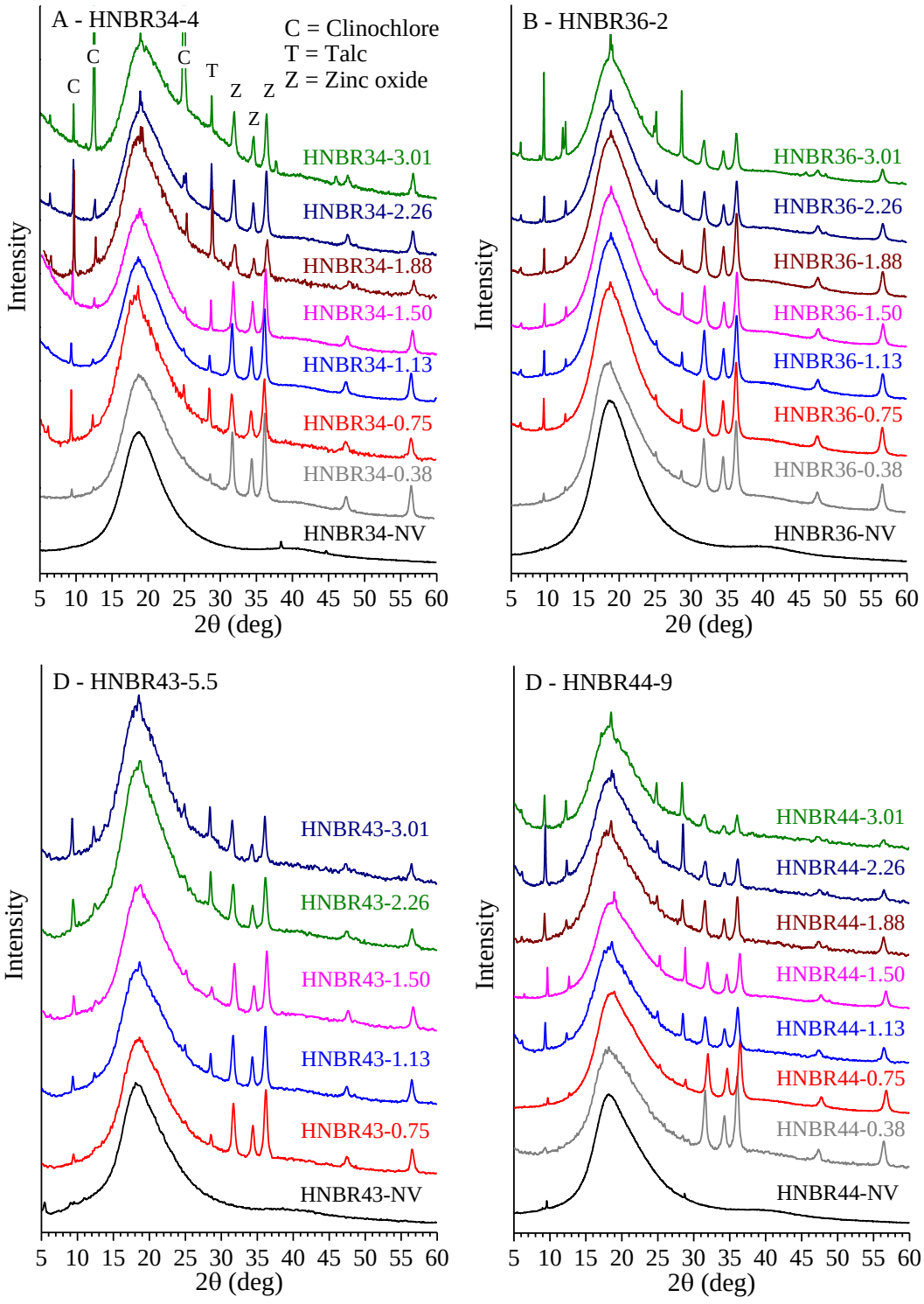

Figure 3.7 WAXS profiles recorded at room temperature of HNBR samples containing 34 (A), 36 (B), 43 (C) and 44 (D) wt% ACN units and iRDB content of 4, 2, 5.5 and 9 mol%, respectively. The main reflections due to the crystalline additives included in the curative package and/or added as fillers, are indicated in (A).

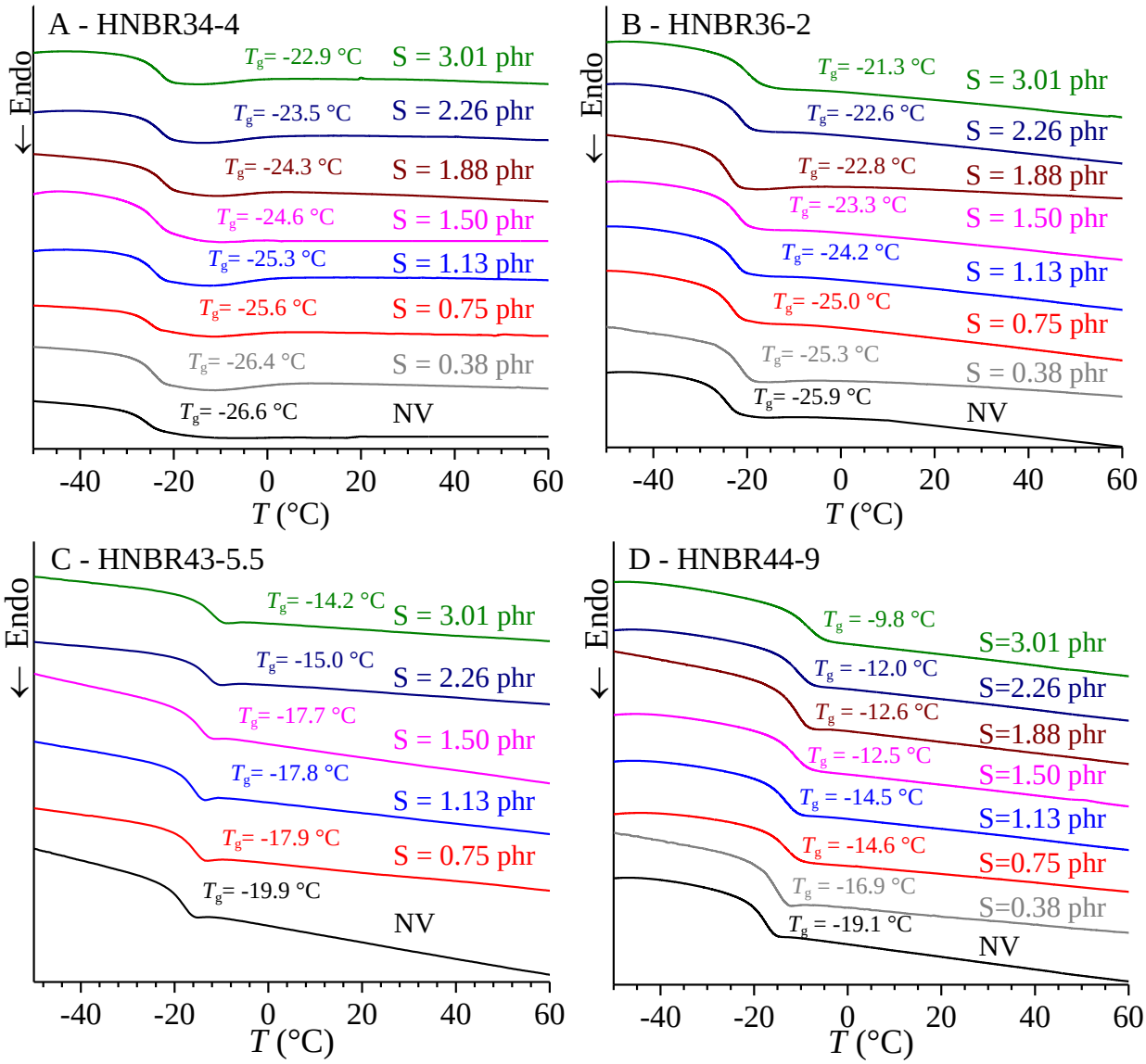

Figure 3.8 Thermograms recorded in the second heating scan of HNBR samples containing 34 (A), 36 (B), 43 (C) and 44 (D) wt% ACN units, iRDB content of 4, 2, 5.5 and 9 mol%, respectively, and the indicated values of added sulfur content.

The values of the glass transition temperature T_g extracted from the second DSC heating scans of Figure 3.8, are reported in Table 3.3 and in Figure 3.9 as a function of the added sulfur content and D_{res}.

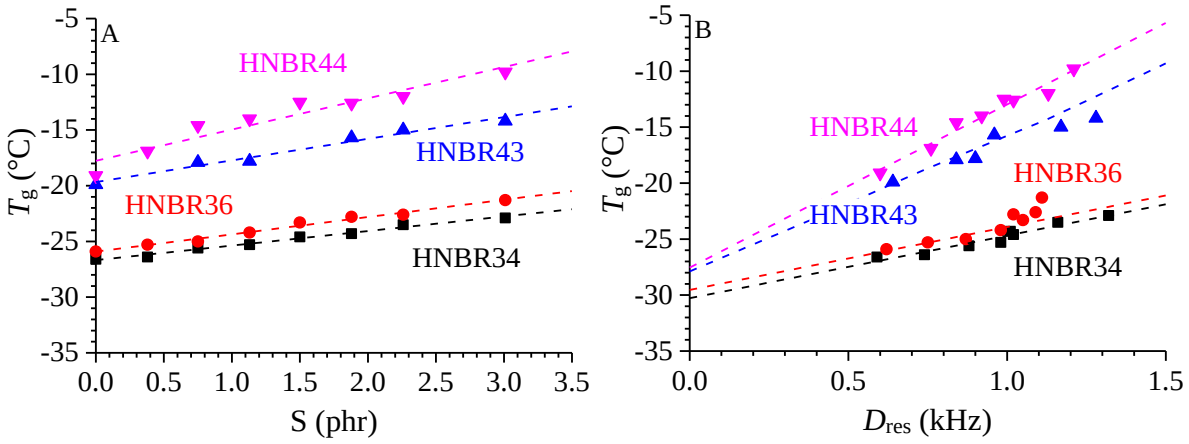

Figure 3.9 Glass transition temperature (T_g) as a function of sulfur content (A) and D_{res} (B) for the samples HNBR34 (black symbols), HNBR36 (red symbols), HNBR43 (blue symbols) and HNBR44 (magenta symbols), and iRDB content of 4, 2, 5.5 and 9 mol%, respectively. The dashed lines are the linear fitting of experimental data.

For all rubbers, the T_g values increase almost linearly as the sulfur and D_{res} increase, which can be attributed to the increase in stiffness due to the decrease in the average length of the network strands. Moreover, at the same crosslink density, the T_g values increase as the ACN content increases. In the previous paragraph, it was observed that the sample with 36 wt% and 2 mol% ACN and iRDB content, respectively, for added sulfur content greater than 1.88 phr reaches an almost constant value of D_{res}, due to the saturation of available sites for crosslinks. Indeed, in Figure 3.9B, the increase of T_g with D_{res} appears linear only for values $D_{res} < 1$ kHz, while at higher D_{res} values, the T_g remains almost constant or increases nonlinearly.

Table 3.3 Values of glass transition temperature T_g, Young's modulus E, strain (ε_b), stress (σ_b) and tension set (t_b) at break for HNBR samples.

Samples	S phr	T_g (°C)	E (MPa)	ε_b (%)	σ_b (MPa)	t_b (%)
HNBR34-NV	NV	-26.6	0.9 ± 0.1	3200 ± 200	1.20 ± 0.03	320 ± 30
HNBR34-0.38	0.38	-26.4	2.3 ± 0.1	900 ± 100	11 ± 3	50 ± 10
HNBR34-0.75	0.75	-25.6	2.0 ± 0.1	940 ± 80	14 ± 2	70 ± 7
HNBR34-1.1	1.13	-25.3	2.4 ± 0.1	700 ± 20	12 ± 1	45 ± 6
HNBR34-1.5	1.50	-24.6	2.6 ± 0.2	600 ± 50	12 ± 3	15 ± 4
HNBR34-1.9	1.88	-24.3	2.9 ± 0.1	530 ± 50	10 ± 1	19 ± 3
HNBR34-2.3	2.26	-23.5	3.0 ± 0.2	450 ± 60	12 ± 5	0
HNBR34-3.0	3.01	-22.9	3.1 ± 0.1	500 ± 50	11 ± 3	0
HNBR36-NV	0	-25.9	0.8 ± 0.1	2300 ± 200	0.66 ± 0.03	210 ± 20
HNBR36-0.38	0.38	-25.3	1.9 ± 0.3	1000 ± 100	17 ± 2	75 ± 5
HNBR36-0.75	0.75	-25.0	2.0 ± 0.2	690 ± 50	18 ± 4	44 ± 7
HNBR36-1.1	1.13	-24.2	2.2 ± 0.1	560 ± 50	15 ± 2	33 ± 6
HNBR36-1.5	1.50	-23.3	2.3 ± 0.2	630 ± 50	18 ± 5	40 ± 10
HNBR36-1.9	1.88	-22.8	2.5 ± 0.1	540 ± 40	16 ± 2	30 ± 10
HNBR36-2.3	2.26	-22.6	2.5 ± 0.1	520 ± 50	16 ± 3	30 ± 10
HNBR36-3.0	3.01	-21.3	2.6 ± 0.2	530 ± 80	16 ± 2	25 ± 5
HNBR43-NV	NV	-19.9	1.8 ± 0.3	1200 ± 100	2.2± 0.4	90 ± 20
HNBR43-0.75	0.75	-17.9	2.4 ± 0.2	820 ± 60	29 ± 4	71 ± 9
HNBR43-1.1	1.13	-17.8	2.4 ± 0.2	710 ± 60	14 ± 3	65 ± 10
HNBR43-1.5	1.50	-17.7	2.8 ± 0.2	660 ± 70	13 ± 4	70 ± 20
HNBR43-2.3	2.26	-15.0	3.0 ± 0.3	440 ± 50	10 ± 4	39 ± 8
HNBR43-3.0	3.01	-14.2	3.2 ± 0.3	490 ± 20	19 ± 7	48 ± 10
HNBR44-NV	NV	-19.1	1.2 ± 0.1	1100 ± 100	3.0 ± 0.8	75 ± 5
HNBR44-0.38	0.38	-16.9	3.1 ± 0.2	750 ± 40	16 ± 3	40 ± 3
HNBR44-0.75	0.75	-14.6	3.1 ± 0.1	790 ± 90	33 ± 4	60 ± 10
HNBR44-1.1	1.13	-14.0	2.8 ± 0.3	640 ± 10	34 ± 2	50 ± 3
HNBR44-1.5	1.5	-12.5	3.2 ± 0.2	650 ± 20	32 ± 1	64 ± 2
HNBR44-1.9	1.88	-12.6	2.9 ± 0.1	360 ± 40	14 ± 1	18 ± 4
HNBR44-2.3	2.26	-12.0	3.1 ± 0.2	350 ± 10	12 ± 1	23 ± 1
HNBR44-3.0	3.01	-9.8	3.3 ± 0.1	300 ± 10	17 ± 2	12 ± 2

3.3 Mechanical properties

Tensile stress-strain curves

The stress-strain curves recorded at room temperature on dumbbell specimens of the non-vulcanized and vulcanized HNBRs containing 34, 36, 43 and 44 wt% ACN, and 4, 2, 5.5 and 9 mol% iRDB, respectively, are shown in Figure 3.10. Data are relative to not previously deformed samples. The average values of the corresponding tensile parameters, namely Young's modulus (E), stress and strain at break (σ_b and ε_b), and tension set at break (t_b), are listed in Table 3.3 and reported in Figures 3.11-3.15 as a function of crosslink density.

Regardless of the ACN content, the stress-strain curves of the non-vulcanized rubbers are characterized by a broad yield, followed by a region of strain-softening due to chains relaxation, then a cold-drawing plateau, and finally a strain-hardening region in which the stress rapidly increases with the strain up to the break (Fig. 3.10A).

The strain at the yield point appears to be unaffected by ACN content, but the samples with 44 (9 mol% iRDB) and 43 (5.5 mol% iRDB) wt% ACN exhibit higher stress at any strain, as well as remarkable strain-hardening at large strains, as compared to the HNBRs with 34 and 36 wt% ACN (Fig. 3.10A). This behavior is due to the reinforcing effect exerted by crystals that form at strains greater than a critical value due to strain-induced crystallization (SIC) occurring for the samples containing 43 and 44 wt% ACN, and to not SIC behavior for the samples with 34 and 36 wt% ACN (vide infra). All non-vulcanized rubbers have good ductility, with strains at break ranging from 1000 to 3000 % and decreasing as ACN concentration increases (Fig. 3.10A and 3.13).

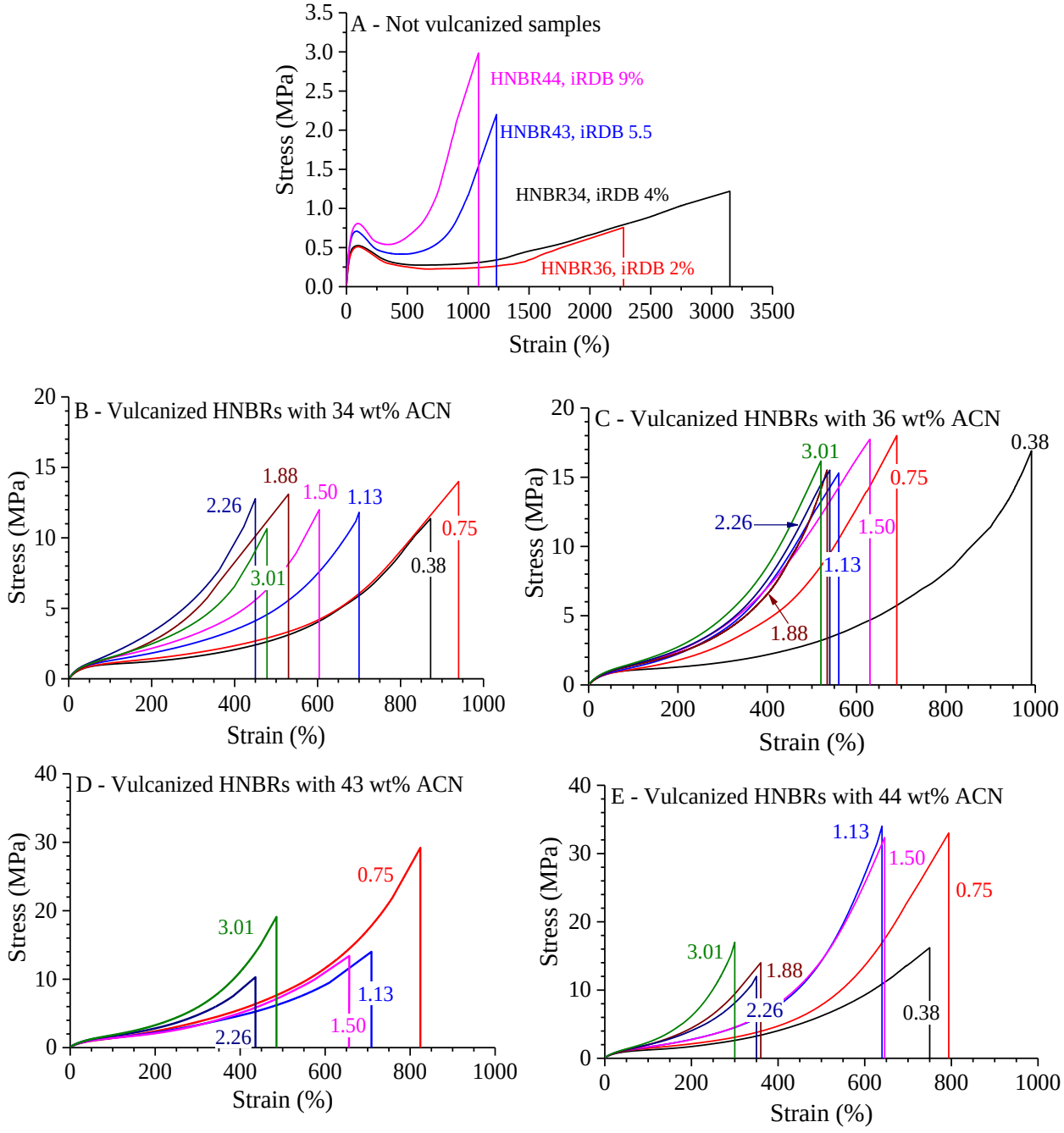

Figure 3.10 Stress-strain curves of the non-vulcanized (A) and vulcanized (B-E) HNBR samples containing 34 (B), 36 (C), 43 (D) and 44 (E) wt% ACN and 4, 2, 5.5 and 9 mol% iRDB, respectively. Data are relative to not previously deformed samples. The quantity of sulfur added for vulcanization are indicated in phr close to each curve in B-E.

Regardless of the ACN content all the crosslinked samples show stress-strain curves typical of elastomers with absence of yielding and strong strain-hardening at high strains (Fig. 3.10B-E). It is also clear from Figure 3.10B-E that for each HNBR subsets, at strains lower than that marking the onset of strain-hardening the values of stress increase with increasing sulfur content, that is with increasing crosslink density. Additionally, for all subsets of HNBR samples, the strain at break decreases as the crosslink density increases (Fig. 3.10B-E and Fig. 3.13). Therefore, for HNBRs the vulcanization results in an increase in the resistance to the tensile strain and a loss of ductility as the crosslink density increases. This is due to the shortening of the network strand lengths, and a consequent decrease in the degree of freedom controlling their segmental mobility.

In agreement with the Flory's theory of rubber elasticity, the values Young's modulus (E) increase linearly as the crosslink density ν_e values increase (Fig. 3.11C,D),[118] extrapolation to zero crosslink density should yield the modulus value of the non-crosslinked sample. However, the experimental values are remarkably lower than the extrapolated values. This is likely due to the fact that the total concentration of entanglements in the non-crosslinked samples are only partially active in the tensile test. The non-crosslinked samples, indeed, experience viscous flow already at low strains during mechanical tests, leading to an underestimation of the modulus value. For all HNBR subsets the values of Young's modulus of the vulcanized samples are much higher than those of non-vulcanized counterparts (Fig. 3.11).

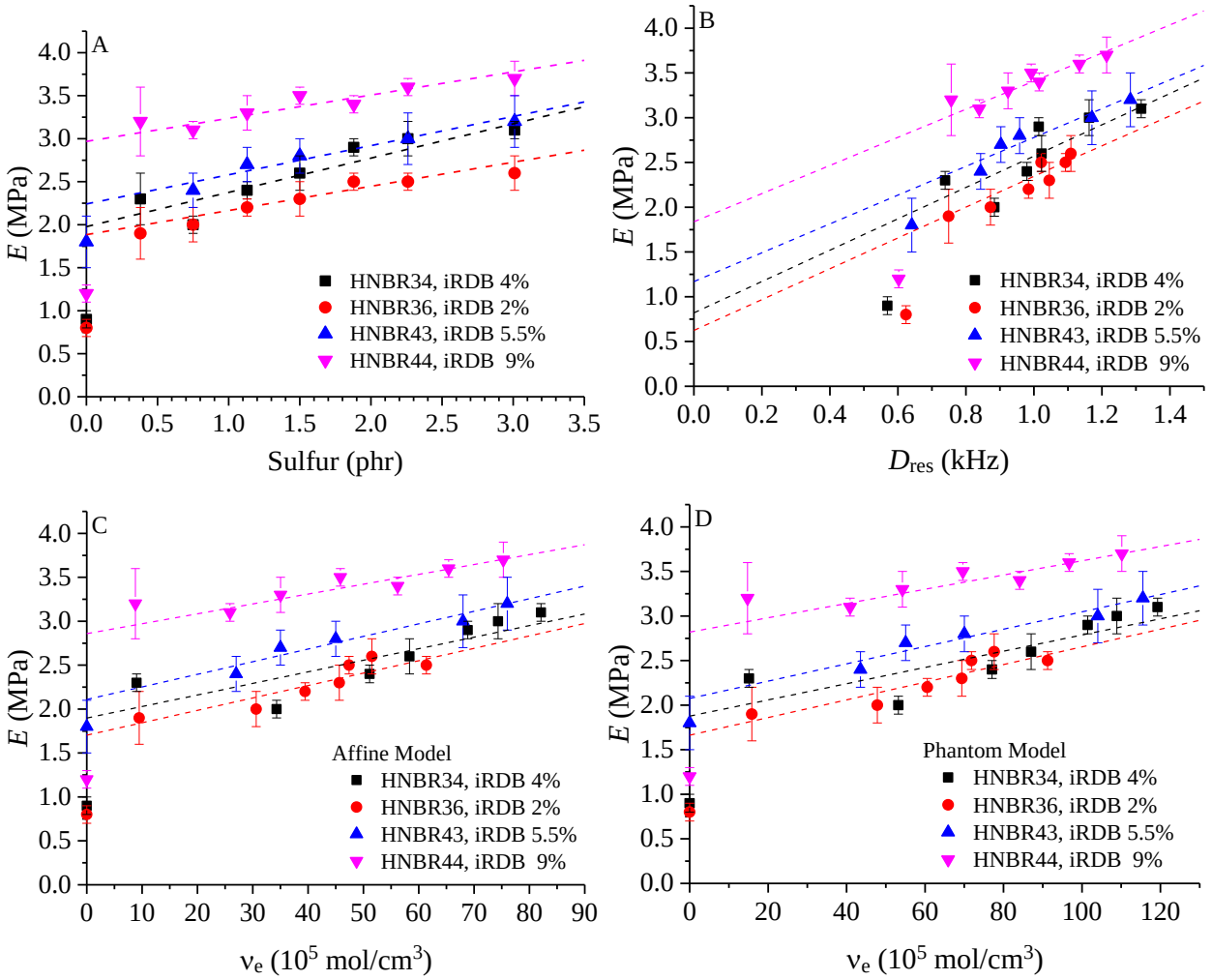

Figure 3.11 Values of Young's modulus as a function of added sulfur content (A), residual dipolar coupling D_{res} (B) and crosslink density ν_e obtained from affine model (C), and phantom models (D) for the samples HNBR34 (black symbols), HNBR36 (red symbols), HNBR43 (blue symbols) and HNBR44 (magenta symbols), and 4, 2, 5.5 and 9 mol% iRDB, respectively.

The values Young's modulus are reported in Figure 3.11B also as a function of the residual dipolar coupling constant D_{res}. Theoretically, a linear relationship is expected, with the interpolating straight line passing through the origin.[83] Discarding the samples with the lowest D_{res} and the non-vulcanized HNBR samples, the crosslinked HNBR samples show that the values Young's modulus E increase almost linearly as D_{res} increases, even though the interpolating straight line extrapolate at null D_{res} to non zero values of the Young's modulus. According to the literature, similar deviations from the theoretical predictions occur for ethylene/propylene/diene elastomers. These deviations have been attributed to the heterogeneities of the network.[83] On the other hand, rubbers

or gels with significant heterogeneity have been found to follow the theoretical predictions. To date, the effects of inhomogeneity are still unclear. These effects are subtle, and the results obtained for inhomogeneous systems cannot be generalized.

The values of stress and strain at break of HNBR samples are shown in Figures 3.12 and 3.13, respectively, as a function of sulfur content, D_{res}, and crosslink density. For the HNBR samples containing 34 and 36 wt% ACN, and 4 and 2 mol% of iRDB, the stress at break (Fig. 3.12) is almost constant regardless of crosslink degree. For the HNBR samples containing 43 and 44 wt% ACN, and 5.5 and 9 mol% of iRDB, instead, the values of stress at break (Fig. 3.12) increase as the crosslink density increases until to reach a quasi-plateau at intermediate crosslink density, then decrease, reaching a new plateau at high crosslink density.

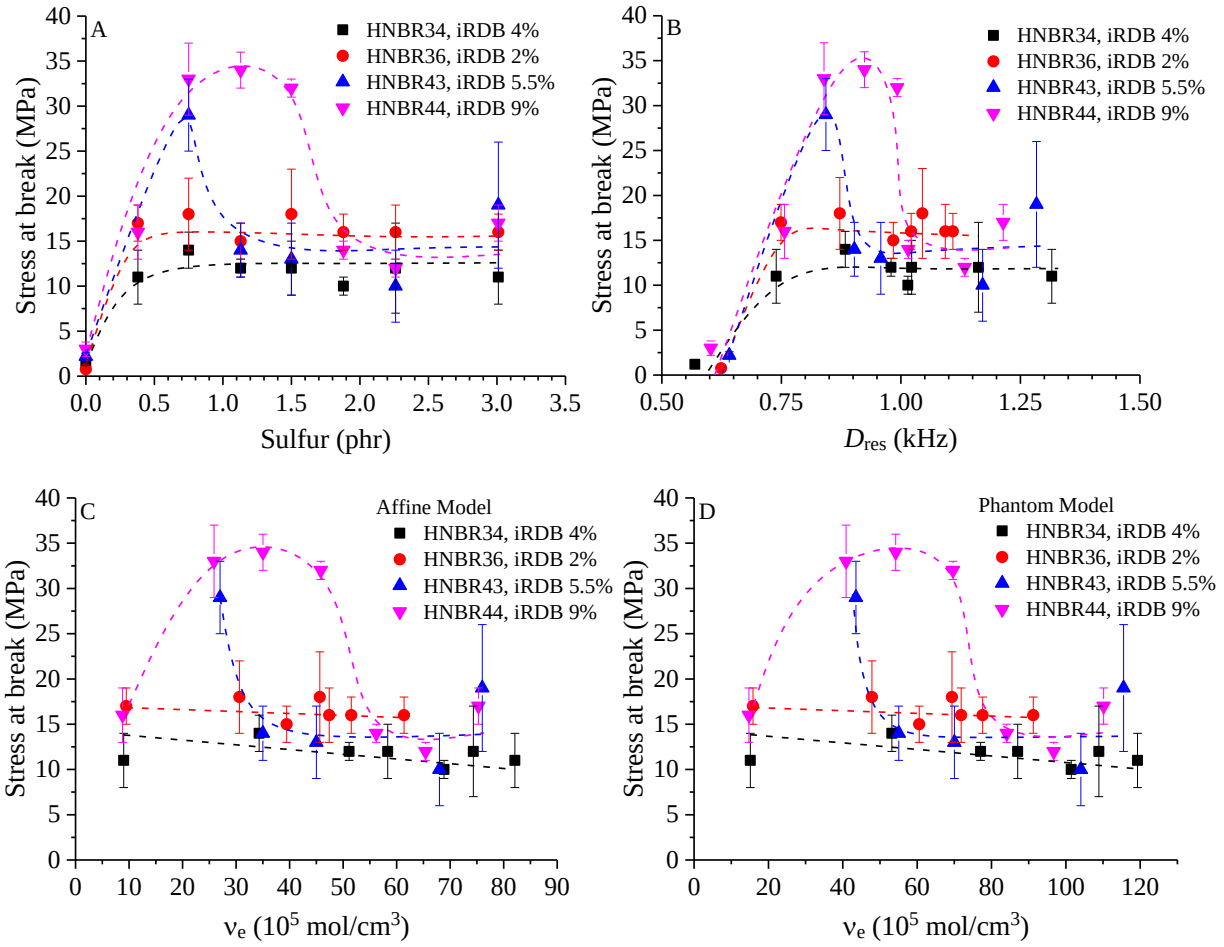

Figure 3.12 Values of stress at break as a function of added sulfur content (A), residual dipolar coupling D_{res} (B) and crosslink density ν_e obtained from affine (C), and phantom models (D) for the samples HNBR34 (black symbols), HNBR36 (red symbols), HNBR43 (blue symbols) and HNBR44 (magenta symbols), with 4, 2, 5.5 and 9 mol% iRDB, respectively.

The non-vulcanized samples HNBR34 and HNBR 36 exhibit values of strain at break 2-3 times higher than samples with higher ACN content (Fig. 3.13A,B). All the crosslinked samples, instead, show an almost linear decrease of strain at break as the crosslink density increases (Fig. 3.13).

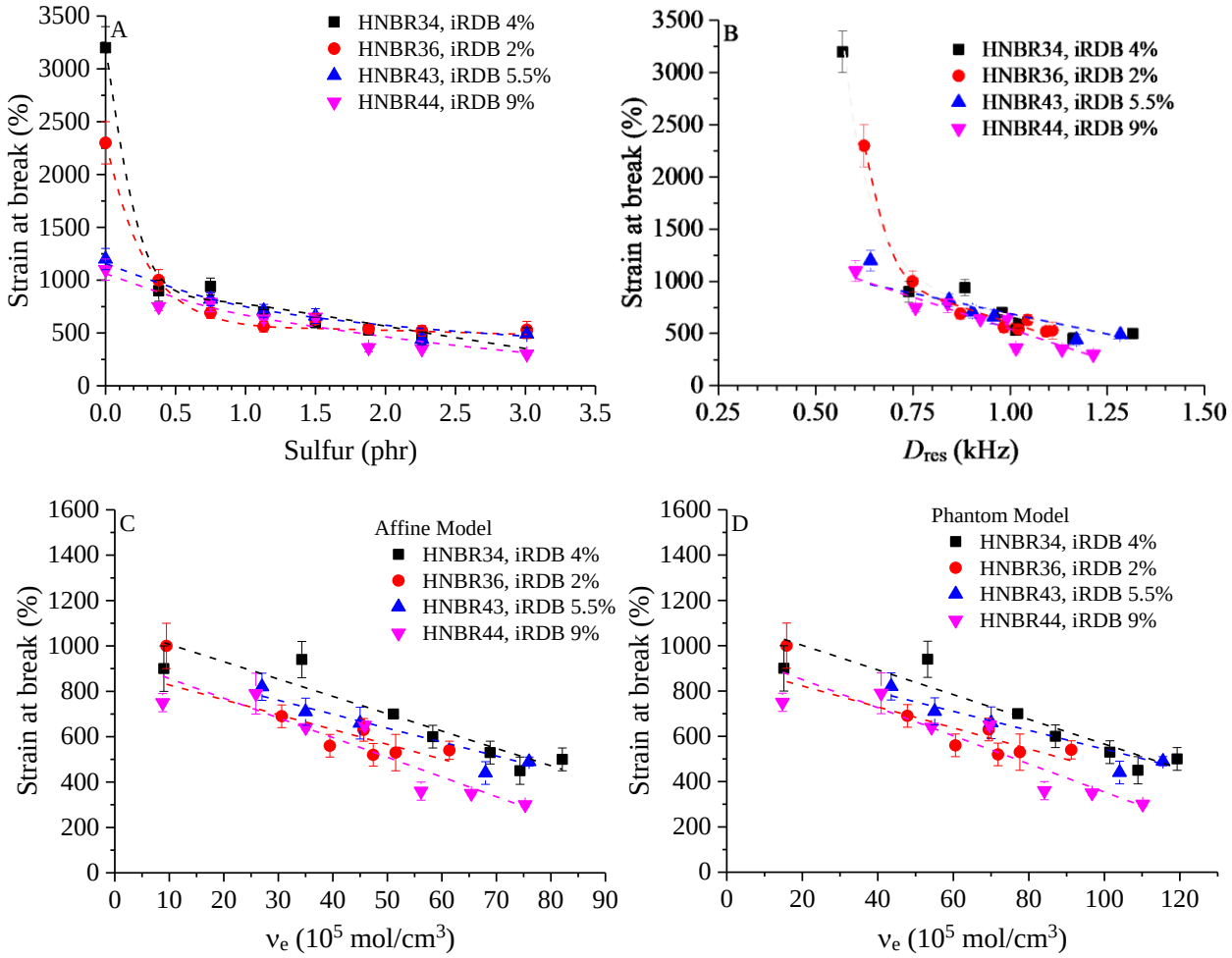

Figure 3.13 Values of strain at break as a function of added sulfur content (A), residual dipolar coupling D_{res} (B) and crosslink density ν_e obtained from affine (C), and phantom models (D) for the samples HNBR34 (black symbols), HNBR36 (red symbols), HNBR43 (blue symbols) and HNBR44 (magenta symbols), with 4, 2, 5.5 and 9 mol% iRDB, respectively.

Figure 3.14 shows the correlation between the tensile strength and ductility of the vulcanized rubbers. For the HNBR samples with 34 and 36 wt% ACN content, the values of stress at break are nearly constant. For the HNBR samples with 43 and 44 wt% ACN stress, instead, the stress at break achieves the maximum values of ≈ 30 MPa at strains of 800 and in between 650-800 %, respectively, corresponding to added sulfur content of 0.75 and 0.75 – 1.5 phr, respectively.

It is worth noting that for vulcanized rubbers the values of the ultimate tensile strength (coincident with the stress at break), is a result of the balance between the contributions of crosslink density, the degree of orientation achieved by the network strands and the possible occurrence of

SIC.[29,35,45,46,119-123] All these factors contribute to the reinforcing effect of elastomers. However, owing to the reduced length of the network strands, highly crosslinked samples may experience fracture at very low strains, occurring before reaching a high degree of alignment of amorphous chains and potential SIC. This may result in a significant reduction in tensile strength.[45,46,121] Moreover, the tensile strength may decrease for highly crosslinked rubbers also because the reduced mobility and the short length of the network strands prevents the formation of large sized crystals by SIC, resulting only in a small reinforcement effect at high strains. [45,46,121] The value of crosslink density at which the tensile strength reaches a maximum is often referred to as the "optimal crosslink density" i.e., the crosslink density that corresponds to the maximum strengthening of a rubber under stretching.[122,123]

Therefore, as it will be shown in the next paragraphs, the presence of a maximum in the values of strain at break for the HNBR sample with ACN content around 43-44 wt% at intermediate crosslink densities in Figure 3.13B-C, may be ascribed to their SIC ability, entailing the formation of highly oriented crystals in the stretching direction, along with the levelling off in the degree of orientation of the amorphous chains.[127] We anticipate that with further increase of crosslink density of these HNBR samples (added sulfur content >1.5 phr and D_e > 1 kHz) the level of crystallinity achieved upon stretching before breaking is very low, and the crystals formed by SIC have small size due to the decrease in length of the network strands and crystallizable sequences. These observations, associated to the decrease in ductility, well explains the lower values of the stress and strain at break of the HNBR44 sample at high crosslink density (Fig. 3.12, 3.13). The optimal crosslink density samples may be hence identified as that occurring at $D_e \approx 0.75$ kHz for the sample HNBR43, for D_{res} comprised in the range between 0.8 and 1 kHz, for the sample HNBR-44.

On the other hand, the similar values of stress at break of the crosslinked HNBR samples with 34 and 36 wt% ACN (Fig. 3.12) can be explained by the fact that they are not able to undergo SIC at

room temperature and that, regardless of the crosslink density, they reach a similar degree of orientation of the amorphous chains along the stretching direction at maximum elongation before fracture (vide infra).

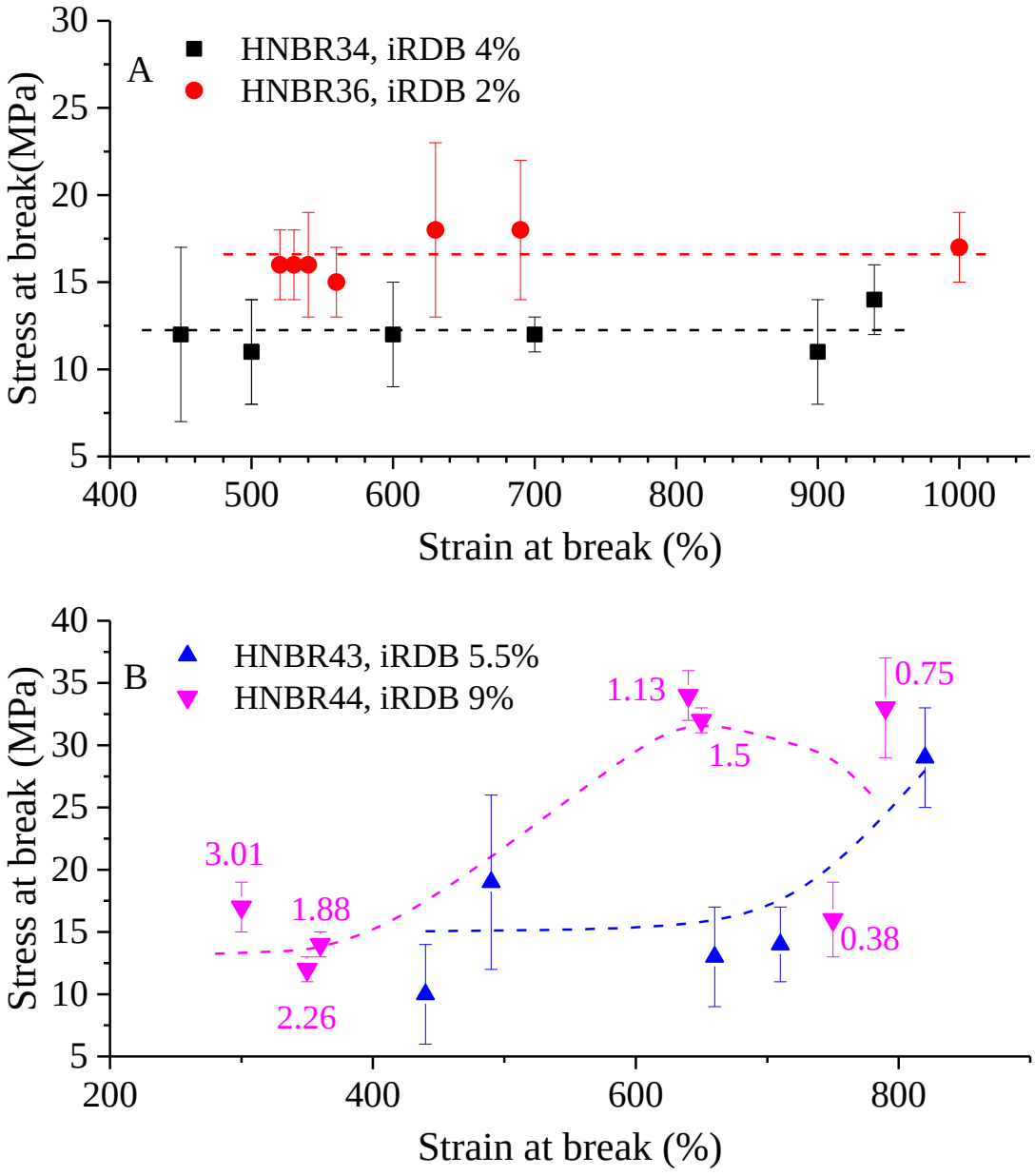

Figure 3.14 Values of stress at break as a function of strain at break for the samples HNBR34 (black symbols) and HNBR36 (red symbols) (A) and HNBR43 (blue symbols) and HNBR44 (magenta symbols) (B), containing 4, 2, 5.5 and 9 mol% iRDB, respectively. The added sulfur content expressed in phr is indicated for the samples with 44 wt% ACN in B.

Finally, all the vulcanized rubbers present good elastomeric properties in the whole range of strain up to the break, as indicated by the low values of tension set at break (Fig. 3.15 and Table 3.3). For the non-vulcanized rubbers only the samples with 43 and 44 wt% of ACN exhibit a good elastic recovery after the break (t_b < 90 %), whereas the samples with 34 and 36 wt% ACN show large residual strains after breaking.

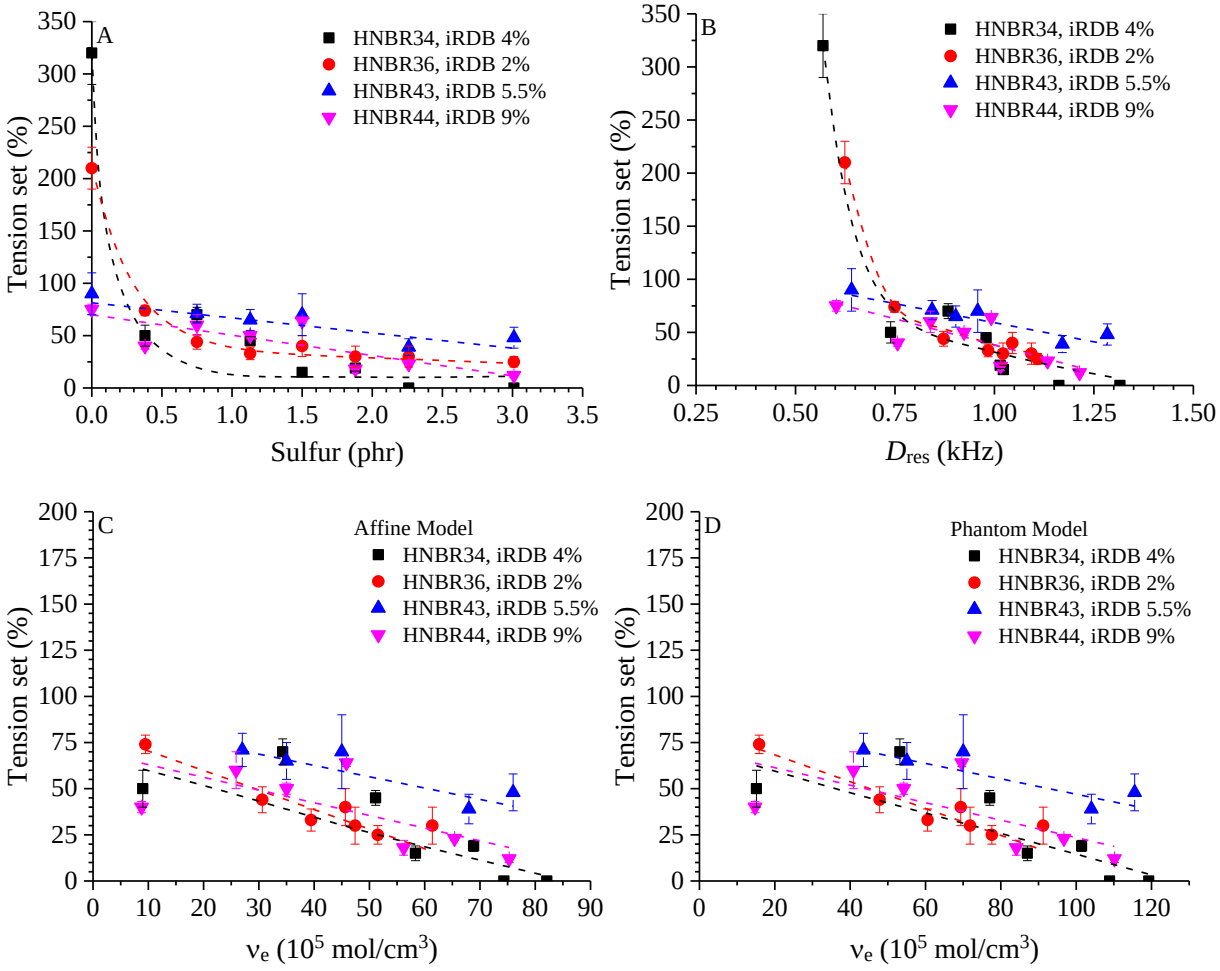

Figure 3.15 Values of tension set at break as a function of added sulfur content (A), residual dipolar coupling D_{res} (B) and crosslink density ν_e obtained from affine (C), and phantom models (D) for the samples HNBR34 (black symbols), HNBR36 (red symbols), HNBR43 (blue symbols) and HNBR44 (magenta symbols), with 4, 2, 5.5 and 9 mol% iRDB, respectively.

Hysteresis cycles

The hysteresis cycles of the subsets of HNBR samples characterized by ACN content of 34, 36, 43 and 44 wt% and iRDB content of 4, 2, 5.5 and 9 mol%, respectively, are reported in Figure 3.16. The values of tension set and dissipated energy (t_s and W_{diss}) measured after the first and successive cycles are listed in Table 3.4. To compare the elasticity of the different rubbers, the values of tension set after each cycle were divided by the maximum strain achieved during the first cycle (ε_{max}), obtaining the percentage of residual strain after the release of the tensile force (percentage of permanent set). The values of the percentage of permanent set and of the percentages of dissipated energy are reported in Figure 3.17 as a function of crosslink density. We recall that, for each sample, the value of ε_{max} has been set equal 70 – 80% of the corresponding average value of strain at break ε_b, listed in Table 3.3.

Table 3.4 Values of tension set (t_s) and dissipated energy (W_{diss}) measured in the hysteresis cycles of the non-vulcanized and vulcanized HNBR samples with different values of ACN and iRDB content and crosslink density. The values of the maximum strain achieved in the first cycle (ε_{max}) are also reported.

HNBR Samples	Samples code	ε_{max} (%)	$t_{s(I)}$ (%)	$t_{s(II-III)}$ (%)	$W_{diss(I)}$ (%)	$W_{diss(II-III)}$ (%)
THERBAN 3446 ACN 34 wt% iRDB 4 mol%	HNBR34-NV	1900	480 ± 10	500 ± 8	90 ± 4	74 ± 2
	HNBR34-0.75	560	53 ± 7	1.6 ± 0.4	46 ± 6	15 ± 1
	HNBR34-1.1	420	43 ± 4	0.5 ± 0.2	40 ± 2	12 ± 1
	HNBR34-1.5	360	36 ± 3	0.8 ± 0.2	36 ± 2	10 ± 1
	HNBR34-2.3	270	31 ± 4	0.7 ± 0.2	38 ± 1	11 ± 2
	HNBR34-3.0	300	35 ± 1	0.20 ± 0.05	39 ± 2	8.4 ± 0.3
THERBAN 3627 ACN 36 wt% iRDB 2 mol%	HNBR36-NV	1800	1250 ± 30	29 ± 4	96 ± 1	82 ± 5
	HNBR36-0.75	500	45 ± 2	0.7 ± 0.2	38 ± 1	12.2 ± 0.4
	HNBR36-1.1	400	50 ± 10	0.9 ± 0.3	38 ± 1	11 ± 1
	HNBR36-1.5	500	65 ± 9	0.6 ± 0.2	44 ± 6	10 ± 1
	HNBR36-2.3	400	38.3 ± 0.4	0.3 ± 0.1	43 ± 1	9.2 ± 0.5
	HNBR36-3.0	300	32 ± 1	0.6 ± 0.1	30 ± 1	9 ± 1
THERBAN 4367 ACN 43 wt% iRDB 5.5 mol%	HNBR43-NV	990	320 ± 40	13 ± 7	86.5 ± 0.3	57 ± 4
	HNBR43-0.75	660	54 ± 4	2.0 ± 0.8	63 ± 5	30 ± 2
	HNBR43-1.1	565	46 ± 4	1.5 ± 0.3	53 ± 4	23 ± 2
	HNBR43-1.5	525	49 ± 1	0.85 ± 0.04	46 ± 1	18 ± 1
	HNBR43-2.3	350	24 ± 2	0.54 ± 0.02	30 ± 6	9.6 ± 0.4
	HNBR43-3.0	390	34 ± 4	0.47 ± 0.03	33 ± 1	8.9 ± 0.5
THERBAN 4498 VP ACN 44 wt% iRDB 9 mol%	HNBR44-NV	900	530 ± 20	21 ± 3	92 ± 2	62 ± 5
	HNBR44-0.75	640	62 ± 2	1.3 ± 0.1	54 ± 1	29 ± 1
	HNBR44-1.1	500	48 ± 1	0.9 ± 0.2	46 ± 2	19 ± 1
	HNBR44-1.5	400	50 ± 1	0.5 ± 0.2	40 ± 1	12.1 ± 0.4
	HNBR44-2.3	280	30 ± 1	0.3 ± 0.1	30 ± 1	7.2 ± 0.2
	HNBR44-3.0	240	20 ± 2	0.20 ± 0.09	30 ± 1	7.2 ± 0.1

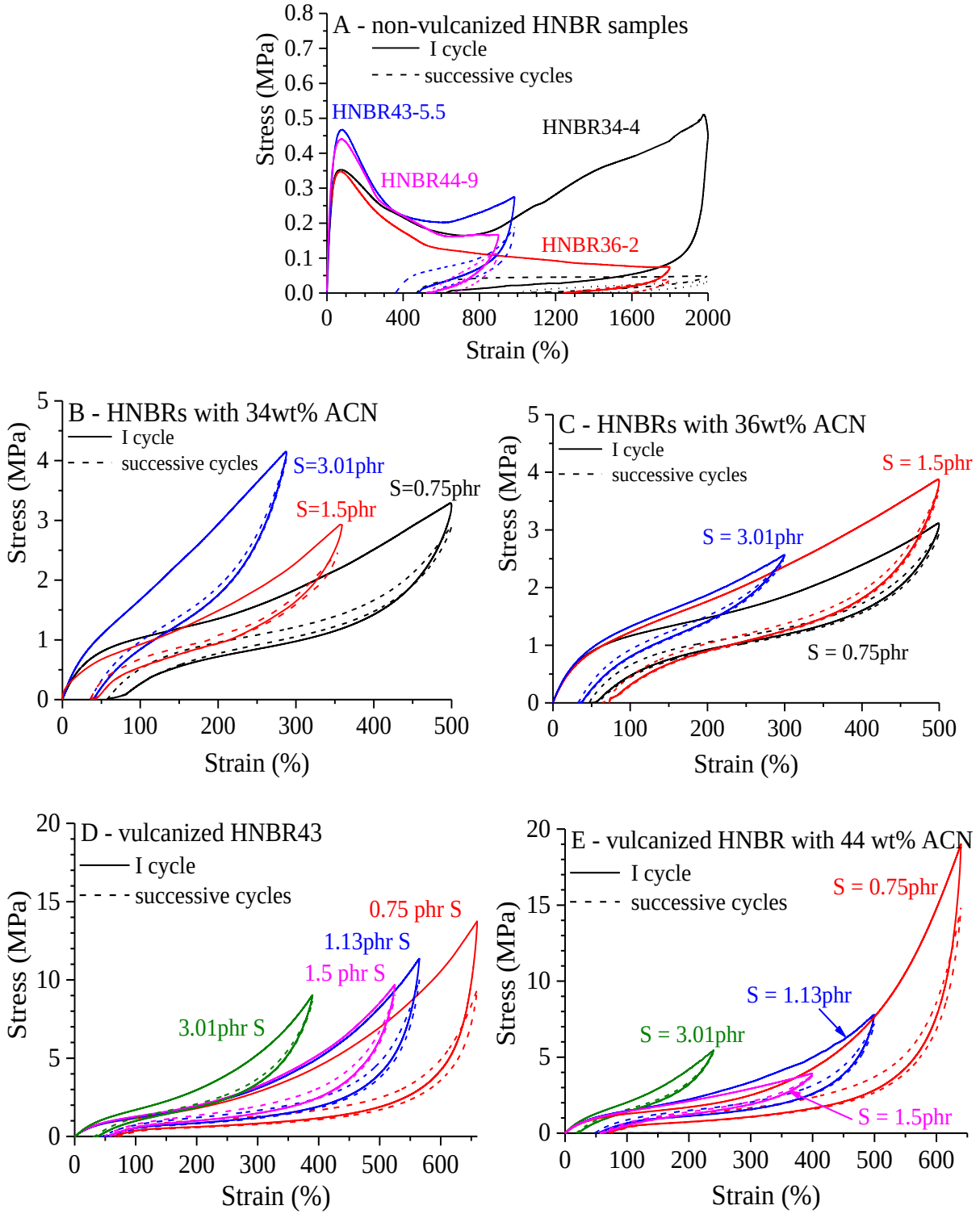

Figure 3.16 Hysteresis cycles of non-vulcanized (A) and vulcanized (B-E) HNBR samples with 34 (B), 36 (C), 43 (D) and 44 wt% of ACN, 4, 2, 5.5 and 9 mol% of iRDB, with the indicated amount of sulfur in phr. The cycles recorded after the first were coincident.

The non-vulcanized samples, exhibit pronounced hysteresis and large residual strains at the end of the first cycle (Fig. 3.16A and Table 3.4) due to the absence of chemical crosslinks between the chains. Hence, the entanglement density acting as physical crosslinks are unable to prevent disentanglement, and large, irreversible segmental relaxations occur.

The vulcanized samples, instead, exhibit good elastomeric properties when subjected to consecutive mechanical cycles of stretching and release of the tension (Fig. 3.16B-E and Table 3.4). The values of percentage of permanent set and dissipated energy are ≈ 10 – 15 % and 30 – 60 %, respectively, after the first hysteresis cycle and reduce to ≈ 0 and 10 – 30 %, respectively, in the successive ones (Fig. 3.17, 3.18 and Table 3.4). An increase of permanent set and a decrease of hysteresis with increasing crosslink density is observed for all vulcanized rubbers (Fig. 3.17, 3.18).

The data in Figures 3.17 and 3.18 also show that the percentages of permanent set and dissipated energy, respectively, are similar for all crosslinked rubbers, regardless of ACN content. The samples HNBR43 and HNBR44 show the highest values of the percentage of dissipated energy in the hysteresis cycles at low and medium crosslink density, corresponding to added sulfur content < 1.5 phr and D_{res} < 1 kHz. The values of percentage of dissipated energy decrease as the crosslink density decreases, until reaching values similar to those of HNBR samples with 34 and 36 wt% ACN (Fig. 3.18). As shown in the next paragraph, the high values of the percentage of dissipated energy experienced by the samples HNBR43 and HNBR44 at low and high crosslink density may be ascribed to the SIC behavior.

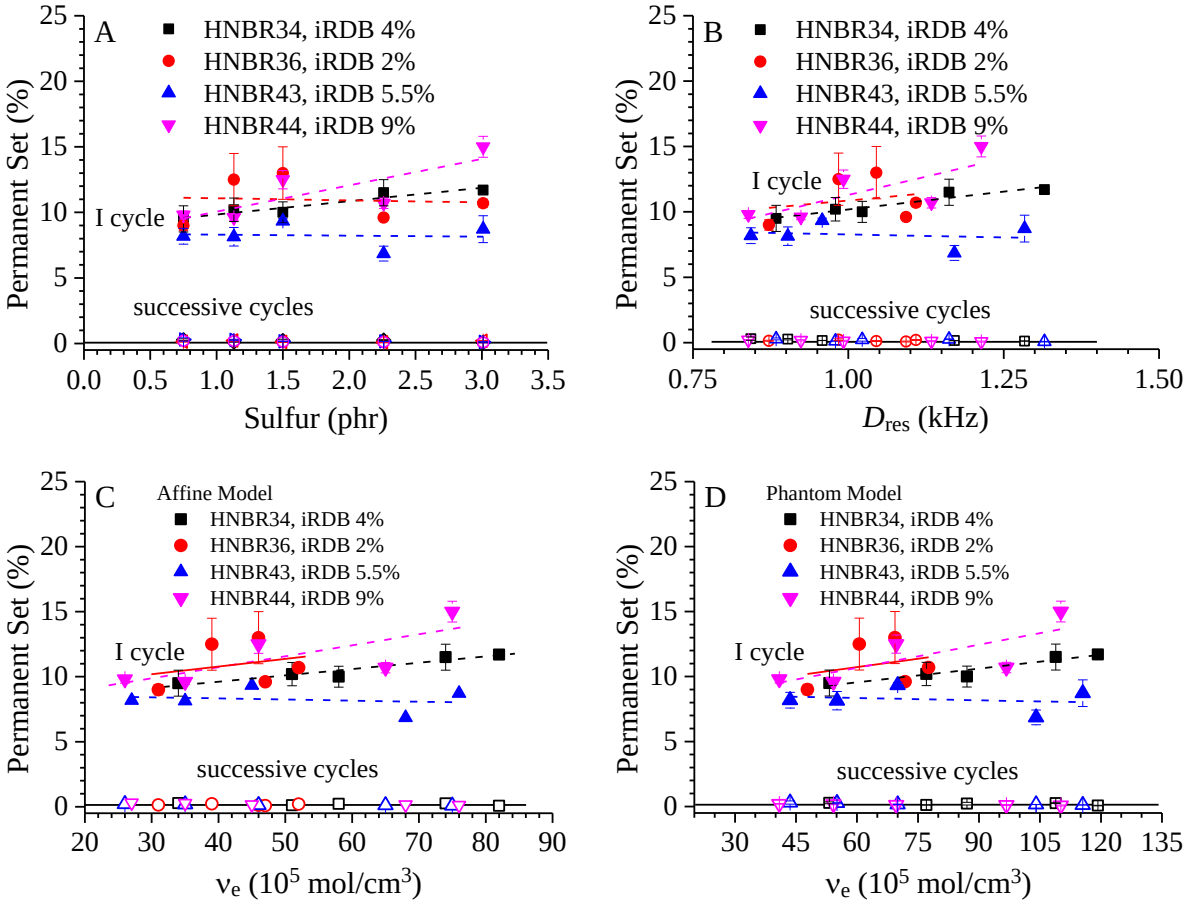

Figure 3.17. Percentage of permanent set after the first (solid symbols) and the successive hysteresis cycles (open symbols) as a function of added sulfur content(A), residual dipolar coupling D_{res} (B) and crosslink density ν_e obtained from affine (C), and phantom models (D) for the samples HNBR34 (black symbols), HNBR36 (red symbols), HNBR43 (blue symbols) and HNBR44 (magenta symbols), with 4, 2, 5.5 and 9 mol% iRDB, respectively.

The additional hysteresis generated by SIC behavior arises from dissymmetry of internal energy changes in loading and unloading cycles, because of the different kinetics of the involved crystallization and melting during the tests.[128] As a matter of fact, the samples HNBR43 and HNBR44 characterized by high crosslink density (D_{res} > 1 kHz), show only faint SIC because of the short length of the network strands, and rupture at strains close to that at SIC onset (vide infra). These samples also show values of the percentage of dissipated energy similar to those of non-crystallizing samples HNBR34 and HNBR36 (Fig. 3.18).

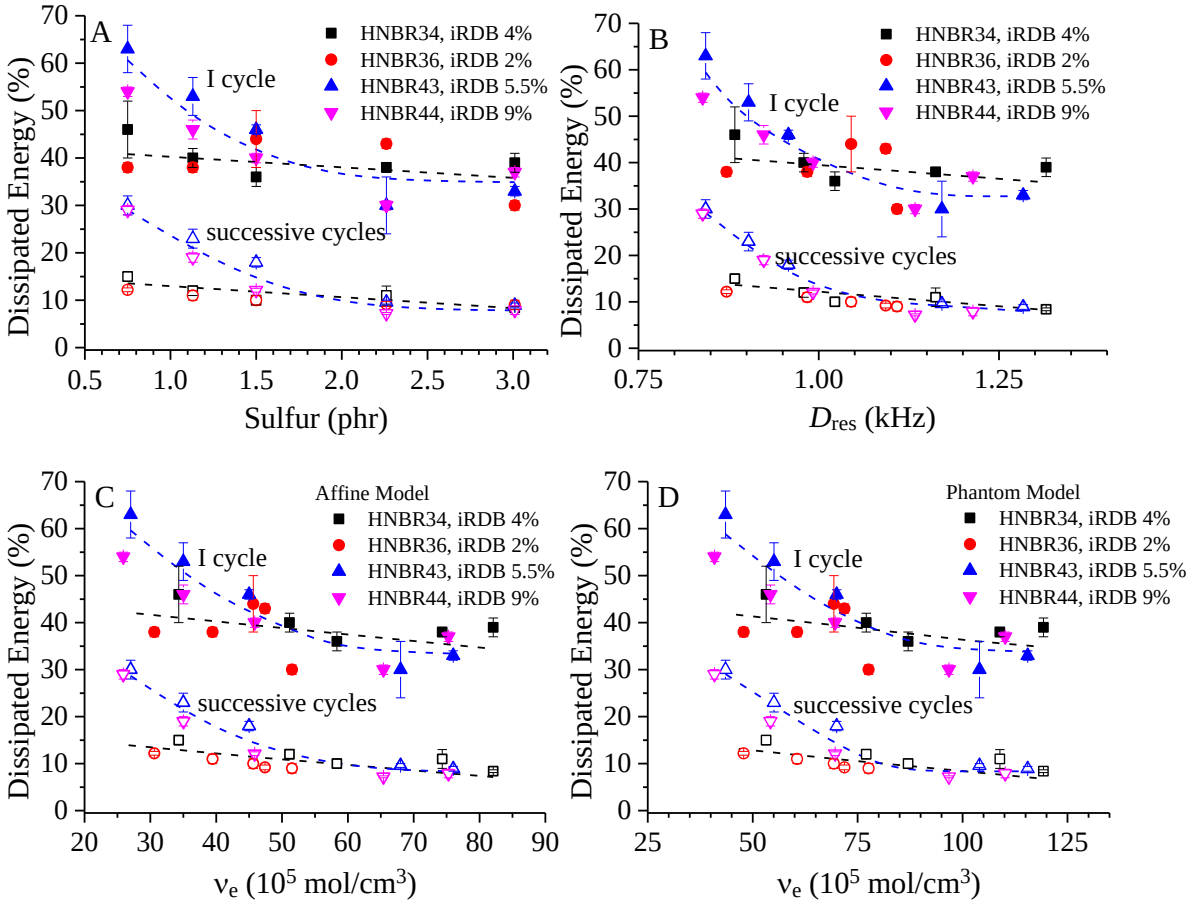

Figure 3.18. Percentage of dissipated energy measured after the first (solid symbols) and the successive hysteresis cycles (open symbols) as a function of of added sulfur content(A), residual dipolar coupling D_{res} (B) and crosslink density ν_e obtained from affine (C), and phantom models (D) for the samples HNBR34 (black symbols), HNBR36 (red symbols), HNBR43 (blue symbols) and HNBR44 (magenta symbols), with 4, 2, 5.5 and 9 mol% iRDB, respectively

3.4 X-ray fiber diffraction analysis of oriented samples and molecular chain orientation

Strain-induced crystallization of HNBR samples with 43 and 44 wt% content of ACN

The two-dimensional (2D) X-ray fiber diffraction patterns of the non-vulcanized and vulcanized HNBR samples with 43 and 44 wt% of ACN and 5.5 and 9 mol% of iRDB, respectively are reported in Figures 3.19, 3.20, A1 and A8. For each sample, the 2D WAXS patterns were recorded on specimens which were not previously subjected to any deformation. They were gradually stretched, at rate of ≈ 30 mm min^{-1} for each step, from the undeformed sample ($\varepsilon = 0$) to different strains ε until reaching a strain ε_{max} close to the break, and successively gradually unloaded until reaching complete release of the tension (Force = 0). The corresponding one-dimensional equatorial, meridional, azimuthal and radial profiles, extracted from the 2D patterns are reported in the Appendices A3-A12.

The 2D WAXS patterns of the unstretched samples (at $\varepsilon = 0$) show a halo centered at $2\theta(MoK\alpha)$ ≈ 8.7° (i.e., $2\theta(CuK\alpha)$ = 19.2°), the intensity of which is uniformly distributed along the whole azimuthal arc (Fig. 3.19,3.20, A1 and A8). This indicates that the samples are initially amorphous and that the amorphous phase is not oriented.

The 2D patterns of the vulcanized samples (Fig. 3.19, 3.20, A1, A8) show, regardless of deformation, narrow Debye-Scherrer rings due to the inorganic crystalline species (talc, clinochlore and ZnO) added as fillers and/or catalysts in the curative package. The distribution intensity of the amorphous halo tends to become anisotropic as the strain increases (Fig. 3.19 and 3.20), as indicated by the increase of intensity on the equator (at $\varphi = 90$) in the azimuthal profiles of Figure A3, A9. The 2θ position of the amorphous halo, instead, regardless of the crosslink density, remains almost constant at $2\theta(MoK\alpha)$ ≈ 8.7°, as evident from the corresponding equatorial and radial profiles of Figure A4, A6, A11 and A12, respectively. This indicates that the chain axes of the

amorphous phase gradually align themselves along the stretching direction with increase of strain. The chain axes alignment, in turn, leads to an increase of intensity on the equator at $2\theta(MoK\alpha) \approx 8.7°$, due to establishment of short range orientational correlation among chain segments at separation distances of about $(2 \sin \theta/\lambda)^{-1} \approx 0.47$ nm.

Upon release of the tension the orientation is gradually lost, and the intensity of the amorphous halo appears again uniformly distributed along the entire azimuthal arc (Fig. 3.19, 3.20 and A3, A9).

It is worth noting that for the non-vulcanized sample (HNBR43-NV and HNBR44-NV), the gradual stretching procedure adopted for the vulcanized counterparts (average loading rate of 30 mm min^{-1}) does not induce any significant change, as indicated by the uniform distribution of intensity of the amorphous halo centered at $2\theta(MoK\alpha) \approx 8.7°$, regardless of strain (Fig. 3.19A-D, 3.20A-D and A2 A-A'''). As shown in Fig. A2 (A'-A''') indeed, during stretching the azimuthal intensity distribution remains flat, and the equatorial, meridional and radial intensity profiles are coincident, regardless of strain. This indicates that in the adopted stretching conditions, in absences of crosslinks, the entanglements are not enough efficient to prevent the viscous flow of the chains. As a result, the elastomeric network is not deformed, because relaxation phenomena occur at the same or shorter time scale as the average loading rate.

The vulcanized HNBR samples with 43 and 44 wt% of ACN and different crosslink density show not only orientation of the amorphous phase but also SIC. For these samples, indeed, whereas at low strains (ε = 100 – 200 %) the sole observed changes are relative to the orientation of the amorphous phase, at strain greater than a critical value (250 – 300 %), well arced diffraction peaks appear on the equator at $2\theta(MoK\alpha) = 8.4$ and 11.6° (interplanar distances $d \approx 0.48$ and 0.35 nm, respectively) and on the meridian $2\theta(MoK\alpha) = 5.7°$ ($d \approx 0.72$ nm) (Fig. 3.19, 3.20, A1, A4 and A5). These reflections are attributed to the crystallization of the alternating tetramethylene/ACN

(TMAC) sequences.[64,70,124] The chain axis periodicity evaluated by the meridional reflection is close to a chain periodicity c = 7.5Å, consistent with a *trans*-planar conformation of the chains, as suggested in literature.[64,70,124] Upon release of the tension, the loss of orientation of the amorphous phase is preceded by the melting of the crystals, as indicated by the disappearance of the crystalline reflections (Fig. 3.19, 3.20, A1, A4 and A5) at strain around 100 – 200 %. For all the samples, the strain of incipient crystallization during stretching is higher than the strain marking the melting of crystals during the release of the tension. This hysteretic behavior is similar to that observed for NR.[29,40-43]

The strain-induced crystallization and melting in consecutive cycles of stretching and release of the tension are namely evident for all the vulcanized HNBR43 and HNBR44 samples. The SIC behavior is especially evident for the HNBR samples with D_{res} lower than 1.1 kHz, vulcanized with 2.26 phr of sulfur in the curative package. As the crosslink density increases, indeed, the crystalline reflections become less evident, due to broadening and the low intensity, indicating that the correlation length of the crystals in the directions parallel and perpendicular to the chain axes decreases (Fig. 3.19, 3.20 and A1, A8).

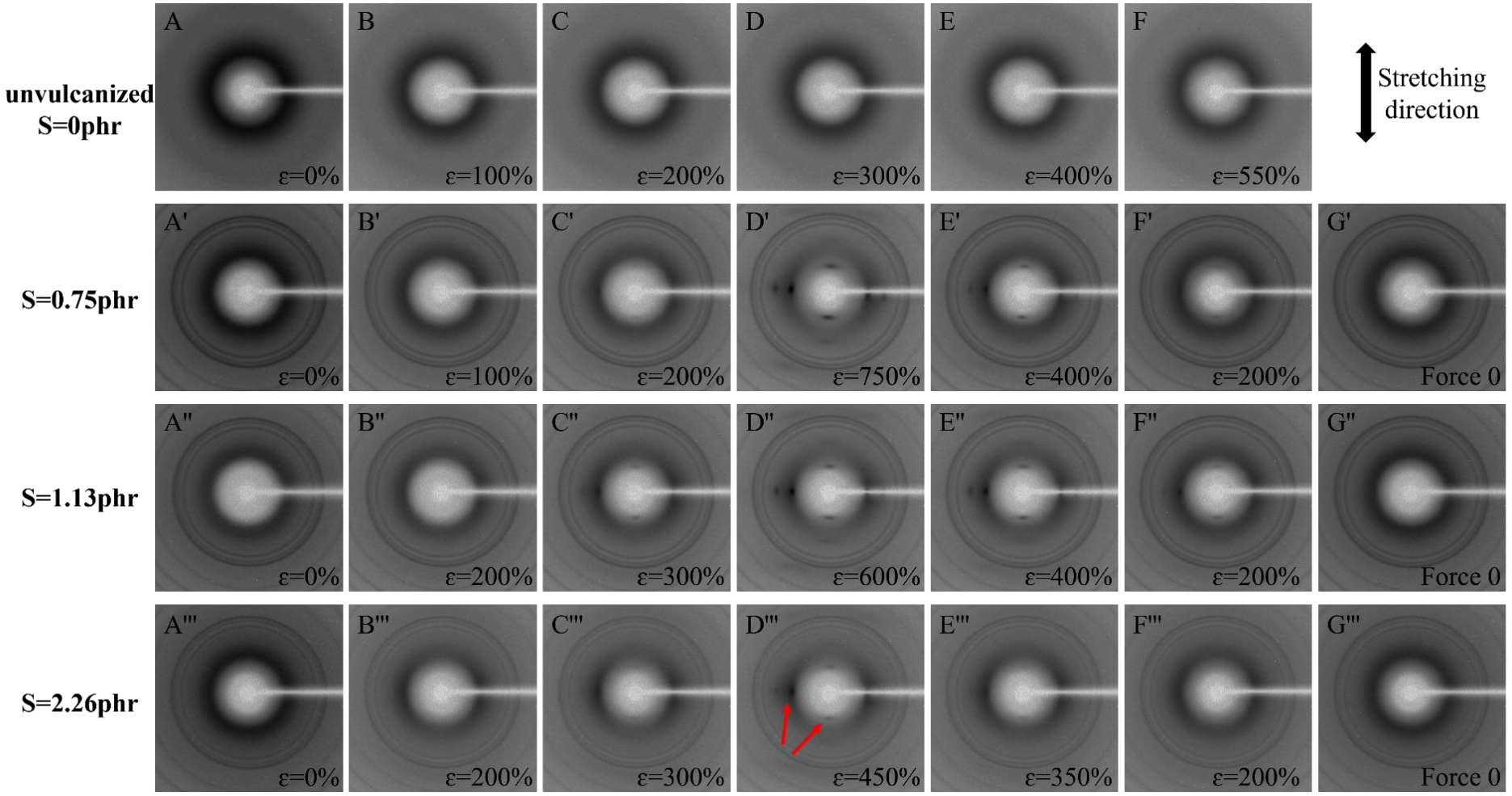

Figure 3.19. 2D WAXS fiber patterns of non-vulcanized (A-D) and vulcanized HNBR samples (A'-G'; A''-G''; A'''-G''') with 43 wt% of ACN, 5.5 mol% of iRDB, and different crosslink densities, recorded at *RT* at the indicated strains ε. Specimens that have not been subjected to any prior deformation are gradually stretched until reaching a strain close to breaking, and then they are gradually unloaded until reaching complete relaxation (force zero, average loading rate 30 mm min^{-1}). Arrows in D''' indicate reflections of faint intensity due to oriented crystallization of TMAC sequences also for the highly crosslinked sample with 2.26 phr of sulfur in the curative package. The stretching direction is indicated.

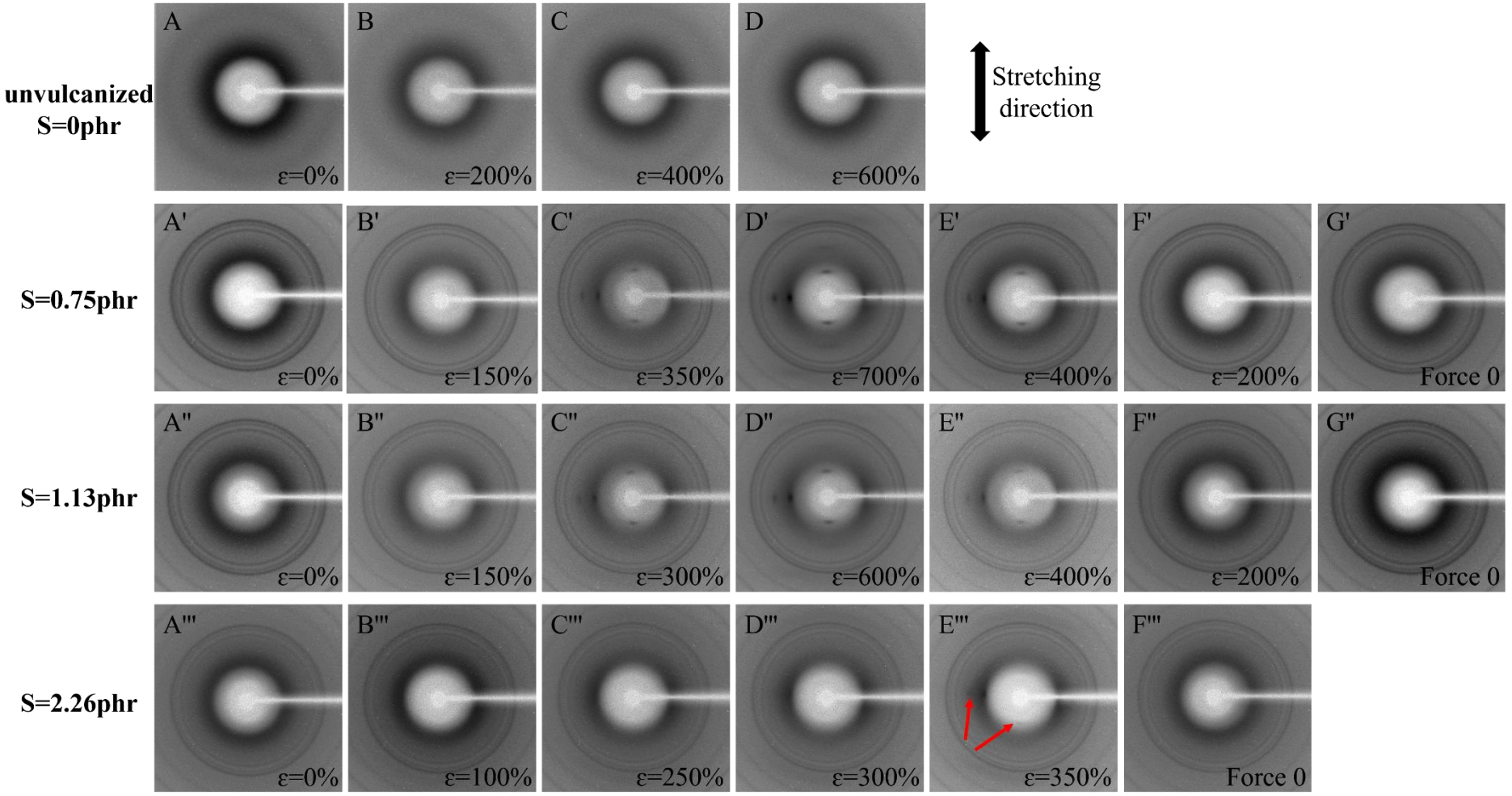

Figure 3.20 2D WAXS patterns of fibers of the non-vulcanized (A-D) and the vulcanized samples (A'-G'; A''-G''; A'''-F''') with 44 wt% of ACN, 9 mol% of iRDB, and different crosslink densities, recorded at *RT* at the indicated strains ε. Specimens that have not been subjected to any prior deformation are gradually stretched until reaching a strain close to the breaking, and then they are gradually unloaded until reaching complete relaxation (force zero, average loading rate 30 mm min^{-1}). The arrows in E''' indicate reflections of faint intensity due to oriented crystallization of the alternating TMAC sequences also for the highly crosslinked sample with 2.26 phr of sulfur in the curative package. The stretching direction is indicated.

Furthermore, inspection of the equatorial and meridional WAXS profiles (Fig. A4, A5, A12 and A13) suggests that the strain of incipient crystallization tends to increase with the increase in crosslink density. For instance, for the samples HNBR44-0.38 and HNBR44-0.75 with the lowest crosslink density (D_{res} = 0.6 and 0.76 kHz and sulfur content of 0.38 and 0.75 phr, respectively) the crystallization onset is in between 200 and 250 % (Fig. A4A,B and A5A,B) whereas for the samples HNBR44-2.3 and HNBR44-3.0 with the highest crosslink density (D_{res} = 1.1 and 1.2 kHz and sulfur content of 2.26 and 3.01 phr, respectively) the crystallization onset shifts to strains higher than 250 % (Fig. A4F,G and A5F,G). For the vulcanized subset of HNBR samples with 43 wt% of ACN, the SIC onset is between 200 and 250 % regardless of crosslink density. The difference in SIC behavior of the vulcanized samples can be explained by assuming that a high crosslink density reduces the chain mobility, hindering the crystals lateral growth and somehow delaying the crystallization kinetics through a shift of the strain marking the crystallization onset toward higher values. It is worth to remark that the strain of incipient crystallization for the samples with the highest crosslink density (HNBR44-2.3 and HNBR44-3.0) is close to the strain at break (Table 3.3).

For the non-vulcanized samples HNBR43-NV and HNBR44-NV gradually stretched in conditions similar to those adopted for the vulcanized samples (average strain rate of 30 mm min^{-1}) the absence of orientation of the amorphous phase is also associated with the absence of SIC (Fig. 3.19A-D, 3.20A-D, A2B and A9-13A). On the other hand, when the specimens are stretched at higher loading rate, the samples show at strains higher than a threshold not only orientation of the amorphous phase, but also SIC. As an example, the results obtained for independent specimens of the sample HNBR44-NV stretched at different strains at a loading rate of 150 mm min^{-1}, are shown in Figures 3.21 and A2A-A'', where the 2D WAXS patterns of fibers and the corresponding azimuthal, equatorial and meridional profiles are reported. It is apparent that the direct stretching at ε = 200 % induces a weak orientation of the amorphous phase, as indicated by the small polarization of the intensity on the equator (Fig. 3.21B

and A2A). The direct stretching at ε = 400 %, instead, induces a higher orientation of the amorphous phase and also SIC (Fig. 3.21C and A2A). Crystallization is indicated by the appearance of well arced and intense diffraction peaks on the equator at 2θ(MoKα) = 8.4 and 11.9° and on the meridian at 2θ(MoKα) = 5.7° (Fig. 3.21C and A2A',A''). Specimens stretched at strains higher than 400 % show better defined crystalline reflections, overlaying a well oriented amorphous phase (Fig. 3.21D,E and A2A-A''). Upon release of the tension, the crystals melt at 200 % strain, and also the orientation of the amorphous phase is lost. These results indicate that the gradual stretching at low loading rates of the non-vulcanized sample does not induce any significant orientation of the amorphous phase neither SIC probably because the solicitation time due to the application of the tensile force along with the time needed for stress transmission are longer than the characteristic segmental relaxation times, so that the viscous flow of the chain prevails. On the other hand, the stretching of independent specimens at high loading rates allows to reach a small orientation of the amorphous phase at low strains and, above a threshold strain, also SIC (Fig. 3.21 and A2). The so-formed crystals prevent the viscous flow of chains, acting as physical knots of the elastomeric network. In these conditions, the amorphous chains achieve a higher degree of orientation, as indicated by the increase of the intensity subtending the equatorial reflection in the azimuthal profiles of Figure A2A. The stretching-rate dependence of the structural behavior of the non-vulcanized sample HNB44-NV, explains well the differences in mechanical behavior observed in the stress-strain curve recorded at loading rate of 150 mm min^{-1} and in the hysteresis cycles recorded at loading rate of 30 mm min^{-1}. In fact, when the sample is stretched at high loading rate, SIC occurs (Fig. 3.21) and it is responsible for the rapid upturn of the stress and the remarkable strain-hardening in the stress-strain curve recorded up to rupture (Fig. 3.10A). When the sample is instead stretched at low rate, SIC does not occur (Fig. 3.20A-D), and the sample undergoes viscous flow, resulting in large values of tension set and dissipated energy measured in successive loading and unloading cycles (Fig. 3.16A and Table 3.4).

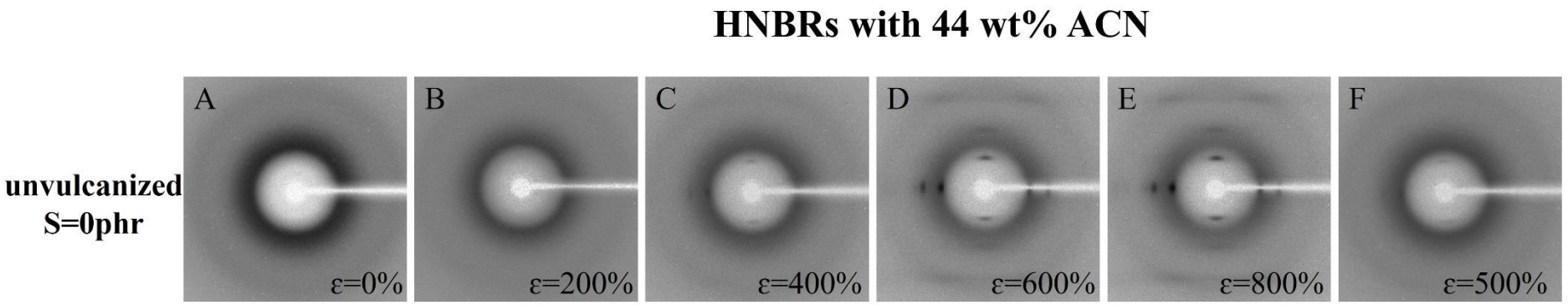

Figure 3.21. 2D WAXS patterns recorded at room temperature of fibers of the non-vulcanized sample HNBR44-NV with 44 wt% of ACN stretched at the indicated strains ε. Measurements are performed on independent specimen stretched at loading rate of 150 mm min^{-1}.

For the vulcanized samples undergoing significant SIC (that is with added sulfur contents comprised between 0.38 to 2.26 phr) an index of crystallinity x_c is calculated from WAXS data, using the relative intensity ratio of the equatorial reflection at $2\theta(\text{MoK}\alpha) \approx 8.4°$ as detailed in Figure 2.23 of Chapter II. This analysis has not been carried out on the highly crosslinked HNBR44-3, with added sulfur content equal to 3.01 phr, due to the excessively high uncertainty in the evaluation of x_c.

The calculated values of x_c are reported in Figure 3.22, as a function of strain.

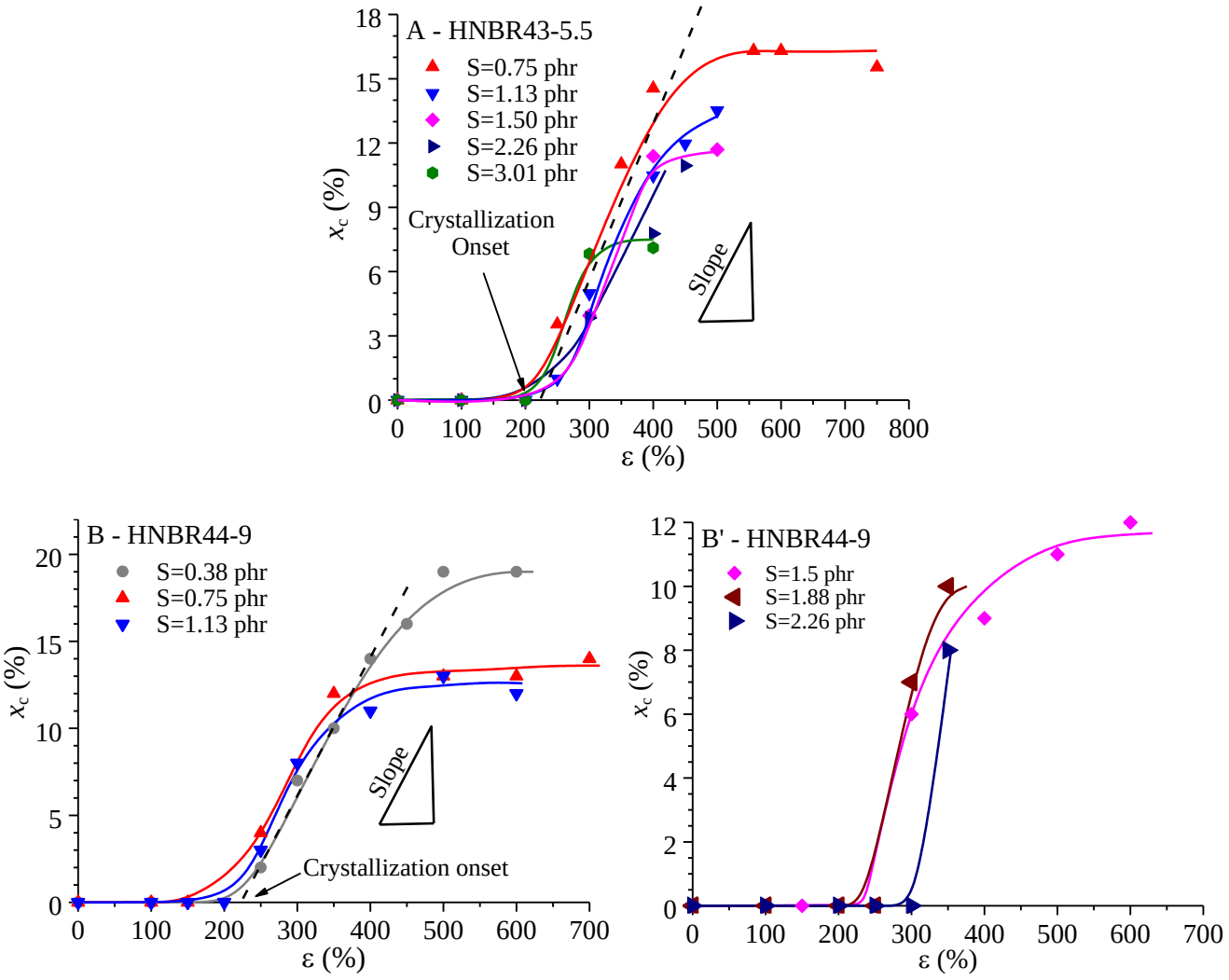

Figure 3.22 Index of crystallinity x_c evaluated from WAXS data using the relative intensity ratio of the equatorial reflection at $2\theta(\text{MoK}\alpha) \approx 8.4°$ as detailed in Fig. 2.23 (Chapter II), as a function of the strain for the HNBR samples containing 43 (A) and 44 wt% (B, B') of ACN, and 5.5 and 9 mol% of iRDB. The dashed line in A and B is the fit to the data with a straight line in the steepest region of the sigma-shaped curve. The intercept with the *x*-axis and the slope of the straight line are assumed to correspond to the strain of incipient crystallization and to incremental crystallinity index with respect to the strain $(dx_c/d\varepsilon)_{max}$, respectively (A and B).

For all the samples the crystallinity index increases as the strain increases according to a sigma-shaped curve, until reaching a maximum value at the highest approached strain, either because it is approached a plateau, or because the sample rupture (Table 3.3 and Fig. 3.22).

The maximum crystallinity index x_c(max) achieved upon stretching before the rupture of the sample decreases almost linearly with increase in crosslink density (Fig. 3.23, right scale). With increase in crosslink density, indeed, the length of the network strands decreases and also the length of crystallizable sequences decreases. Extrapolation of the straight line of Figure 3.23 indicates that crystallization does not occur anymore for the HNBR43 and HNBR44 vulcanized samples, for crosslink densities higher than ≈1.45 and 1.25 kHz, respectively. This indicates that the chemical crosslinks act as a sort of constitutional defects of the rubber networks that not only shorten the length crystallizable sequences, but also introduce topological constrains that reduce the segmental mobility, causing a decrease of ductility too (Fig. 3.13). Based on results of Table 3.1, the minimum number of average monomeric units/network strand able to crystallize by SIC should be slightly lower than 10. This figure is estimated considering that the sample HNBR44-3.0, vulcanized with high sulfur content, characterized by a number of average monomeric units/network strand close to 10, shows a faint crystallinity at 300 % strain (Fig. A1C'''), even though it breaks at slightly greater strain.

The fit to the data with a straight line in the most-steep region of the sigma-shaped curves is shown in Figure 3.22A,B, as an example. The intercept with the *x*-axis and the slope of the straight line are assumed to correspond to an approximate value of the strain of incipient crystallization and of incremental crystallinity index with respect to the strain (dxc/dε)max, respectively. It is apparent that the values of strain of incipient crystallization occur around 200– 250 % for the vulcanized HNBR43 samples, regardless of crosslink density, around 200– 240 % for the vulcanized HNBR44 samples with D_{res} comprised between 0.8 and 1 kHz (added sulfur content comprised between 0.38 and 1.88 phr) and around 300 % for the highly crosslinked sample HNBR44 with D_{res} of 1.1 kHz (added sulfur content

equal to 2.26 phr). Therefore, although the values of strain of incipient crystallization are affected by a large error, it seems that the strain at the onset of SIC is about constant for crosslink density below a threshold (≈ 1 kHz, sulfur content ≈ 1.9 phr) and tends to increase above this threshold. As stated before, this behaviour is similar to that of sulfur vulcanized natural rubber. [17,18,25,32,33]

The values $(dx_c/d\varepsilon)_{max}$ are reported in Figure 3.23 as a function of D_{res} (left scale). Since the fibers are stretched at similar loading rate (≈ 30 mm min^{-1}) and the WAXS profiles are recorded while keeping the samples in tension at each strain for about 15 min, the values of incremental crystallinity index with respect to the strain may be considered a sort of a kinetic parameter of SIC ("SIC rate"), marking how fast the crystallinity increases by effect of stretching step-by-step. Inspection of Figure 3.23 indicates that the maximum crystallinity achieved upon stretching decreases monotonically with increasing D_{res} (proportional to the crosslink density). The values of $(dx_c/d\varepsilon)_{max}$ relative to the crosslinked HNBR43 and HNBR44 samples instead, are nearly constant for D_{res} lower than a critical value equal to 1.17 kHz (sulfur content < 2.26 phr) (Fig. 3.23A) and 1 kHz (sulfur content < 1.50 phr) (Fig. 3.23B), respectively, and then, above this critical crosslink density, increase (Fig. 3.23). In both cases $(dx_c/d\varepsilon)_{max}$ starts to increase when the x_c(max) falls below approximatively 12 %. The small, but significant differences in the SIC behavior of the crosslinked HNBR43 and HNBR44 samples, may not be ascribed to differences in iRDB content, equal to 5.5 and 9 mol%, respectively, as the samples with the lowest number of interruptions (HNBR43) show SIC rate increment at higher crosslink density. We argue that the SIC behavior is rather influenced by small differences in the populations of crystallizable alternated tetramethylene/ACN (TMAC) sequences of high length. The higher ACN content of the HNBR44 samples, indeed, implies that the HNBR44 samples show a major concentration of long TMAC sequences, making the SIC behavior easier than that of the HNBR43 samples.

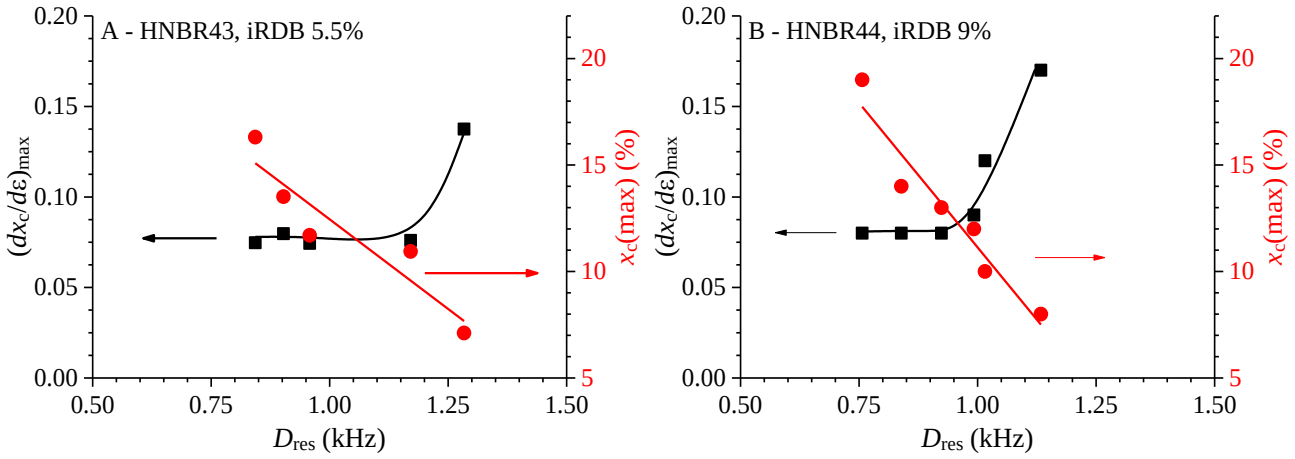

Figure 3.23. Values of SIC rate $(dx_c/d\varepsilon)_{max}$ (left scale) and crystallinity index achieved upon stretching at the maximum approached strain close to the break x_c(max) (Table 3.3) (right scale) as a function of D_{res} for the crosslinked subsets of the samples HNBR43 (A) and HNBR44 (B).

It is worth noting that the increase of "SIC rate" as the crosslink density increases, as well as the associated decrease of crystal size and crystallinity index observed for the HNBR samples, are similar to the SIC behavior of natural rubber. For NR, indeed, it has been shown that higher crosslink density results in a faster crystallization.[30,31,38] This increase has been ascribed to the increase of nucleation density, as nucleation is controlled by the local stretch ratio of the network strands, which for highly crosslinked networks should be enhanced. The increase of nucleation density with the increase of crosslink density, in turn, causes also the formation of crystallites of smaller size due to the restricted mobility of stems that hinders their lateral growth.[30,31,38] As a result of reduced mobility, also a decrease of the degree of crystallinity occurs.[28,45,46]

Segmental orientation of the HNBR43 and HNBR44 samples

The segmental orientation of the HNBR samples stretched at different strains is calculated from the azimuthal profiles extracted from the 2D WAXS patterns as detailed in Chapter 2, Fig. 2.22. The values of the order parameters $P_2^{\text{WAXS-am}}$ and $P_2^{\text{WAXS-cr}}$ was determined by equations 2.71 and 2.69. Considering that for the standard statistics of polymer chains in the Gaussian approximation the order parameter of the amorphous segments depends on the stretch ratio $\lambda = L/L_0$ (= ε/100+1) through equation:[38]

$$P_2^{WAXS-am} = \frac{K}{5N}(\lambda^2 - 1/\lambda) \qquad (3.10)$$

where N is the average number of freely jointed statistical segments (proportional to the number of monomeric units) per chain and K is a factor related to the local structure of the amorphous phase,[129] the values of $P_2^{\text{WAXS-am}}$ relative to the amorphous phase in Fig. 3.24 is reported as a function of the elongation parameter (λ^2-1/λ). The values of $P_2^{\text{WAXS-cr}}$ relative to the crystalline phase, instead, are reported in Figure 3.26 as a function of the same quantity (λ^2-1/λ). We recall that, since the order parameters are calculated considering the polarization of the WAXS intensity of the amorphous halo and Bragg's peaks on the equator, the calculated values of the order parameters $P_2^{\text{WAXS-am}}$ and $P_2^{\text{WAXS-cr}}$ are negative. As discussed in Chapter II, a perfect orientation of the chain axes along the stretching direction corresponds to values of the P_2^{WAXS} parameter equal to -0.5, for the amorphous and crystalline phases. It is apparent that the values of the order parameter associated to the amorphous segments experience a steep increase in absolute value at low strains until reaching a plateau or a quasi-plateau value for values of (λ^2-1/λ) close to the range of 9-12 (i.e. ε ≈ 200-250 %) and 9-16 (i.e. ε ≈ 200-300 %) for the HNBR43 (Fig. 3.24A) and HNBR44 (Fig. 3.24B) samples, respectively. Furthermore, the degree of orientation achieved by the amorphous segments at any strain increases as the crosslink density increases. Since also the values of stress level at any strain increase as the orientational order increases,[38] the dependence of order parameter achieved by the vulcanized HNBR samples on the crosslink density explains well the increase of mechanical resistance as the D_{res} values increase (Fig. 3.12B). The presence of a plateau in $P_2^{\text{WAXS-am}}$

as a function of (λ^2-1/λ) indicates that when crystallization occurs, the orientation of the amorphous segments does not increase anymore with strain because crystallization leads to a partial relaxation of the amorphous chains linked to the crystallites, as predicted by Flory theory[27] and observed in vulcanized samples of natural rubber[37,39-42] and synthetic elastomers such as polyisoprene, polybutadiene, and butyl rubber.[42] Furthermore, when the plateau is reached the value of the order parameter is approximately constant and equal to -0.032 for the HNBR43 samples and 0.029 for the HNBR44 samples. This indicates that for the samples HMBR44 containing a major population of long TMAC sequences, the amorphous segments reach a lower degree of orientation at strains close to that of crystallization onset than that achieved by the samples HNBR43.

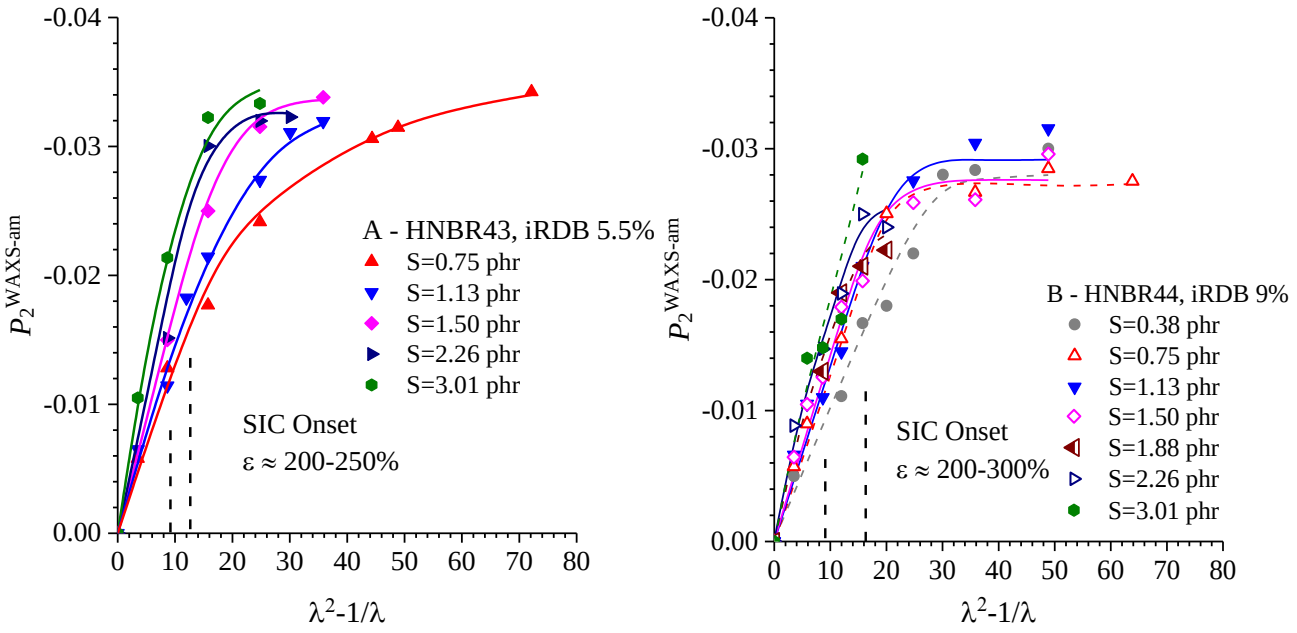

Figure 3.24 Values of the order parameters for the amorphous segments $P_2^{WAXS-am}$ as a function of the elongation parameter (λ^2-1/λ) of the HNBR samples with 43 (A) and 44 wt% of ACN (B), 5.5 and 9 mol% of iRDB, respectively, and different crosslink density. The dashed vertical bars mark the strains of range comprised between 200 and 250 (A) and between 200 and 300 % (B).

According to equation 3.10, the straight line interpolating the values of $P_2^{WAXS-am}$ vs. (λ^2-1/λ) at low strains (i.e. before SIC) in Figure 3.24 correspond to a slope equal to $K/(5N)$, with N the number of statistical segments or monomers/network strand. In agreement with theory, the value of the slope increases as the amount of added sulfur increases, i.e., as the D_{res} parameter increases.[129]

A further insight into the deformation behavior of HBR samples may be achieved by dividing the first and second member of equation 3.10 by D_{res}:

$$\frac{P_2^{WAXS-am}}{D_{res}} = \frac{K}{5N}\frac{1}{D_{res}}(\lambda^2 - 1/\lambda) \qquad (3.11)$$

The values of the $\frac{P_2^{WAXS-am}}{D_{res}}$ ratio (reduced order parameter) relative to the HNBR43 and HNBR44 samples are reported as a function of the elongation parameter λ^2-1/λ in Figure 3.25. It is apparent that, since $D_{res} \propto 1/N$, the values of the reduced order parameter $\frac{P_2^{WAXS-am}}{D_{res}}$ of the vulcanized samples increase as the elongation parameter increases according to a common straight line passing through the origin at low strains. Deviation from the straight line occur at strains higher than that marking the crystallization onset, as this parameter tends to approach a plateau at values that decrease as the crosslink density increases. The values of the slope of the straight line $Q = \frac{K}{5N}\frac{1}{D_{res}}$ are reported in Table 3.5. Although the accuracy of this evaluation could be improved extending measurements at strains lower than 100 % (i.e. for λ^2-1/λ lower than 3.5), the estimated values of Q may be considered a good approximation to the effective ones.

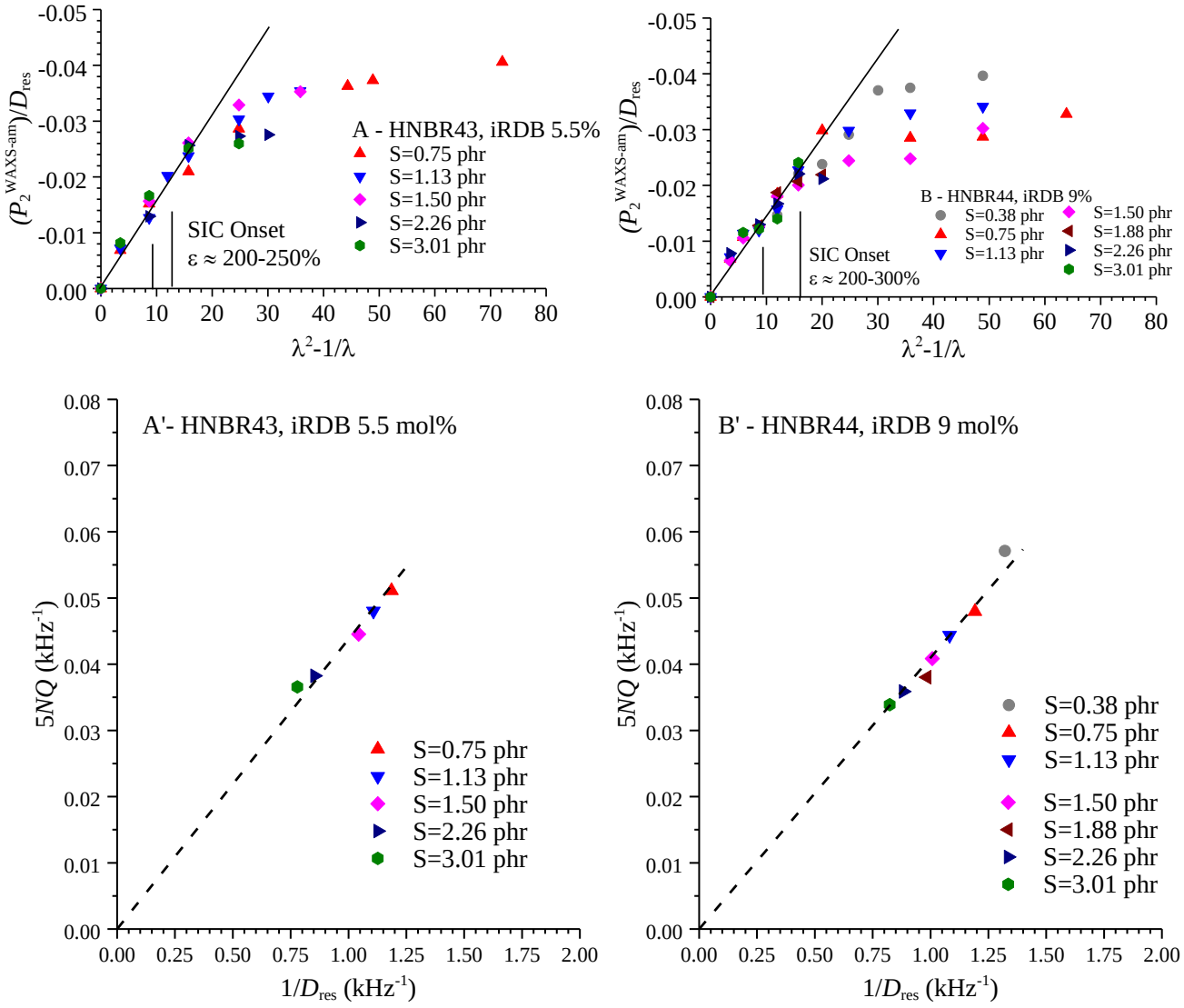

Figure 3.25 Values of the $\frac{P_2^{WAXS-am}}{D_{res}}$ ratio as a function of the elongation parameter λ^2-1/λ relative to the HNBR43 (A) and HNBR44 (B) samples with 5.5 and 9.9 mol% iRDB content, and different crosslink density. The black line is the fit to data at low strain with a straight line having slope $Q = \frac{K}{5N}\frac{1}{D_{res}}$. The vertical bars indicate the strain ranges marking the SIC onset at ≈ 200-250 (A) and 200-300 % (B). Values of the quantity 5*NQ* as a function of 1/ D_{res} for the samples HNBR43 (A') and HNBR44 (B'), with 5.5 and 9 mol% of iRDB. The slope of the straight line interpolating the data is the constant *K* of equation 3.10.

The so calculated values of Q allow to evaluate the value of K in equation 3.10, by rearranging equation 3.11 as it follows:

$$5NQ = K\frac{1}{D_{res}} \qquad (3.12)$$

Equation 3.12 has been obtained by considering that $Q = \frac{K}{5N}\frac{1}{D_{res}}$ is also equal to $Q = \frac{P_2^{WAXSq-am}}{(\lambda^2-1/\lambda)D_{res}}$. However, in order to find the K value, the unknown quantity N, corresponding to the number of statistical segments/network strand has to be found. This quantity can be evaluated considering that $\frac{\nu_e}{\rho_r} = \frac{1}{2\langle M_N\rangle}$ (see equation 3.4), and that $\frac{\langle M_M\rangle}{\langle M_N\rangle} = \frac{1}{N_N}$ (see equation 3.5). Here M_N and N_N are the number average molecular mass and the average number of statistical segments (or monomers) included in a network strand extracted from equilibrium swelling measurements using the phantom model to obtain the values of crosslink density ν_e (see Table 3.1). The quantity M_M, instead, is the molecular mass of a statistical segments or average monomeric unit. Therefore, through the rearrangement of equation 3.9, the value of the number of statistical segments or monomers/network strand N can be calculated as:

$$\frac{1}{N} = \frac{2M_M D_{res}^0}{u} + \frac{1}{N_N} \qquad (3.13)$$

where the following relationships have been taken into account: $\frac{D_{res}}{u} = \frac{1}{2M_c}$ and $\frac{\langle M_M\rangle}{\langle M_c\rangle} = \frac{1}{N}$. In this way the value of the quantity $5NQ$ relative to the HNBR samples with 43 and 44 wt% of ACN can be easily calculated. These values are reported in Figure 3.25A',B' as a function of of $1/D_{res}$.

A nice fit to data was obtained using a straight line, the slope of which corresponds to the values of K equal to 0.044 and 0.041, for the vulcanized subsets of HNBR samples with 43 and 44 wt% of ACN, respectively (Table 3.5).

Table 3.5 Values of the quantities $Q=\frac{K}{5N}\frac{1}{D_{res}}$ in equation 3.10 and K in equation 3.12 relative to the vulcanized subset of HNBR samples with 34, 36, 43 and 44 wt% ACN content.

Sample Sub-Sets	Q ($10^{-3}Hz^{-1}$)	K
HNBR34, iRDB 4%	-1.48	0.032
HNBR36, iRDB 2%	-1.45	0.039
HNBR43, iRDB 5.5%	-1.90	0.044
HNBR44, iRDB 9%	-1.64	0.041

As for the crystalline phase, it reaches a degree of orientation higher than the amorphous phase (Fig. 3.26). In particular, the values of the order parameter $P_2^{WAXS\text{-}cr}$ is constant and equal to ≈ -0.5, regardless of the deformation and the crosslink density. This indicates that once the strain of incipient crystallization is reached the formed crystallites are highly oriented with their chain axes parallel to the stretching direction and their alignment degree does not increase significantly by further stretching, neither with the increase in crosslink density.

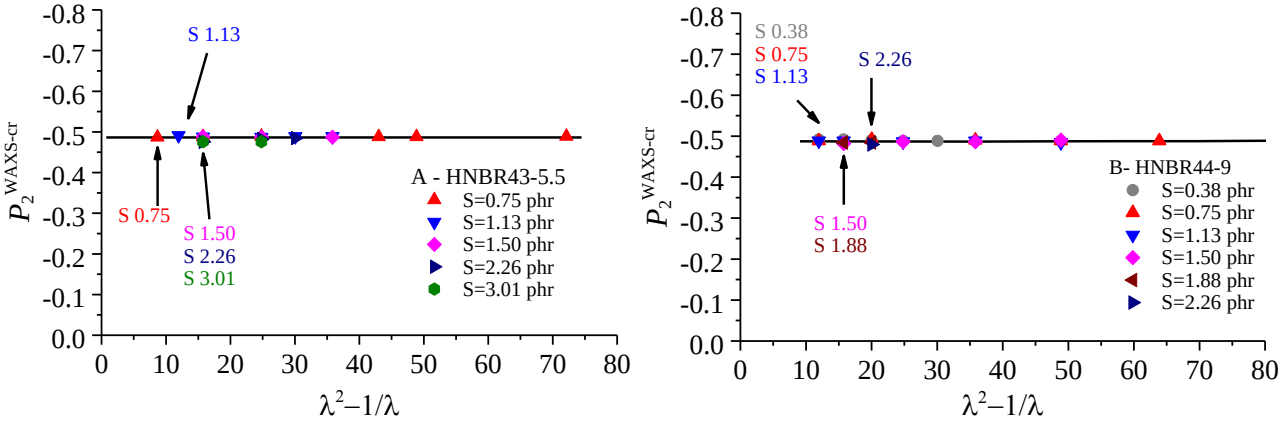

Figure 3.26. Values of the order parameters for crystalline segments $P_2^{WAXS\text{-}cr}$ as a function of the elongation parameter (λ^2-1/λ) of the HNBR samples with 43 (A) and 44 wt% of ACN (B), 5.5 and 9 mol% of iRDB, and different crosslink density. The arrows mark the elongation parameter where crystallization begins.

This result is in agreement with the prediction of Flory theory[27] and suggests that the oriented amorphous segments are precursors of the crystallites formed by SIC and they are responsible not only for the high degree of orientation of the SIC crystals, but also for the fast crystallization rate (Fig. 3.23). The extension of the amorphous chains preceding SIC, indeed, induces a decrease of the barrier for primary nucleation and growth of the crystals through a decrease in the entropy penalty for the incorporation of the chain segments into the crystalline aggregates (entropy barrier effect). The non-monotonous change of the incremental crystallinity index with respect to the $(dx_c/d\varepsilon)_{max}$ as a function of D_{res} may be due to competition between the entropy barrier effect and the reduction in segmental mobility with increase of D_{res} (dynamic effect). At low D_{res}, indeed, the degree of orientational order achieved by the amorphous segments is not so high. Consequently, the "SIC rate" is either constant, or decreases with a small increase of D_{res} because the dynamic effect prevails over the entropy barrier effect. However, with further increase of D_{res}, the degree of orientation achieved by the amorphous segments increases above a threshold, inducing a neat decrease of the barrier for primary nucleation and crystal growth. Since the segmental mobility is reduced only a little, the entropy barrier effect becomes prevalent over the dynamic effect. It is expected that the dynamic effect would become again prevalent, for very high crosslink density. However, this expectation cannot be checked because the HNBR samples become also fragile and unable to crystallize by increasing D_{res}, as shown by the highly crosslinked HNBR43 and HNBR44 sample with D_{res} equal to 1.28 and 1.21 kHz (added sulfur content 3.01 phr), respectively, that crystallize only a little and break at strains very close to the strain of incipient crystallization (300-350 %, Fig. A4 and A5). As a further remark, it is worth pointing out that the high degree of orientation achieved by the crystals generated by SIC, along with the (relatively) high degree of crystallinity is responsible for the high strain hardening shown by the weakly and medium crosslinked HNBR samples at high strains (Fig. 3.10D,E).

Segmental orientation of HNBR34 and HNBR36 samples

The 2D X-ray fiber diffraction patterns of the non-vulcanized and vulcanized HNBR samples with 34 and 36 wt% of ACN and 2 and 4 mol% of iRDB, respectively are reported n Figures 3.27 and 3.28. For each sample, the 2D WAXS patterns were recorded on specimens which were not previously subjected to any deformation. They were gradually stretched, at loading rate of ≈ 30 mm min^{-1} for each step, from the undeformed sample ($\varepsilon = 0$) to different strains ε until reaching a strain ε_{max} close to the break, and successively gradually unloaded until reaching complete release of the tension (Force = 0). For the non-vulcanized HNBR with 34 wt% of ACN the 2D WAXS patterns were not recorded because fibers of this sample undergo remarkable viscous flow under stress, at least at the adopted stretching rate of ≈ 30 mm/min. The one-dimensional equatorial and azimuthal profiles, obtained from the 2D patterns by using the software Fit2D[110] as described in Figure 2.22 of the Chapter II, are reported in Figures A14 and A15. For all HNBR samples, the 2D WAXS patterns of the unstretched samples ($\varepsilon = 0$) show a halo at $2\theta_{MoK\alpha}$ = 8.8° (i.e., $2\theta_{CuK\alpha}$ = 19.2°) due to the amorphous rubber, the intensity of which is uniformly distributed along the whole azimuthal ring, indicating absence of preferred orientation of the chains (Fig. 3.27 and 3.28). Also in this case, the narrow Debye Scherrer rings apparent in the 2D patterns of the vulcanized rubbers are due to the crystalline components of the curative package and/or fillers. Regardless of crosslink density and ACN content, the stretching induces alignment of the amorphous chains along the stretching direction, as indicated by the polarization of the intensity of amorphous halo on the equator in the diffraction patterns of Figures 3.27 and 3.28. As the strain increases, the intensity polarization on the equator of the amorphous halo increases, while the 2θ position is invariant at any strain, as evident from the corresponding equatorial profiles reported in Figures A14 and A15. This indicates that the chain axes of the amorphous network strands gradually align themselves along the stretching direction as the strain increases while the intrachain correlation distances along the transverse direction remain almost constant

during elongation. Upon unloading the chain orientation progressively decreases, and the intensity of the amorphous halo comes back uniform along the azimuthal ring (Fig. 3.27, 3.28 and A14, A15).

The non-vulcanized sample HNBR36-NV with ACN content of 36 wt% shows very low degree of orientation of the amorphous chains and loss of orientation at high strains (Fig. 3.28A-E), probably due to the occurrence of viscous flow and disentanglements of the chains under stress, not allowing to record the 2D WAXS patterns during fiber retraction.

No crystalline reflections due to SIC are detected in the 2D WAXS patterns of the vulcanized samples stretched at different strains until reaching strains close to rupture (Fig. 3.27 and 3.28), as confirmed by the equatorial profiles of Figures A14 and A15 that show, besides the crystalline peaks due to the additives, only an amorphous halo at $2\theta_{MoK\alpha} = 8.8°$.

Therefore, in agreement with the previous literature,[124,125] the HNBR samples with 34 and 36 wt% of ACN do not crystallize by stretching at room temperature. For these ACN content, indeed, the tetramethylene segments are not long enough to crystallize because of the random incorporation of the ACN units that interrupt the regular tetramethylene sequences and prevent SIC.

The degree of orientation of the amorphous network chains for the vulcanized samples of the HNBR34 and HNBR36 samples stretched at different strains was estimated using the coefficient of the second order Legendre polynomial $P_2^{WAXS\text{-}am}$ of the function adopted to fit the azimuthal profiles of Figures A14 and A15 (equations 2.61, Chapter II, see also Fig. 2.23). The values of $P_2^{WAXS\text{-}am}$ of crosslinked samples HNBR34 and HNBR36, determined at different strains during the elongation of the specimens, are listed in Tables S4 and S5, respectively. Also in this case, the values of $P_2^{WAXS\text{-}am}$ are negative, due to the equatorial polarization of the amorphous halo at $2\theta_{MoK\alpha} = 8.8°$, arising from spatial correlations in the transverse direction to the stretching direction.

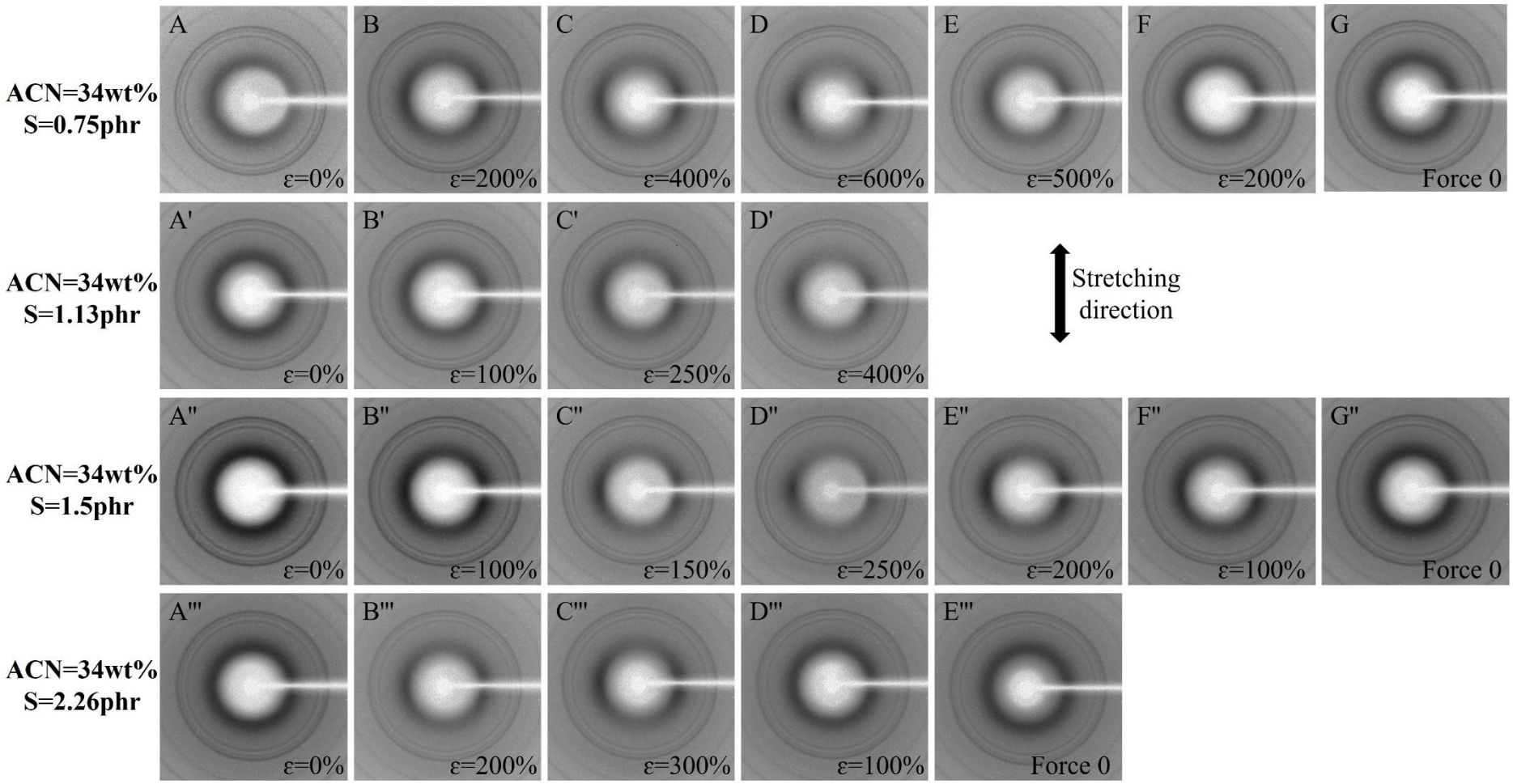

Figure 3.27. 2D WAXS patterns of vulcanized HNBR samples with 34 wt% ACN, 4 mol% iRDB, and different crosslink densities, recorded at room temperature at the indicated strains ε. Specimens that have not been subjected to any prior strain are gradually stretched until reaching a strain close to rupture, and then gradually unloaded until reaching zero stress (Force 0) The average loading rate is 30 mm min^{-1}.

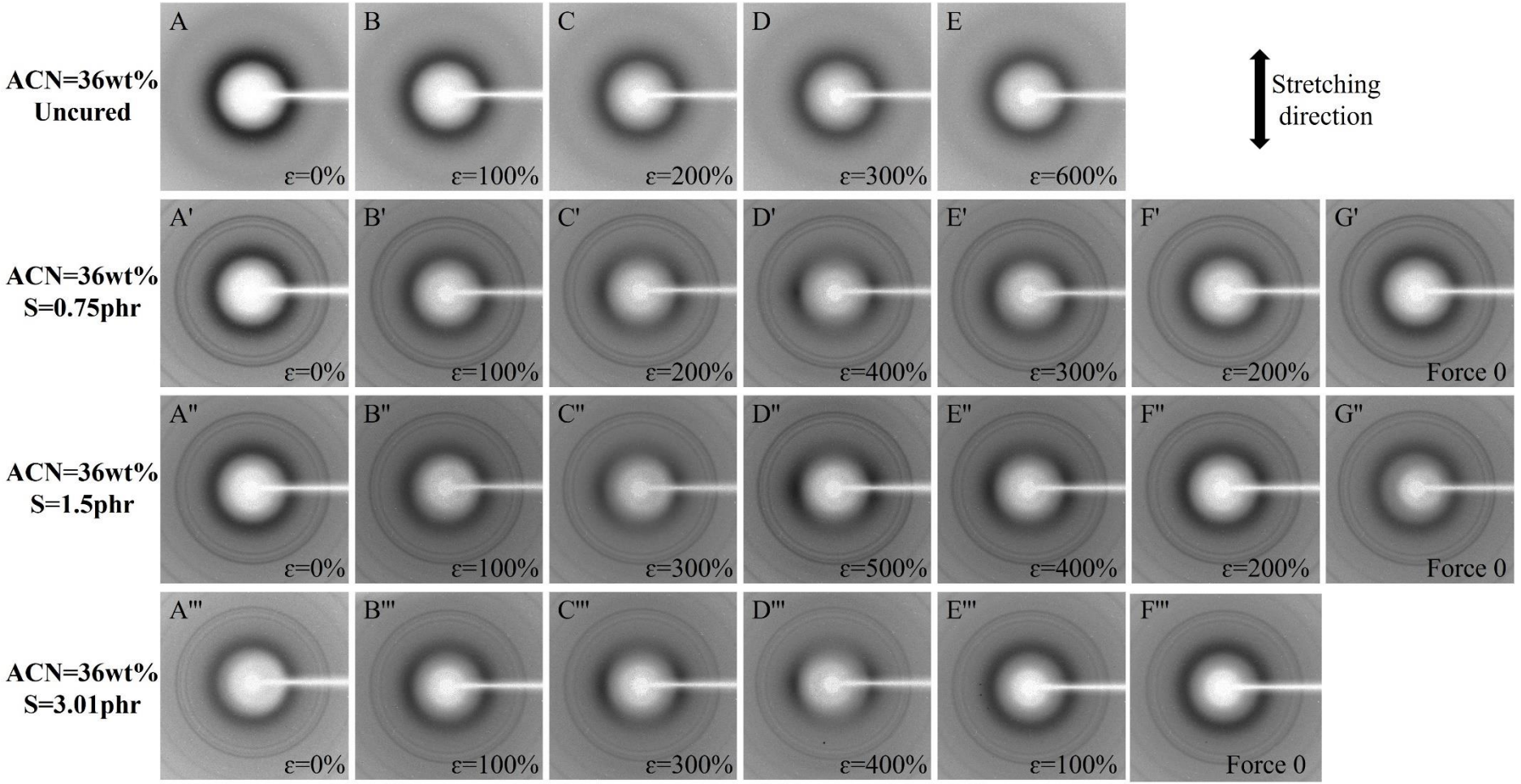

Figure 3.28. 2D WAXS patterns of vulcanized HNBRs with 36 wt% ACN, 2 mol% iRDB, and different crosslink densities, recorded at room temperature at the indicated strains ε. Specimens that have not been subjected to any prior strain are gradually stretched until reaching a strain close to breaking, and then gradually unloaded until reaching zero stress (Force 0) The average loading rate is 30 mm min^{-1}.

In the assumption of the classic model of rubber elasticity, which relates to a network of chains in which the stress is transmitted to the molecular chains only via the junction points that are considered to deform affinely[126], the values of $P_2^{\text{WAXS-am}}$ depends on the elongation ratio λ through the equation 3.10.[50] Accordingly, the values of $P_2^{\text{WAXS-am}}$ determined for vulcanized samples of HNBR34 and HNBR36 are hence reported as a function of the parameter ($\lambda^2 - 1/\lambda$) in Fig. 3.29A,B. The data in Figure 3.29A,B show that regardless of the ACN content for all the vulcanized HNBRs the order parameter $P_2^{\text{WAXS-am}}$ already at low strains assumes negative values that increase with increasing stretching deformation, indicating that the amorphous network chains promptly align in direction parallel to the stretching direction as soon as a specimen is elongated.

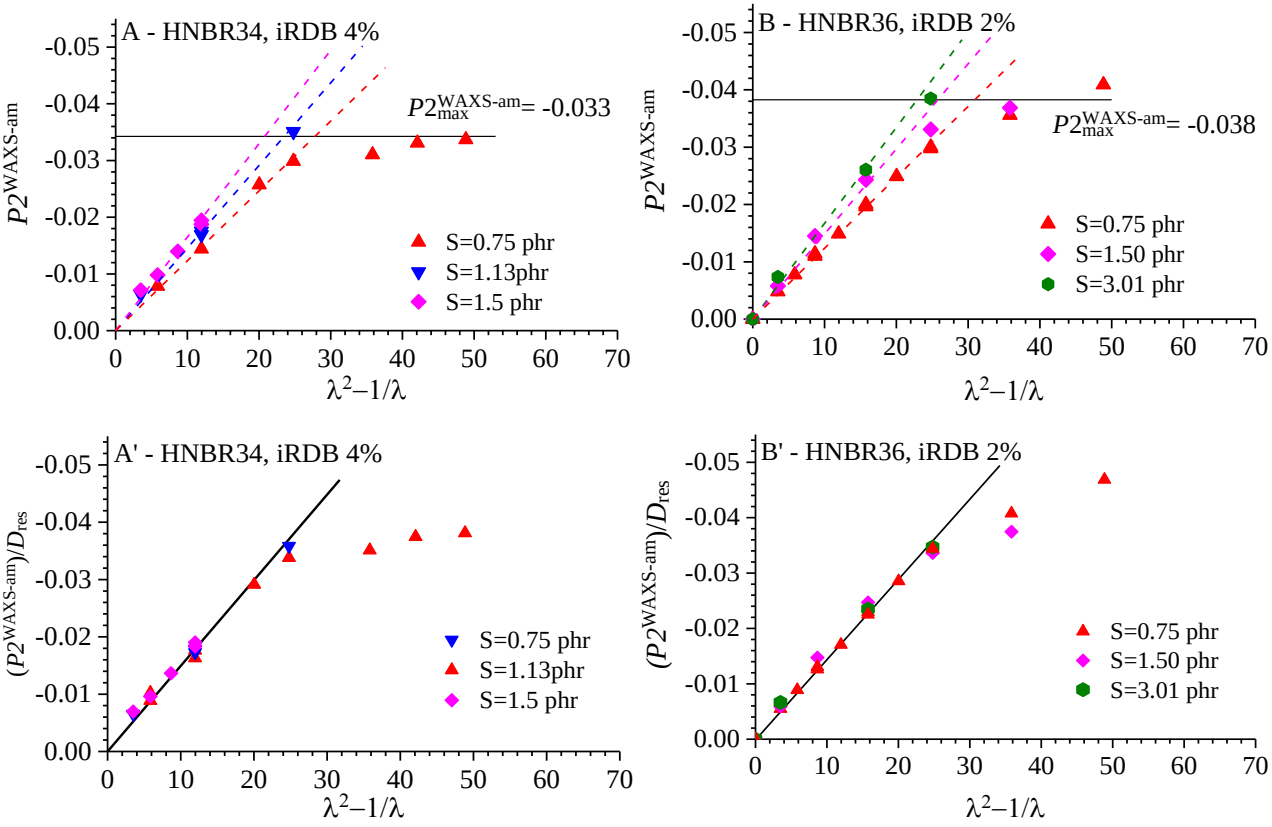

Figure 3.29 Values of the order parameter $P_2^{\text{WAXS-am}}$ (A, B) and of the $\frac{P_2^{WAXS-am}}{D_{res}}$ ratio (A', B') as a function of the elongation parameter (λ^2-1/λ), associated with the orientation of amorphous chains of HNBR34 (A, A') and HNBR36 (B, B') samples with 34 and 36 wt% of ACN, 4 and 2 mol% of iRDB, and different crosslink density, stretched at different deformations. The black lines in A', B' are the fit to data at low strain with a straight-line having slope $Q = \frac{K}{5N}\frac{1}{D_{res}}$. The content of added sulfur (S) is indicated in phr.

From the plot in Figure 3.24 it is observed that for the vulcanized HNBR43 and HNBR44 samples, which undergo SIC, the absolute values of the order parameter $P_2^{waxs\text{-}am}$ after a steep increase at low strains reach a quasi-plateau for values of $(\lambda^2\text{-}1/\lambda) \approx 9 - 16$, i.e., at strains $\varepsilon \approx 200\text{-}300$ %, corresponding to the onset of crystallization. This behavior has been attributed to the relaxation of the amorphous segments pinned to the crystals formed by SIC. For the crosslinked samples HNBR34 and HNBR36, with D_{res} greater than 0.98 kHz (added sulfur content greater than ≈1 phr), the values of $P_2^{WAXS\text{-}am}$ increase as the strain increases, until reaching strains close to rupture. For the less vulcanized samples, instead, the values of $P_2^{WAXS\text{-}am}$ linearly increase as the strain increases until to reach values of the parameter $(\lambda^2 - 1/\lambda)$ of 25 (i.e., $\varepsilon = 400$ %), then, at strain greater than this threshold, they reach a quasi-plateau. This behavior is similar to that observed for the HNBR43 and HNBR44 samples, subjected to SIC at high strains. Since the HNBR34 and HNBR36 samples do not show evidence for SIC behavior even at low crosslink densities (Fig. 3.27 and 3.28), the approach of a quasi-plateau at high strain cannot be due to relaxation of the amorphous segments associated to SIC. It could be instead explained by the presence of a non-negligible number of transient and/or loosely bound entanglements (defects) that are subjected to disentanglement at high strain through slippage motion, over a suitable timescale which is higher than that involved during WAXS measurements. Indeed, given that the WAXS measurements were not carried out continuously, but in steps consisting in a stretching step carried out at ≈ 30 mm min^{-1}, followed by a holding step of the specimens in tension for approximately 15 min, the less crosslinked samples, containing the highest concentration of defects (Fig. 3.4A), may easily experience disentangling of the non-elastically active chains (defects) and relaxation of the longest network strands. Therefore, the deviation from linearity of the order parameter of $P_2^{WAXS\text{-}am}$ as a function of $(\lambda^2 - 1/\lambda)$ predicted by theory (equation 3.10) can be explained by occurrence of relaxation phenomena and disentanglements. This is especially true for the samples with low crosslink density., a high fraction of defects (Fig. 3.4) and not subject to SIC such as HNBR34-0.75 and HNBR36-0.75. However, the occurrence of relaxation of defects/disentangling may also contribute, at least in part, to the levelling off in the values of the order

parameter $P_2^{\text{WAXS-am}}$ occurring at high stain, observed for the HNBR samples characterized by a low crosslink density and exhibiting SIC.

The data in Figure 3.29A, B also show that the order parameter $P_2^{\text{WAXS-am}}$, regardless of crosslink density, reaches similar values at high strains, corresponding to ≈ -0.033 and -0.037 for the HNBR34 and HNBR36 vulcanized samples, respectively. Similarly, for the HNBR43 and HNBR44 vulcanized samples, the values of the order parameter $P_2^{\text{WAXS-am}}$ reached at high strain, regardless of crosslink density, correspond to -0.032 and -0.029, respectively. This indicates that the maximum degree of alignment reached by the amorphous chains along the stretching direction is almost the same within each subset of HNBR samples and does not depend on the crosslink density.

The values of the $\frac{P_2^{WAXS-am}}{D_{res}}$ ratio relative to the HNBR34 and HNBR36 crosslinked samples are reported as a function of λ^2-1/λ in Figure 3.29A', B'. For strains below 400 % ((λ^2-1/λ)<20) the values of the reduced order parameter $\frac{P_2^{WAXS-am}}{D_{res}}$ may be fitted to a common straight line passing through the origin, with slope Q (= K/(5ND_{res}), equation 3.11) equal to -1.48 and -1.45 for the subsets of HNBR samples with 34 and 36 wt% ACN content, respectively (Table 3.5). As discussed before, deviations from the straight line occur at strains higher than 400 % ((λ^2-1/λ)>20) for the samples HNBR34-0.75 and HNBR36-0.75 characterized by low crosslink density, due to occurrence of relaxation of defects/disentangling processes. Applying the equations 3.12 and 3.13, the values of the constant K may be found (Table 3.5) as the slope of the straight line used to fit the values of the quantity $5NQ$ vs. D_{res}^{-1}, reported in Figure 3.30. Values of K equal to 0.032 and 0.039 are found for the subsets of the samples HNBR34 and HNBR36, respectively (Table 3.5). The values of K relative to the subsets of the samples HNBR43 and HNBR44, instead, are 0.044 and 0.041, respectively. Although the values of K are found using data relative to less than eight samples with different crosslink density for each subset of HNBR samples, and therefore they are affected by about 10-20% relative error, the differences in the K values estimated for the HNBR samples possibly reflect differences in the local structure of the amorphous phase, arising from differences in chemical

composition.[111] The *K* parameter, indeed, is related to form factor of the amorphous segments, and allows evaluating the second moment of the orientation distribution of chain segments in the direct space from the values of the orientation parameter P_2^X such as $P_2^{WAXS-am}$ extracted from X-ray scattering data.[112]

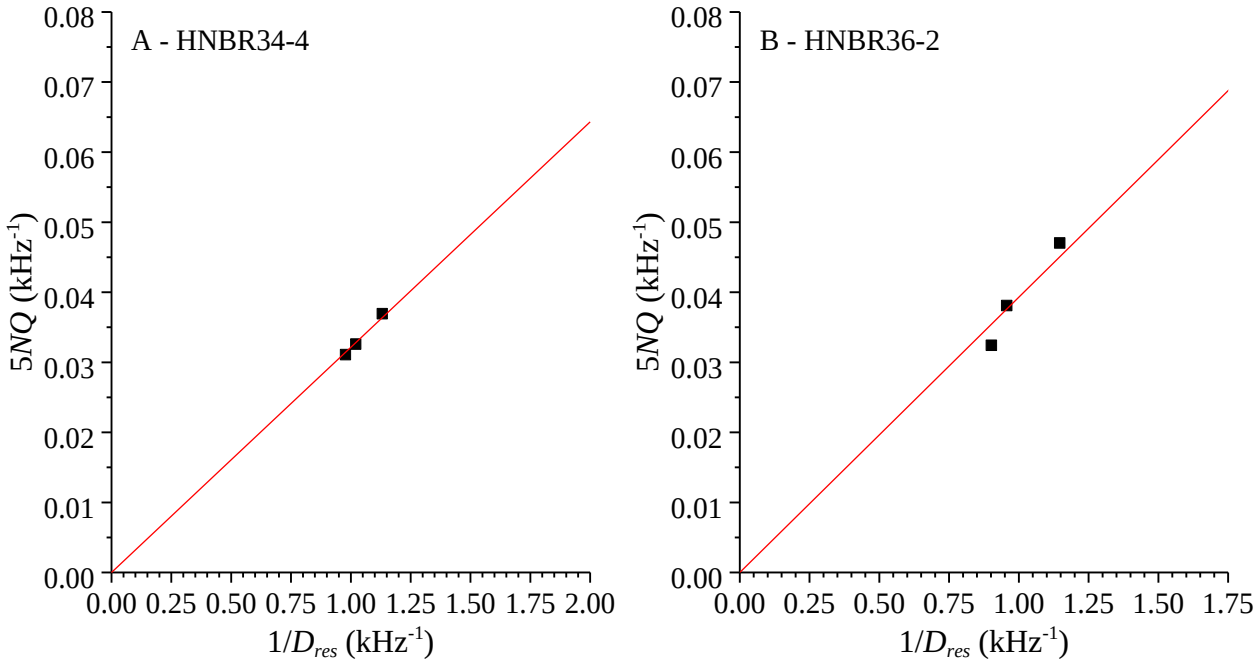

Figure 3.30 Values of the quantity 5*NQ* as a function of $1/D_{res}$ for the samples HNBR34 (A) and HNBR36 (B), with 4 and 2 mol% of iRDB. The slope of the straight line interpolating the data is the constant *K* of equation 3.10.

In-Situ WAXS analysis of HNBR samples stretched at different strain rate

The sample HNBR44-0.75 with 44 wt% of ACN, 9 % of iRDB and initial sulfur content equal to 0.75 phr was subjected to in situ WAXS analysis during mechanical test cycles of loading and unloading using the high flux of X-ray generated at ESRF synchrotron light facility in Grenoble. As described in Chapter II, specimens, which were not previously subjected to any deformation, were stretched from the undeformed state (ε = 0) to a maximum strain of 400 %, and then unloaded until achieving zero stress, in two consecutive hysteresis cycles, separated by a pause of 10 min. The loading rate (LR) used in these experiments were 60, 30, 20, and 2 mm min^{-1}. The simultaneous collection of WAXS data was carried out by recording a frame every 1, 2, 3, and 30 s, respectively. As an example,

selected 2D images collected at loading rate of 60 mm/min for various strain, in the second loading/unloading hysteresis cycle are reported in Figure 3.31.

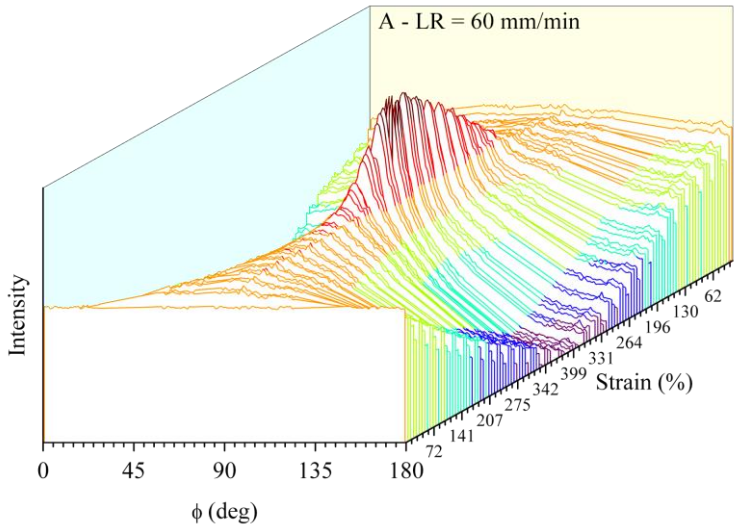

Figure 3.31 Evolution of the azimuthal profiles of the equatorial reflections centered at $q \approx 1.2$ and 1.8 $Å^{-1}$ during the second hysteresis cycle at loading rate (LR) of 60 mm min^{-1}. The intensity was integrated in q range comprised between 1.1 $Å^{-1}$ and 1.9 $Å^{-1}$.

One-dimensional azimuthal profiles relative to the second hysteresis cycles were extracted from the 2D patterns by using the software Bubble[114] as described in Figure 2.22 of the Chapter II. They are reported in Fig. A16.

Regardless of strain rate, the stretching induces alignment of the amorphous chains along the stretching direction, as indicated by the polarization of the intensity of the amorphous halo on the equator in the 1D equatorial azimuthal profiles of Figure A16. The intensity of the amorphous halo on the equator increases as the strain increases. This indicates that the chain axes of the network strands gradually align themselves along the stretching direction, as the strain increases. Upon release of the tension the chain orientation gradually decreases, and the intensity of the amorphous halo recovers a uniform distribution along the azimuthal ring (Fig. A16). These results are in agreement with data extracted from WAXS analysis carried out ex-situ, by stretching HNBR samples step-by-step.

In Figure 3.32A, the second hysteresis cycles of the sample HNBER43-0.75 recorded at different stretching rates are shown. It is apparent that, regardless of stretching rate, the stress-strain curves recorded during the loading step show, after a region of quasi-plateau, strain hardening at strains greater than 310 %. The maximum stress reached at the maximum strain decreases as the stretching rate decreases, from the values of about 3.5-3.8 MPa at SR = 30-60 mm min^{-1}, to about 1.75 MPa, at LR = 2 mm min^{-1}. The stress-strain curves recorded during stretching at LR of 60 and 30 mm/min are nearly coincident for strains lower than 300 %. However, at strain values exceeding 300 %, the sample stretched at loading rate of 30 mm min^{-1} exhibits values of strain slightly higher than those achieved at LR = 60 mm min^{-1}. These differences are small and are within the experimental error of the measurements. The stress-strain curves recorded during stretching at LR of 20 mm/min show values of stress at any strain lower than those achieved at higher SL during stretching. However, the stress-strain curves recorded during unloading at LR = 20, 30 and 60 mm min^{-1} are nearly coincident. Finally, the stress-strain curves recorded at LR = 2 mm min^{-1} show, at any strain, values of stress definitely lower than those recorded at higher LR.

From data analysis of the azimuthal profiles extracted from 2D WAXS patterns, the crystallinity index, and the degree of orientation of the amorphous and crystalline phases have been obtained (see Chapter II in Fig. 2.23). The values of crystallinity index attained during the mechanical test cycles of Figure 3.32A are shown in Figure 3.32B. Regardless of the adopted SR value, melting and crystallization present large hysteresis. For all strain rates, indeed, the strain at which crystallinity disappears (melting end) are remarkably lower than the strain marking SIC onset. This "overstraining" is common to several elastomers undergoing SIC, including natural rubber.[30,31,38,45–47] It entails that the crystallinity index achieved at any strain comprised in between the strain of end melting and ε_{max}, during unloading is systematically greater than that achieved in the loading step. Exceptions occur for the sample stretched at LR of 2 mm min^{-1}, which at strain comprised between 310 % and ε_{max} exhibits a crystallinity index during the unloading step lower than that achieved in the loading step. However, for strain s lower than 310 %, the hysteretic behavior of

melting/crystallization curves become similar to that of the other samples. It is worth noting that the maximum value of crystallinity index achieved by the here analyzed HNBR sample decreases as the stretching rate decreases. This rather surprising result may be due to the occurrence of strong relaxation phenomena of the amorphous segments that compete with the tendency of the oriented chain stretches to crystallize. The occurrence of relaxation phenomena at low stretching rate is also indicated in Figure 3.32A by the low stress values attained at any strain when operating at LR = 2 mm min^{-1}, compared with the stress level achieved at greater SR values. At SR values greater than a threshold, the fast crystallization of the amorphous segments contributes to prevents relaxation phenomena, creating additional crosslinks, and strong strain hardening at high strains.

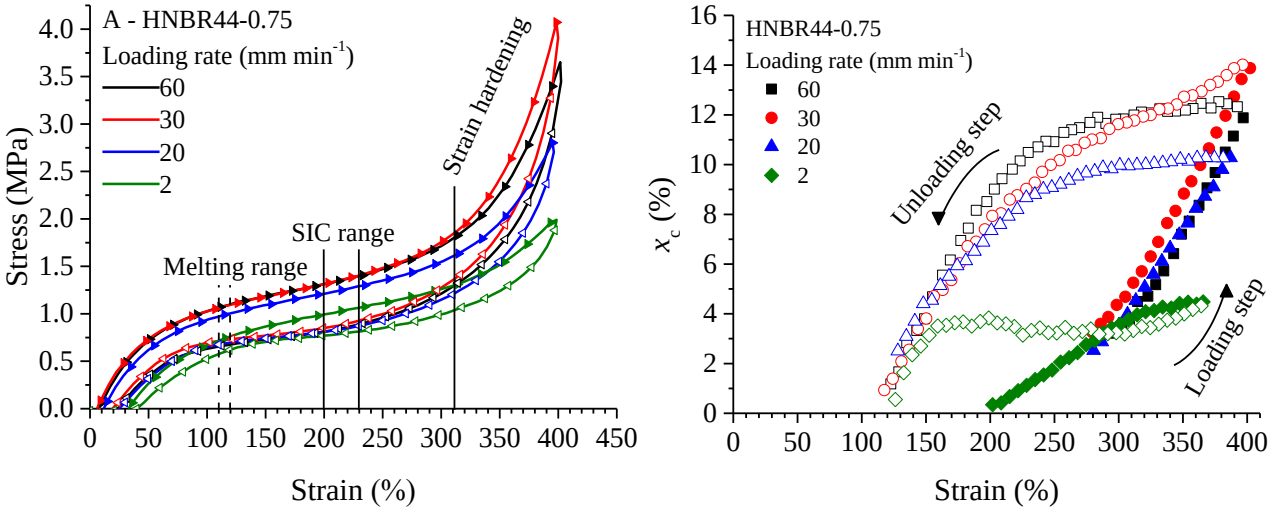

Figure 3.32 (A) Second hysteresis cycle recorded at the indicated stretching rates for the HNBR44-0.75 sample. Filled and empty symbols indicate the loading and unloading steps, respectively. The vertical bars mark the strains of incipient crystallization (solid lines), and of melting end (dashed lines). (B) Values of the crystallinity index as a function of strain. Filled and empty symbols indicate the loading and unloading steps, respectively.

The values of the crystallinity index measured during the loading and unloading steps of Figure 3.32B, are plotted separately, on an enlarged *x*-scale in Figures 3.33A and 3.33B. The data of Figure 3.33A highlight that for the samples drawn at LR = 20, 30 and 60 mm min^{-1}, the crystallinity index increases rather slowly at strains lower than that marking the strain hardening onset ≈ 310 %, and more rapidly for strains greater than 310 %. Roughly, the linear interpolation of the section of crystallization curves in the low strain range (for ε < 310%), relative to the samples drawn at LR =

20, 30 and 60 mm min^{-1}, gives a value of incremental crystallinity index with respect to the strain (SIC rate) $dx_c/d\varepsilon$ of ≈ 0.06, and an extrapolated value of the strain at SIC onset of ≈ 230 %. For the sample drawn at LR = 2 mm min^{-1}, instead, the crystallinity index increases rapidly at strain < 310 % and slows down at strains greater than 310 %. The linear interpolation of data for strain lower than 310 % gives a SIC rate of ≈ 0.03, and a strain at SIC onset of ≈ 200 %. Hence, although the sample stretched at LR = 2 mm min^{-1} reaches the lowest crystallinity levels at any strain, it starts crystallizing at lower strains than the samples stretched at higher rates.

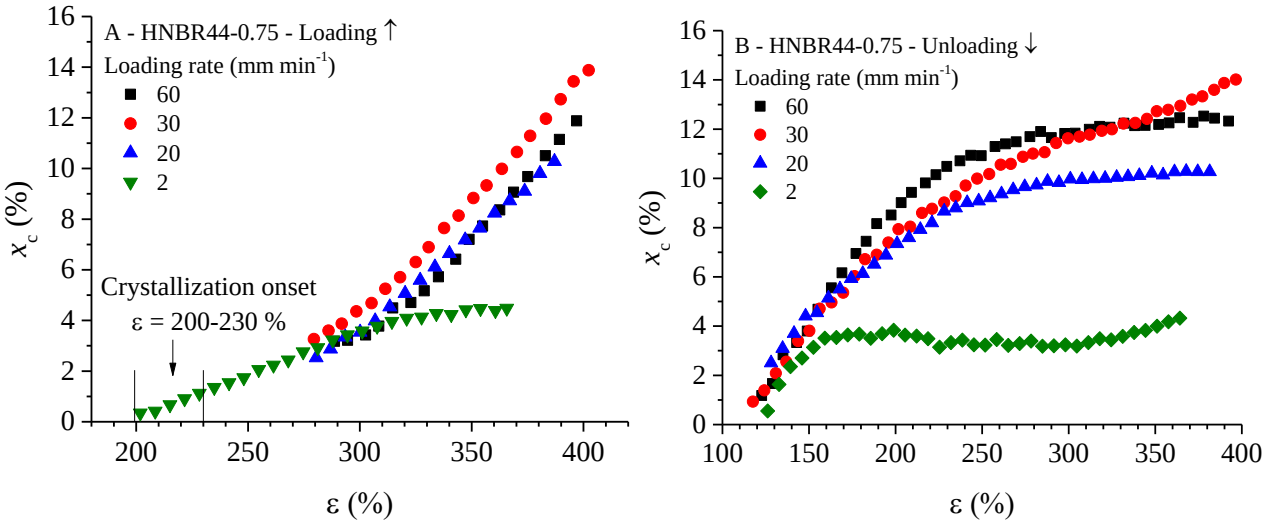

Figure 3.33 Values of the crystallinity index as a function of strain determined in the loading (A) and unloading steps (B).

As for the melting curves of Figure 3.33B, it is apparent that the during unloading, the crystallinity index remains almost constant until it reaches the strains of 200-250 %, and then decreases for strains lower than this value. For the sample unloaded at rate of 2 mm min^{-1}, the strain marking the change in melting rate corresponds to ≈ 150 %. The linear interpolation of the section the of the melting curves in the low strain range gives values of melting rate by effect of unloading of ≈ 0.08, and of the strain of melting end of ≈ 110 %, regardless of unloading rate.

The results of the present analysis suggest that, during stretching, the values of strain marking the SIC onset and those of crystallization rate are not greatly dependent on the stretching rate for LR values greater than a threshold, and only at low stretching rates the strain at SIC onset shifts toward

lower values. Simultaneously also the SIC rate decreases. During the successive release of the tension, the crystallinity degree remains almost constant up to 150-200 % strain, regardless of the unlading rate. Then, the crystals start to melt at a rate greater than the SIC rate and, regardless of the unloading rate, approach complete melting at the same strain.

The values of the order parameters $P_2^{WAXS\text{-}am}$ and $P_2^{WAXS\text{-}cr}$, determined from the azimuthal profiles by eq. 2.59-2.60 (see Chapter II) are reported as a function of the elongation parameter (λ^2-1/λ) in Figures 3.34 and 3.35, respectively. Data are reported only for values of the elongation parameter (λ^2-1/λ) comprised in between 0 and 14 ($\varepsilon < \approx 300$ %), that is for strains only slightly greater than that marking the SIC onset. At higher strains, indeed, the amorphous contribution of the azimuthal profiles cannot be approximated by a linear combination of even order Legendre polynomials truncated to the 4th order, as higher order Legendre polynomials would be needed (see Chapter II).[111,112] It is apparent that the values of the order parameter associated to the amorphous segments gradually increase (in absolute value) during the loading step and decrease during the unloading step (Fig. 3.34). This increase (decrease) is rather steep for values of the elongation parameter (λ^2-1/λ) lower than 4 and becomes smoother at higher deformations. The fit to data with a straight line for values of the elongation parameter (λ^2-1/λ) < 4, give values of a slope that tend to decrease as the stretching rate decreases, both in the loading and unloading steps. In particular, the value of this slope for the data collected at loading rate of 60 and 30 mm min^{-1} is ≈ 0.05 and decreases to 0.04 and 0.03 for the data collected at SR = 20 and 2 mm min^{-1}, respectively. For the data collected at unloading rate of 60 and 30 mm min^{-1} the slope is ≈ 0.04 and decreases to ≈ 0.03 for the data collected at LR = 20 and 2 mm min^{-1}.

As for the crystalline phase is concerned, it reaches a high degree of orientation, with values of the order parameter $P_2^{WAXS\text{-}cr}$ close to ≈ -0.5, regardless of the deformation achieved during the loading and unloading steps of the hysteresis cycle, and the adopted stretching rate (Fig. 3.35).

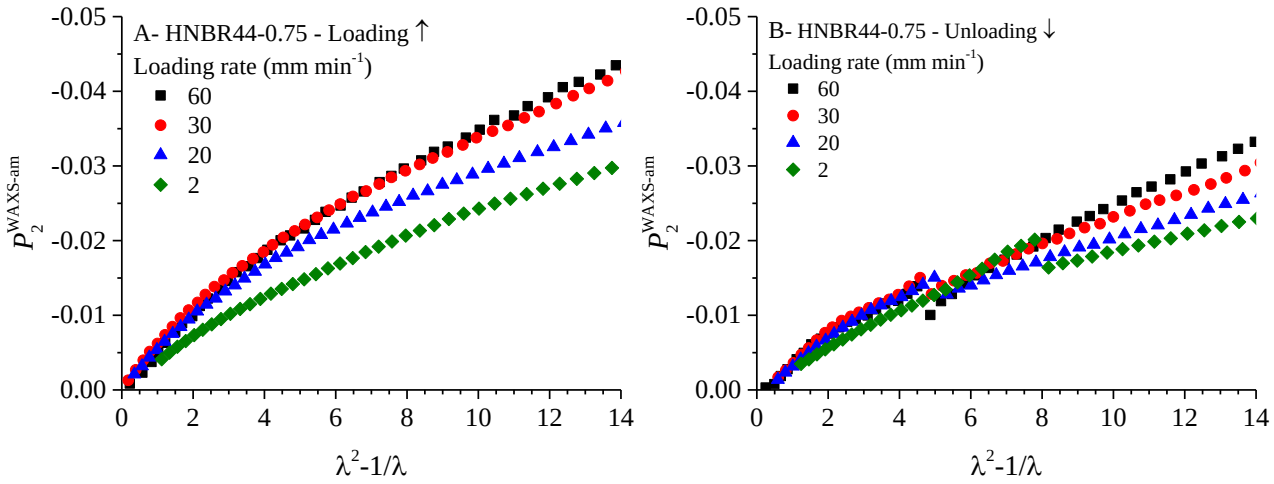

Figure 3.34 Values of the order parameters for the amorphous segments $P_2^{WAXS\text{-}am}$ as a function of the elongation parameter (λ^2-1/λ) of the HNBR44-0.75, during the loading (A) and loading (B) steps, recorded at the indicated strain rate.

This indicates that once the strain of incipient crystallization is reached the crystallites formed are highly oriented with the chain axes parallel to the stretching direction, and their degree of alignment does not increase significantly with further stretching. Furthermore, during release of the tension too, the crystals remain perfectly oriented until their fusion (Fig. 3.35B). A high orientation of the crystals occurs even operating at low loading rate, although the crystallinity level achieved in these conditions may be very low.

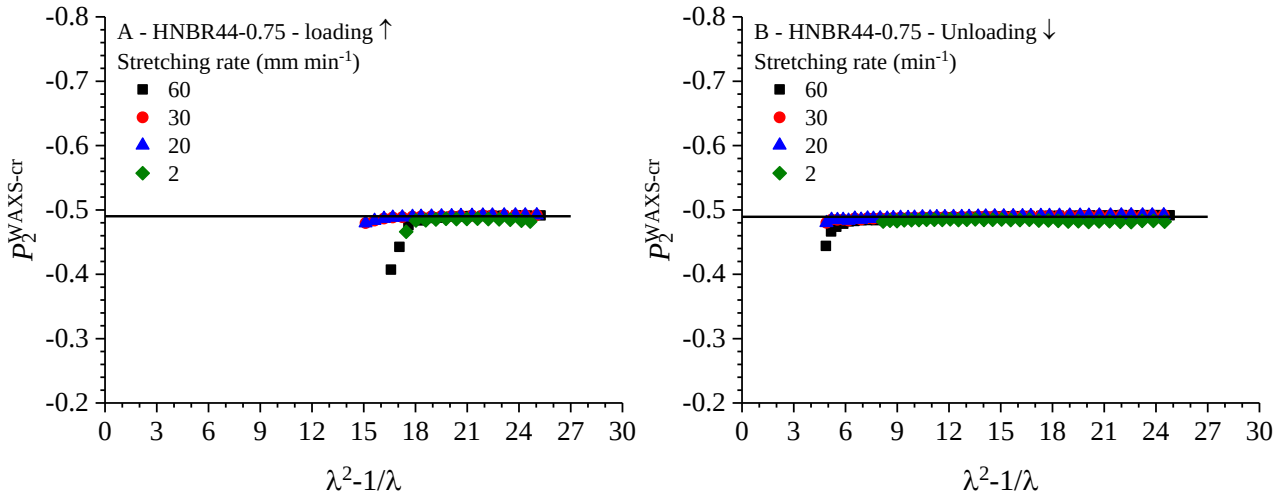

Fig. 3.35 Values of the order parameters for crystalline $P_2^{WAXS\text{-}cr}$ segments as a function of the elongation parameter (λ^2-1/λ) of the HNBR samples with 44 wt% of ACN and sulfur content of 0.75 phr, during the loading (A) and unloading (B) and different strain rate.

In summary, the above analysis indicates that:

i. the orientation degree achieved by the crystals during the loading and unloading step cycles is constant and very high (Fig. 3.35).
ii. The surrounding amorphous chains achieve a degree of orientation during the unloading step lower than that achieved during the loading step at any strain (Fig. 3.34).
iii. The crystallinity index achieved during the unloading step is greater than that achieved in the loading step at any strain (Fig. 3.32).

The above observations are somehow related to some kind of undercooling effect, that is the survival of a greater amount of crystals in the unloading step (point iii) is similar to the fact that crystallization temperature of a polymer is always lower than the melting temperature. The width of T_m-T_c generally decreases as the heating/cooling rates decrease. Similarly the gap between the crystallinity index achieved in the loading/unloading step cycles tends to decrease as the loading rate decreases. The degree of orientation of the crystals remains constant in the hysteresis cycle because crystals probably experience similar local tension in the loading and unloading step. Meanwhile, the surrounding amorphous chains achieve at any strain a lower degree of orientation than that reached in the loading step, due to a fast relaxation mechanism triggered by the gradual release of the tension. Once again, the gap in orientation degree of the amorphous phase in the loading/unloading steps tends to decrease as the loading rate decreases.

Chapter IV

Peroxide vulcanized HNBR samples

This chapter is focused on the characterization of chemical, physical and mechanical properties of a set of vulcanized HNBR samples with epoxide curative packages, and of the corresponding non-vulcanized counterparts. The set includes seven subsets. Each subset consists of two samples with identical content of ACN units and iRDBs, that is a non-vulcanized HNBR sample and a sample that was crosslinked with a peroxide-based curative package in presence of carbon black (CB) as reinforcing filler. Five subsets are characterized by samples with iRDB content < 0.9 mol% and ACN content of 21, 34, 39, 43 and 50 wt%, whereas two subsets by samples with iRDB content ≈ 5.5 mol% and ACN content of 34 and 43 wt%. The characteristics of these samples are indicated in Table 2.3.

4.1 Crosslink density Characterization

Swelling Tests and DQ-NMR characterization

The peroxide-vulcanize HNBR samples were subjected to equilibrium swelling tests in methyl ethyl ketone to measure the crosslink density as detailed in Chapter II. The values of ν_e calculated using the affine and phantom models of rubber elasticity (equations 3.2 and 3.3, respectively) are reported in Table 4.1 and in Figure 4.1A as a function of ACN content. It is apparent that the values of ν_e are not constant, despite the identical composition of the curative packages. In particular, the crosslink density is the highest for the samples with an ACN content of 34 wt% and decrease for ACN content greater and lower than 34 wt%. Furthermore, the samples with an iRDB content of 5.5 mol% exhibit higher values of crosslink density compared to the those with iRDB content ≤.0.9 mol%. The crosslink density was also determined by carrying out ^{1}H DQ-NMR measurements. We recall that the values of residual dipolar coupling constant D_{res} extracted from DQ-NMR data are proportional to ν_e. They are reported in Table 4.2 and in Fig. 4.1B as a function of ACN content. It is apparent that the values of D_{res} for the vulcanized samples are somehow greater than those of the corresponding

non-vulcanized counterparts. In all cases the D_{res} values are nearly constant for the samples with ACN contents ≥ 34 wt%, and only the samples with ACN content equal to 21 wt% show lower values. In contrast to the results of equilibrium swelling tests, the HNBR samples with iRDB = 5.5 mol% display values of D_{res} that are only slightly lower than those of the counterparts with iRDB ≤ 0.9 mol%.

Table 4.1 Values of crosslink density ν_e determined from equilibrium swelling measurement in methyl ethyl ketone using the affine and phantom models of rubber elasticity and of the average number of monomers/network strand N_N relative to HNBR samples vulcanized with a peroxide-based curative package.

Samples	ACN (wt%)	iRDB (mol%)	ν_e 10^5 (mol/cm^3)[a,b]	N_N	ν_e 10^5 (mol/cm^3)[a,b]	N_N
			Affine Model		Phantom Model	
HNBR21-0.9PC	21	0.9	30	33	47	21
HNBR34-0.9PC	34		40	25	62	16
HNBR39-0.9PC	39		37	28	57	18
HNBR43-0.9PC	43		24	38	43	24
HNBR50-0.9PC	50		22	47	35	29
HNBR34-5.5PC	34	5.5	53	19	80	13
HNBR43-5.5PC	43		33	31	52	20

[a] Obtained by swelling test

[b] Data are affected by 10% relative error

Table 4.2 Values of residual dipolar coupling constant D_{res}, fraction of defects, and overall relative distribution width of D_{res}, σ/D_{res}, determined from ^{1}H DQ-NMR experiments, relative to non-vulcanized HNBR samples, and vulcanized ones with a peroxide-based curative package.

Samples	ACN (wt%)	iRDB (mol%)	D_{res} (kHz)	Defect Fraction	σ/D_{res}
HNBR21-0.9NV	21	0.9	0.46	0.42	0.30
HNBR34-0.9NV	34		0.69	0.38	0.21
HNBR39-0.9NV	39		0.72	0.39	0.18
HNBR43-0.9NV	43		0.69	0.39	0.16
HNBR50-0.9NV	50		0.71	0.35	0.20
HNBR34-5.5NV	34	5.5	0.56	0.37	0.23
HNBR43-5.5NV	43		0.67	0.37	0.21
HNBR21-0.9PC	21	0.9	0.57	0.20	0.29
HNBR34-0.9PC	34		0.77	0.18	0.20
HNBR39-0.9PC	39		0.76	0.11	0.21
HNBR43-0.9PC	43		0.81	0.20	0.19
HNBR50-0.9PC	50		0.82	0.25	0.19
HNBR34-5.5PC	34	5.5	0.73	0.21	0.21
HNBR43-5.5PC	43		0.75	0.14	0.21

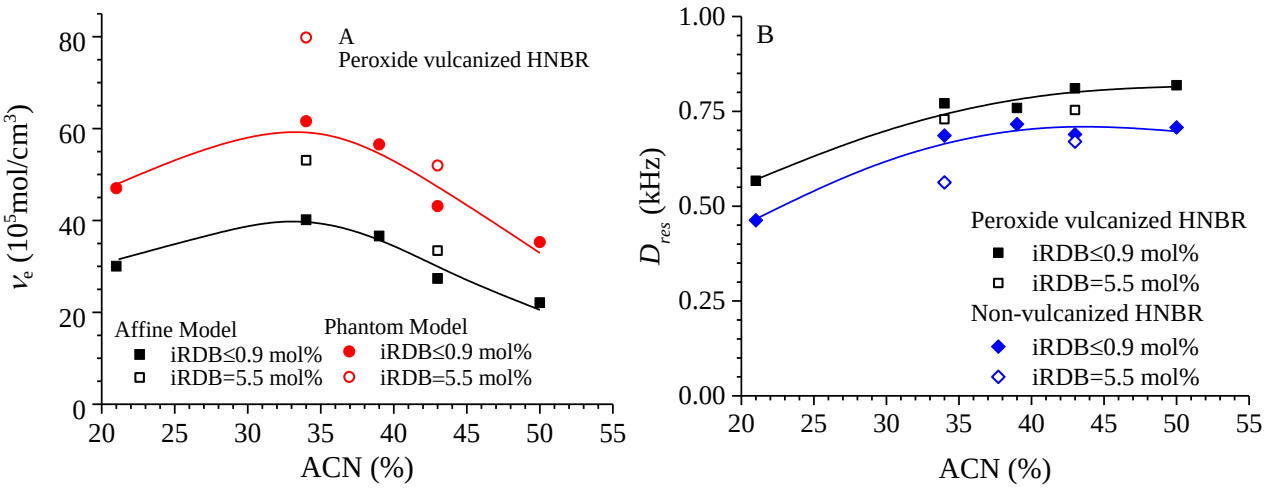

Figure 4.1 Values of crosslink density ν_e (A) and of the residual dipolar coupling constant D_{res} (B) as a function of ACN content, for peroxide vulcanized HNBR samples with iRDB content ≤ 0.9 mol% (full symbols) and equal to 5.5 mol% (empty symbols), In A, the ν_e values calculated by using the affine (black squares) and phantom (red dots) models are indicated. In B, the D_{res} values relative to the vulcanized (squares) and non-vulcanized samples (diamonds) are compared. The solid lines are guided for eyes.

The lognormal distribution functions of the $\widetilde{D}_{res}$ values obtained by fitting the normalized DQ signals (Fig. A19) of the HNBR samples with equation 2.27 (Chapter II) are shown in Figure 4.2. From these distributions, the values of the ratio between the standard deviation of the distribution and the values of D_{res} (σ/D_{res}, the overall relative distribution width) are extracted, and reported in Table 4.2 and Figure 4.3A as a function of ACN content. As discussed in Chapter III, since the values of the σ/D_{res} ratio are low (they are centered around 0.2) the non-vulcanized and peroxide vulcanized HNBR samples of Table 2.3 exhibit homogeneous crosslink density distribution.[49] It appears that the non-vulcanized samples and the peroxide vulcanized sample with 21 wt% of ACN have the lowest homogeneous distribution of crosslinking compared to the other samples, with σ/D_{res} values around 0.3.

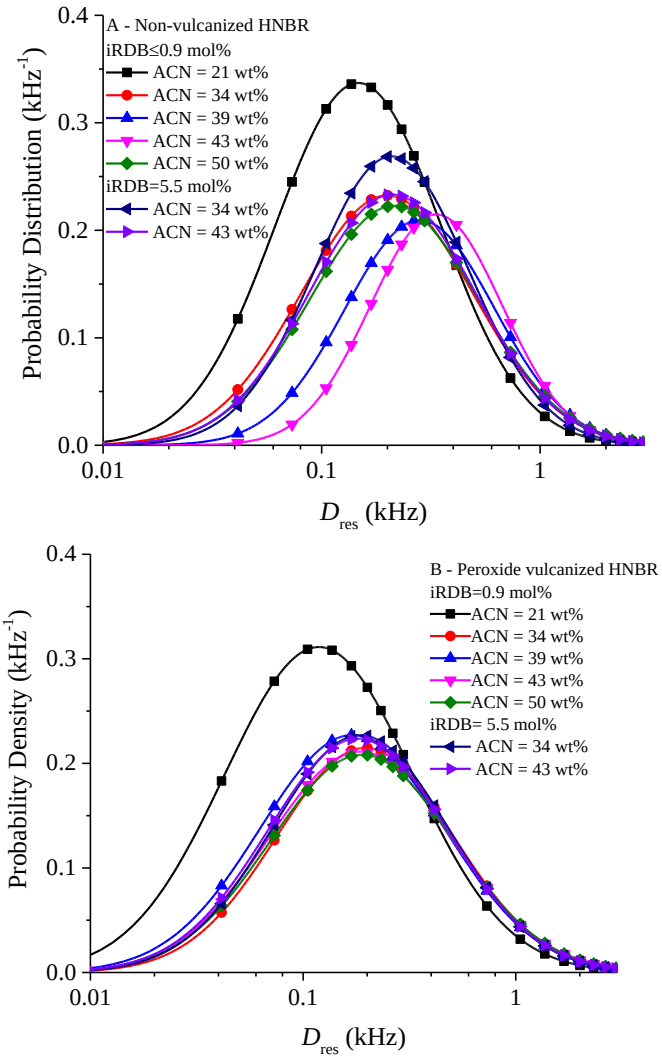

Figure 4.2 The lognormal distribution functions of the $\widetilde{D}_{res}$ values for non-vulcanized (A) and peroxide vulcanized (B) HNBR samples with the indicated values of ACN and iRDB contents.

The fraction of defects determined from the analysis of the ^{1}H DQ-NMR data are shown in Table 4.2 and reported in Figure 4.3B as a function of ACN content. It is apparent that the values of defect fraction extracted from NMR data are scarcely dependent on ACN and iRDB content. In particular, for non-vulcanized samples, the defect fraction tends to decrease only slightly, from 0.4 to 0.35, whereas for the corresponding peroxide vulcanized counterparts it oscillates between 0.1 and 0.2, and only the sample with 50 wt% of ACN show a slightly greater value (0.25). The presence of these defects may explain why the peroxide vulcanized sample with 50 wt% of ACN exhibits the lowest value of crosslink density ν_e measured through equilibrium swelling tests (Fig. 4.1A), suggesting that

these defects principally consist of temporary entanglements, able to disentangle during the prolonged solvent immersion.

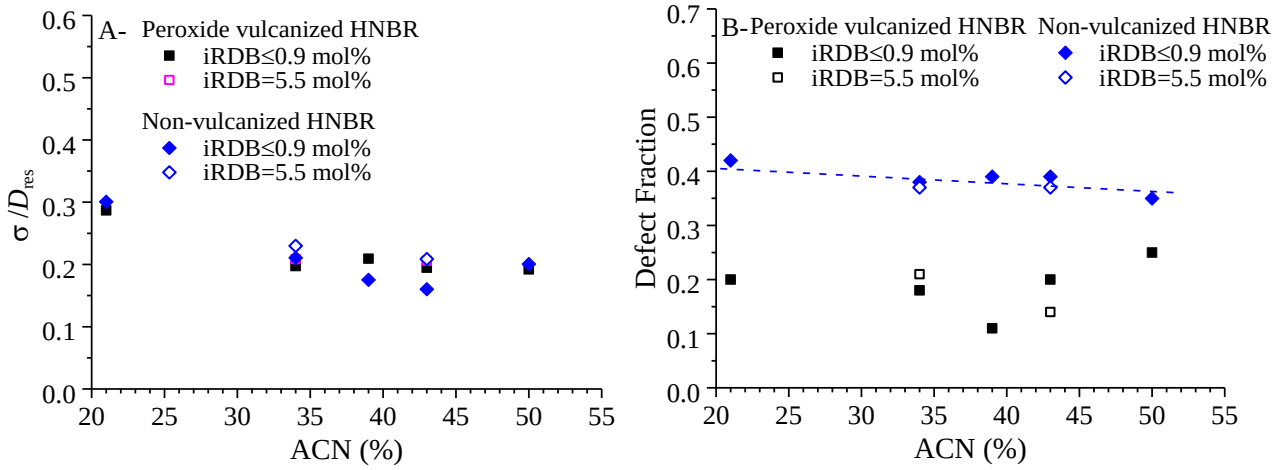

Figure 4.3 A) Values of the ratio between the standard deviation of $\widetilde{D}_{res}$ distribution σ and the average value of $\widetilde{D}_{res}$ (i.e. overall relative distribution width σ/D_{res}, with D_{res} the average value) (A) and of defect fraction (B) as a function of ACN content for peroxide vulcanized (squares) and the corresponding non-vulcanized (diamonds) HNBR samples. The filled and empty symbols are relative to the samples with iRDB = 0.9 and 5.5 mol%, respectively.

4.2 Thermal and structural analysis

The thermal properties of the HNBR samples were analyzed through DSC analysis as illustrated in Section 2.2.3 of Chapter II. The DSC traces recorded in the I and II heating scans are identical, so that only the DSC thermogram relative to the I scan are reported.

The DSC thermograms of peroxide vulcanized and the corresponding non-vulcanized samples are shown in Figure 4.4 and 4.5, respectively. The DSC thermograms of the vulcanized samples do not present any endothermic peak, but only an inflection point below *RT*, due to the glass transition (Fig. 4.4). This indicates that they are amorphous.

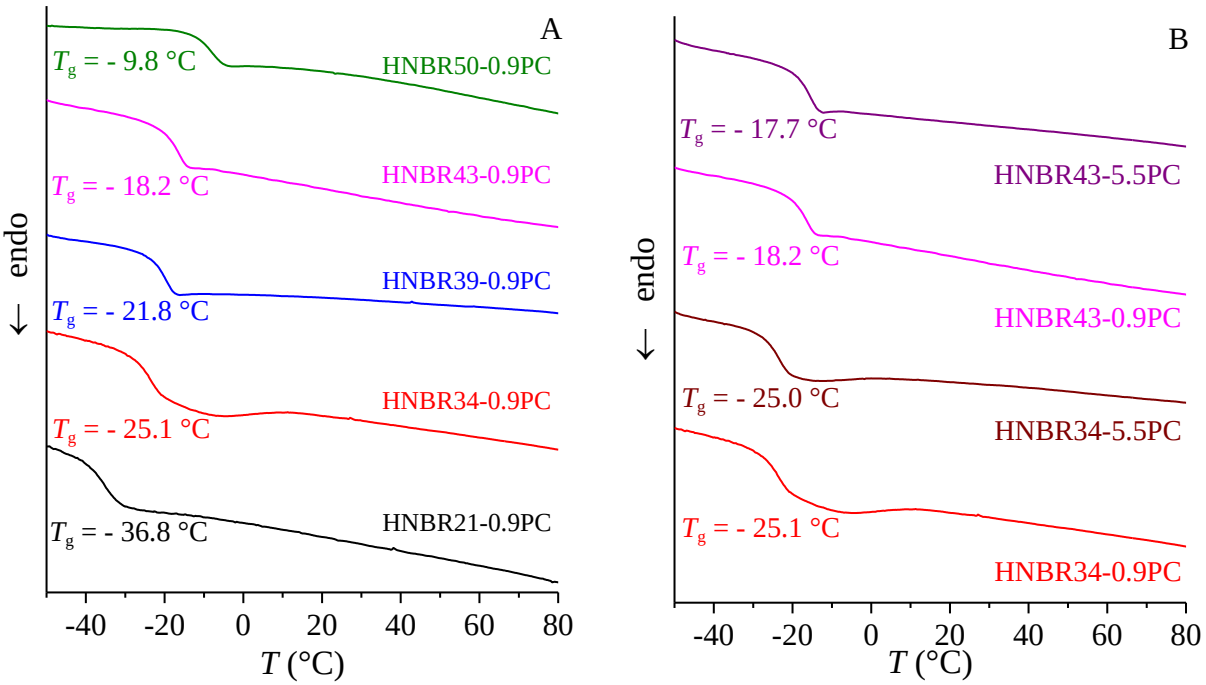

Figure 4.4 DSC thermograms of peroxide vulcanized HNBR samples with iRDB ≤ 0.9 mol%. Data relative to the HNBR samples with iRDB equal to 5.5 mol% are shown in B.

The corresponding non-vulcanized samples too are amorphous (Fig. 4.5), except for the samples HNBR43-0.9NV and HNBR50-0.9NV, with 43 and 50 wt% ACN content, respectively, and iRDB content ≤0.9 mol%, that show a broad endothermic peak at ≈ 42 °C. This endotherm is attributed to the melting of crystals formed by long alternating tetramethylene/ACN (TMAC) sequences. Figure 4.5B shows that the sample HNBR43-5.5NV with 43 wt% of ACN and 5.5 % of iRDB does not exhibit any melting endotherm, indicating that the presence of a major concentration of unsaturation inhibits the crystallization of TMAC sequences. It is worth noting that DSC thermograms of the vulcanized and non-vulcanized HNBR samples with ACN content of 34 wt% and iRDB content ≤ 0.9 mol% (Fig. 4.4 and 4.5) present, at temperature close to T_g, broad endotherms, originating from relaxation phenomena of amorphous segments (vide infra).

The values of T_g determined from the inflection point of the DSC thermograms of Fig. 4.4 and 4.5 are collected in Table 4.3 and reported in Figure 4.6 as a function of ACN content.

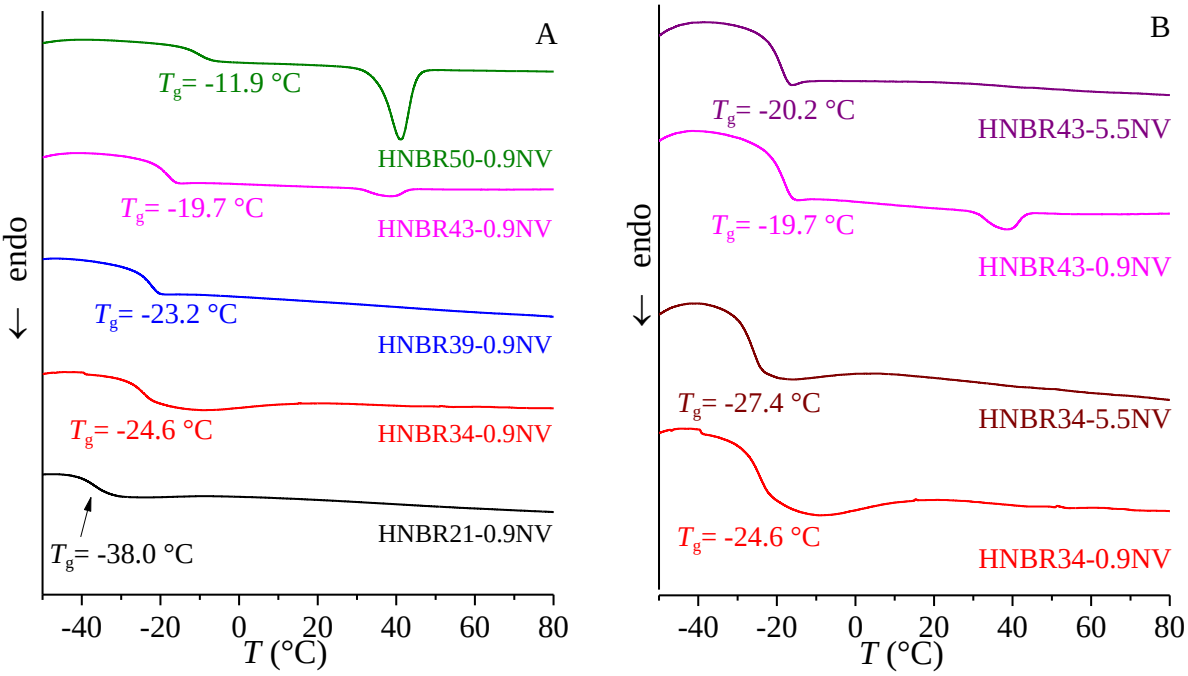

Figure 4.5 DSC thermograms of non-vulcanized HNBR samples with iRDB ≤ 0.9 mol%. Data relative to the HNBR samples with iRDB equal to 5.5 mol% are shown in B.

Figure 4.6 shows that the T_g values increase as the ACN content increases and that the T_g values of the non-vulcanized samples are only slightly lower than those of the vulcanized ones. Moreover, at the same ACN content, the T_g values of the HNBRs with 5.5 mol% iRDB are lower than those of the samples with iRDB content ≤ 0.9 mol%.

Table 4.3 Values of the glass transition temperature T_g relative to the non-vulcanized and corresponding peroxide vulcanized HNBR samples, with different ACN and iRDB content.

Vulcanized HNBR	iRDB (mol%)	T_g (°C)	Non-vulcanized HNBR	iRDB (mol%)	T_g (°C)
HNBR21-0.9PC	0.9	-36.8	HNBR21-0.9NV	0.9	-38.0
HNBR34-0.9PC		-25.1	HNBR34-0.9NV		-24.6
HNBR39-0.9PC		-21.8	HNBR39-0.9NV		-23.2
HNBR43-0.9PC		-18.2	HNBR43-0.9NV		-19.7
HNBR50-0.9PC		-9.8	HNBR50-0.9NV		-11.9
HNBR34-5.5PC	5.5	-25.0	HNBR34-5.5NV	5.5	-27.4
HNBR43-5.5PC		-17.7	HNBR43-5.5NV		-20.2

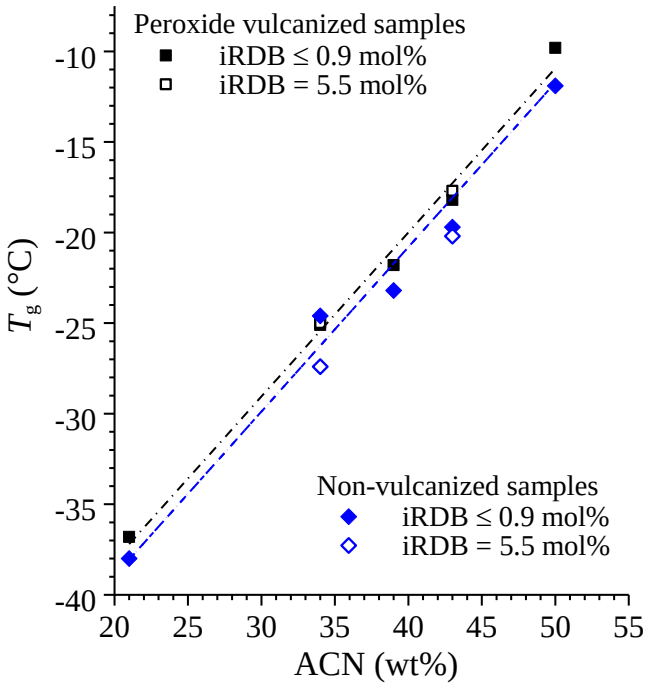

Figure 4.6 Values of the glass transition temperature T_g as a function of ACN content of the non-vulcanized (diamonds) and corresponding peroxide vulcanized (squares) HNBR samples with iRDB = 5.5 mol% (empty symbols) and iRDB ≤ 0.9 mol% (solid symbols).

The X-ray powder diffraction profiles of the peroxide vulcanized and non-vulcanized HNBR samples are shown in Figures 4.7 and 4.8, respectively. All samples exhibit the presence of an amorphous halo centered at a 2θ value of ~18.8°. The vulcanized samples are amorphous (Fig. 4.7). They also show narrow Bragg peaks overlaying the amorphous halo, due to the contribution from inorganic crystalline components of the curative package. In particular, the peaks at 2θ = 29.4 and 43.2° are assigned to MgO.

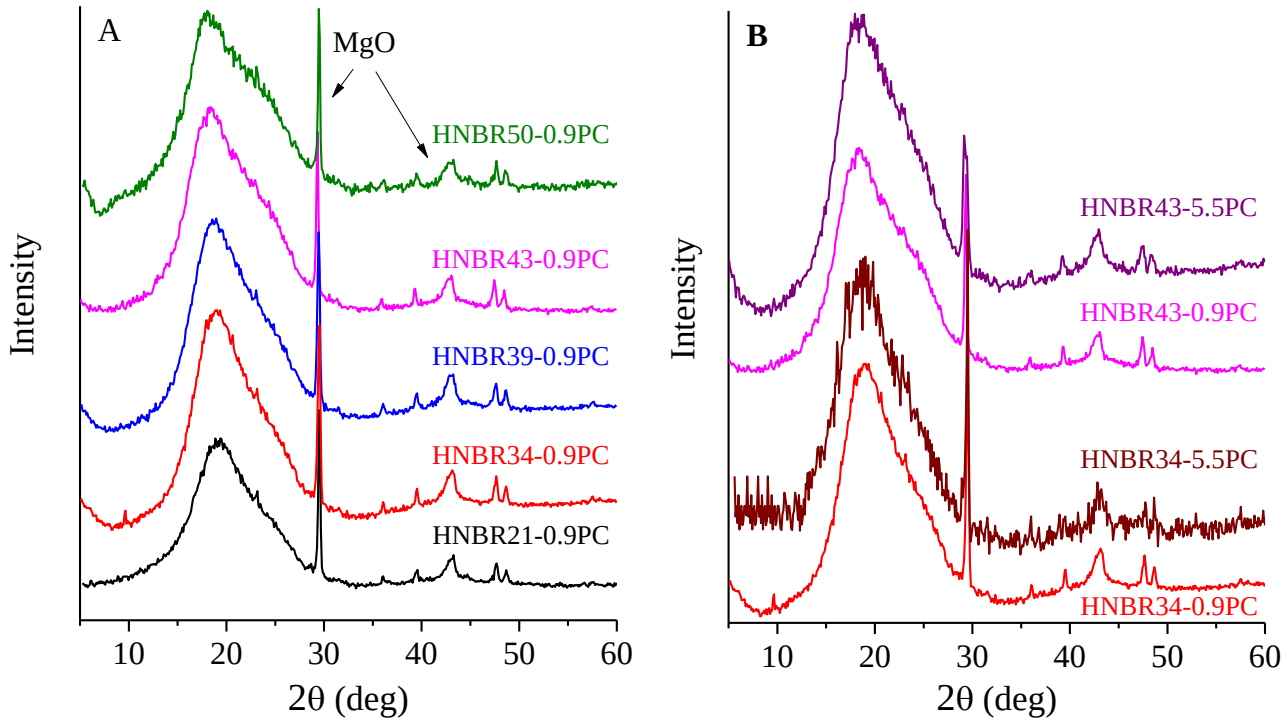

Figure 4.7 X-ray powder diffraction profiles of peroxide vulcanized HNBR samples with iRDB ≤ 0.9 mol%. Data relative to the HNBR samples with iRDB equal to 5.5 mol% are shown in B. Peaks at 2θ = 29.4 and 43.2° are due to MgO.

The non-vulcanized HNBR samples are amorphous too (Fig. 4.8). Exceptions occur for the samples HNBR43-0.9NV and HNBR50-0.9NV, with 43 and 50 wt% ACN content, respectively, and iRDB content ≤ 0.9 mol% that, in agreement with DSC results (Fig. 4.5), show Bragg peaks at 2θ ≈ 11.9, 17.8 and 25.2°, due to the crystallization of TMAC sequences.

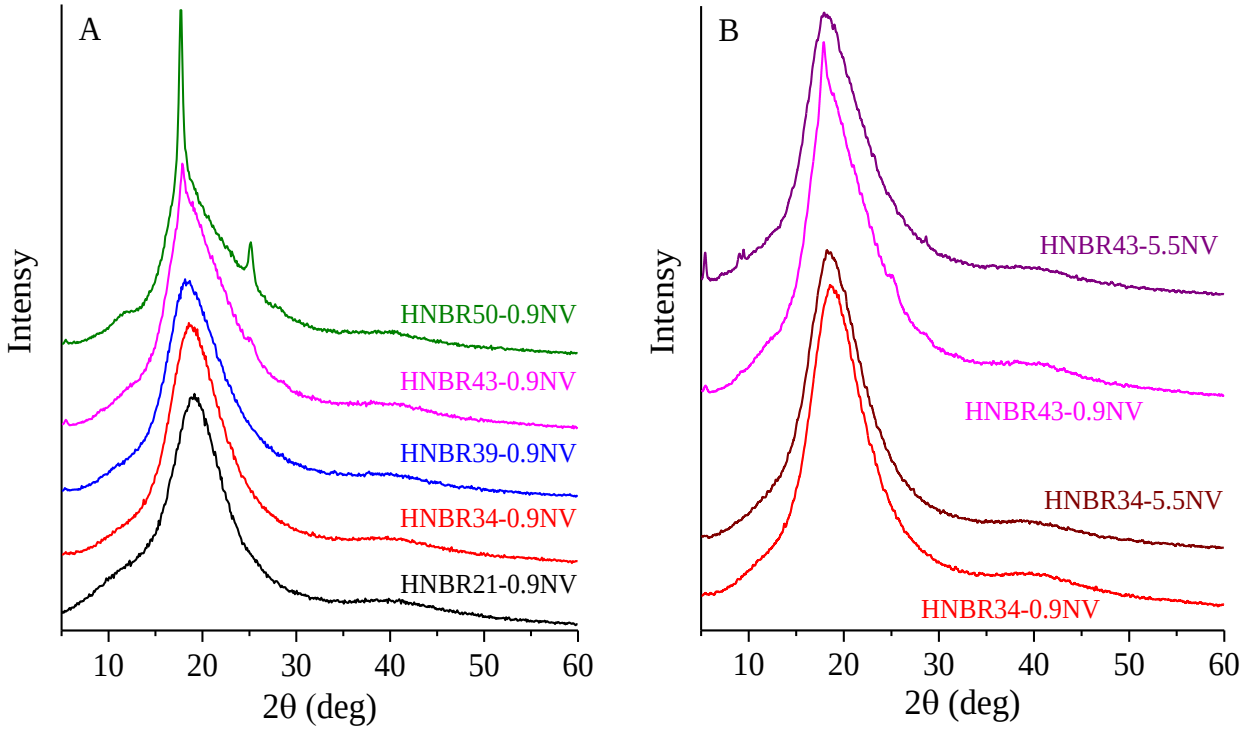

Figure 4.8 X-ray powder diffraction profile of non-vulcanized HNBR samples with iRDB ≤ 0.9 mol%. Data relative to the HNBR samples with iRDB equal to 5.5 mol% are shown in B.

The diffraction profiles relative to the sample HNBR43-5.5NV with 43wt% ACN content and iRDB content =5.5% do not show any Bragg peak, and only the typical amorphous halo of HNBR at 2θ ≈ 18.8° is present. This confirms that, at 43 wt% ACN content, the presence of a higher unsaturation concentration prevents the crystallization of the TMAC sequences. As a further remark, the DSC (Fig. 4.4 and 4.5) and WAXS data (Fig. 4.7 and 4.8) highlight that the non-vulcanized HNBR samples with 43 and 50 wt% of ACN and iRDB content ≤ 0.9 mol% which are initially crystalline, become amorphous after vulcanization. This indicates that the junction points created in the vulcanization process exert a disturbance effect on the crystallization ability of the TMAC sequences.

The values of crystallinity index relative to the samples HNBR43-0.9NV and HNBR50-0.9NV, determined with equation 2.57 (Chapter II), result equal to 5 and 13%, respectively. For the sample HNBR50-0.9NV, the level of crystallinity was also evaluated by performing solid state Magic Sandwich Echo (MSE)-NMR measurements (see Fig. 4.9), as described in the Chapter II. The

crystallinity index, calculated by equation 2.33, was of 10.6 %, in a good agreement with that evaluated from WAXS analysis.

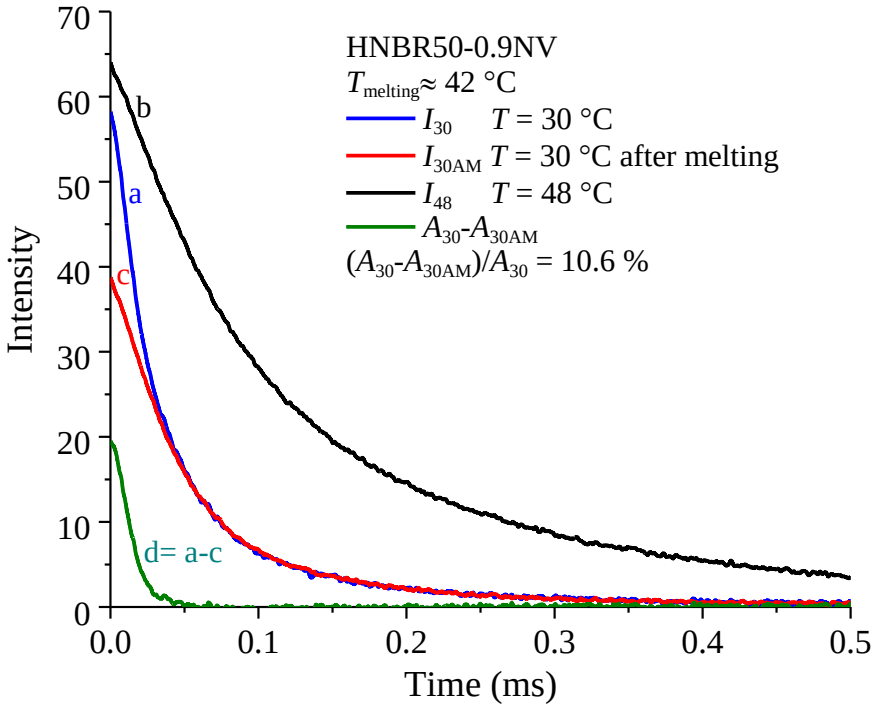

Figure 4.9 Magic Sandwich Echo free induction decay (MSE-FID) of the sample HNBR50-0.9NV, obtained by MSE-NMR experiments. The MSE-FID decay (a) is measured at 30 °C for the semicrystalline sample. The signal at time less than 0.1 ms contains information about the relaxation of protons located in the rigid (crystalline) fraction. The MSE-FID decay (b) is measured at 48 °C and corresponds to the spin-spin (T_2) relaxation curve of the sample in the molten state. The MSE-FID decay (c) is measured at 30 °C for the sample cooled from 48 °C. As the samples does not crystallize upon cooling from the melt to 30 °C even after long time (data not shown), curve b contains information about the amorphous phase. The green curve is the difference between the MSE-FID decays measured at 30 °C for the semicrystalline and amorphous sample. The MSE-FID decay d is obtained as the difference between the a and c curves. The ratio between the area of d and a curves corresponds to the crystallinity index of the sample HNBR50-0.9NV.

4.3 Mechanical properties

Tensile stress-strain curves

The stress-strain curves recorded at room temperature on dumbbell specimens of non-vulcanized and peroxide vulcanized HNBRs containing different amount of ACN and iRDB are shown in Figures 4.10 and 4.11. Measurements were performed on not previously deformed specimens. The average values of the tensile parameters, that is Young's modulus (E), stress, strain and tension set at break (σ_b, ε_b, t_b, respectively), are reported in Table 4.4 and 4.5 and in Figure 4.12 as a function of ACN content.

Regardless of the ACN content, the stress-strain curves of the non-vulcanized HNBRs are characterized by diffuse yield followed by strain-softening due to chains relaxation, then a cold-drawing plateau, and finally a strain-hardening region in which the stress rapidly increases as the strain increase until to rupture (Fig. 4.10). Only the non-crosslinked sample with 21 wt% ACN content does not show strain hardening, as, at strains higher than 1500%, it experiences viscous flow of the chains and does not break even at the maximum strain allowed by the adopted instrumental set-up. All non-vulcanized samples have good ductility, with values of strain at break greater than 900-1000 %. These values tend to decrease as the ACN content increases (Fig. 4.10 and 4.12C).

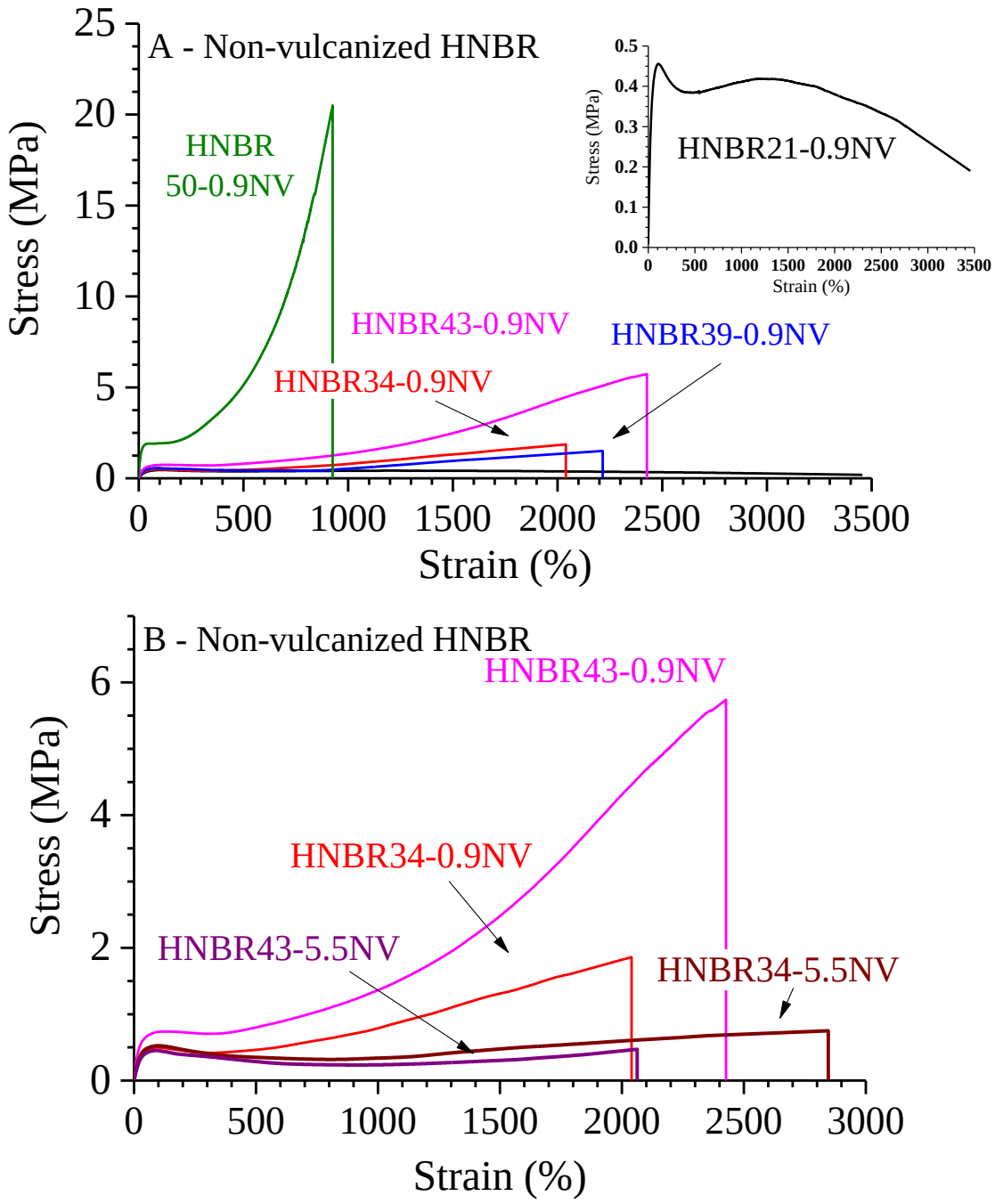

Figure 4.10 Stress-strain curves of non-vulcanized HNBR samples with different ACN content and iRDB content ≤ 0.9 and equal to 5.5 mol%.

The non-vulcanized semicrystalline samples with 43 and 50 wt% of ACN exhibit stress-strain curves with stress values at a given strain significantly higher than those of all the other samples. This is particularly evident for the sample HNBR50-0.9NV, that shows the highest crystallinity level. In Figure 4.10B, the stress-strain curves of the non-vulcanized HNBR samples with 34 and 43 wt%

ACN and iRDB content ≤ 0.9 mol%, are compared with those of the non-vulcanized samples containing the same ACN amount, but iRDB content of 5.5 mol%. It is apparent that the samples with greater unsaturation level (iRDB = 5.5 mol%) show markedly lower mechanical strength compared to samples with iRDB content ≤ 0.9 mol%. This is essentially due to the higher intrinsic flexibility of chains, owing to the low torsion barriers around the C-C simple bonds adjacent to C=C double bonds. For the samples with 43 wt% of ACN, the greater mechanical strength of the semicrystalline sample with iRDB content ≤ 0.9 mol% (HNBR43-0.9NV) may be also due to the reinforcing effect exerted by the crystals. In fact, since the corresponding sample with a higher level of unsaturation (HNBR43-5.5NV) is amorphous, the above reinforcing mechanism cannot come into play.

Table 4.4 Average values of Young's modulus (*E*), strain and stress at yield (ε_y, σ_y), and strain, stress and tension set at break (ε_b, σ_b, t_b) relative to the non-vulcanized HNBR samples.

Samples	ACN (wt%)	iRDB (%)	*E* (MPa)	ε_y (%)	σ_y (MPa)	ε_b (%)	σ_b (MPa)	t_b (%)[a]
HNBR21-0.9NV	21	≤0.9	0.81 ± 0.03	96 ± 4	0.45 ± 0.01	> 3000[b]	< 0.19[b]	640 ± 60
HNBR34-0.9NV	34	≤0.9	1.18 ± 0.08	98 ± 9	0.50 ± 0.02	2000 ± 300	1.9 ± 0.2	210 ± 40
HNBR39-0.9NV	39	≤0.9	1.3 ± 0.2	91 ± 6	0.56 ± 0.02	2200 ± 500	1.5 ± 0.2	190 ± 30
HNBR43-0.9NV	43	≤0.9	1.8 ± 0.5	99 ± 4	0.7 ± 0.1	2430 ± 80	5.7 ± 0.8	160 ± 20
HNBR50-0.9NV	50	≤0.9	15 ± 2	-	-	900 ± 80	20 ± 2	60 ± 10
HNBR34-5.5NV	34	5.5	0.9 ± 0.3	104 ± 3	0.52 ± 0.01	2800± 200	0.8 ± 0.2	450 ± 50
HNBR43-5.5NV	43	5.5	0.6 ± 0.2	90± 10	0.46 ± 0.03	2100 ± 200	0.5 ± 0.1	120 ± 30

[a] For HNBR21-0.9NV the value of tension set is relative to strain of 3000 %; [b] The sample shows viscous flow at high strains

Table 4.5 Average values of Young's modulus (*E*), strain and stress at yield (ε_y, σ_y), and strain, stress and tension set at break (ε_b, σ_b, t_b) relative to peroxide vulcanized HNBR samples.

Samples	**ACN (wt%)**	**iRDB (mol%)**	***E*** **(MPa)**	ε_b **(%)**	σ_b **(MPa)**	t_b **(%)**
HNBR21-0.9PC	21	≤0.9	3.7 ± 0.2	450 ± 30	22 ± 2	37 ± 5
HNBR34-0.9PC	34	≤0.9	5.5 ± 0.2	500 ± 50	34 ± 6	50 ± 10
HNBR39-0.9PC	39	≤0.9	5.6 ± 0.3	600 ± 40	44 ± 2	60 ± 6
HNBR43-0.9PC	43	≤0.9	4.9 ± 0.4	600 ± 70	42 ± 3	50 ± 10
HNBR50-0.9PC	50	≤0.9	4.1 ± 0.7	600 ± 30	40 ± 3	48 ± 6
HNBR34-5.5PC	34	5.5	5.3 ± 0.3	500 ± 50	34 ± 4	50 ± 10
HNBR43-5.5PC	43	5.5	5.2 ± 0.6	600 ± 20	40 ± 3	53 ± 6

The stress-strain curves of the peroxide vulcanized HNBR samples are shown in Figure 4.11. Due to the reinforcing effect of carbon black (CB), the samples exhibit similar stress-strain behavior, faint yield behavior at strain around 10 % due to the Payne effect[7] and strain hardening already starting at low strain. The ductility of peroxide vulcanized samples increases as the ACN content increases. The values of strain at break are comprised in between 450 and 650 % and are in all cases remarkably lower than those of the corresponding non-vulcanized samples. This is due to the fact that the lengths of the network strands in the peroxide vulcanized samples are shorter than the length of the portions of chain comprised between adjacent entanglements in the non-vulcanized counterparts. Furthermore, the peroxide vulcanized samples with the 34 and 43 wt% of ACN and iRDB content of 5.5 mol% show stress-strain curves similar to those of samples with identical ACN content but iRDB ≤ 0.9 mol% (Fig. 4.11B). The corresponding non-vulcanized samples (Fig. 4.10), instead, present large differences in the stress-strain behavior.

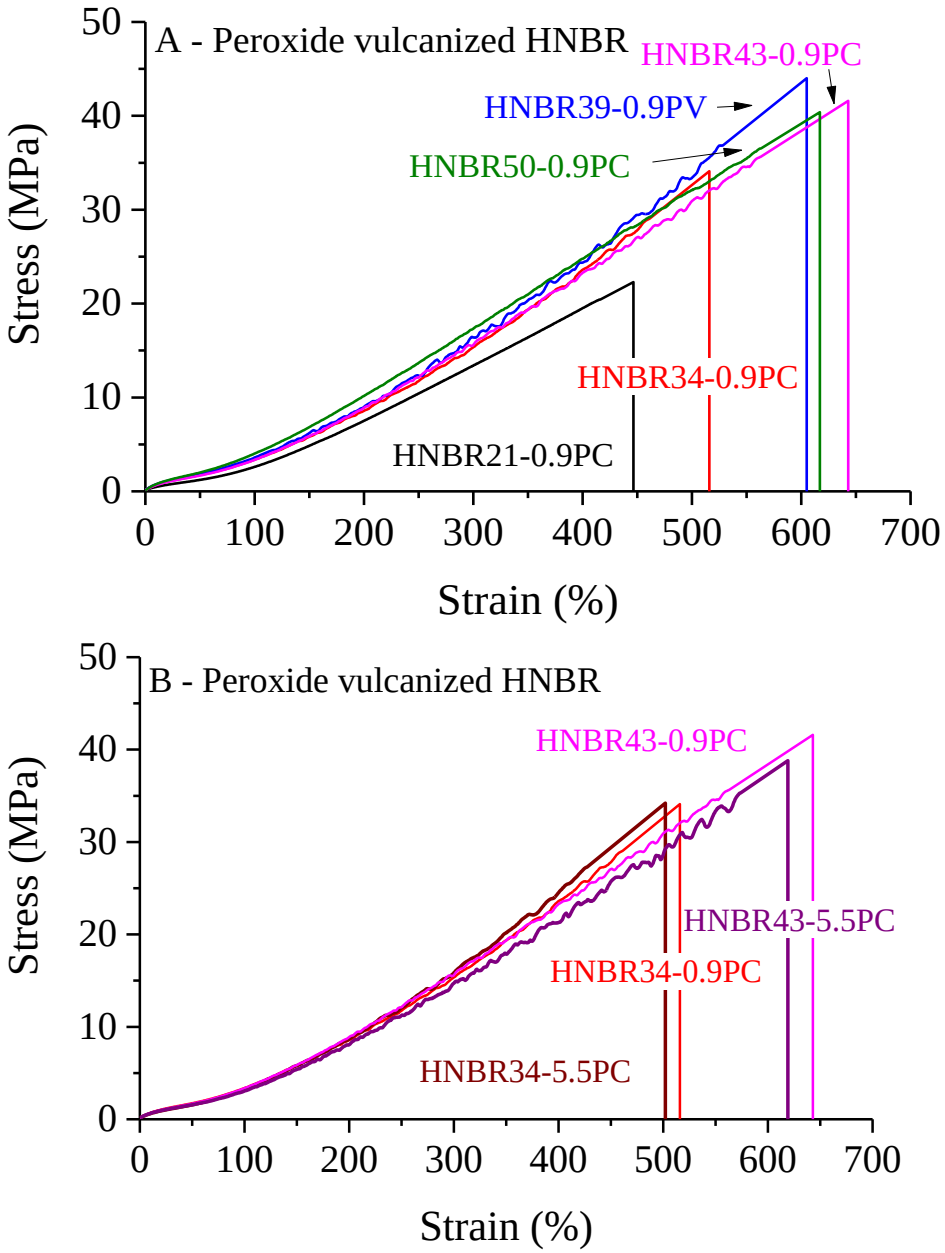

Figure 4.11 Stress-strain curves of peroxide vulcanized HNBR samples with different ACN content and iRDB content ≤ 0.9 and equal to 5.5 mol%.

Regardless of ACN and iRDB content all peroxide vulcanized HNBR samples show values of Young's modulus *E* (Fig. 4.12A) and stress at break σ_b (Fig. 4.12B) around 5 and 30 MPa, respectively. The sample with 21 wt% ACN exhibits a slightly lower modulus and stress at break, in agreement with the slightly lower crosslink density.

The non-vulcanized samples too exhibit nearly constant values of Young's modulus *E* (Fig.4. 12A) and stress at break σ_b (Fig. 4.12B), equal to ≈ 1 and 3 MPa, respectively. The values of *E* and σ_b

relative to the peroxide vulcanized samples are remarkably greater than those of non-vulcanized samples. This is due to the reinforcing effect exerted not only by the chemical crosslinks but also by the carbon black present in the peroxide vulcanized samples. Exceptions occur for the non-vulcanized semicrystalline sample with 50 wt% of ACN that shows a Young's modulus of ≈ 15 MPa, which, after vulcanization, becomes amorphous and less rigid too (Fig. 4.12A).

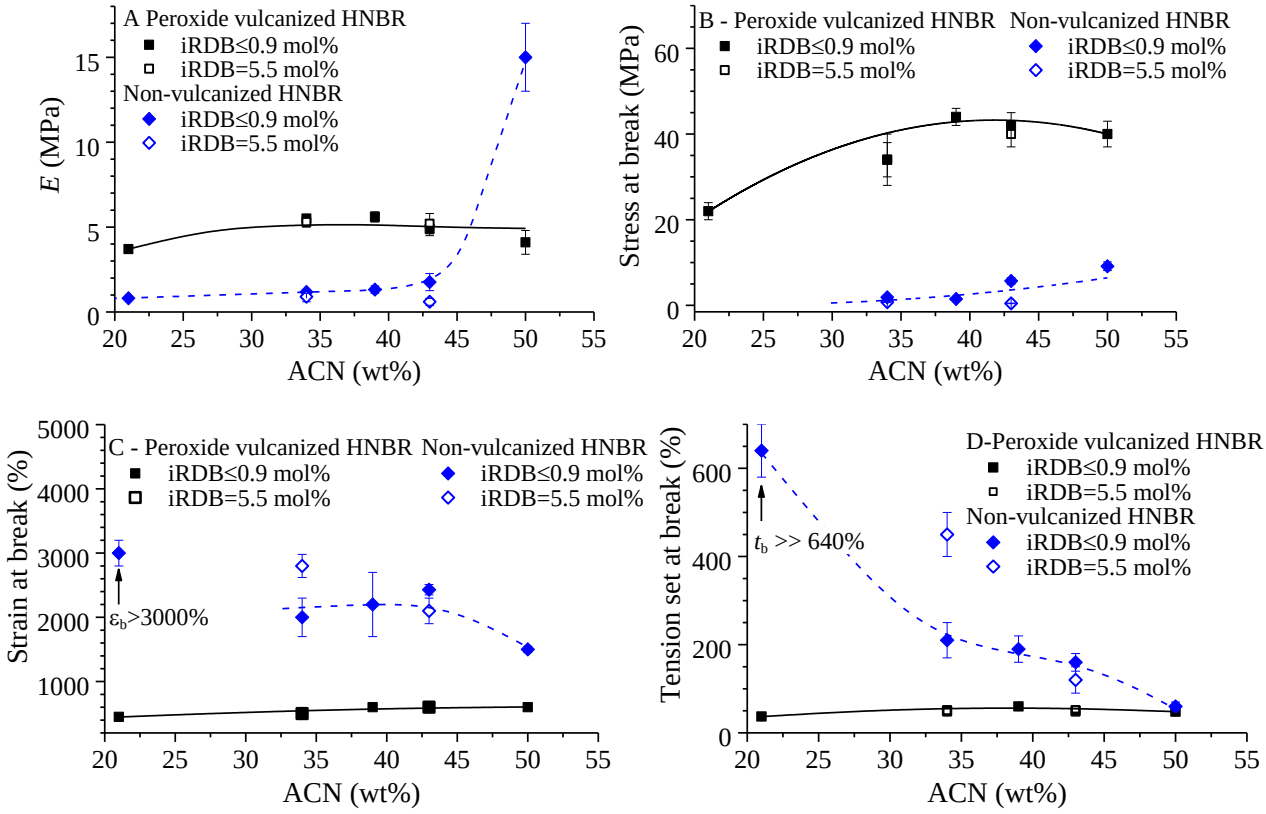

Figure 4.12 Values of Young's modulus *E* (A), stress σ_b (B), strain ε_b (C), and tension set t_b (D) at break as a function of ACN content of non-vulcanized (squares) and peroxide vulcanized (diamonds) HNBR samples with iRDB content ≤ 0.9 (full symbols) and equal to 5.5 mol% (empty symbols). The non-vulcanized sample with 21 wt% of ACN shows viscous flow at high strains.

The strain ε_b (Fig. 4.12C) and tension set t_b (Fig. 4.12D) at break relative to the peroxide vulcanized HNBR samples assume values that are almost constant, regardless of ACN and iRDB content, which are around 500 and 50 %, respectively. The low values of tension set at break indicates that the vulcanized HNBR samples recover a significant portion of the strain after the rupture, even in the pristine state, that is for specimens not subject to any strain prior the mechanical test. For the non-vulcanized HNBR samples, the values of strain ε_b (Fig. 4.12C) and tension set t_b (Fig. 4.12D) at break,

are rather insensitive to the chemical composition for ACN content comprised in between 34 and 45 wt%, then decrease for a further increase of the ACN content. In all cases, they are greater than those of peroxide vulcanized counterparts (Fig. 4.12C, D). For the non-vulcanized HNBR sample with 21 wt% of ACN, the values of the parameters ε_b and t_b could not be measured, as the sample experiences viscous flow at high strains, without breaking. Finally, it is worth noting that the tension set at break relative to the semi-crystalline HNBR sample with 50 wt% of ACN is similar to that of the crosslinked samples, probably because the crystals act as physical knots of the rubber network.

Hysteresis cycles

The hysteresis cycles of the non-vulcanized and peroxide vulcanized HNBRs with different ACN and iRDB content are shown in Figure 4.13. The corresponding values of tension set and percentage of dissipated energy (t_s and W_{diss}) measured after each hysteresis cycle are listed in Table 4.6 and 4.7. To compare the elasticity of the different rubbers, the values of tension set after each cycle were divided by the maximum strain achieved during the cycles (ε_{max}= 70 – 80 % the values of the strain at break), obtaining the percentage of residual strain after the release of the tensile force (percentages of permanent set). This parameter along with the percentages of dissipated energy are reported in Figure 4.14 as a function of ACN content. It has been observed that for all samples, the hysteresis cycles recorded after the first one are superimposable.

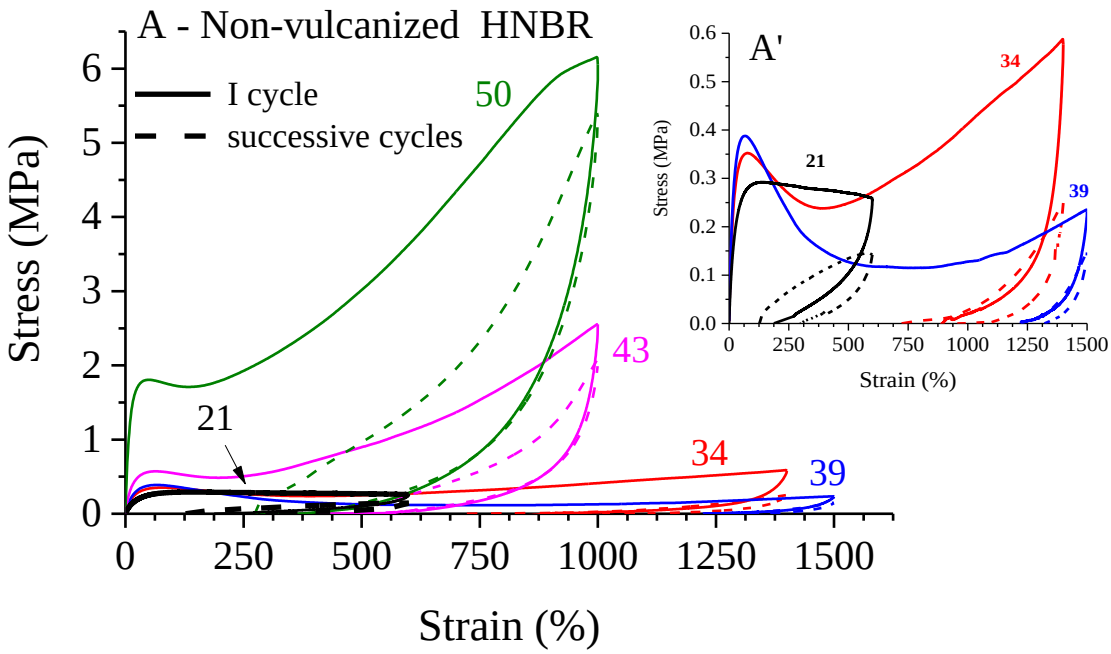
A - Non-vulcanized HNBR
I cycle
successive cycles
50
43
21
34
39
Stress (MPa)
Strain (%)
A'
34
21
39
Stress (MPa)
Strain (%)

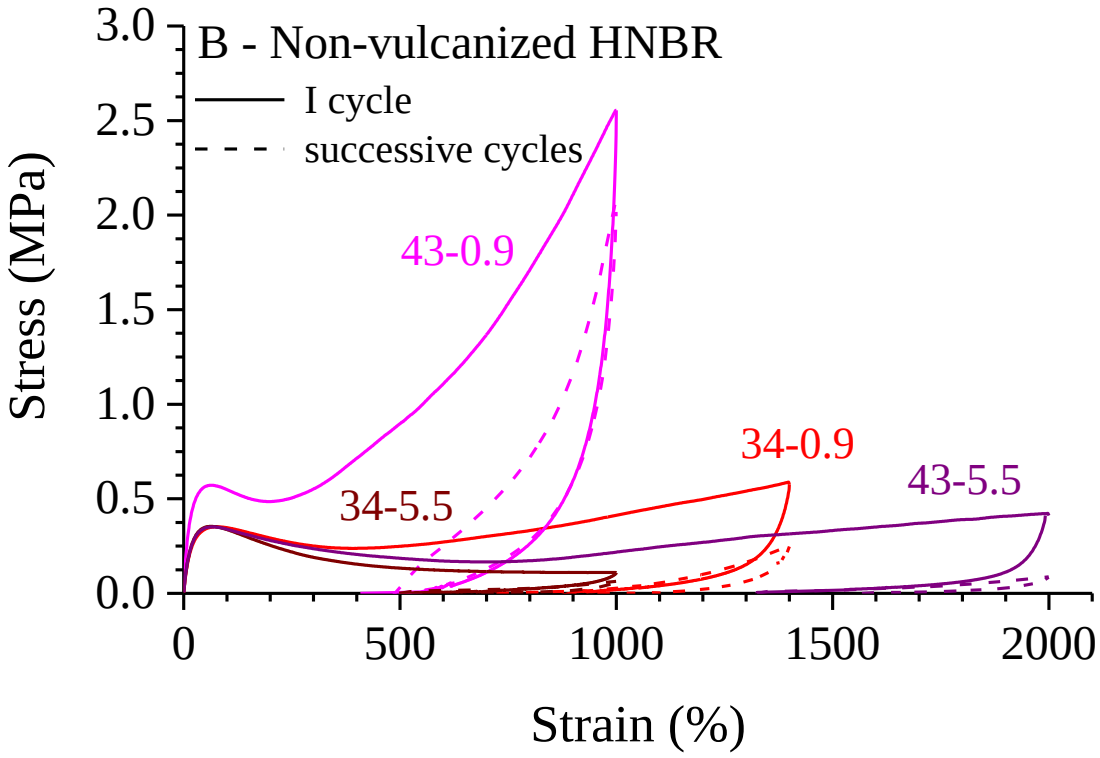
B - Non-vulcanized HNBR
I cycle
successive cycles
43-0.9
34-0.9
43-5.5
34-5.5
Stress (MPa)
Strain (%)

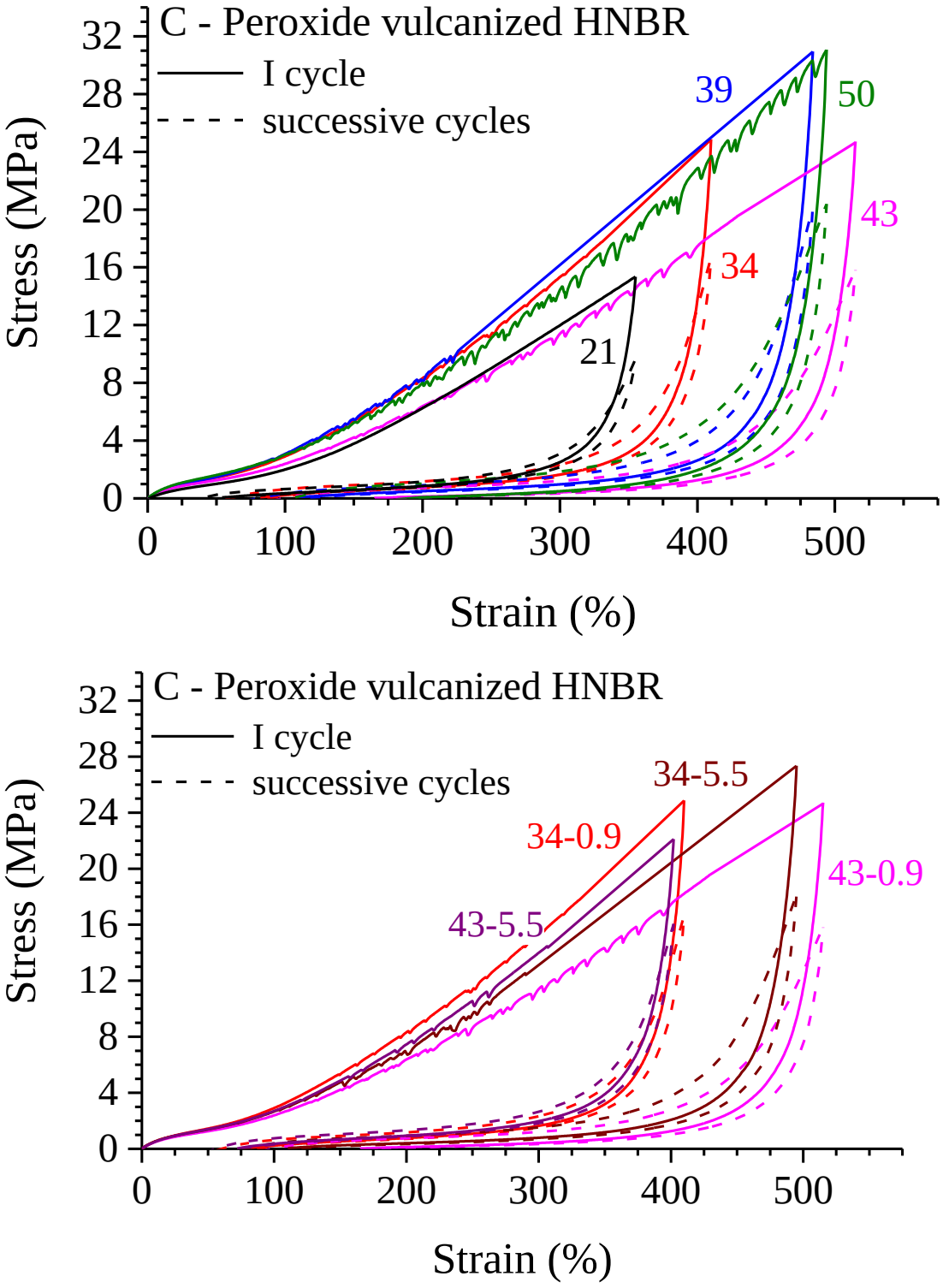

Figure 4.13 Hysteresis cycles relative to non-vulcanized (A,B) and peroxide vulcanized (C,D) HNBR samples with iRDB ≤ 0.9, and equal to 5.5 mol%. Curves are recorded during a first (solid line) and successive (dashed line) cycles at rate of 30 mm min^{-1}. The ACN content (wt%) is indicated in A, and C, for the samples with iRDB ≤ 0.9 mol%. The numbers close to each curve in B and D specify the ACN (wt%) and iRDB (mol%) contents. The inset A' is the same as in A for the non-vulcanized samples with ACN content of 21, 34 and 39 wt%, on an enlarged *y*-scale.

Table 4.6 Values of tension set (t_s) and percentage of dissipated energy (W_{diss}) measured in the hysteresis cycles of the non-vulcanized HNBR samples with different ACN content, and iRDB content ≤ 0.9 and = 5.5 mol%. The values of the maximum strain achieved in the cycles (ε_{max}) are also reported.

Samples	ε_{max} (%)	t_s^{I} (%)	$W_{diss.}^{I}$ (%)	t_s^{II-III} (%)	$W_{diss.}^{II-III}$ (%)
HNBR21-0.9NV	600	130±20	82±1	38±6	72±1
HNBR34-0.9NV	1350	820±70	90.1±0.5	15±4	62±2
HNBR39-0.9NV	1500	1230±20	94.8±0.4	4.2±0.9	50±2
HNBR43-0.9NV	1000	460 ± 60	84 ± 1	4.1± 0.8	52 ± 1
HNBR50-0.9NV	1000	270 ±50	80.1± 0.2	6±1	55±1
HNBR34-5.5NV	2000	1100±200	100±5	22±9	65±3
HNBR43-5.5NV	1000	500 ± 200	93 ±2	13±3	64 ± 2

Table 4.7 Values of tension set (t_s) and percentage of dissipated energy (W_{diss}) measured in the hysteresis cycles of the peroxide vulcanized HNBR samples with different ACN content, and iRDB content ≤ 0.9 and = 5.5 mol%. The values of the maximum strain achieved in the cycles (ε_{max}) are also reported.

Samples	ε_{max} (%)	t_s^{I} (%)	$W_{diss.}^{I}$ (%)	t_s^{II-III} (%)	$W_{diss.}^{II-III}$ (%)
HNBR21-0.9PC	355	40 ± 7	75 ± 2	2 ± 1	30 ± 2
HNBR34-0.9PC	410	60 ± 9	80 ± 1	1.5 ± 0.5	34 ± 3
HNBR39-0.9PC	484	80 ± 11	84 ± 2	2 ± 1	40 ± 3
HNBR43-0.9PC	515	100 ± 13	86.2 ± 0.4	4 ± 1	55 ± 3
HNBR50-0.9PC	494	100 ± 9	86.2 ± 0.2	4 ± 2	60 ± 2
HNBR34-5.5PC	402	60 ± 8	77.2 ± 0.7	1.0 ± 0.6	30 ± 3
HNBR43-5.5PC	495	78 ± 4	83.8 ± 0.7	2 ± 1	48 ± 3

The hysteresis cycles of the non-vulcanized HNBR with different ACN (Fig. 4.13A) and iRDB contents (Fig. 4.13B), show remarkable differences. However, after vulcanization these differences become much smaller (Fig. 4.13C and D). In particular, the non-vulcanized samples exhibit large hysteresis (Fig. 4.14B) and high values of the tension set (Fig. 4.14A) in the first cycle. The percentage of permanent set in the first cycle achieves values comprised in between 20 and 80 % (Fig. 4.14A), whereas the values of the percentage of dissipated energy are on order of 80-90 % (Fig. 4.14B). However, the values of stress at any strain (Fig. 4.13A,B) along with the values of the percentage of dissipated energy (Fig. 4.14D) and tension set (Fig. 4.14C) are subjected to a remarkable decrease in the hysteresis cycles recorded after the first one. In fact, the percentage of permanent set in the cycles successive to the first one achieves values on order of 1-6 % (Fig. 4.14C), whereas the values of percentage of dissipated energy are on order of 50-70 % (Fig. 4.14D). Therefore, the mechanical behavior of the non-vulcanized HNBR samples during the hysteresis cycles evidences that they exhibit good elastomeric properties only after the first one. This is because, during the first hysteresis cycle, in the absence of chemical crosslinks, irreversible phenomena such as disentangling, chain sliding, viscous flow, massive segmental relaxations occur. However, specimens obtained after the first hysteresis cycle, having undergone irreversible transformations that involve remarkable changes in the topology of the elastomeric network due to disentangling and consequent decrease in the density of physical crosslinks, exhibit good elastomeric properties, even in the absence of vulcanization.

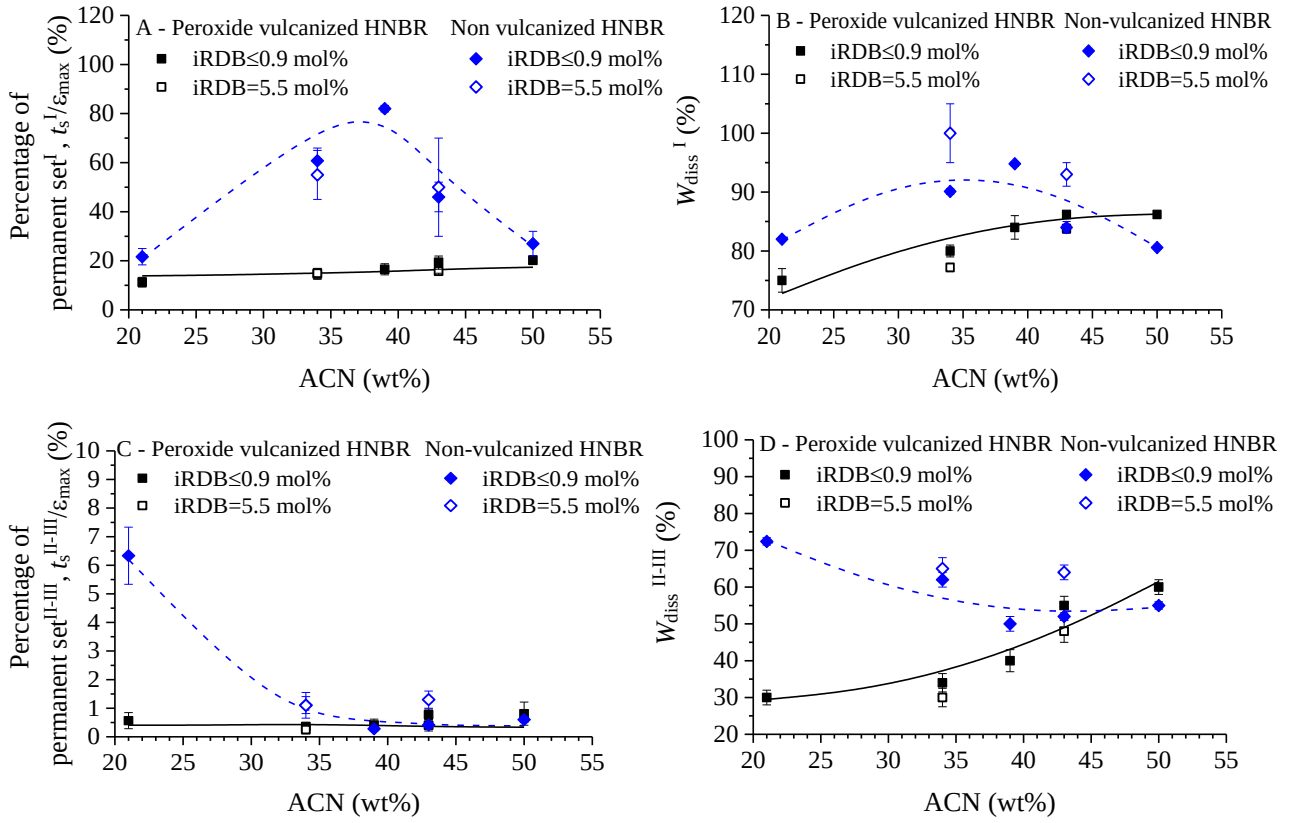

Figure 4.14 Values of percentage of permanent set (t_s^I/ε_{max}) (A) and percentage of dissipated energy (W_{diss}^I) (B) during the first hysteresis cycle and values of percentage of permanent set ($t_s^{II-III}/\varepsilon_{max}$) (C) and percentage of dissipated energy (W_{diss}^{II-III}) (D) during the successive hysteresis cycles, relative to peroxide vulcanized (squares) and non-vulcanized (diamonds) HNBR samples, with iRDB content ≤ 0.9 mol% (full symbols) and equal to 5.5 mol% (empty symbols).

The values of the tension set and percentage of permanent set of the peroxide vulcanized samples are comparatively lower than those of the non-vulcanized counterparts. Typically, for the vulcanized samples, the percentage of permanent set in the first cycle is almost constant, regardless of ACN content, with values below 20 % (Fig. 4.14A), while the percentage of dissipated energy achieves values comprised in between 70 and 80 % (Fig. 4.14B). As for the hysteresis cycles that follow the first one, the percentage of permanent set drops to values of ≈ 5 % (Fig. 4.14C), while the percentage of dissipated energy becomes on order of 30-50 % (Fig. 4.14D). Furthermore, as the ACN content increases, percentage of dissipated energy tends to decrease for the non-vulcanized samples, and to increase for the vulcanized samples. It is worth remarking that the values of the percentage of dissipated energy in the hysteresis cycles of the vulcanized and non-vulcanized HNBR samples with 50 wt% of ACN content (and 0.9 mol% of iRDB) are nearly coincident, and equal to ≈ 75 % in the

first cycles and 50 % in the successive cycles. This is probably due the fact that both samples are characterized by a three-dimensional network topology, where the junctions consist in small crystallites for the non-vulcanized sample, chemical crosslinks for the vulcanized counterpart. In this perspective, it is not surprising that the two kinds of elastomeric networks behave similarly in mechanical tests, even though the values of stress coming into play for the deformation of the chemical network are about 5 times greater those involved for the deformation of the physical network, also due to the reinforced effect of CB (Fig. 4.13).

4.4 X-ray diffraction analysis of stretched samples and molecular chain orientation

Strain-induced crystallization of HNBR43-0.9NV and HNBR50-0.9NV

The non-vulcanized, semicrystalline HNNBR samples with with 43 and 50 wt% of ACN and iRDB ≤ 0.9 mol% were subjected to ex-situ X-ray fiber diffraction analysis, to study the structural and textural transformations of the crystalline and amorphous phases. As discussed before, these samples, indeed, are partially crystalline at room temperature in the undeformed state, due to the crystallization of alternating tetramethylene/ACN (TMAC) sequences in Form II (see Chapter I).[64,70,124] They present reflections at 2θ values relative to the CuKα radiation $2\theta_{CuK\alpha} \approx 11.9$, 17.8 and 25.22° (interplanar spacing $d \approx 0.74$, 0.50 e 0.35 nm, respectively). For the MoKα radiation these reflections occur at $2\theta_{MoK\alpha} \approx 5.6$, 8.2, and 11.6°, respectively.

The 2D WAXS patterns of fibers, during loading and unloading, at room temperature at different strains relative to the non-crosslinked samples HNBR43-0.9NV and HNBR50-0.9NV are reported in Figures 4.15 and 4.16, respectively. For each sample, the 2D WAXS patterns were recorded starting from the undeformed sample ($\varepsilon = 0$) during the stretching at different strains ε up to a strain ε_{max} close to the break and then during the successive retraction from ε_{max} up to complete release of the tension (Force = 0). For the sample HNBR50-0.9NV a 2D WAXS pattern was also recorded 36 h after the release of the tension.

The one-dimensional equatorial, meridional, azimuthal and radial profiles, obtained from the 2D patterns of all HNBRs recorded at the different loading and unloading strains are reported in Figure A17.

For all samples, the 2D WAXS patterns of the unstretched samples (at $\varepsilon = 0$) show a broad halo in a range of 8-12°centered at $2\theta(\text{MoK}\alpha) \approx 8.7°$ (i.e., $2\theta(\text{CuK}\alpha) \approx 19°$), the intensity of which is uniformly distributed along the whole azimuthal arc (Fig. 4.15 and 4.16). This indicates that the amorphous phase is not oriented.

The distribution intensity of the amorphous halo tends to become anisotropic as the strain increases (Fig. 4.15 and 4.16), as indicated by the increase of intensity on the equator (at $\varphi = 90$) in the azimuthal profiles of Figure A17D, D'. The 2θ position of the amorphous halo remains almost constant at $\approx 8.7°$ (MoKα) during the stretching. This indicates that the chain axes of the amorphous phase gradually align themselves along the stretching direction with increasing strain due to establishment of orientational correlations in the short range among chain segments, while the separation distance of intrachain segments remain constant at about $(2\sin\theta/\lambda)^{-1} \approx 0.47$ nm. For the HNBR43-0.9NV sample, the polarization of the amorphous phase during stretching is lower compared to that achieved by the HNBR50-0.9NV sample. As the initial degree of crystallinity of the sample HNBR50-0.9NV (10-13 %) is greater than that of the sample HNBR43-0.9NV (≈ 5%), this difference can be attributed to differences in the content of topological constrains exerted by the crystals initially present in the two samples, acting as physical crosslinks and stress transmitters of the elastomeric networks. During each stretching steps at a rate of 30 mm min^{-1}, followed by a step in which the samples are kept with fixed ends for at least 15 min before WAXS measurements, the low content of physical crosslinks for the HNBR43-0.9NV is not able to prevent relaxation, so that the amorphous segments do not reach a high degree of orientation. On the contrary, the greater content of physical junctions of the elastomeric network for the sample HNBR50-0.9NV allow for achieving a good alignment of the amorphous chains. Upon release of the tension, the orientation of amorphous

phase is gradually lost, and the intensity of the amorphous halo recovers a uniform distribution along the entire azimuthal ring (Fig. 4.15 and 4.16).

The WAXS patterns recorded in the undeformed state show also Debye-Scherrer rings at $2\theta_{MoK\alpha} \approx$ 5.6, 8.2, and 11.6° (Fig. 4.15A,A' and 4.16A, A'), corresponding to unoriented crystals of Form II.[64,70,124] The intensity of these reflection is very weak in Figures 4.15A, A', and A16A-A', especially for the sample HNBR43-0.9NV.

As the strain increases, the intensity of the reflections at $2\theta_{MoK\alpha} \approx$ 5.6, 8.2, and 11.6° becomes gradually polarized, on the meridian for the reflection at $2\theta_{MoK\alpha} \approx$ 5.6°, on the equator for the reflections at $2\theta_{MoK\alpha} \approx$ 8.2, and 11.6° (Fig. 4.15 and 4.16). This is evident starting from the critical strain $\varepsilon \approx 100\%$ for the most crystalline sample HNBR50-0.9NV (Fig. 4.16B), and $\varepsilon \approx 400\%$ for the less crystalline sample HNBR43-0.9NV (Fig. 4.15C). The identity period *c* of the chains in the crystalline Form II, evaluated from the position of the meridional reflection at $2\theta_{MoK\alpha} \approx 5.6°$ is close to 7.4 Å, suggesting that the TMAC sequences crystallize in a nearly a trans-planar conformation, in agreement with the literature.[64,70,124]

During the gradual release of the tension the degree of orientation achieved by the crystals and the amorphous phase is gradually lost (Fig. 4.15F-I and 4.15F-H), and only in the most crystalline sample HNBR50-0.9NV, the crystals remain partially oriented even in the fully relaxed state (Fig. 4.16H). This indicates that the pristine crystals experience irreversible textural transformations.

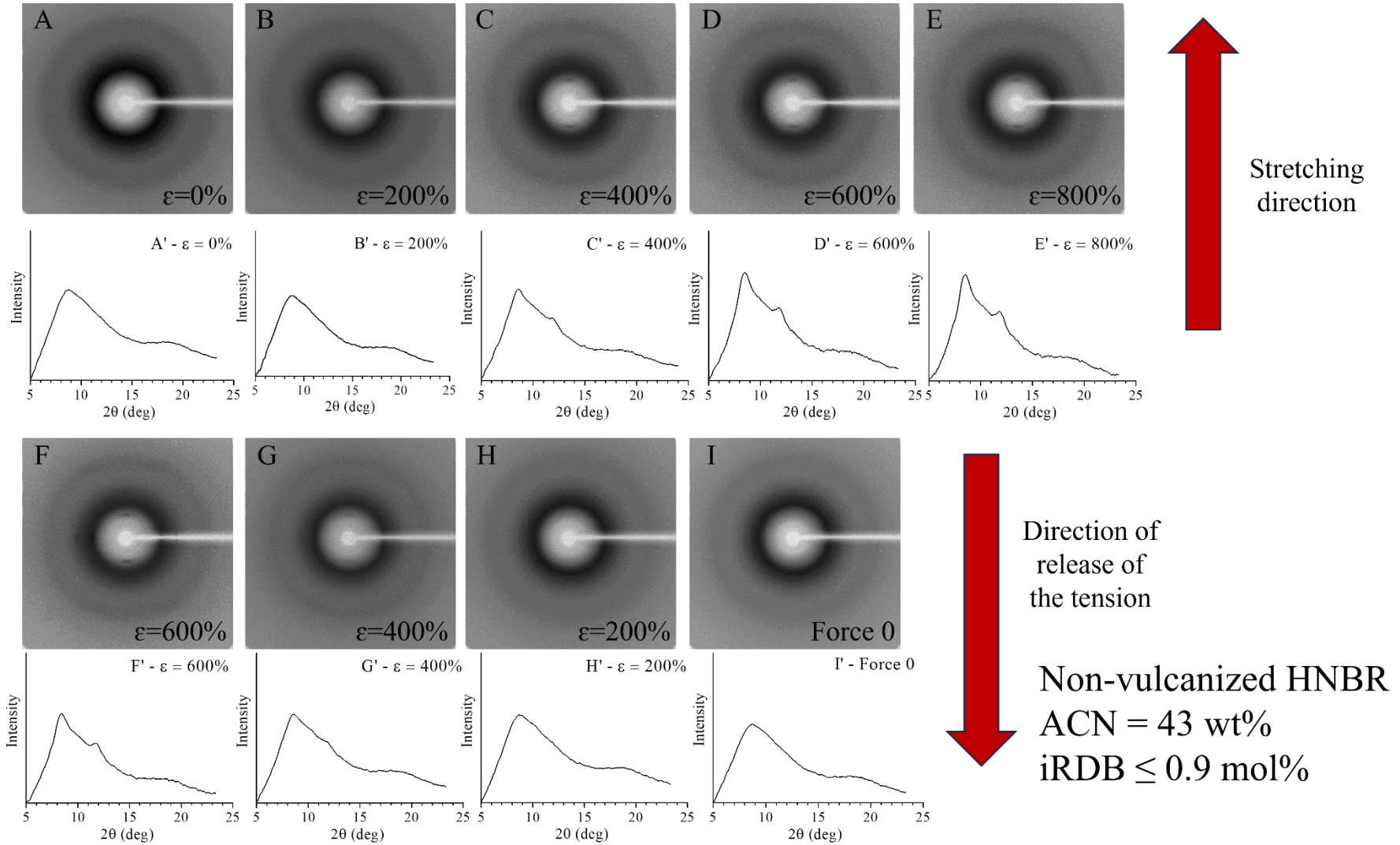

Figure 4.15 2D WAXS fiber patterns (A-I) and corresponding equatorial profiles (A'-I') of non-vulcanized HNBR43-0.9NV sample, with 43 wt% of ACN and iRDB content ≤ 0.9 mol%, recorded at *RT* at the indicated strains ε. A specimen that has not been subjected to any prior strain is gradually stretched until reaching a strain close to breaking (A,E, A'-E'), and then is gradually unloaded (F-I, F'-I') until reaching the release of the tension (force zero, average loading rate 30 mm min^{-1}). The directions of loading and unloading are indicated.

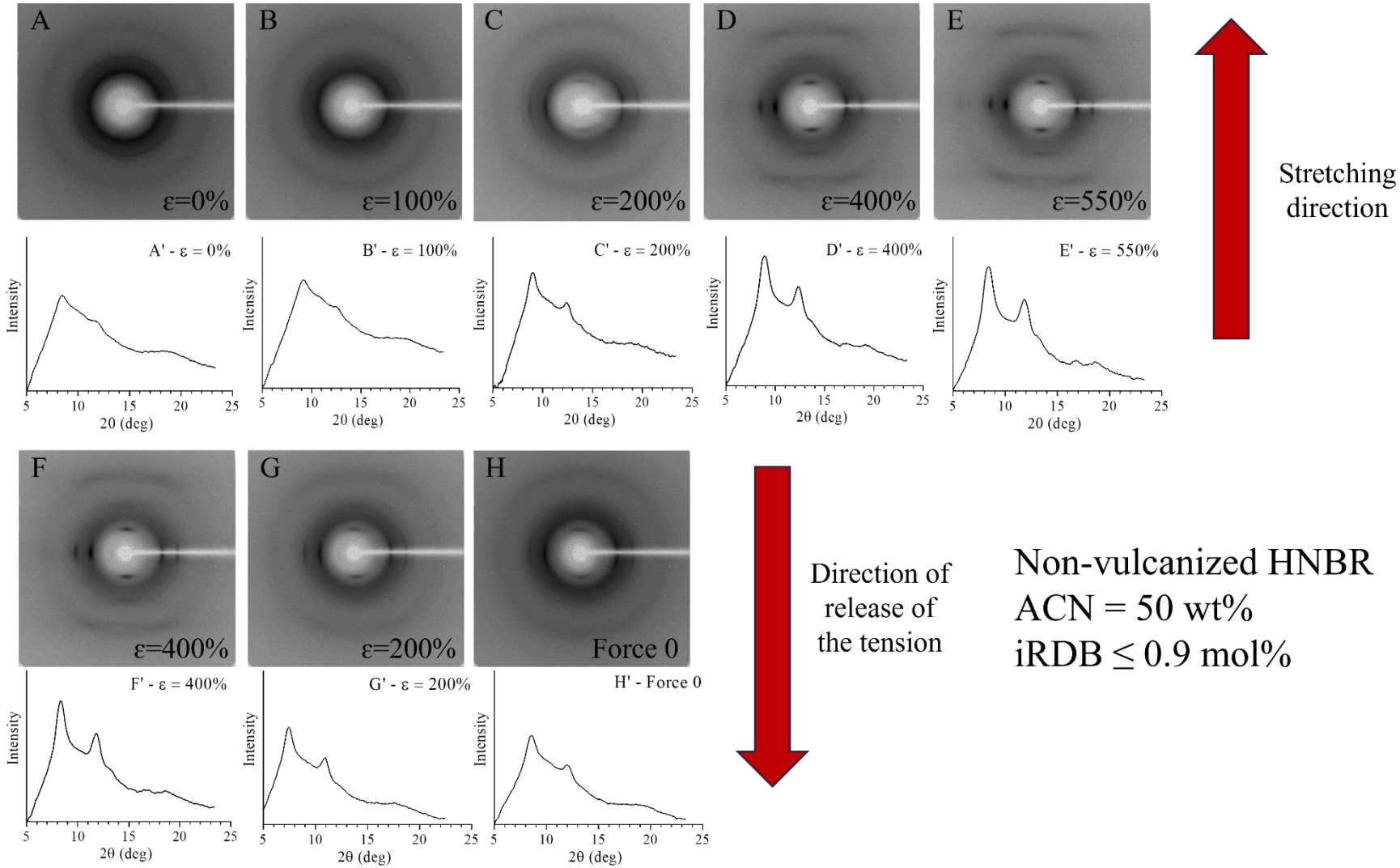

Figure 4.16 2D WAXS fiber patterns (A-I) and corresponding equatorial profiles (A'-I') of non-vulcanized HNBR50-0.9NV sample, with 50 wt% of ACN and iRDB content ≤ 0.9 mol%, recorded at *RT* at the indicated strains ε. A specimen that has not been subjected to any prior strain is gradually stretched until reaching a strain close to breaking (A,E, A'-E'), and then is gradually unloaded (F-H, F'-H') until reaching complete release of the tension(force zero, average loading rate 30 mm min^{-1}). The directions of loading and unloading are indicated.

Considering that both samples are initially crystalline, the possible occurrence of strain-induced crystallization may be probed by comparing the X-ray diffraction intensity distribution of the radial profiles extracted from 2D WAXS patterns of the deformed samples with those corresponding to zero strain (Fig. A17A, A'). In particular, the incremental crystallinity index $\Delta x_c(\varepsilon_i)$ was calculated as:

$$\Delta x_c(\varepsilon_i) = 100\,\frac{A(\varepsilon_i)-A(\varepsilon=0)}{A(\varepsilon_i)} \qquad (4.1)$$

where $A(\varepsilon_i)$ and $A(\varepsilon = 0)$ represent the area under the radial profile at strain ε_i and at zero strain, respectively, after subtraction of a background approximated by a straight line, whereas the difference $A(\varepsilon_i)$-$A(\varepsilon = 0)$ represents the increment of crystallinity index achieved at strain ε_i. The so calculated values of $\Delta x_c(\varepsilon_i)$ are reported as a function of strain in Figure 4.17.

It is apparent, that the incremental crystallinity index of the sample HNBR43-0.9NV tends to increase as the strain increases already starting from ε = 100 %, even though this increase is hardly visualized in the 2D WAXS images (Fig. 4.15). The value of $\Delta x_c(\varepsilon_i)$ reaches a quasi-plateau of ≈ 3%, at strains close to the rupture. During the gradual release of tension, the values of $\Delta x_c(\varepsilon_i)$ decrease as strain decrease, with no or small hysteresis. After the release of the tension, the sample (Force = 0) shows that the value of incremental crystallinity index does not return to zero but reaches a value of about 1 %.

The HNBR50-0.9NV sample shows a similar behavior, but with a significantly higher increase in $\Delta x_c(\varepsilon_i)$ value at any strain. In particular, the values of $\Delta x_c(\varepsilon_i)$ tend to increase as the strain increases already starting from ε = 100 %, in agreement with information extracted from the 2D WAXS images of Figure 4.16. The parameter $\Delta x_c(\varepsilon)$ keeps increasing until it approaches a value close to 6 %, at strains close to the rupture. During the gradual release of the tension, the $\Delta x_c(\varepsilon_i)$ values gradually decreases, also in this case with null hysteresis. Finally, at zero force, the sample does not recover the initial state, as $\Delta x_c(\varepsilon_i)$ reaches a value of ≈ 3 % and, after 36 h at rest, a value of ≈ 1 %. Therefore, also for the sample HNBR50-0.9NV a small fraction of newly formed crystals survives at the end of

the unloading step, probably because these crystals remain entrapped in the elastomeric network by effect of local tension. As a matter of fact, by aging the unhooked sample for longer than 36 h, these crystals disappear, and the initial level of crystallinity is almost fully recovered (data not shown). The increment of crystallinity during the loading step is reversible, as indicated by the null hysteresis of the $\Delta x_c(\varepsilon_i)$ values measured in the loading and unloading steps. The null hysteresis and the almost immediate crystallization occurring upon stretching suggest that the driving force for the formation of new crystals is namely due to the nucleation effect exerted by the initially present crystals in the samples HNBR43-0.9NV and HNBR50-0.9NV in the pristine state and that this effect possibly overrides the SIC mechanism.

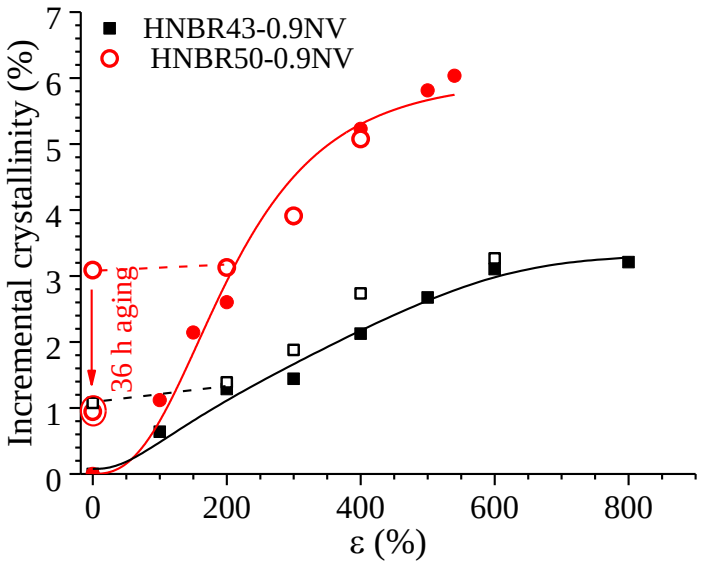

Figure 4.17 Values of the incremental crystallinity index $\Delta x_c(\varepsilon_i)$ as a function of strain. The black squares and red dots correspond to the non-vulcanized samples HNBR43-0.9NV and HNBR50-0.9NV with ACN content of 43 and 50 wt% respectively, and iRDB content ≤ 0.9 mol%. The full and empty symbols indicate the values associated with the loading and unloading steps, respectively. The arrow shows that by aging the unhooked sample HNBR50-0.9NV for 36 h, the newly formed crystals that remain entrapped in the elastomeric network at the end of the unloading step, tend gradually to melt.

Segmental orientation of HNBR43-0.9NV and HNBR50-0.9NV

The segmental orientation of the HNBR samples stretched at different strains is calculated from the azimuthal profiles extracted from the 2D WAXS patterns as detailed in Chapter II, Figure 2.22.

The values of the order parameters $P_2^{WAXS\text{-}am}$ and $P_2^{WAXS\text{-}cr}$ was determined by equations 2.71 and 2.69. The values of $P_2^{WAXS\text{-}am}$ and the values of $P_2^{WAXS\text{-}cr}$ relative to the amorphous and crystalline phases are reported in Figure 4.18 as a function of the elongation parameter (λ^2-1/λ).

It is apparent that the order parameter associated to the amorphous segments experience in absolute value a steep increase at low strain without reaching a clear plateau. In particular, the increase in the degree of orientation of the amorphous phase slows down at values of (λ^2-1/λ) in the range of 25-35 (i.e. $\varepsilon \approx$ 400-500 %), for the sample HNBR43-0.9NV, and (λ^2-1/λ) in the range 9-16 (i.e. $\varepsilon \approx$ 200-300 %), for the sample HNBR50-0.9NV. The degree of orientation achieved by the amorphous segments at any strain for the more crystalline sample HNBR50-0.9NV is greater than that achieved by the sample HNBR43-0.9NV. At strain close to the break, the order parameter reaches values of $\approx$ -0.01 for the less crystalline sample HNBR34-0.9NV and $\approx$ -0.034 for the more crystalline sample HNBR50-0.9NV. These differences may be ascribed to differences in the crosslink density of the rubber network created by the crystals acting as physical junction. Since the degree of orientation of amorphous phase increases as the crosslink density increases, the sample HNBR43-0.9NV characterized by a lower degree of crystallinity, is also characterized by a lower crosslink density, so that also the degree of orientation of the amorphous phase is lower than that reached by the more crystalline sample HNBR50-0.9NV at any strain.

The absence of true plateau in the values of the order parameter of the amorphous phase at high strain confirms the prevalence of the non-SIC behaviour of the here analyzed HNBR samples, over the effect of nucleation exerted by the pre-existing crystals on the formation of new crystals during stretching, as discussed before (Fig. 4.17 and related discussion). In fact, the SIC behavior entails that when crystallization occurs, the orientation of the amorphous segments does not increase anymore

with strain because crystallization leads to a partial relaxation of the amorphous chains linked to the crystallites, as predicted by Flory theory[42] and observed for a large number of elastomers,[51,54-57,49] including some amorphous HNBR samples analyzed in Chapter III.

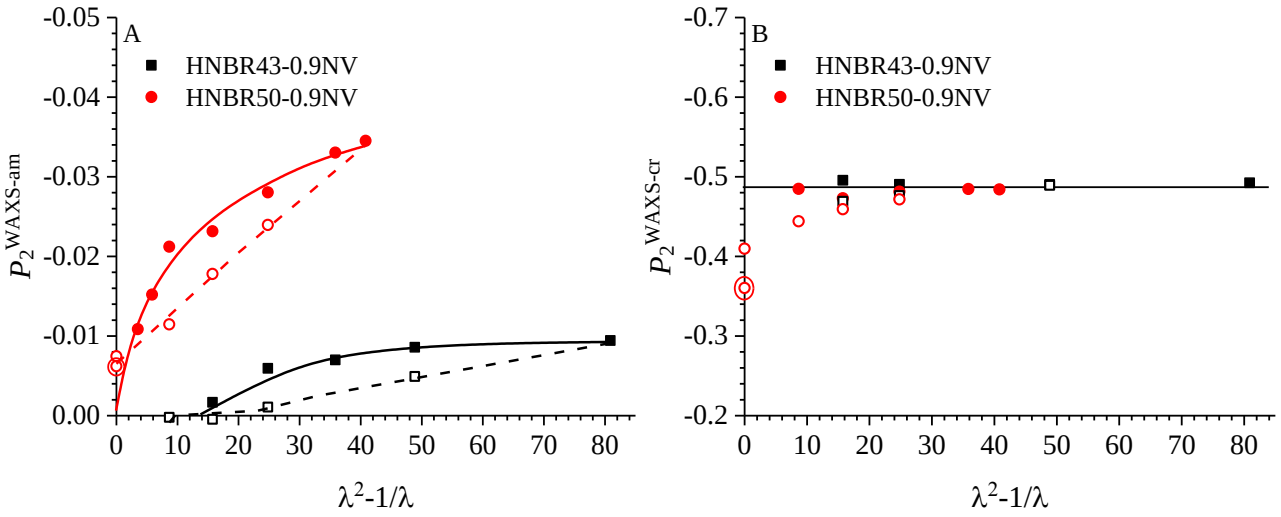

Figure 4.18 Values of the order parameters for the amorphous $P_2^{WAXS-am}$ (A) and crystalline $P_2^{WAXS-cr}$ (B) phases as a function of the elongation parameter (λ^2-1/λ). The black squares and red dots correspond to the non-vulcanized HNBR samples with ACN content of 43 and 50 wt% respectively, and iRDB content ≤ 0.9 mol%. The full and empty symbols indicate the values measured in the loading and unloading steps, respectively. The double encircled dots are relative to the unhooked sample HNBR50-0.9NV, aged for 36 h.

During releasee of the tension, the order parameter value of the amorphous phase decreases in absolute value, as the stain decreases. For the HNBR43-0.9NV sample, the amorphous phase completely loses its orientation at values of (λ^2-1/λ) < 24 (i.e., ε < 400 %). In contrast, for the HNBR50-0.9NV sample, at the end of unloading step (zero force), the order parameter of the amorphous phase is approximately -0.008, and becomes equal to ≈ -0.006, after aging the sample for 36 h at rest. This behavior is linked to the fact that the crystals remain oriented in the unhooked sample (see below), also influencing the orientation of the amorphous phase.

The order parameter of the crystalline phase is approximately -0.5 and remains constant during the stretching step. The orientation of the crystalline phase could be probed for values of (λ^2-1/λ) ≥ 16 and 9 (i.e., ε ≥ 300 and 200 %) for the HNBR43-0.9NV and HNBR50-0.9NV samples, respectively. During release of the tension, a decrease in the absolute value of the order parameter of the crystalline

phase is observed for $(\lambda^2-1/\lambda) \leq 25$ (i.e., $\varepsilon \approx 400$ %) for both samples. However, while for the HNBR43-0.9NV sample, for $(\lambda^2-1/\lambda) \leq 16$ (i.e., $\varepsilon \leq 300$ %) a complete loss of orientation of the crystalline phase is noted, for HNBR50-0.9NV sample, the orientation of the crystals is partly retained, even at zero force, with values of the order parameter of ≈ -0.4 at the end of the unloading step and ≈ -0.36 after aging the sample at rest for 36 h.

Chapter V

Relaxation Phenomena

5.1 Relaxation phenomena induced by annealing at temperature near T_g

As reported in section 1.7.3, recent studies[65,66] have reported that HNBR samples with ACN content of 34 and 36 wt% exhibit endothermic DSC peaks centered at temperatures slightly higher than the glass transition temperature following annealing treatments at temperatures slightly above T_g. These endothermic phenomena have been attributed to the melting of crystals formed by long tetramethylene sequences susceptible to crystallization in the orthorhombic form of polyethylene (PE) from the amorphous phase, during the low-temperature isothermal annealing. The hypothesis that the DSC endothermic peaks may be due to relaxation phenomena following physical aging of the amorphous phase in the glassy state has been completely neglected.[65,66]

In order to investigate the nature of the endothermic peaks observed during heating subsequent to low-temperature thermal annealing of HNBR samples, this chapter reports the results of a study conducted through DSC on selected HNBR samples.

A first series of experiments was carried out on peroxide vulcanized samples reinforced with 30 phr of carbon black (see Chapter II) and with ACN content of 21 and 34 wt% and iRDB content ≤0.9 mol%, corresponding to samples HNBR21-0.9PC (T_g = -36.8 °C) and HNBR34-0.9PC (T_g = -25.1 °C) of Table 2.3, respectively. Since the concentration of long tetramethylene sequences increases as the ACN content decreases, the study is also conducted on the sample with 21 wt% ACN units. In the assumption that long tetramethylene sequences crystallize at low temperatures due to annealing, lower ACN content samples are expected to show an amplification of endothermic phenomena observed in the DSC heating thermograms following annealing.

In this study, HNBR samples undergo isothermal annealing at various temperatures close to the glass transition temperature, equal to -36.8 and -25.1 °C for the samples with 21 and 34 wt% ACN, respectively. The DSC curves recorded during subsequent heating, from -90 °C to high temperatures, are analyzed.

The DSC curves recorded during heating from -90 to 100°C after imposing an isothermal annealing for a time (t_a) of 60 min at different annealing temperatures (T_a) ranging from -50 to -10 °C are shown in Figure 5.1. The experiments are relative to the samples HNBR21-0.9PC and HNBR34-0.9PC.

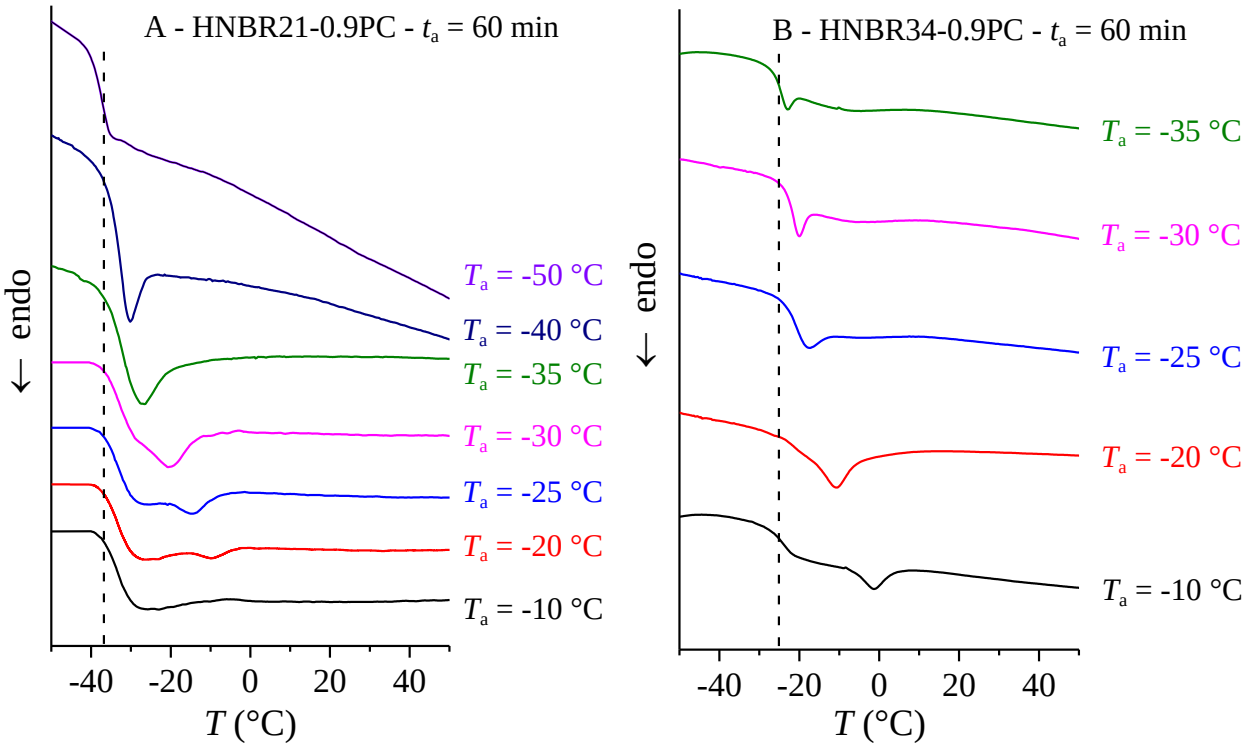

Figure 5.1 DSC thermograms recorded during heating from -90 to 100°C for peroxide vulcanized HNBR samples with ACN content of 21 (A) and 34 (B) wt% and iRDB ≤ 0.9 mol%. The DSC thermograms are recorded after subjecting the samples to annealing at the indicated temperatures T_a for an annealing time t_a of 60 min, and successive rapid cooling from T_a to -90 °C. The vertical bars mark the glass transition temperature of the pristine samples HNBR21-0.9PC and HNBR34-0.9PC at -36.8 and -25.1 °C, respectively.

From the DSC thermograms of Figure 5.1, it emerges that the sample HNBR21-0.9PC with 21 wt% ACN content (Fig. 5.1A) exhibits endothermic peaks close to T_g after annealing at T_a comprised between -40 and -20 °C. The sample with 34 wt% ACN, instead, shows such endothermic peaks due to annealing at all sampled T_a values. In all cases, the position of the endothermic peak (T_{peak}) falls at temperature greater than T_g by about 3-25 °C

The values of enthalpy (ΔH_{peak}) and the temperature of the endothermic peak (T_{peak}), extracted from the DSC thermograms of Figure 5.1 are reported in Table 5.1 and in Figure 5.2 as a function of T_a.

Table 5.1 Values of enthalpy (ΔH_{peak}) and temperature (T_{peak}) of the endothermic (annealing) peaks extracted from the DSC thermograms in Figure 5.1, relative to the samples HNBR21-0.9PC and HNBR34-0.9PC. The specimens were annealed at the indicated temperatures T_a for a fixed time t_a of 60 min.

Annealing time (t_a) = 60 min				
Samples	HNBR21-0.9PC 9PC (T_g = -36.8 °C)		HNBR34-0.9PC (T_g = -25.1 °C)	
T_a (°C)	**ΔH_{peak} (Jg^{-1})**	**T_{peak} (°C)**	**ΔH_{peak} (Jg^{-1})**	**T_{peak} (°C)**
-10	-	-	3.2	-1.4
-20	0.4	-9.35	6.2	-10.7
-25	1.5	-14.7	4.2	-17.5
-30	2.8	-20.7	3.8	-20.0
-35	2.7	-26.7	3.0	-23.0
-40	2.3	-30.2	-	-
-50	0.8	-33.9	-	-

It is apparent that the values of T_{peak} relative to the annealing peaks extracted from the thermograms of Figure 5.1A tend to increase with increasing T_a for both samples (Fig. 5.2B). Furthermore, both samples show that the enthalpy values (ΔH_{peak}) related to the annealing peak detected in the DSC thermograms of Figure 5.1 initially tend to increase as the annealing temperature T_a increases, then reach a maximum in the T_a range comprised between -35 to -30 °C for the sample with an ACN content of 21 wt% and at $T_a \approx$ -20°C for the sample with an ACN content of 34 wt%, and subsequently decrease (Fig. 5.2A). It is also observed that the values of ΔH_{peak} that evolve from the sample HNBR21-0.9PC are significantly lower than those evolving from the sample HNBR34-0.9PC, despite the fact that first sample is characterized by a higher amount of long crystallizable tetramethylene sequences than the second one. This suggests that the annealing peaks observed in the DSC thermograms of Figure 5.1 may arise not only from the

melting of crystals formed during annealing at T_a above the T_g, but also from the occurrence of relaxation phenomena related to physical aging of the amorphous phase in the glassy state, that is by annealing at temperatures below or close to T_g.

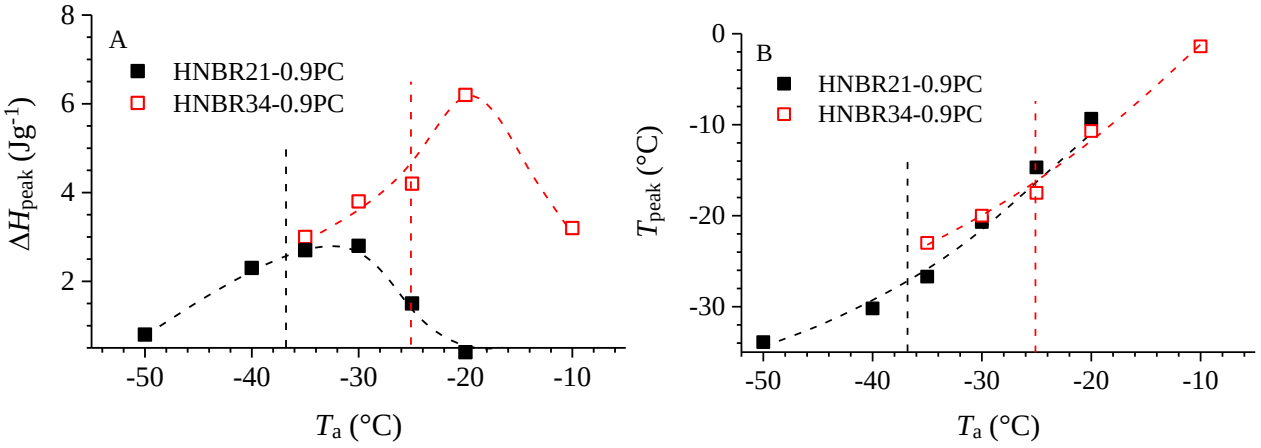

Figure 5.2: Values of enthalpy (ΔH_{peak}) (A) and temperature (T_{peak}) (B) of the endothermic peak extracted from the DSC thermograms in Figure 5.1, as a function of annealing temperature T_a, for the HNBR21-0.9PC (black squares) and HNBR34-0.9PC (red squares) samples. The vertical bars mark the glass transition temperature of the pristine samples HNBR21-0.9PC and HNBR34-0.9PC at -36.8 and -25.1 °C, respectively.

A second series of experiments was carried out to assess the annealing time (t_a) dependence of the values of T_{peak} and ΔH_{peak} at selected values of the annealing temperature T_a. These tests were carried out by annealing, for different amounts of time, not only the peroxide vulcanized samples HNBR21-0.9PC (T_g = -36.8 °C) and HNBR34-0.9PC (T_g = -25.1 °C), but also the non-vulcanized sample HNBR34-0.9NV (T_g = -24.6 °C) with 34 wt% of ACN and iRDB ≤ 0.9 mol%, as well as the couple of non-vulcanized and peroxide vulcanized HNBR samples HNBR34-5.5NV (T_g = -27.4 °C) and HNBR34-5.5PC (T_g = -25.0 °C), with 34 wt% of ACN, but iRDB content of 5.5 mol%. To emphasize the possible occurrence of thermally induced crystallization, these experiments were carried out by fixing the annealing temperature ≈ 5 °C above the glass transition temperature T_g, that is at -20 °C for the HNBR samples with 34 wt% of ACN, and -30 °C for the HNBR sample with 21 wt% of ACN. For comparison, the HNBR sample with 21 wt% of ACN was also tested at -20 °C. The annealing temperatures T_a of -20 and -30°C were selected

based on the results of Figure 5.2, that indicate that the sample with 34 and 21 wt% of ACN show the greatest values of ΔH_{peak} at these T_a.

The DSC thermograms collected in the annealing experiments are reported in Figures 5.3 and 5.4, while the values of ΔH_{peak} and T_{peak} extracted from thermal analysis are collected in Table 5.2 and 5.3 and reported as a function of annealing time in Figure 5.5.

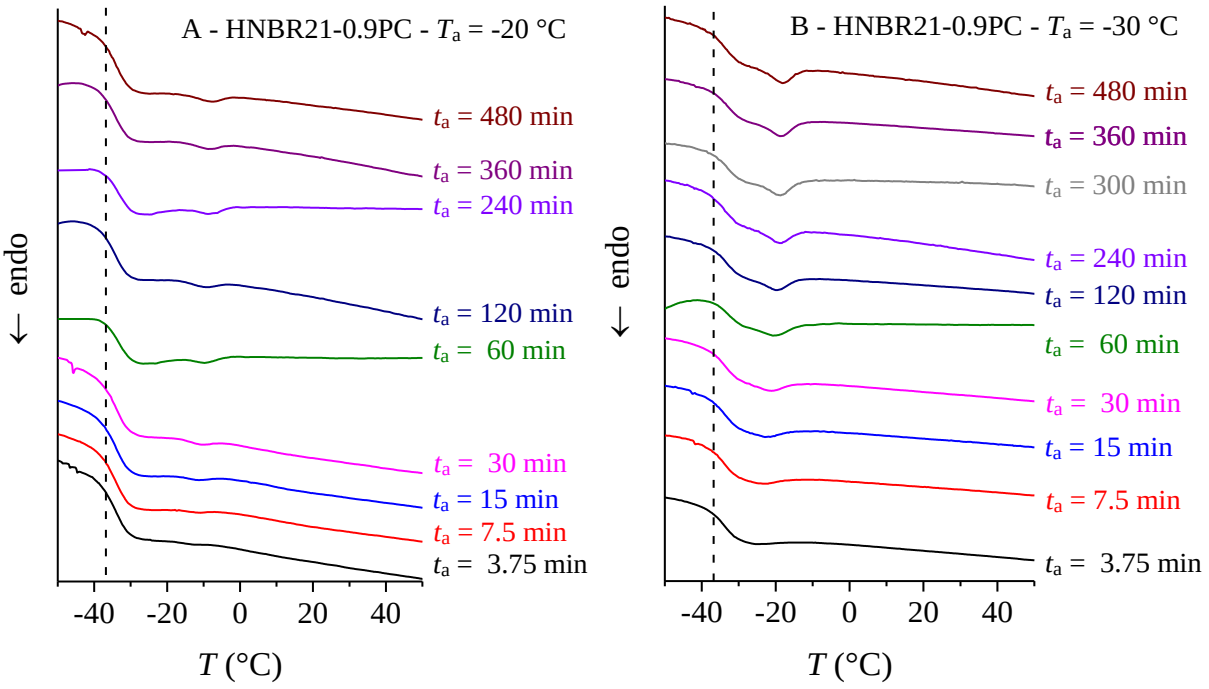

Figure 5.3: DSC thermograms recorded during heating from -90 to 100°C for peroxide vulcanized HNBR samples with ACN content of 21 wt% and iRDB ≤ 0.9 mol%. The DSC thermograms are recorded after subjecting the samples to annealing at temperatures T_a = -20 (A) and -30 (B) °C, for the indicated annealing times t_a, and successive rapid cooling from T_a to -60 °C. The vertical bars mark the glass transition temperature of the pristine sample HNBR21-0.9PC at -36.8 °C.

Table 5.2: Values of enthalpy (ΔH_{peak}) and temperature (T_{peak}) of the endothermic (annealing) peaks extracted from the DSC thermograms in Figure 5.3, relative to the sample HNBR21-0.9PC. The specimens were annealed at T_a = -20 and -30 °C, for the indicated annealing times t_a.

T_a (°C)	Sample		T_a (°C)	Sample	
-20	HNBRR21-0.9PC (T_g = -36.8 °C)		-30	HNBRR21-0.9PC (T_g = -36.8 °C)	
t_a (min)	ΔH_{peak} (Jg^{-1})	T_{peak} (°C)	t_a (min)	ΔH_{peak} (Jg^{-1})	T_{peak} (°C)
0	0.3	-24.7	0	0.3	-24.7
3.75	0.4	-14.5	3.75	2.3	-25.7
7.5	0.8	-14.5	7.5	2.5	-24.7
15	1.0	-12.8	15	2.6	-22.9
30	0.9	-12.0	30	2.8	-21.7
60	0.9	-10.7	60	2.8	-20.7
120	1.8	-10.2	120	3.1	-20.0
240	1.4	-9.0	240	3.0	-19.0
360	1.6	-8.8	300	3.0	-18.7
480	2	-8.3	360	3.3	-18.9
			480	3.5	-18.2

For the crosslinked sample with 21 wt% ACN, annealing at -30 °C induces annealing peaks with greater values of ΔH_{peak} (Fig. 5.5A), and lower temperatures T_{peak} (Fig. 5.5B), compared to those obtained for annealing at -20 °C. The values of ΔH_{peak} and T_{peak} reach a quasi-plateau after about 60 min, corresponding to ≈ 3 J/g and ≈ 19 °C, respectively, for annealing carried out at -30 °C, and ≈ 2 J/g and ≈ -9 °C, for annealing carried out at -20 °C.

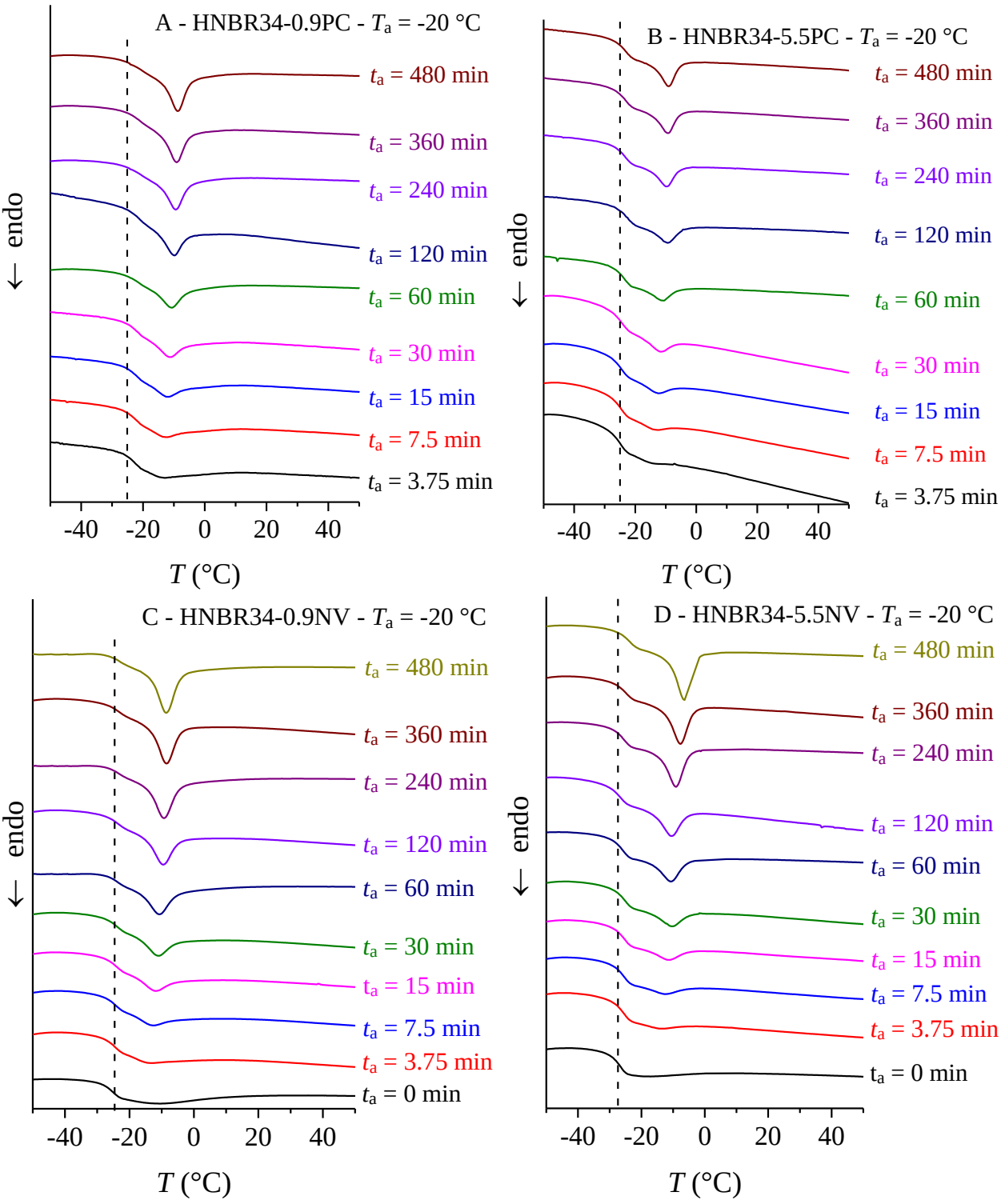

Figure 5.4: DSC thermograms recorded during heating from -90 to 100°C for peroxide vulcanized (A, B) and non-vulcanized HNBR samples (C, D) with ACN content of 34 wt% and iRDB ≤ 0.9 (A, C) and = 5.5 (B, D) mol%. The DSC thermograms are recorded after subjecting the samples to annealing at T_a = -20 °C, for the indicated annealing times t_a, and successive rapid cooling from T_a to -90 °C. The vertical bars mark the glass transition temperature of the pristine samples HNBR34-0.9PC, HNBR34-5.5PC, HNBR34-0.9NV and HNBR34-5.5NV at -25.1, -25.0, -24.6 and -27.4 °C, respectively.

Table 5.3: Values of enthalpy (ΔH_{peak}) and temperature (T_{peak}) of the endothermic (annealing) peaks extracted from the DSC thermograms in Figure 5.4, relative to the samples HNBR34-0.9PC, HNBR34-5.5PC, HNBR34-0.9NV, and HNBR34-5.5NV. The specimens were annealed at T_a = -20 °C, for the indicated annealing times t_a.

T_a (°C)	Samples			
-20	HNBR34-0.9PC (T_g = -25.1 °C)		HNBR34-5.5PC (T_g = -25.0 °C)	
t_a (min)	ΔH_{peak} (Jg^{-1})	T_{peak} (°C)	ΔH_{peak} (Jg^{-1})	T_{peak} (°C)
0	2.3	-13.5	1.2	-15.0
3.75	3.7	-13.0	1.8	-14.7
7.5	4.7	-12.9	1.6	-14.2
15	5.0	-12.2	2.2	-12.5
30	5.2	-11.5	2.4	-11.9
60	6.2	-10.7	2.6	-10.9
120	6.1	-9.9	2.9	-9.4
240	7.3	-9.3	3.1	-9.7
360	6.5	-9.0	3.5	-9.4
480	7.2	-8.9	3.8	-9.0
T_a (°C)	Samples			
-20	HNBR34-0.9NV (T_g = -24.6 °C)		HNBR34-5.5NV (T_g = -27.4 °C)	
t_a (min)	ΔH_{peak} (Jg^{-1})	T_{peak} (°C)	ΔH_{peak} (Jg^{-1})	T_{peak} (°C)
0	5.0	-14.6	1.9	-18.7
3.75	5.5	-13.7	2.3	-14.4
7.5	5.7	-12.7	3.1	-12.7
15	6.2	-11.9	3.3	-11.4
30	7.4	-11.0	5.1	-10.4
60	10.2	-10.7	5.1	-10.7
120	9.7	-9.6	5.8	-8.9
240	12.5	-9.4	7.8	-9.0
360	10.9	-8.6	6.8	-7.7
480	12.6	-8.5	9.4	-8.4

As for the samples with 34 wt% of ACN, the annealing at -20 °C produces annealing peaks centered at the same temperature T_{peak} (Fig. 5.5D) but with enthalpy values ΔH_{peak} that depend on the iRDB content and vulcanization. In particular, for HNBR samples with the same iRDB content, the values of ΔH_{peak} of the non-vulcanized species are greater than those of the peroxide vulcanized counterparts (Fig. 5.5C). Furthermore, for the peroxide vulcanized HNBR samples HNBR34-0.9PC and HNBR34-5.5PC and the non-vulcanized HNBR samples HNBR34-0.9NV, HNBR34-5.5NV, the greater the iRDB content the lower the ΔH_{peak} (Fig. 5.5C).

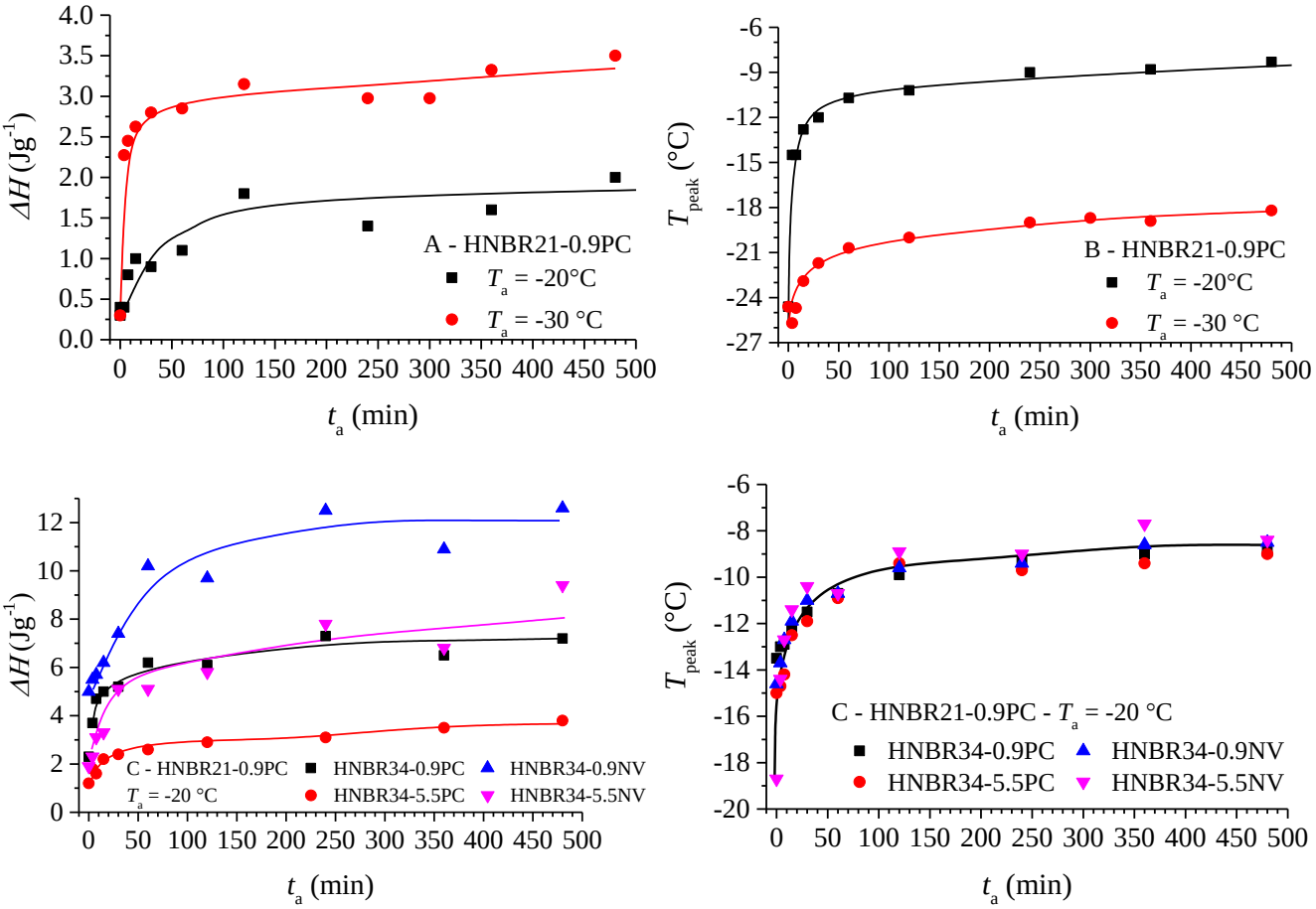

Figure 5.5 Values of enthalpy (ΔH_{peak}) (A,C) and temperature (T_{peak}) (B,D) of the annealing peaks extracted from the DSC thermograms in Figure 5.3 (A,B) and 5.4 (C,D), as a function of the annealing time t_a, relative to the peroxide vulcanized HNBR samples HNBR21-0.9PC (A, B) and HNBR34-0.9PC, HNBR34-5.5PC, and the non-vulcanized HNBR samples HNBR34-0.9NV, HNBR34-5.5NV (C,D). The specimens were annealed at T_a = -20 and -30 °C for the indicated annealing times t_a.

Although the increase of T_{peak} as the annealing temperature increases (Fig. 5.2B and 5.5B) complies with the hypothesis that the annealing peaks are due to the melting of crystals generated by thermally induced crystallization, the almost invariance of T_{peak} for the peroxide vulcanized and non-vulcanized HNRB samples with 34 wt% of ACN but different iRDB content (Fig. 5.5D), and the low tendency of the HNBR sample with 21 wt% of ACN to "crystallize" even after long annealing times at suitable "undercoolings" (Fig. 5.5B), suggests that the annealing peak is due to chain relaxation of the amorphous chains induced by physical aging, rather than to the melting of crystals formed during annealing. This hypothesis is also in agreement with the results of a recent study that shows that HNBR samples with low crosslink density exhibit, at 25 °C, SIC, for ACN content of 19 wt% and no SIC behavior, for ACN content of 33 wt%.[70] Based on that, the thermally induced crystallization that occurs by annealing at sub-zero temperatures

above the T_g should be more easy and marked for the sample HNBR21-0.9PC with 21 wt% ACN than for the sample HNBR34-0.9PC with 34 wt%. However, this does not occur, since the values ΔH_{peak} are greater for the sample HNBR34-0.9PC than those relative to the sample HNBR21-0.9PC, supporting the hypothesis that the annealing peak is due to relaxation.

A third series of experiments was finally carried out to assess how the annealing peak varies with crosslink density. The study was focused on the subset of HNBR34 samples with 34 wt% of ACN, and 4 mol% of iRDB, that includes the non-vulcanized sample (Tg = -26.6 °C), and the sulfur vulcanized counterparts with different crosslink density (-26.4 °C < Tg < -22.9 °C). Experiments were carried out at T_a equal to -20 °C for various annealing times. The DSC thermograms recorded in the annealing experiments are reported in Figure A18. Also in this case, the annealing treatment generates annealing peaks at temperatures higher than the glass transition temperature.

The values of ΔH_{peak} and T_{peak} are reported in Table A2 and in Figure 5.6 as a function of annealing time. It is apparent that for all the samples, the values of ΔH_{peak} (Fig. 5.6A) and T_{peak} (Fig. 5.6B) increase as the annealing time t_a increases, until reaching a plateau at $t_a \approx 30$ min, except for the HNBR samples with added sulfur content of 2.26 and 3.01 phr, which reach a plateau at $t_a \approx 60$ min. Furthermore, at any annealing time, the values of ΔH_{peak} and T_{peak} decrease, as the added sulfur content increases. In particular, the values of T_{peak} recorded at the longest annealing time decrease from ≈ -8 °C relative to the non-vulcanized sample, to ≈ -10 °C for the sample with the greatest crosslink density (Fig. 5.6B). Furthermore, as shown in Figure 5.6C, the value of ΔH_{peak} achieved at the longest annealing time decreases almost linearly as the values of residual dipolar coupling constant D_{res}, proportional to the crosslink density, increase. This behavior can be explained by the fact that the increase in the crosslink density results in a decrease in the length of the network strands, and hence also in the chain mobility. Since the chain mobility is markedly dependent on the temperature, in order to compare the annealing behavior of the HNBR samples measured at the same T_a, the annealing enthalpy values ΔH_{peak} of each sample are divided by the difference between the annealing temperature and the corresponding glass transition temperature (T_a-T_g). The values of the reduced parameter ΔH_{peak} $(T_a\text{-}T_g)^{-1}$ are reported in Figure 5.6D as a function of the

annealing time. It is apparent that this reduced parameter takes on similar values at the same annealing time, regardless of crosslink density.

The main results of the present analysis consist in having evidenced that even the highly crosslinked HNBR sample (added sulfur content 3.01 phr) exhibits annealing phenomena. This makes challenging to attribute the endothermic annealing peaks to the melting of crystals formed by long ethylene sequences via thermally induced crystallization, and once again reinforces the hypothesis that the annealing behavior reflects relaxation phenomena of the amorphous phase.

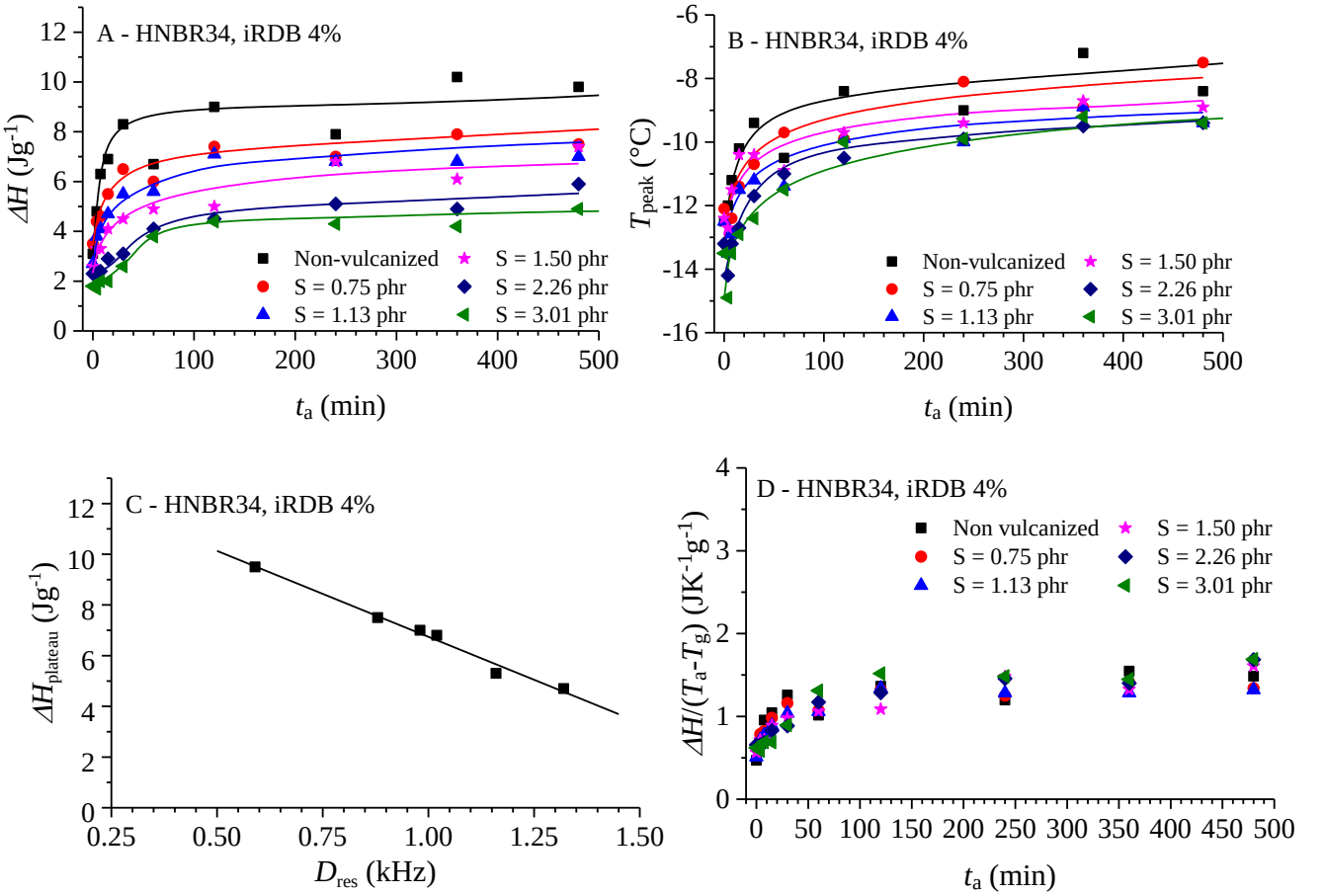

Figure 5.6 Values of enthalpy (ΔH_{peak}) (A,C,D) and temperature (T_{peak}) (B) of the annealing peaks extracted from the DSC thermograms in Figure A18, as a function of the annealing time t_a, relative to the sulfur vulcanized HNBR samples with 34 wt% ACN and 4 mol% of iRDB, and the corresponding non-vulcanized samples. The specimens were annealed at T_a = -20 for the indicated annealing times t_a. In D, the values of ΔH_{peak} have been divided by the difference (T_a-T_g), (ΔH_{peak} (T_a-T_g)$^{-1}$).

5.2 Measurement of chain mobility via Dielectric Spectroscopy

The peroxide vulcanized HNBR samples HNBR21-09PC and HNBR34-09PC were subjected to dielectric spectroscopy analysis. The aim was to compare chain mobility by measuring the characteristic time of alpha relaxation.

Dielectric spectroscopy is an experimental technique used to study the dielectric properties of materials as a function of frequency. In polymer dielectric spectroscopy, the Havriliak-Nagami equation is often used to describe dipolar relaxation in the material. The characteristic time (τ_{HN}) is a measure of the average time the dipoles or functional groups take in the polymer to respond to the applied electric field. The values of τ_{HN} are obtained by fitting the experimental data with the Havriliak-Nagami equation described in Chapter II. This quantity represents an important point in the distribution of relaxation times and can indicate the dominant time scales in the relaxation processes of a material.

The characteristic alpha relaxation time τ_{HN} measured for the peroxide vulcanized HNBR samples HNBR21-0.9PC and HNBR34-0.9PC are reported as a function of temperature in Figure 5.7. At high temperatures, the samples show similar relaxation times τ_{HN} of about 0.3 μs. At lower temperatures, the characteristic relaxation times increase, and, at the same temperature, those of the HNBR21-0.9PC sample are remarkably lower than those of the sample HNBR34-0.9PC. This means that the segmental mobility of the peroxide vulcanized sample HNBR21-0.9PC is greater than that of the peroxide vulcanized HNBR34-0.9PC, in the temperature range between 240 and 290 K. At the annealing temperatures of -20 °C (253 K) for the sample HNBR34-0.9PC, and -30 °C (243 K) for the sample HNBR21-0.9PC, the relaxation times are 11.3 and 31.2 ms, respectively. Therefore, at the temperature at which the annealing experiments were conducted (Fig. 5.3B and 5.4A), the segmental mobility in the two samples is comparable, given the very similar values of the relaxation times. Therefore, if crystallization of polyethylene segments were to occur, it would be of similar magnitude for the two samples, as the dynamic barriers for crystallization (both nucleation and growth) would be similar. From the fit to the

experimental data of Figure 5.7, with the empirical equation by Vogel-Fulcher-Tammann (see Chapter II, equation 2.57), the values of Vogel temperature of -63 and -43 °C can be obtained, for the peroxide vulcanized HNBR samples HNBR21-0.9PC and HNBR34-0.9PC, respectively.

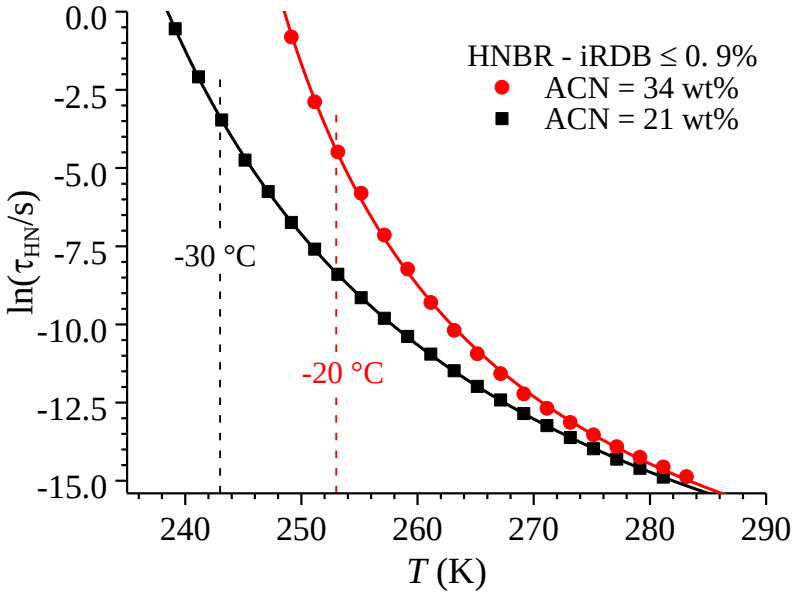

Figure 5.7 Characteristic dielectric relaxation time as a function of temperature, for the peroxide vulcanized samples HNBR21-0.9PC (black squares) and HNBR34-0.9PC (red dots). The solid line represents the fit to data with the empirical Vogel-Fulcher-Tammann equation (see Chapter II).

Further measurements of dielectric spectroscopy (DS) were carried out at a constant temperature, set equal to -20 and -10 °C, by performing frequency scans on the peroxide vulcanized HNBR sample HNBR34-0.9PC aged in situ at those temperature, before the measurements, for different amounts of time. The DS spectra recorded at -20 and -10 °C are shown in Figure 5.8. For both the temperatures, the peak of the loss permittivity shifts to lower frequencies and decreases in intensity, as the annealing time increases. These changes are more pronounced at -20 °C.

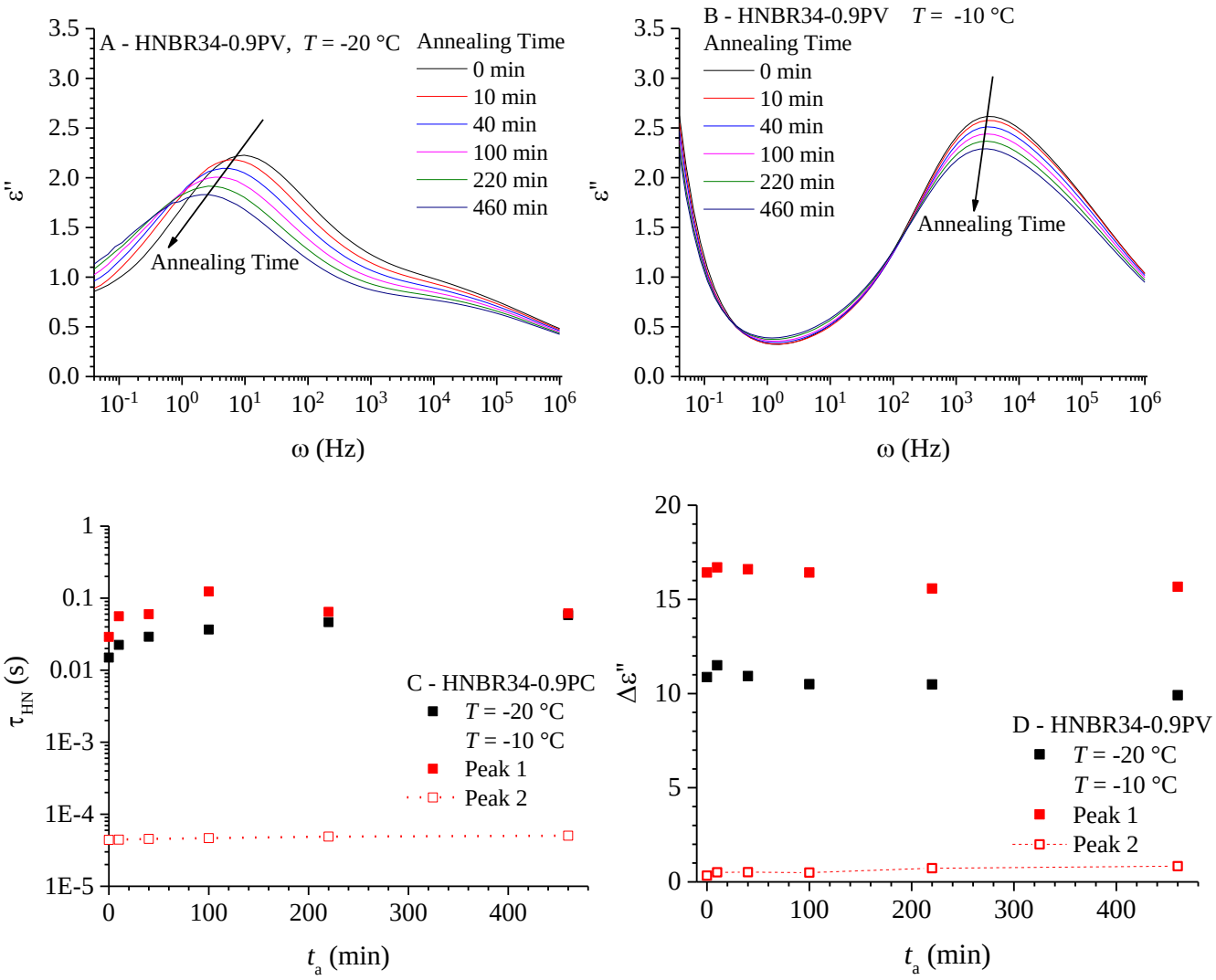

Figure 5.8 Value of loss permittivity as a function of frequency recorded at the temperatures of -20 (A) and -10 °C (B), relative to the peroxide vulcanized HNBR sample HNBR34-0.9PC, aged in situ for the indicated annealing times. Values of characteristics relaxation time τ_{HN} (C) and of dielectric strength of relaxation $\Delta\varepsilon$'', as a function of annealing time t_a. Data obtained at -20 °C (black squares) and -10 °C (red squares). The solid and empty squares in C are the values of the characteristic relaxation times obtained by the combination of two HN function used for fitting the data recorded at T_a = -10 °C.

The curves recorded at -20 °C were fitted to single HN function, whereas for those recorded at -10 °C a combination of two HN functions was used (see Chapter II). The values of the characteristic relaxation time, τ_{HN} extracted from this analysis, are reported in Figure 5.8C as a function of annealing time t_a. At T = -20 °C, the values of the relaxation time τ_{HN} initially increase until they approach a constant value of ≈ 55 ms for annealing times > 100 min. The same occurs at -10 °C for the main peak. At this temperature, the values of τ_{HN} are lower than those measured at -20 °C, for values of the annealing time t_a < 100 min, but for t_a > 100 min, the values of τ_{HN} measured at -10 and -20 °C approach approximatively the same

plateau. The contribution of the second relaxation peak at -10 °C, gives a values of relaxation time of about 45 μs, regardless of annealing time. From the fitting parameters, the dielectric strength of relaxation (Δε'') is also obtained. The values of Δε'' are reported in Figure 5.8D as a function of annealing time. This parameter represents the change in dielectric permittivity associated with molecular relaxation and is related to the dielectric force of relaxation and the amount of energy stored and then released during the molecular relaxation process. As shown in Figure 5.8D, Δε'' decreases only slightly as the annealing time increases. Although this behaviour does not rule out the occurrence of crystallization, the presents of two relaxation peaks for the sample annealed at -10 °C suggests the possible occurrence of microphase separation of segments richer of tetramethylene sequences from sequence richer in ACN units. The resultant phase separated domains would be characterized by different segmental mobility and hence different relaxation and also different aging effects.

5.3 Further evidence of occurrence of relaxation phenomena during annealing at low temperatures.

Another clue indicating that the endothermic phenomena observed in Figures 5.1-5.4 are due to relaxation processes of the amorphous phase rather than to crystal melting is provided by the WAXS measurements collected at low temperature. Since the peroxide vulcanized HNBR sample HNBR34-0.9PC exhibits a significant value of enthalpy of the annealing peak ΔH_{peak} upon thermal annealing at -20 °C for 60 min, low-temperature WAXS profiles were acquired for this sample. Figure 5.9 shows the X-ray powder diffraction profiles collected at room temperature and at -20 °C before (t_a = 0 min) and after annealing for 60 min (t_a = 60 min) at that temperature. No significant differences are observed between the WAXS profiles of Figure 5.9.

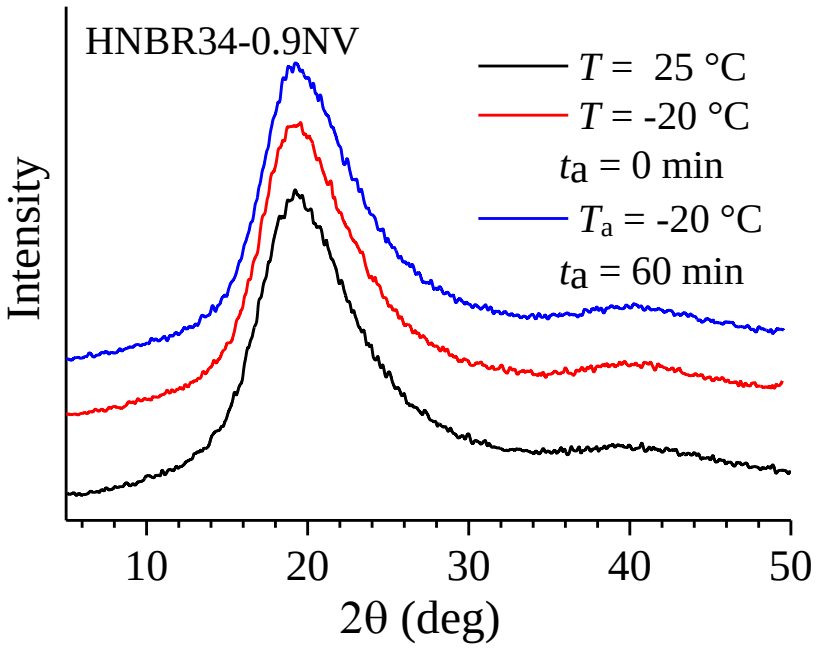

Figure 5.9 X-ray powder diffraction profiles of the peroxide vulcanized HNBR sample HNBR34-0.9PC, recorded at 25 (black curve) and -20 °C, before (t_a = 0 min, red curve) and after annealing at -20 °C for 60 min (blue curve).

Further evidence aimed at clarifying the nature of the low-temperature thermal behavior of amorphous HNBR samples was conducted by determining the effect of low-temperature thermal annealing on the mechanical properties of the peroxide vulcanized sample HNBR34-0.9PC. In Figure 5.10, the stress-strain curves of the HNBR34-0.9PC sample acquired at -20 °C are shown, before (t_a = 0 min) and after annealing at that temperature for t_a = 60 min. From Figure 5.10A, it is evident that the stress-strain curves recorded at -20 °C are practically coincident with each other at high strains. Compared to the stress-strain curve recorded at RT (Fig. 4.11), they exhibit lower stress values at any strain, which is typical of rubber elasticity. In fact, it is well-known that, for elastomers, at the same strain, the stress decreases with increasing temperature (thermoelasticity) due to the negative entropy change upon stretching, and negligible enthalpic contributions.[12,118]

The most significant result in Figure 5.10 is the evidence that thermal annealing at -20 °C does not induce significant differences in the mechanical behavior of this sample. If annealing had induced crystallization, the sample annealed at -20 °C should have shown an increase in mechanical strength compared to the non-annealed one. As for the behavior at low strains, Figure 5.10B shows, on an amplified *x*-*y* scale, that

the slope of the stress-strain curves at low strains, which corresponds to the Young's modulus, decreases as the temperature decreases, and, for the measurements carried out at -20 °C, decreases even more after annealing. If crystallization had occurred during the annealing time at -20°, the slope would have increased, even considering the small relaxation of the amorphous chains pinned to the crystals.[27]

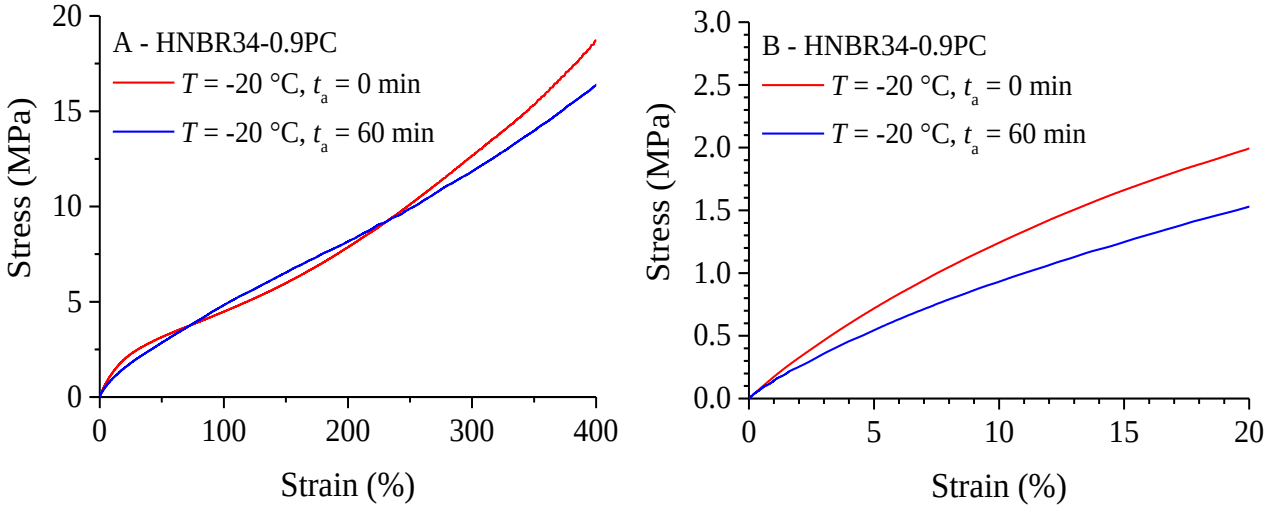

Figure 5.10 Stress strain curves of the peroxide vulcanized HNBR34-0.9PC sample acquired at -20 °C before (t_a = 0 min, red curve) and after annealing at the same temperature for 60 min (blue curve) (A). The curves in B amplify the behavior of the stress-strain curves of A at low strains.

Although the tests conducted to clarify the low-temperature thermal behavior of amorphous HNBR samples provide only indirect evidence, it can be inferred that the endothermic phenomena observed at low temperatures due to isothermal heat treatments at temperatures slightly above the glass transition temperature correspond to relaxation phenomena of the amorphous phase, coupled with the occurrence of microphase separation of segments richer of tetramethylene sequences from sequence richer in ACN units, of different mobility. Such relaxations are somehow reminiscent of the physical aging of amorphous chains in conditions close to the glassy state. In fact, even though the melting of crystals formed by tetramethylene sequences during annealing may not ruled out, the fact that endothermic phenomena induced by annealing are minimal for the sample with 21 wt% ACN content compared with the annealing behaviour of the sample with 34 wt% ACN, strongly supports the hypothesis that relaxation phenomena are prevalent.

Chapter VI

Conclusions

Rubbers are essential raw materials widely employed in industrial sectors due to their unique viscoelastic characteristics. Among various types of rubbers, natural rubber (NR) stands out for its high tensile and tear strength, excellent crack growth resistance, and low hysteresis, positioning itself as one of the most utilized materials. Strain-Induced Crystallization (SIC) is considered a fundamental cause of the mechanical superiority of NR. SIC, among the other advantages, endows the rubber with a self-reinforcing mechanism, capable of dissipating energy and increasing ductility until high strain are reached. In addition to NR, isoprene rubber (IR), butyl rubber (BR), chloroprene rubber (CR), and isoprene-isobutylene rubber (IIR) can also undergo SIC when subjected to external stretching. The crystal structure, the effect external factors such as stretching temperature and stretching rate on the NR properties, and the relationship between SIC and the mechanical response of NR have been extensively studied so far using various techniques. Exploring the relationships between structure and mechanical properties of self-reinforced rubbers during stretching is crucial for the production of advanced rubber products.

Hydrogenated nitrile butadiene rubbers (HNBRs), thanks to their significant main chain saturation, exhibits excellent properties such as high-temperature, ozone and chemical resistance, making them high-quality specialties. The acrylonitrile (ACN) content is a key structural parameter, as it influences the SIC behavior, providing significant mechanical strength to rubber sheets. However, there are only a few studies on the SIC behavior of HNBR. Moreover, the orientation behavior of the amorphous chains also plays a crucial role in the SIC of rubbers during stretching. To date, there are still limited studies on the behavior of molecular chain orientation during the stretching of HNBR and its relationship with SIC.

Another characteristic of these rubbers is the endothermic phenomena that occur after annealing at temperatures near the glass transition (T_g). These phenomena are influenced by various factors, such as ACN content, degree of unsaturation, and crosslink density. In the literature, these phenomena are attributed to the crystallization of polyethylene sequences, but studies on this topic are still limited.

This PhD work moves in this framework. The aim is to investigate the structure-properties relationships of HNBR samples. Samples with different chemical content of ACN and initial residual double bond (iRDB), and different crosslink density were investigated. The study is focused on the analysis of conformation and dynamics of the chains in the crystalline and amorphous states and the mechanisms inducing SIC at room temperature. Additionally, it aims at understanding how SIC is influenced by the degree of crosslinking and the ACN content. The objectives of this project are significant for both the fundamental understanding of polymer physics and rubber elasticity and practical aspects related to rubber processing.

After the Introduction (Chapter I and Experimental Section of Chapter II) the thesis is divided into three parts. Part 1 is focused on the characterization of chemical, physical, and mechanical properties of a set of vulcanized HNBR samples with sulfur curative packages, as well as their corresponding non-vulcanized counterparts. In particular, studies were conducted on the elastomeric network structure, SIC behavior, and chain orientation during stretching, exploring their correlation with crosslink density at a constant ACN and iRDB contents.

Part 2 is centered on the chemical, physical, and mechanical characterization of a subset of HNBR samples with varying ACN content, specifically 21, 34, 39, 43, and 50 wt% of ACN with iRDB $\leq$ 0.9 mol%. Another subset consists of samples with 34 and 43 wt% of ACN with iRDB = 5.5 mol%. This part includes non-vulcanized samples and peroxide vulcanized samples containing 30 phr (part per hundreds of rubber) of carbon black, utilized as a reinforcing filler. Notably, a study on possible occurrence of SIC and orientation of amorphous chains during stretching of initially crystalline HNBR samples with 43 and 50 wt% of ACN and iRDB $\leq$ 0.9 mol% was conducted.

Part 3 delves into the investigation of endothermic phenomena occurring after annealing at temperatures near the T_g. The study employs thermal analysis and dielectric spectroscopy on HNBR samples with 21 wt% of ACN and iRDB $\leq$ 0.9 mol%, as well as HNBR samples with 34 wt% of ACN and different iRDB content, subjected to different degrees and types of vulcanization.

The obtained results can be summarized as follows.

In part 1 a study of the thermal and mechanical properties, along with the characterization of the elastomeric network, the molecular chain orientation and SIC behavior of HNBR samples with ACN content of 34, 36, 43 and 44 wt% and different crosslink density are reported. From the analysis of the sulfur vulcanized HNBR samples through swelling tests and DQ-NMR experiments in the time domain, it emerged that all samples exhibit a homogeneous distribution of sulfur bridges, as they show that the crosslink density ν_e values and the those of residual dipolar coupling constant D_{res} (proportional to ν_e) increase as the added sulfur content increases. Deviation from linearity occur at low added sulfur content because the network created by chemical crosslinking was too loose, and failed to trap physical entanglements, able to contribute to crosslink density. Trapped entanglements are instead formed by adding a quantity of sulfur greater than a threshold. The sample with ACN = 36 wt% and the lowest iRDB content (2 mol%) evidenced the gradual saturation of all available functionalities for added sulfur content close to 2 phr, and consequent formation of polysulfur instead of monosulfur bridges by addition of quantities of sulfur greater than 2 phr.

DQ-NMR experiments allowed to evaluate the defect content in each sample. For non-vulcanized samples and those with low D_{res} values, the defect content exceeds 20 %, while the remaining samples have a defect content oscillating in the range of 5-15 %. The D_{res} distribution is fairly homogeneous across all samples, although non-vulcanized samples and those vulcanized with a low-sulfur content exhibit less homogeneous networks. The values of D_{res} show a linear increase as the ν_e values increase and give by extrapolation to $\nu_e = 0$ the D^0_{res} value of the non-vulcanized samples, with a slope corresponding to the conversion constant between D_{res} and ν_e. The D_{res} values obtained by direct measurement of DQ-NMR signal for the non-vulcanized samples are in a good agreement with the extrapolated D^0_{res} values. This agreement holds for all samples, especially for the values of D^0_{res} obtained by extrapolation of D_{res} vs. ν_e data to $\nu_e = 0$, with ν_e values evaluated using the phantom model of rubber elasticity.

The glass transition temperature (T_g) of HNBRs linearly increases as the ACN content and crosslink density increase, because of decrease in the chain mobility due to the shortening of the chains connecting

adjacent crosslinks (network strands) and the increase in the number of bulky -CN side groups. All HNBR samples are amorphous at room temperature.

The vulcanized HNBR rubbers present tensile stress-strain curve typical of hard elastomers with high ductility and marked strain-hardening at high strain. The main effect of vulcanization results in an increase in mechanical strength and in a decrease in ductility as the crosslink density increases.

The values of the Young's modulus E of the vulcanized samples are three times greater than those of the non-vulcanized counterparts and increase linearly as the D_{res} values increase as predicted by theory. However, in contrast with the theory, the interpolating straight lines of E vs. D_{res} data extrapolate at null D_{res} to non zero values of E. According to the literature, similar deviations from the theoretical predictions occur for ethylene/propylene/diene elastomers. These deviations have been attributed to the heterogeneities of the network.[83] On the other hand, rubbers or gels with significant heterogeneity have been found to follow the theoretical predictions. To date, the effect of network inhomogeneity is still unclear. These effects are subtle, and the results obtained for inhomogeneous systems cannot be generalized.

For the HNBR samples with 34 and 36 wt% of ACN content, the values of stress at break are nearly constant, regardless of crosslink density. For the HNBR samples with 43 and 44 wt% of ACN, instead, the stress at break achieves the maximum values of ≈ 30 MPa at strains of 800 and in between 650-800 %, respectively, for the samples with added sulfur content of 0.75 and 0.75–1.5 phr, respectively. Thus, these measurements, have allowed to determine for these HNBR samples the value of crosslink density at which the tensile strength reaches a maximum, often referred to as the "optimal crosslink density" i.e., the crosslink density that corresponds to the maximum strength that a rubber subject to stretching may achieve.

The HNBR samples with 43 and 44 wt% of ACN, above a critical value of strain, show SIC, due to the crystallization of the alternating sequences of tetramethylene and ACN units (TMAC) in the so-called Form II. From the time-resolved WAXS analysis carried in situ during stretching and release of the tension at different stretching rates at the ESRF Synchrotron Facility it emerged that the strain at SIC onset and

at melting end of the crystals are independent of the stretching rate, with value equal to 220 and 110 % respectively. This entails that the crystals formed by SIC melt in the unloading step at strains significantly lower than the strains marking the SIC onset during the loading step. Furthermore, the crystallinity level measured at any strain in the unloading step, are systematically greater than those achieved at the same strain in the loading step. This hysteretic behavior is the hallmark of SIC.

The crystallinity index decreases as the crosslink density increases, due to the shortening of crystallizable sequences. However, samples with crosslink density above a threshold do not crystallize at all or undergo rupture at strain only slightly greater than that marking the SIC onset. Furthermore, the crystallinity index increases as the strain increases according to a sigmoidal shape, until reaching a maximum value either because it reaches a plateau, or because of sample rupture.

The crystallization of the TMAC sequences is always preceded by the orientation of the amorphous segments. The degree of orientation of the amorphous phase increases as the strain increases until reaching a plateau at strain close to that of incipient crystallization. The orientational order achieved by the crystals is much higher than that of the amorphous phase, remains constant with strain and does not depend on the crosslink density. These results indicate that the SIC behavior of the HNBR samples is similar to that of vulcanized natural rubber and are in agreement with predictions of the Flory theory.[12] The occurrence of SIC together with the high degree of orientation of the so-formed crystals account well for the high tensile strength and strain hardening especially for the samples with low and medium crosslink density.

Specific descriptors are introduced to analyze the SIC behavior of the HNBR samples, namely the maximum crystallinity achieved by stretching (x_c(max)) before breaking, the order parameter of the amorphous phase at plateau and the incremental crystallinity index with respect to the deformation $(dx_c/d\varepsilon)_{max}$ ("SIC rate").

In particular, it is shown that the values of x_c(max) decrease almost linearly as D_{res} increases, due to the disturbance effect exerted by the chemical crosslink that cause a shortening of the crystallizable sequences and reduction of the segmental mobility in the amorphous phase.

The “SIC rate” depend on the crosslink density in a rather complex way. It is argued that this complexity arises because, as the crosslink density increases, two competing effects come into play, namely the decrease of entropy barrier for the primary nucleation and growth of the crystals and the simultaneous decrease of segmental mobility of the amorphous phase.

The presence of a plateau in the orientation parameter of the amorphous chains as a function of elongation indicates that when crystallization occurs, the orientation of the amorphous segments does not increase anymore with strain because crystallization leads to a partial relaxation of the amorphous chains pinned to the crystals, as predicted by Flory theory[27] and observed in vulcanized samples of natural rubber[37,39-42] and synthetic elastomers such as polyisoprene, polybutadiene, and butyl rubber.[34] Furthermore, when the plateau is reached the value of the order parameter is approximately constant and equal to -0.032 for the non-vulcanized HNBR43 samples and -0.029 for the HNBR44 samples. This indicates that for the samples HNBR44 containing a major population of long TMAC sequences, the amorphous segments reach a lower degree of orientation at strain close to that of crystallization onset than that achieved by the samples HNBR43.

As a further remark, it is worth pointing out that the high degree of orientation achieved by the crystals generated by SIC, along with the (relatively) high degree of crystallinity is responsible for the high strain hardening shown by the weakly and medium vulcanized HNBR samples at high strain.

The rubbers with ACN content of 34 and 36 wt% do not experience SIC at room temperature and stretching only induces the orientation of the amorphous chains along the stretching direction. It is shown that for the subsets of HNBR samples with 34 and 36 wt% of ACN, the samples with the greatest crosslink density undergo affine deformation with values of the order parameter that linearly increase in absolute values as the strain increases. The samples with low crosslink density, instead, follow the affine deformation model only for strains below 250 – 300 %. At strains greater than 250 – 300 %, the increase of the order parameter with the deformation slows down, probably due to slip motions of chains caused by disentanglement of transient entanglements. However, regardless of the crosslink density, the

orientation degree of the amorphous segments achieved at the maximum strain is almost the same for all rubbers.

In the part 2 of PhD work, the structure, thermal and mechanical properties of HNBR samples with different ACN content were analyzed. The properties of peroxide vulcanized samples with identical composition of the curative package plus 30 phr of carbon black as reinforcing filler were compared to those of the non-vulcanized counterparts.

From the powders WAXS analysis, it was observed that the non-vulcanized samples are amorphous at room temperature, except for those with 43 and 50 wt% of ACN and iRDB ≤ 0.9 mol%, crystallizing in the Form II. In contrast, peroxide-vulcanized samples are amorphous. The crystallinity index derived from WAXS data is 5 and 13% for the samples with 43 and 50 wt% ACN, respectively. For HNBR with 50 wt% of ACN this result was confirmed by determination of crystallinity index with MSE-NMR measurements which gave a value of ≈ 11 %.

Calorimetric measurements carried out for the samples with 43 and 50 wt% ACN and iRDB ≤ 0.9 mol%, indicate that the Form II crystals melt at ≈ 42 °C. The T_g increases as the ACN content increases, both for vulcanized and non-vulcanized samples. Vulcanized samples have slightly higher T_g values than those of non-vulcanized counterparts at identical ACN content.

DQ-NMR experiments revealed that the crosslink density of vulcanized and non-vulcanized samples is constant, regardless of ACN and iRDB content. All samples exhibit a homogeneous crosslink density distribution with a low overall relative distribution width. Compared with the other samples, the non-vulcanized and peroxide vulcanized HNBR sample with 21 wt% of ACN shows a lower crosslink density and the least homogeneous crosslinking distribution.

The non-vulcanized HNBR rubbers show stress-strain curves of weak elastomers, regardless of iRDB content. Exceptions were observed for the semi-crystalline samples, which show significantly greater tensile strength and values of Young's modulus three times greater (15 MPa) than that achieved upon vulcanization (5 MPa). In contrast, peroxide vulcanized samples exhibit properties of stiff elastomers with similar values of stress and strain at break, regardless of ACN and iRDB content. Only the peroxide

vulcanized sample with 21 wt% of ACN shows slightly lower stress and strain at break values than the other vulcanized samples.

The possible crystallization and chain orientation occurring during stretching was studied only for the semi-crystalline non-vulcanized samples with 43 and 50 wt% ACN. The stretching of these samples to high strains was feasible due to presence of crystals that hinder viscous flow and act as physical crosslinks. The samples exhibit a gradual increase of crystallinity level during stretching not due to SIC, but rather due to the nucleation effect exerted by the crystals initially present in the samples. The increase in the percentage of crystalline phase is more pronounced in the sample with 50 wt% of ACN, due to the greater population of TMAC sequences of high length.

Upon release of the tension, the crystalline phase formed during stretching melts as the strain decreases. The values of the incremental crystallinity $\Delta x_c(\varepsilon)$ measured at any given strain during the loading and unloading steps are coincident (null hysteresis). However, as the strain of 200% is approached, the tensile force goes to zero and, at the end of the unloading steps, a small fraction of the newly formed crystals (1% and 3% for the samples with 43 and 50 wt% of ACN) remains entrapped in the rubber network. The null hysteresis is in contrast with the large hysteresis originating from SIC behavior. In fact, the SIC mechanism entails that the crystallinity level achieved at any given strain during the unloading step are significantly greater than those achieved in the loading step.

The orientation degree of the amorphous and crystalline phases tends to increase (decrease) as the strain increases (decreases) during stretching (release of the tension). For the amorphous segments these changes are gradual, and the related order parameter does not reach a true plateau. Furthermore, at the end of the retraction step, while for the sample with 43 wt% of ACN the amorphous phase becomes completely disoriented, for the sample with 50 wt% of ACN the amorphous phase retains some residual orientation.

The orientation degree of the crystalline phase increases *ex abrupto* already at low strain reaching a constant value. The so achieved value remains constant even during the release of the tension step, and only at the end of the retraction step a sudden decrease of the degree of orientation occurs. However, whereas for the sample with 43 wt% of ACN, the degree of orientation achieved by the crystalline and

amorphous phases is completely lost, for the sample with 50 wt% of ACN, the crystalline and amorphous phases remain partially oriented, even after aging of the sample at rest for long time, probably because some crystals and the surrounding amorphous chains remain entrapped in the elastomeric network by effect of local tensions.

The null hysteresis, the almost immediate crystallization occurring upon stretching, along with the absence of true plateau in the values of the order parameter of the amorphous phase suggest that the driving force for the formation of new crystals is namely due to the nucleation effect exerted by the initially present crystals in the samples and that this effect possibly overrides the SIC mechanism.

Part 3 delves into the study of the DSC endothermic peaks generated by annealing treatments at temperatures near T_g, of some amorphous HNBR samples.[65,66] These annealing peaks have been attributed to the melting of crystals formed by long tetramethylene sequences susceptible to crystallize in the orthorhombic form of polyethylene (PE) from the amorphous phase, during low-temperature isothermal annealing. The hypothesis that the annealing peaks may be due to relaxation phenomena, similar to those associated to physical aging of the amorphous phase in the glassy state has been completely overlooked.[65,66]

The nature of annealing peaks was studied for a peroxide vulcanized HNBR samples with 21 wt% of ACN and iRDB ≤ 0.9 mol% and for non-vulcanized, sulfur vulcanized and peroxide vulcanized HNBR samples with 34 wt% of ACN, different iRDB content (≤ 0.9, 4 and 5.5 mol%) and different crosslink density.

In the assumption that long tetramethylene sequences crystallize at low temperatures due to annealing, the HNBR sample with 21 wt% of ACN was expected to show an amplification of the endothermic phenomena observed in the DSC heating thermograms recorded following annealing. However, for the HNBR sample with 21 wt% of ACN, in all experiments the enthalpy values relative to the annealing peak ΔH_{peak} results systematically lower than those measured, ceteris paribus, for the HNBR samples with 34

wt% of ACN. It is also shown that the temperature of the annealing peak T_{peak} increases as the annealing temperature T_a increases, for all the samples.

Although the increase of T_{peak} as T_a increases complies with the hypothesis that the annealing peaks can be due to the melting of crystals generated by thermally induced crystallization, the almost invariance of T_{peak} for the peroxide vulcanized and non-vulcanized HNBR samples with 34 wt% of ACN but different iRDB content, and the low tendency of the HNBR sample with 21 wt% of ACN to "crystallize" even after long annealing times at suitable "undercoolings", suggests that the annealing peak is due to chain relaxation of the amorphous chains induced by physical aging, rather than to the melting of crystals formed during annealing.

This hypothesis was also supported by additional experiments showing that for non-vulcanized and sulfur vulcanized HNBR samples with 34 wt% of ACN, iRDB of 4 mol% and different crosslink density, the values of ΔH_{peak} measured adopting the same annealing protocol decrease only slightly as the crosslink density increases. Since the chemical crosslinks exert a disturbance effect on crystallization, if the annealing peak had been due to the melting of the crystals formed by thermally induced crystallization, a remarkable decrease in enthalpy would have occurred. However, since these experiments were carried out by fixing the annealing temperature T_a at -20 °C, and the glass transition temperature of these sample T_g are not equal, but increases as the crosslink density increases, the values of ΔH_{peak} measured at the same annealing time t_a for the different samples were not identical. Nevertheless, the values of the ratio ΔH_{peak} $(T_a\text{-}T_g)^{-1}$ measured at the same t_a were shown to be almost equal for all samples. Based on these results and considering that even the HNBR sample with the highest crosslink density show annealing peaks in annealing experiments, it is challenging to attribute the annealing peaks to the melting of the crystals formed by long ethylene sequences via thermally induced crystallization. This supports the hypothesis that the annealing behavior reflects relaxation phenomena of the amorphous phase, coupled with the occurrence of microphase separation of segments richer of tetramethylene sequences from sequence richer in ACN units, of different mobility.

Further clues supporting the above hypothesis were provided resorting to dielectric spectroscopy. These measurements showed that at the temperature at which the annealing experiments were carried out in the DSC apparatus, the segmental mobility of the HBNR samples with 21 and 34 wt% ACN were similar. This result makes sound the conclusions extracted from DSC measurements based on the comparison of the quantities ΔH_{peak} relative to a couple of samples with different glass transition temperatures. Dielectric spectroscopy measurements also showed that the dielectric relaxation force measured in isothermal conditions at these same annealing temperatures, also remains constant as the annealing time increases. This finding allows to rule out that crystallization processes occur during annealing, as the values of dielectric force would decrease upon crystallization.

Occurrence of crystallization during annealing was also ruled out by the absence of Bragg's peaks in the WAXS profiles recorded at low temperature for a HNBR annealed sample, and by the decrease in stress as a function of the strain, for measurements carried out at low temperature, on an annealed sample.

In conclusion, the present study has allowed to address different aspects of rubber science, linked to SIC, relaxation of the amorphous segments, orientation of the crystalline and amorphous phases, phase transitions etc. We show that through the judicious selection of the appropriate techniques, quantitative structure-properties relationships (QSPR) of HNBR samples may be elucidated. This approach has allowed to make a step forward in the understanding of the polymer properties at the molecular level.

Appendix

Table A1 Values of density, total amount of rubber and components in the curative package (Rubber + Curative Package), sulfur content in phr and mol/cm^3, crosslink density estimated from equilibrium swelling experiments ν_e on the basis of affine and phantom model and average number of sulfur atoms per bridge ($N_{\text{Sulfur Atoms}}$ per bridge), for the different subsets of sulfur vulcanized HNBR samples and the corresponding non-vulcanized ones.

Samples		Density (g/cm^3)	Rubber + Curative Package (phr)	Sulfur (phr)	Sulfur 10^5 (mol/cm^3)	ν_e 10^5 (mol/cm^3)[a]	$N_{\text{Sulfur Atoms}}$ per bridge	ν_e 10^5 (mol/cm^3)[a]	$N_{\text{Sulfur Atoms}}$ per bridge
						Affine Model		Phantom Model	
HNBR34-0.38	ACN 34 wt%	0.991	107	0.38	11	9.0	2.4	15	1.7
HNBR34-0.75		0.994	108	0.75	22	34	1.2	53	0.8
HNBR34-1.1		0.997	109	1.13	32	51	1.3	77	0.8
HNBR34-1.5		0.999	110	1.50	43	58	1.5	87	1.0
HNBR34-1.9		1.002	111	1.88	53	69	1.5	101	1.0
HNBR34-2.3		1.005	112	2.26	63	74	1.7	109	1.2
HNBR34-3.0		1.010	114	3.01	83	82	2.0	119	1.4
HNBR36-0.38	ACN 36 wt%	1.002	107	0.38	11	9.5	2.3	16	1.4
HNBR36-0.75		1.004	108	0.75	22	31	1.4	48	0.9
HNBR36-1.1		1.007	109	1.13	33	39	1.6	61	1.1
HNBR36-1.5		1.010	110	1.50	43	46	1.9	69	1.2
HNBR36-1.9		1.012	111	1.88	54	61	1.7	91	1.2
HNBR36-2.3		1.015	112	2.26	64	47	2.7	72	1.8
HNBR36-3.0		1.020	114	3.01	84	51	3.3	78	2.2
HNBR43-0.75	ACN 43 wt%	1.024	108	0.75	22	27	1.6	44	1.0
HNBR43-1.1		1.027	109	1.13	33	35	1.9	55	1.2
HNBR43-1.5		1.029	110	1.50	44	45	1.9	70	1.2
HNBR43-2.3		1.034	112	2.26	65	68	1.9	104	1.3
HNBR43-3.0		1.039	114	3.01	88	76	2.3	116	1.5
HNBR44-0.38	ACN 44 wt%	1.022	107	0.38	44	8.8	2.6	15	1.5
HNBR44-0.75		1.025	108	0.75	22	26	1.7	41	1.1
HNBR44-1.1		1.027	109	1.13	33	35	1.9	54	1.2
HNBR44-1.5		1.030	110	1.50	44	46	1.9	70	1.3
HNBR44-1.9		1.032	111	1.88	55	56	1.9	84	1.3
HNBR44-2.3		1.035	112	2.26	65	65	2.0	97	1.4
HNBR44-3.0		1.039	114	3.01	86	75	2.3	110	1.6

[a] Obtained by swelling test

[b] Data are affected by 10% relative error

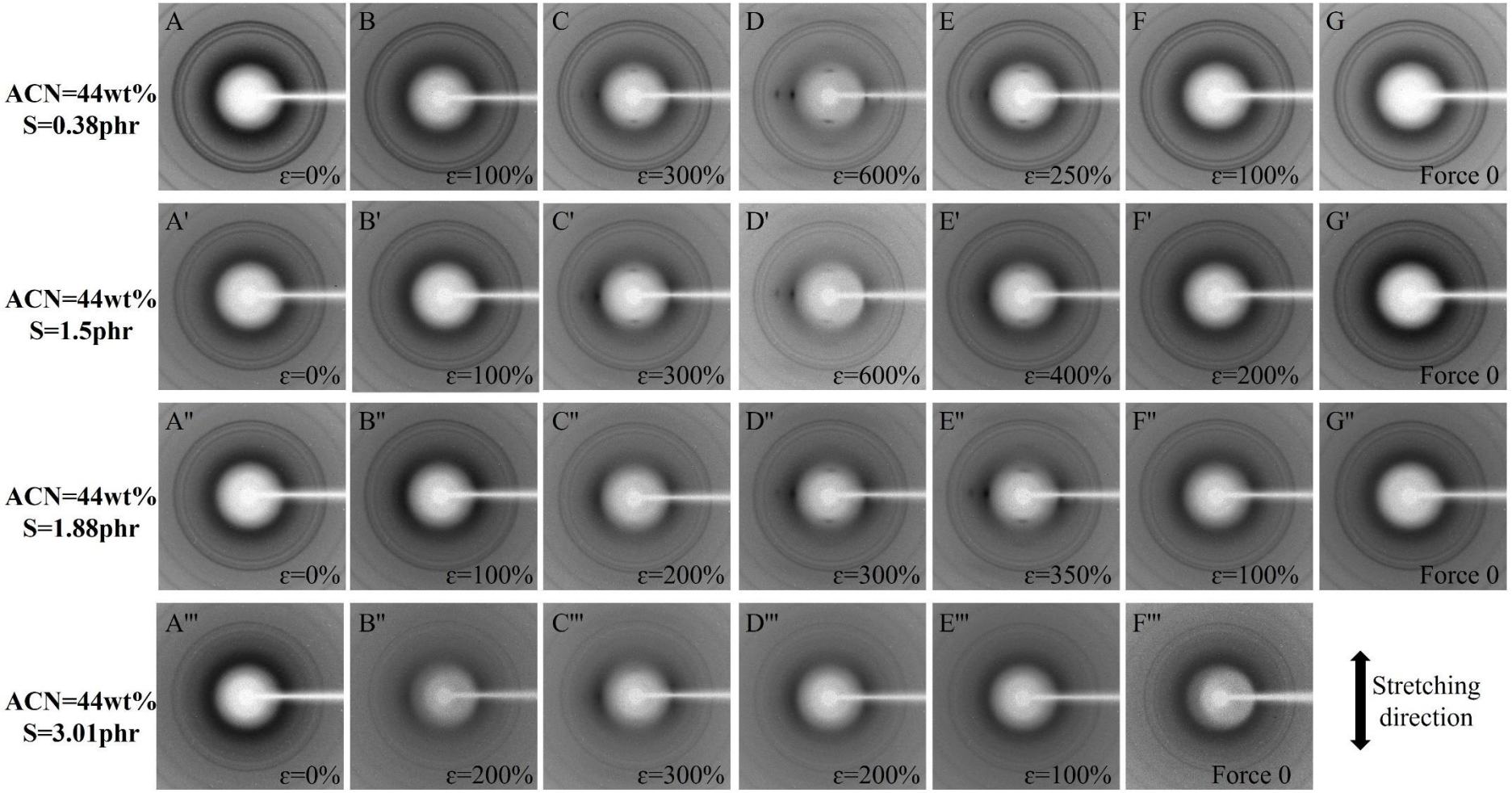

Figure A1. 2D WAXS patterns of fibers of the vulcanized samples with different crosslink density of the HNBR sample with 44 wt% of ACN, recorded at room temperature during the loading at strain ε up to strains close to break and the unloading at strain ε up to complete release of the tension (Force 0). The stretching direction is indicated.

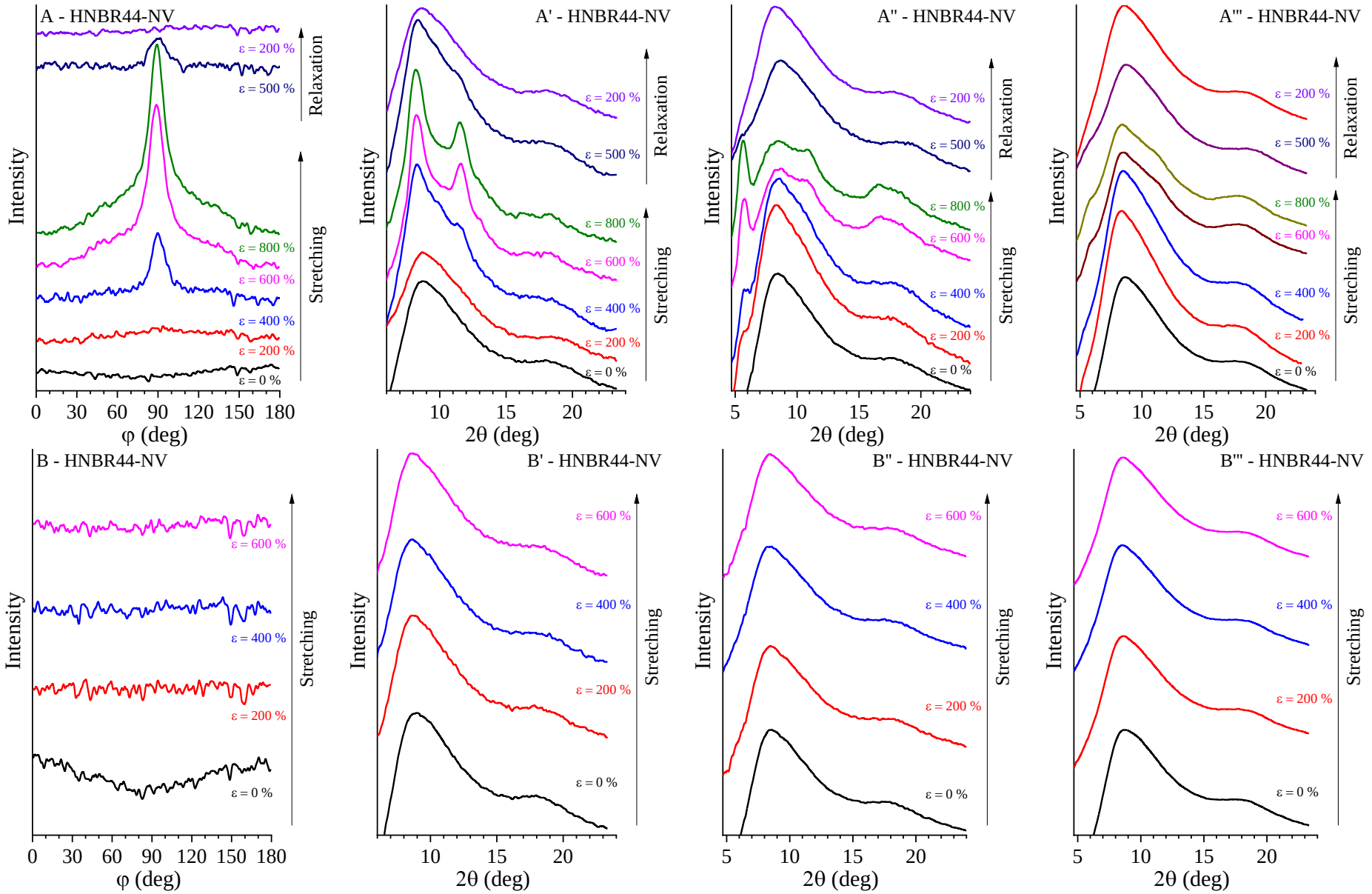

Figure A2. WAXS profiles of the non-vulcanized HNBR sample with 44 wt% of ACN stretched at fast rate equal to 10 times the initial gauge length (A-A'") and at slow average rate of ≈30 mm/min (B-B'"). Azimuthal (A,B), equatorial (A',B'), meridional (A",B") and radial profiles (A'",B'").

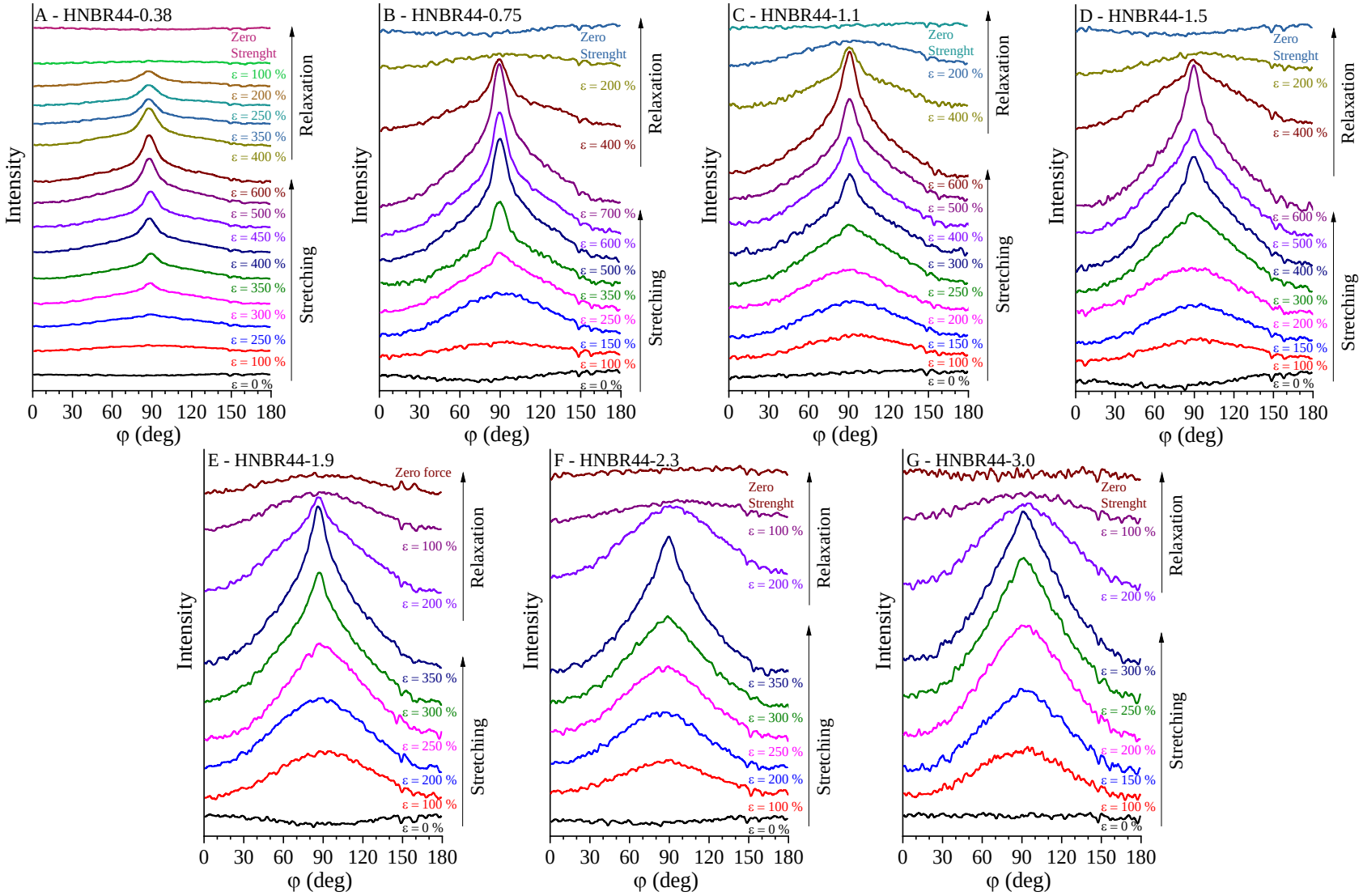

Figure A3. Azimuthal WAXS profiles of equatorial reflex at 8.4°of vulcanized samples of the HNBR with 44 wt% of ACN. The sulfur content (phr) for each sample is 0.38 (A), 0.75 (B), 1.13 (C), 1.50 (D), 1.88 (E), 2.26 (F) and 3.01 (G).

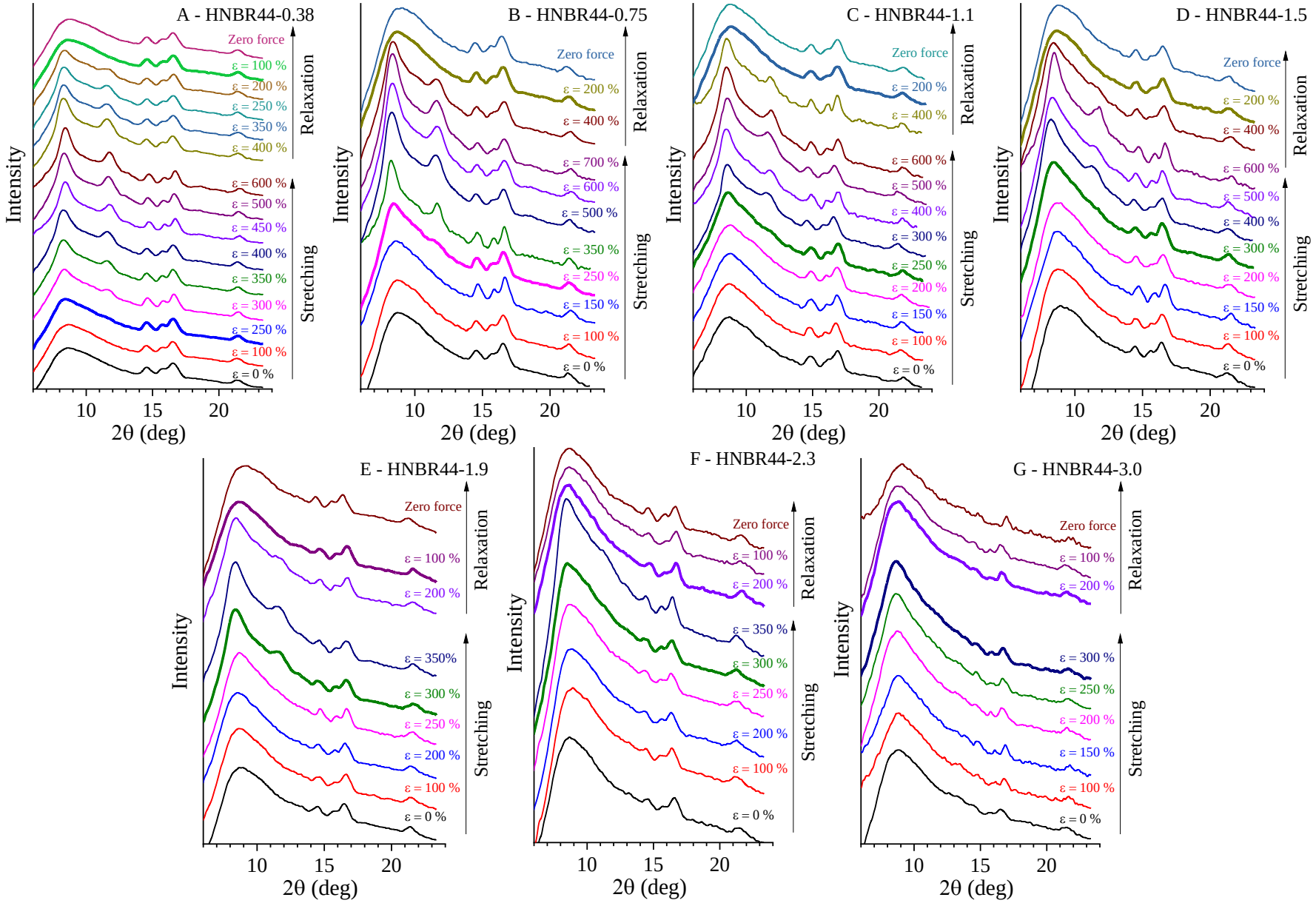

Figure A4. Equatorial WAXS profiles of vulcanized HNBR sample with 44 wt% of ACN, and different crosslink density. The sulfur content (phr) for each sample is 0.37 (A), 0.75 (B), 1.13 (C), 1.50 (D), 1.88 (E), 2.26 (F) and 3.01 (G). The profiles marking the onset of crystallization during stretching and the melting of the so formed crystal during the release of tension are bold.

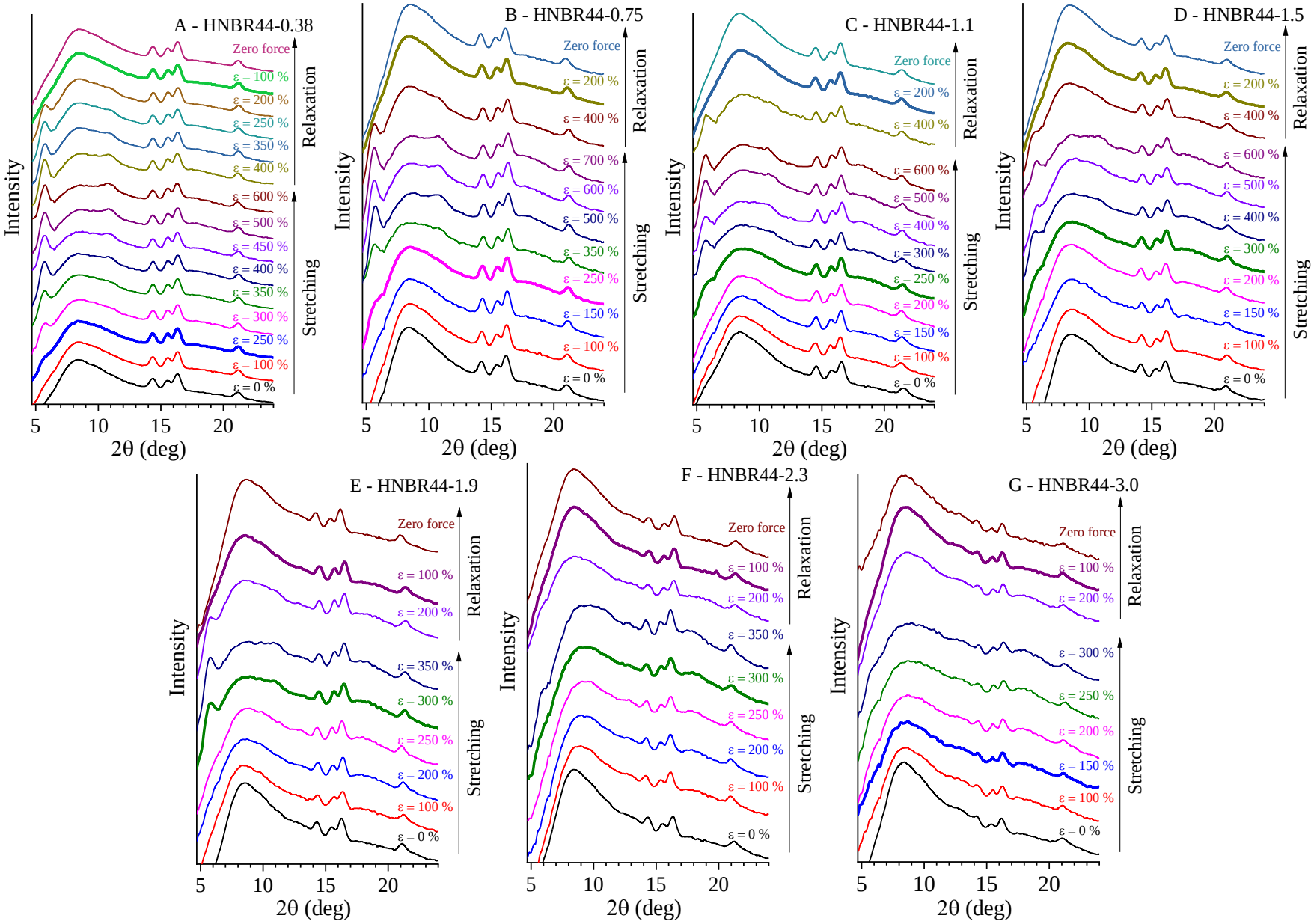

Figure A5. Meridional profiles of vulcanized HNBR sample with 44 wt% of ACN, and different crosslink density. The sulfur content (phr) for each sample is 0.37 (A), 0.75 (B), 1.13 (C), 1.50 (D), 1.88 (E), 2.26 (F) and 3.01 (G). The profiles marking the onset of crystallization during stretching and the melting of the so formed crystal during the release of tension are bold.

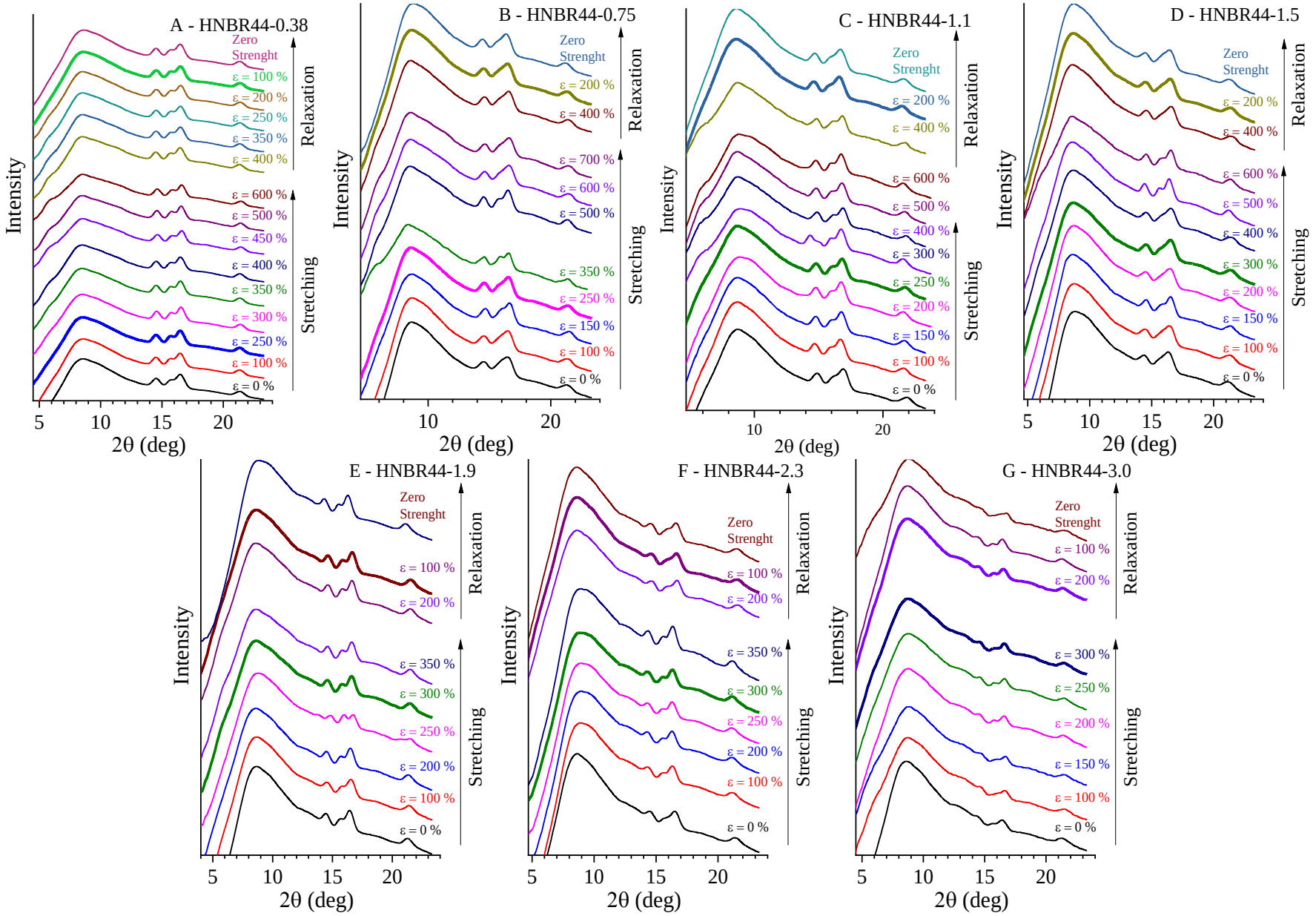

Figure A6. Radial profiles of vulcanized samples of the HNBR with 44 wt% of ACN. The sulfur content (phr) for each sample is 0.37 (A), 0.75 (B), 1.13 (C), 1.50 (D), 1.88 (E), 2.26 (F) and 3.01 (G). The profiles marking the onset of crystallization during stretching and the melting of the so formed crystal during the release of tension are bold.

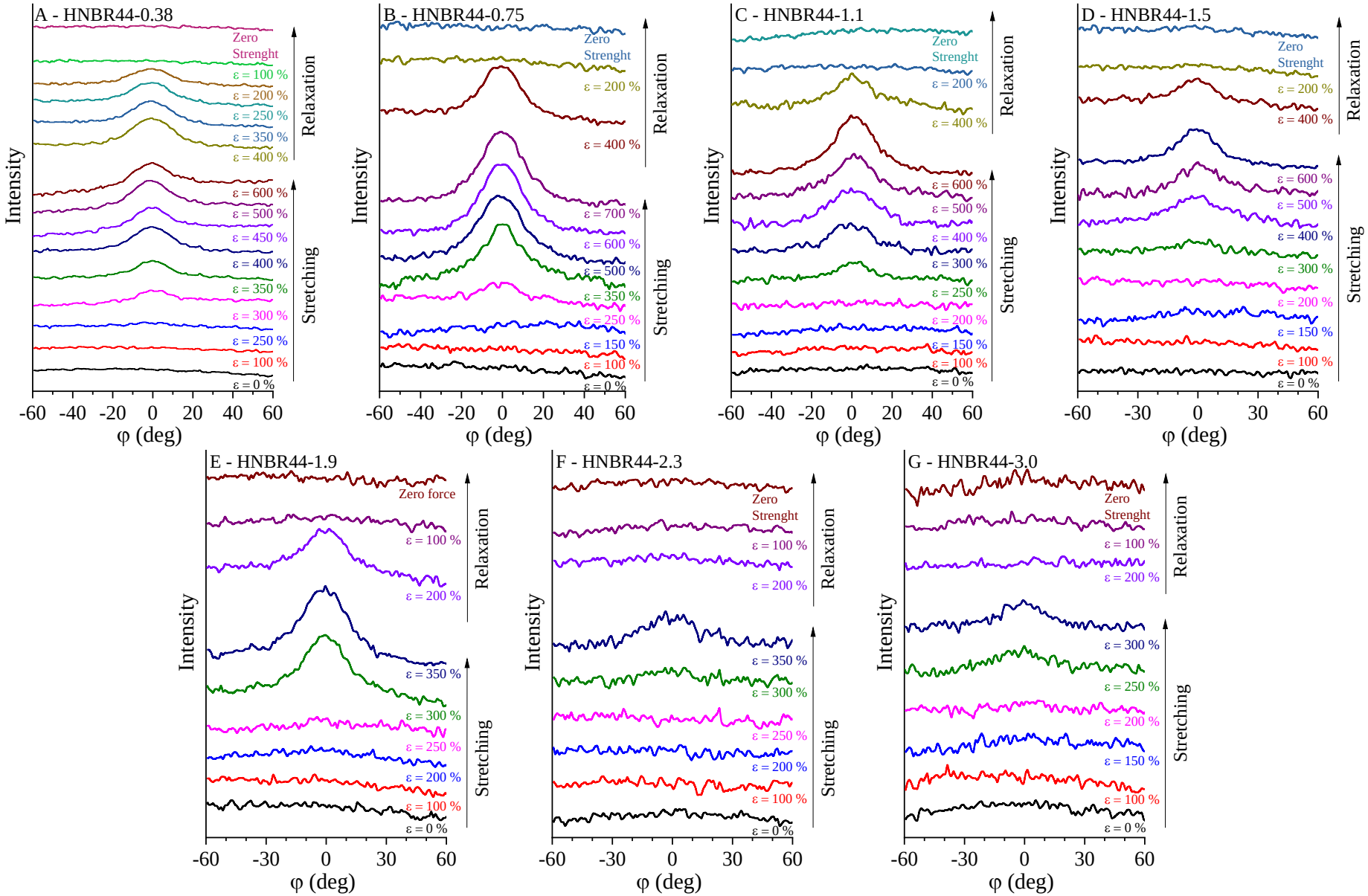

Figure A7. Azimuthal WAXS profiles of meridional reflex at 5.7° of vulcanized samples of the HNBR with 44 wt% of ACN. The sulfur content (phr) for each sample is 0.38 (A), 0.75 (B), 1.13 (C), 1.50 (D), 1.88 (E), 2.26 (F) and 3.01 (G).

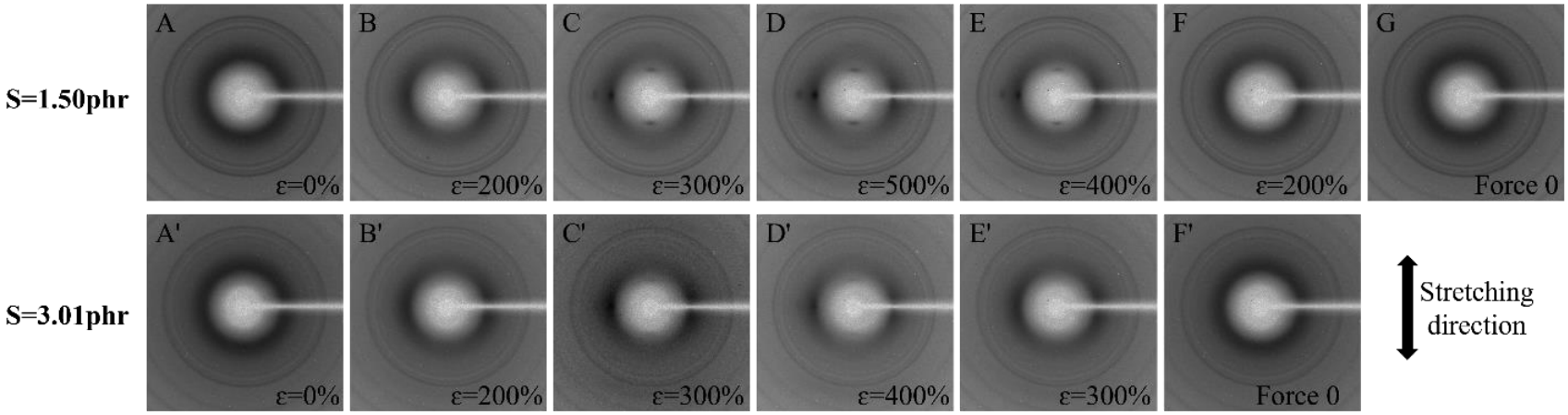

Figure A8 2D WAXS fiber patterns of vulcanized HNBR samples with 43 wt% ACN and different crosslink densities, recorded at room temperature during the loading at strain ε up to strains close to break and the unloading at strain ε up to complete release of the tension (Force 0). The stretching direction is indicated.

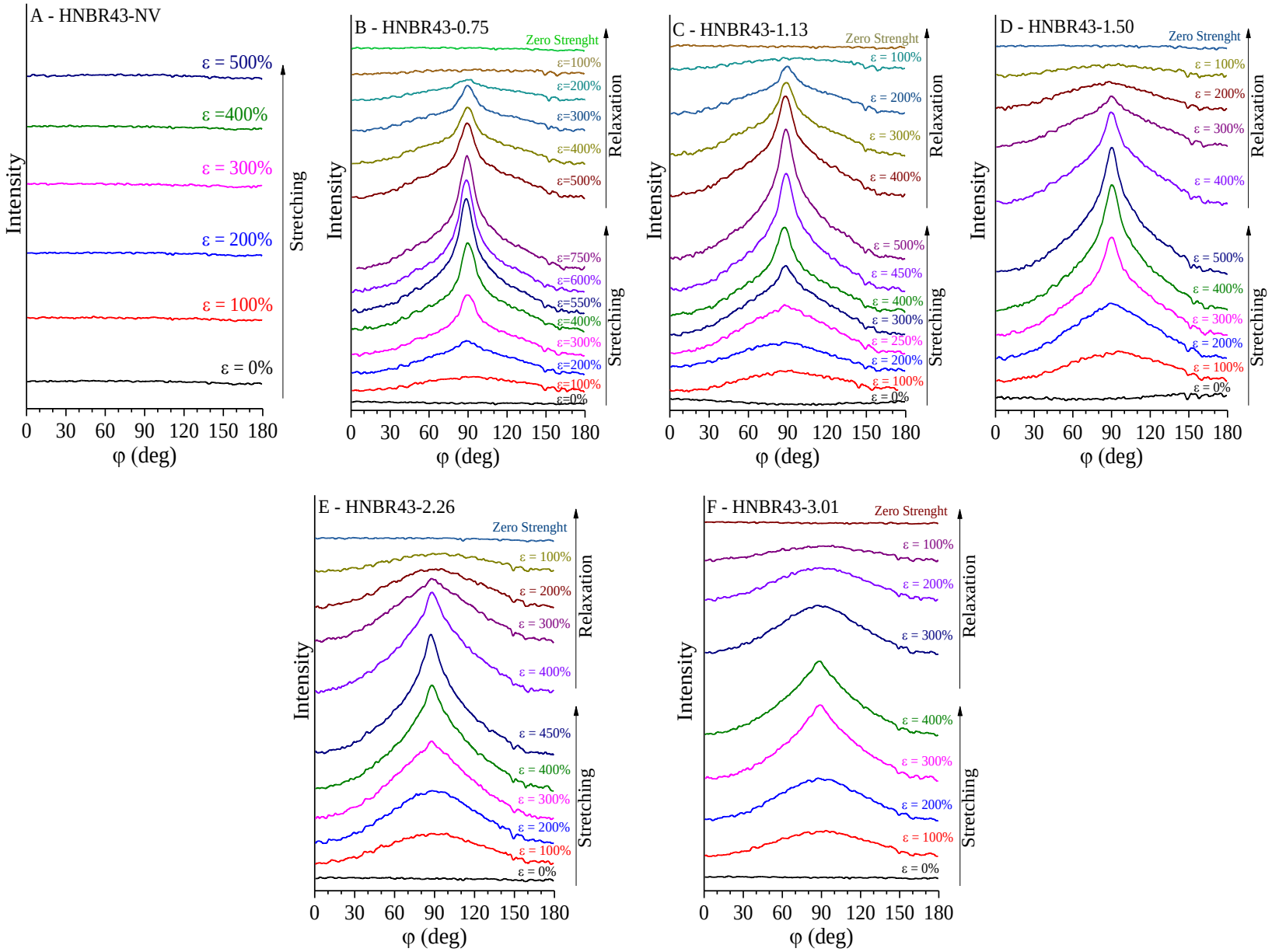

Figure A9 Azimuthal WAXS profiles centered on the equatorial reflection at 8.4°for the non-vulcanized (A) and vulcanized (B-F) HNBR samples with 43 wt% of ACN. The added sulfur content (phr) is 0 (A), 0.75 (B), 1.13 (C), 1.50 (D), 2.26 (E) and 3.01 (F).

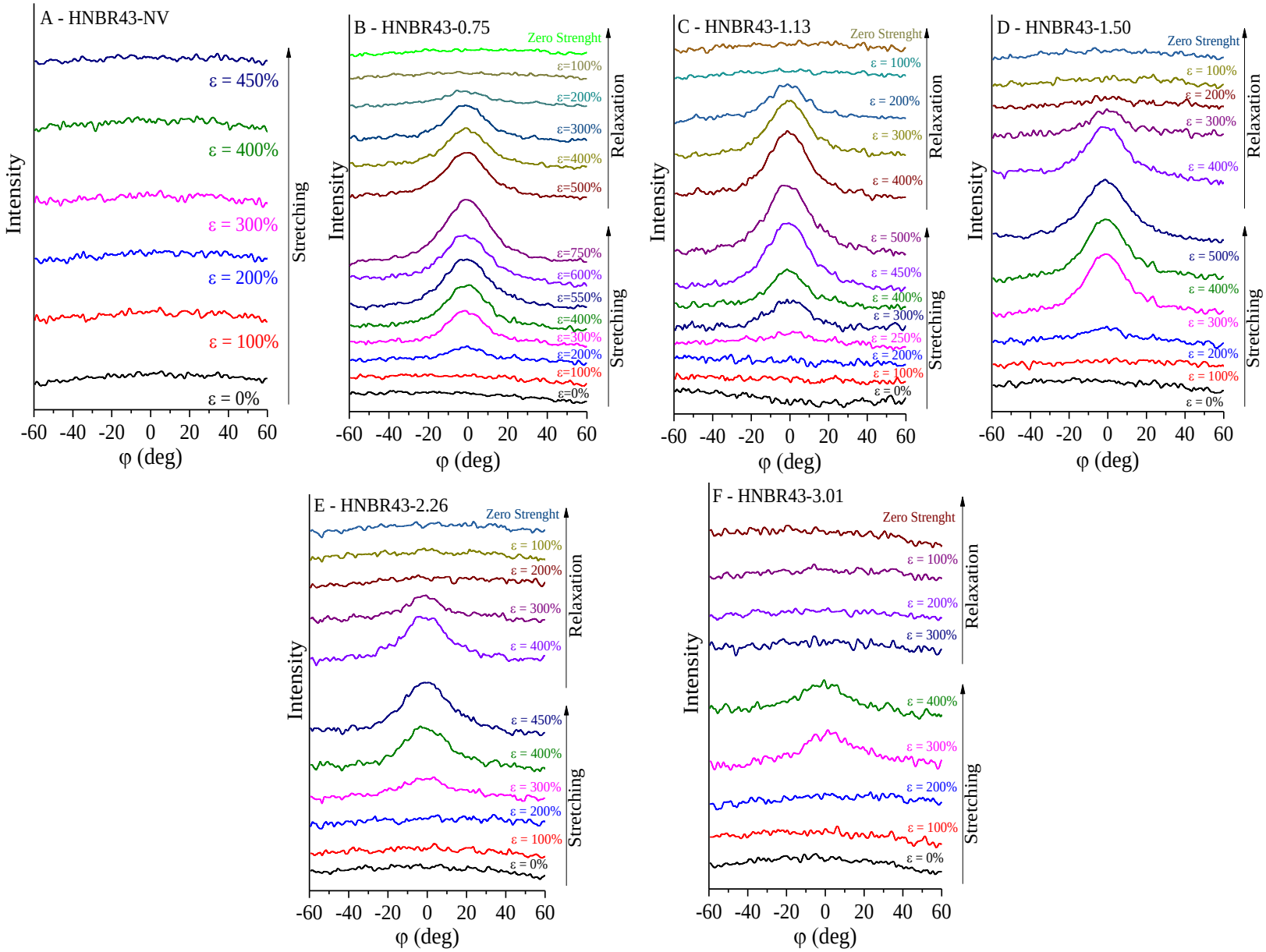

Figure A10 Azimuthal WAXS profiles centered on the meridional reflection at 5.7° for the non-vulcanized (A) and vulcanized (B-F) HNBR samples with 43 wt% of ACN. The added sulfur content (phr) is 0 (A), 0.75 (B), 1.13 (C), 1.50 (D), 2.26 (E) and 3.01 (F).

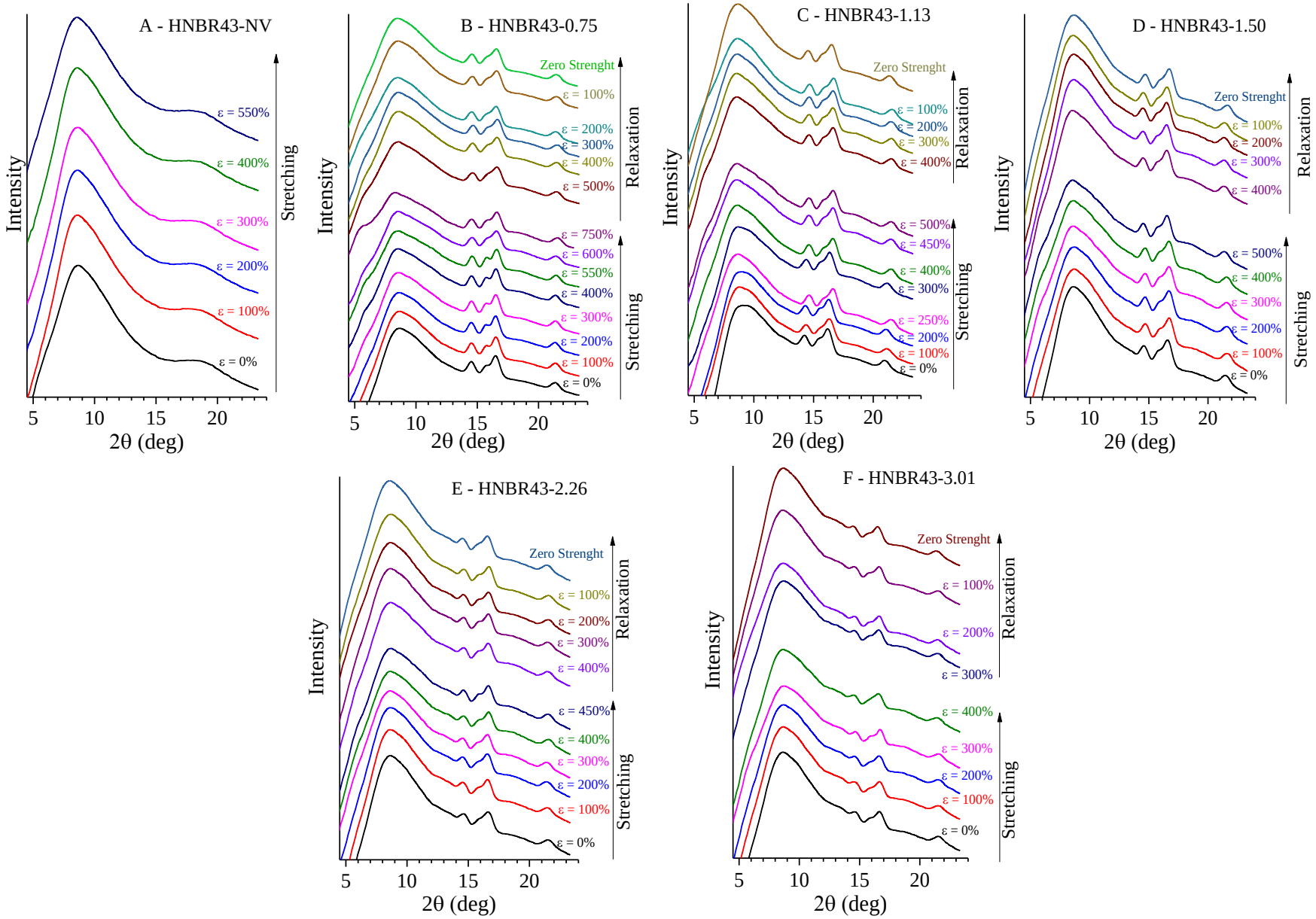

Figure A11 Radial profiles of non-vulcanized (A) and vulcanized (B-F) HNBR samples with 43 wt% of ACN, and different crosslink density. The sulfur content (phr) is 0 (A), 0.75 (B), 1.13 (C), 1.50 (D), 2.26 (E) and 3.01 (F).

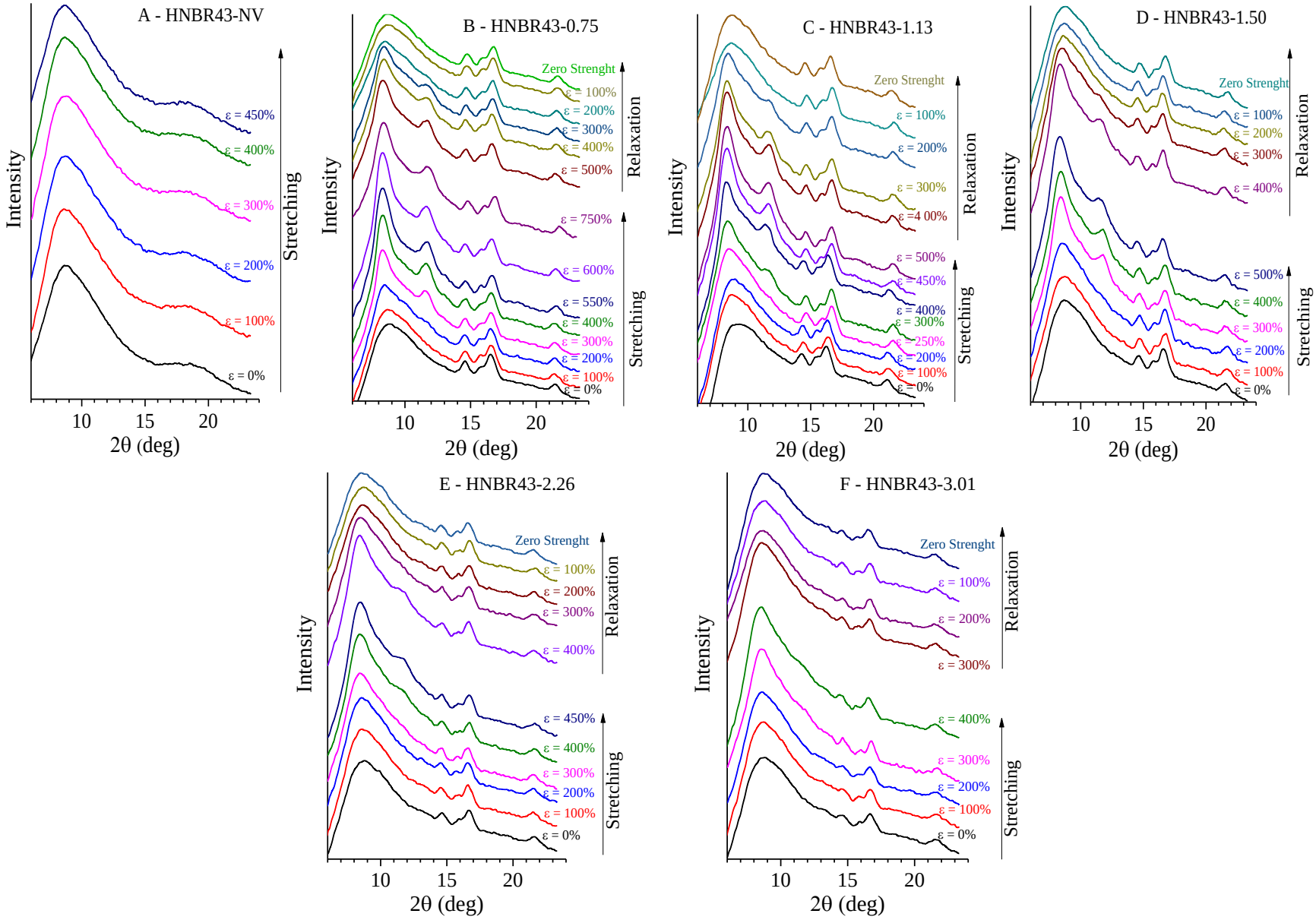

Figure A12 Equatorial profiles of non-vulcanized (A) and vulcanized (B-F) HNBR samples with 43 wt% of ACN, and different crosslink density. The sulfur content (phr) is 0 (A), 0.75 (B), 1.13 (C), 1.50 (D), 2.26 (E) and 3.01(F).

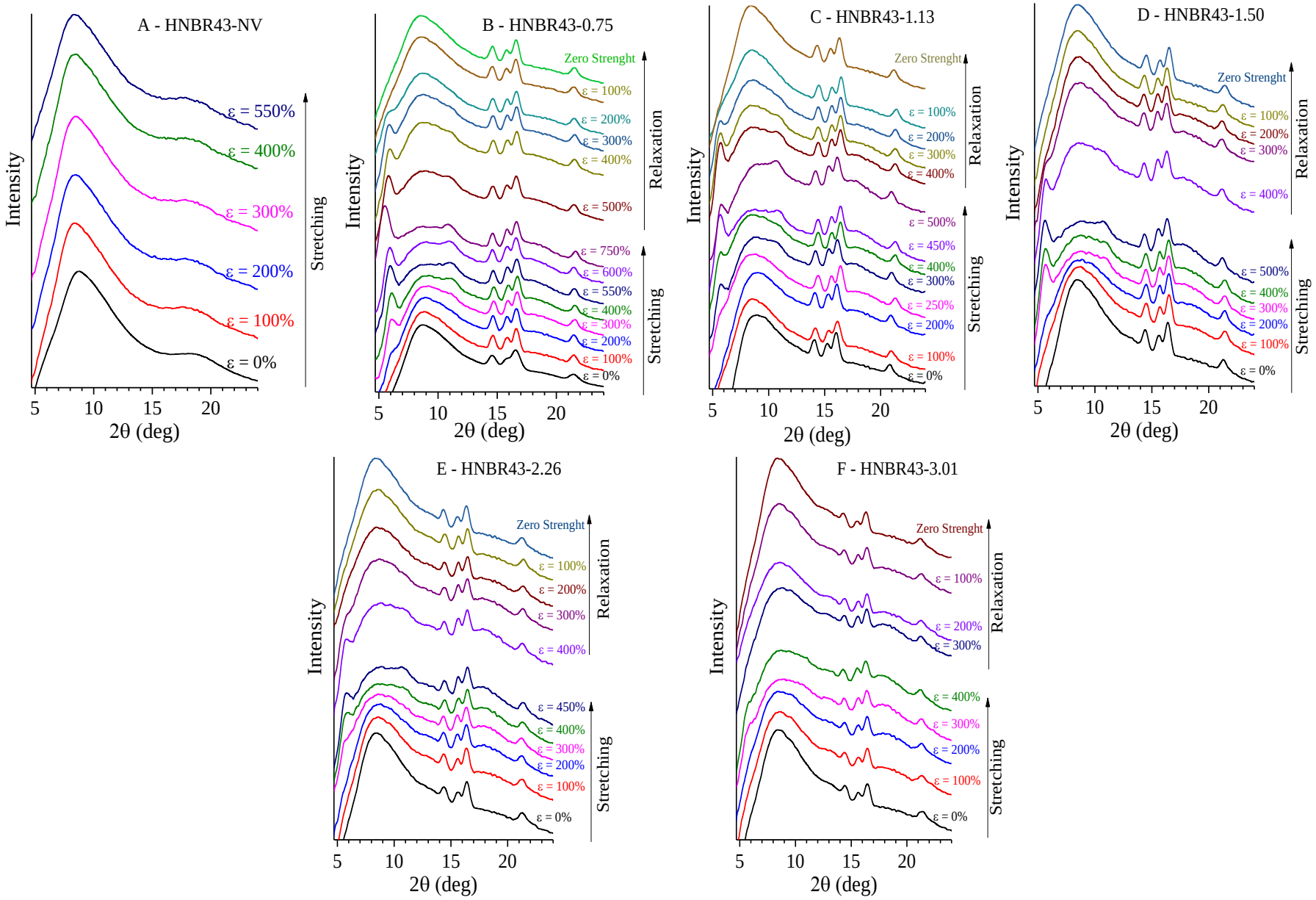

Figure A13 Meridional profiles non-vulcanized (A) and vulcanized (B-F) HNBR samples with 43 wt% of ACN, and different crosslink density. The sulfur content (phr) for each sample is 0 (A), 0.75 (B), 1.13 (C), 1.50 (D), 2.26 (E) and 3.01 (F).

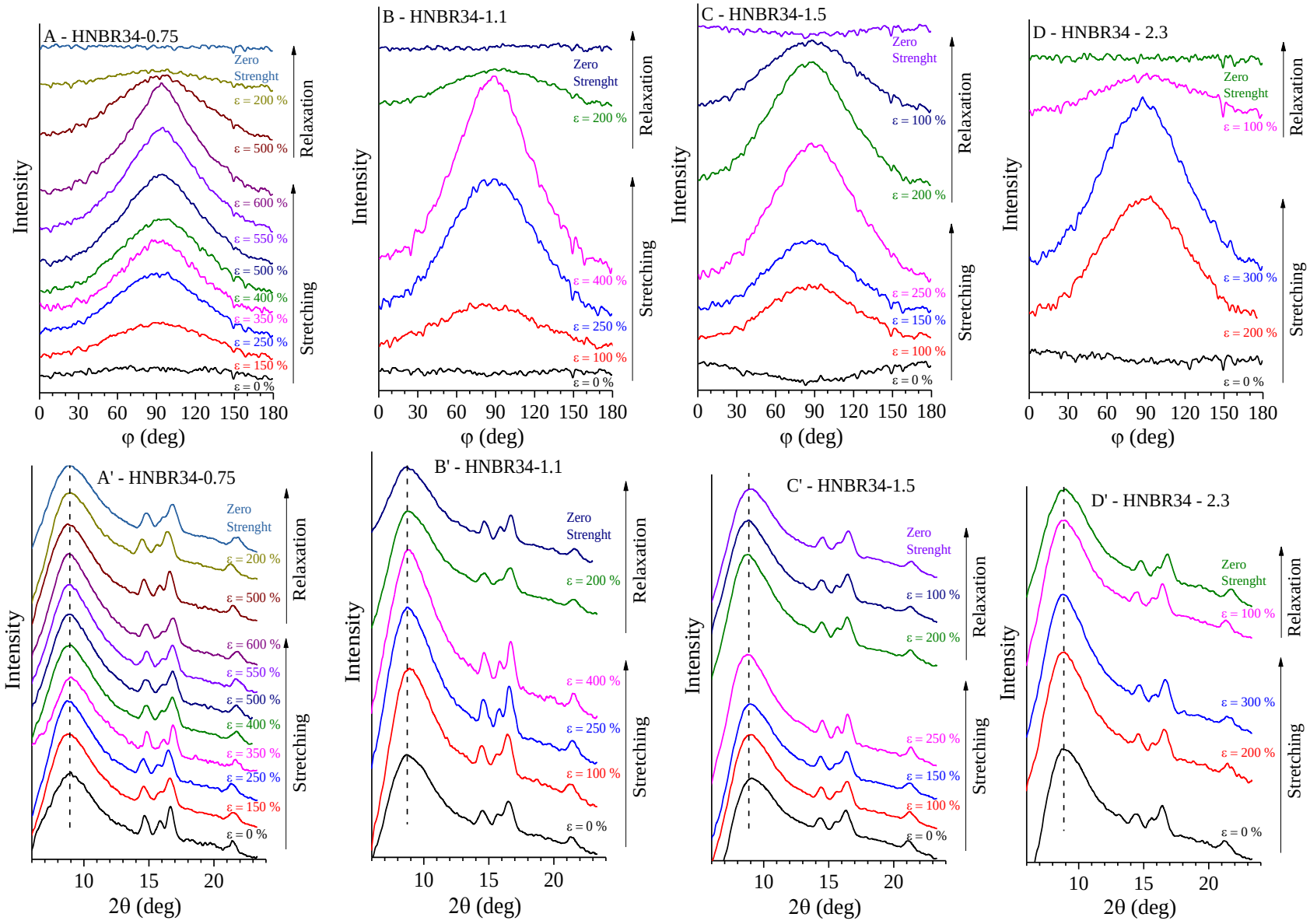

Figure A14. Azimuthal (A-D) and equatorial (A'-D') profiles of sulfur vulcanized samples of the HNBR with 34 wt% of ACN.

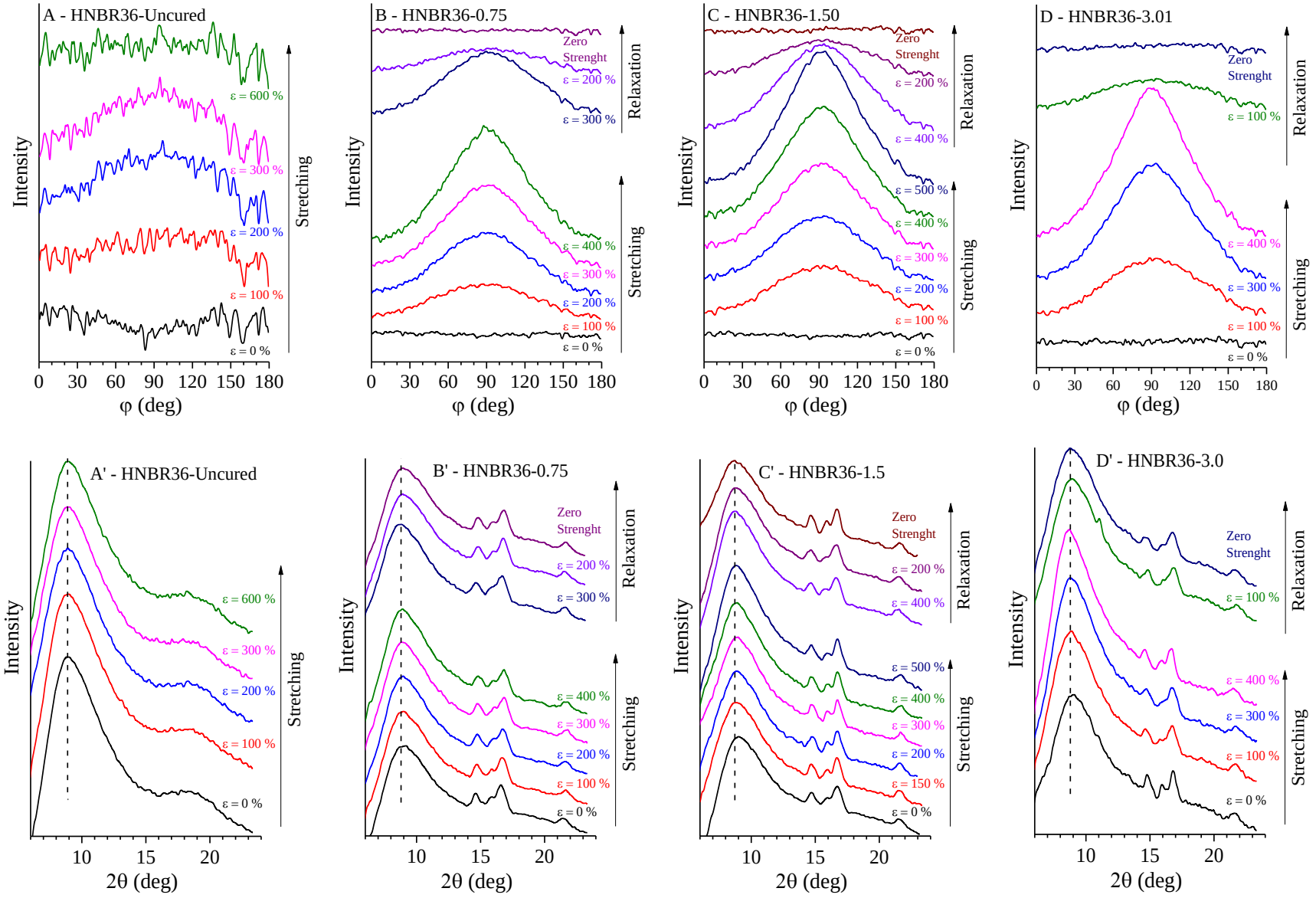

Figure A15. Azimuthal (A-D) and equatorial (A-D') profiles of non-vulcanized (A,A') and sulfur vulcanized (B,B'-D,D') samples of the HNBR with 36 wt% of ACN.

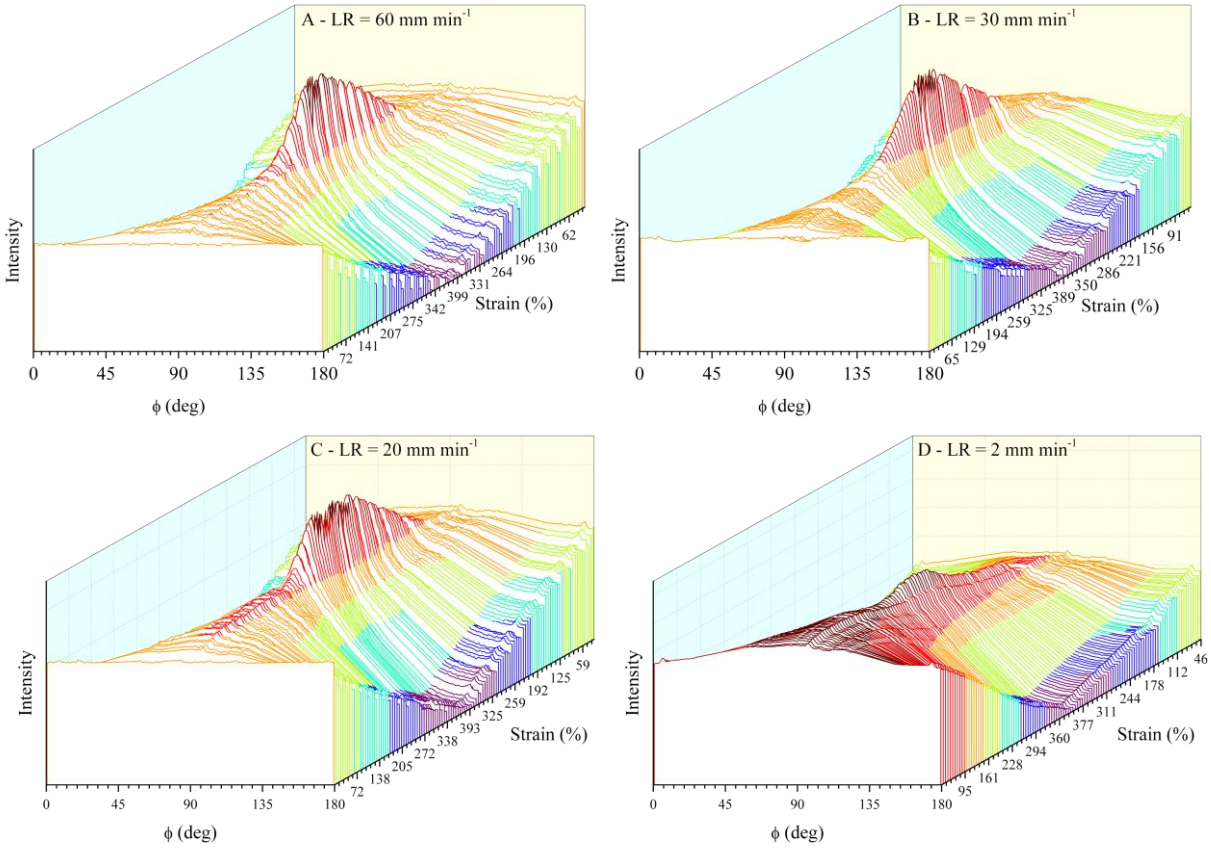

Figure A16. Evolution of the azimuthal profiles of the equatorial reflection during the second hysteresis cycle at different loading rate (LR): A) 60 mm min^{-1}, B) 30 mm min^{-1}, C) 20 mm min^{-1} and D) 2 mm min^{-1}. The profiles reported is related to HNBR44-0.75.

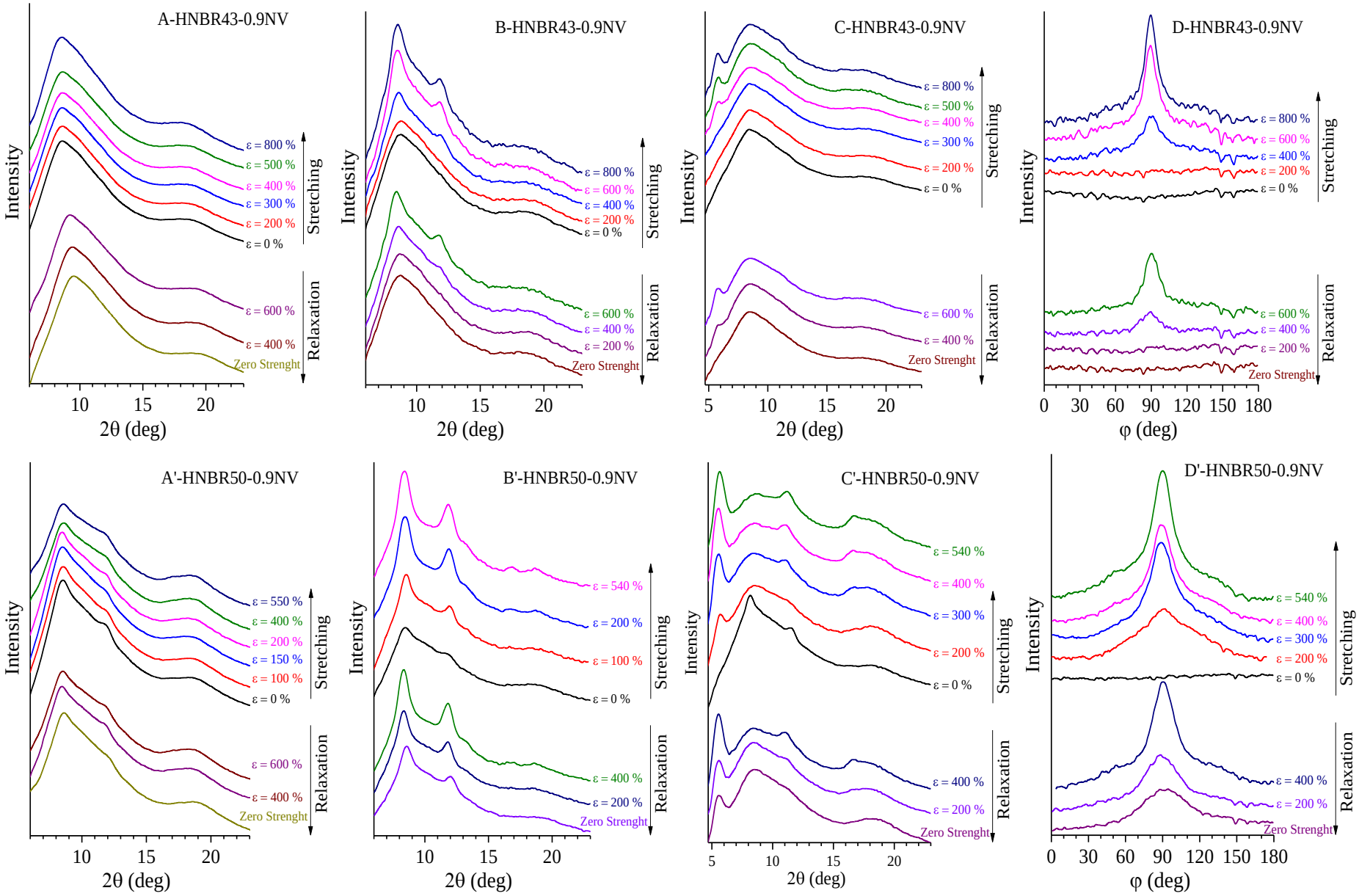

Figure A17 Radial (A, A'), equatorial (B, B'), meridional (C, C') and azimuthal (D, D') WAXS profiles of the non-vulcanized HNBR sample with 43 and 50 wt% of ACN and iRDB ≤ 0.9 mol%.

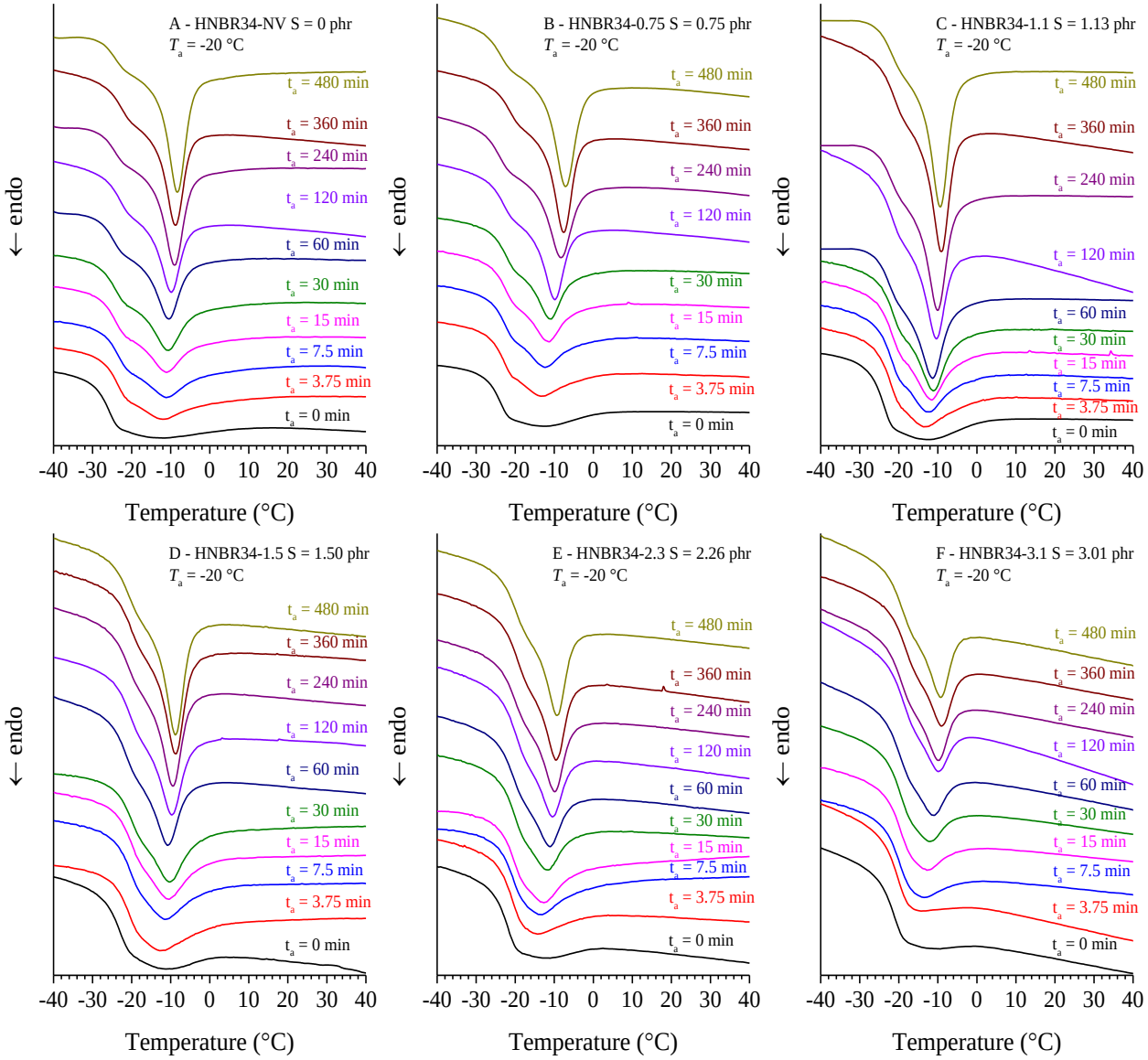

Figure A18 DSC thermograms recorded during heating from -90 to 100 °C for sulfur vulcanized HNBR samples (B-F) and non-vulcanized samples (A) with ACN content of 34 wt% and iRDB = 4 mol%. The DSC thermograms are recorded after subjecting the samples to annealing at temperatures T_a of -20 °C, for the indicated annealing times t_a, followed by rapid cooling from -20 to -90 °C. The sulfur content of the analyzed samples was 0.75, 1.13, 1.50, 2.26 and 3.01 (B-F respectively).

Table A2: Values of enthalpy (ΔH_{peak}) and temperature (T_{peak}) of the endothermic (annealing) peaks extracted from the DSC thermograms in Figure A18, relative to the HNBR samples with 34 wt% of ACN and 4 mol% of iRDB, non-vulcanized and sulfur vulcanized with added sulfur content of 0.75, 1.13, 1.50, 2.26 and 3.01 phr. The samples were annealed at T_a = -20 °C, for the indicated annealing times t_a.

T_a (°C)	HNBR with 34 wt% ACN and iRDB = 4 mol%					
-20	ΔH_{peak} (Jg^{-1})					
t_a (min)	HNBR 34-NV	HNBR 34-0.75	HNBR 34-1.1	HNBR 34-1.5	HNBR 34-2.2	HNBR 34-3.0
0	3.1	3.5	2.7	2.6	2.3	1.8
3.75	4.8	4.4	3.8	3.3	2.3	1.7
7.5	6.3	4.6	4.1	3.3	2.4	2.0
15	6.9	5.5	4.7	4.1	2.9	2.0
30	8.3	6.5	5.5	4.5	3.1	2.6
60	6.7	6	5.6	4.9	4.1	3.8
120	9.0	7.4	7.1	5.0	4.5	4.4
240	7.9	7.0	6.8	6.8	5.1	4.3
360	10.2	7.9	6.8	6.1	4.9	4.2
480	9.8	7.5	7.0	7.4	5.9	4.9
T_a (°C)	HNBR with 34 wt% ACN and iRDB = 4 mol%					
-20	T_{peak} (°C)					
t_a (min)	HNBR 34-NV	HNBR 34-0.75	HNBR 34-1.1	HNBR 34-1.5	HNBR 34-2.2	HNBR 34-3.0
0	-12.5	-12.1	-12.5	-12.4	-13.2	-13.5
3.75	-12.0	-13.4	-13.5	-12.7	-14.2	-14.9
7.5	-11.2	-12.4	-12.9	-11.5	-13.2	-13.5
15	-10.2	-11.4	-11.5	-10.4	-12.7	-12.9
30	-9.4	-10.7	-11.2	-10.4	-11.7	-12.4
60	-10.5	-9.7	-11.4	-10.9	-11.0	-11.5
120	-8.4	-9.9	-9.9	-9.7	-10.5	-10.0
240	-9.0	-8.1	-10.0	-9.4	-9.9	-9.9
360	-7.2	-8.9	-8.9	-8.7	-9.5	-9.2
480	-8.4	-7.5	-9.4	-8.9	-9.4	-9.4

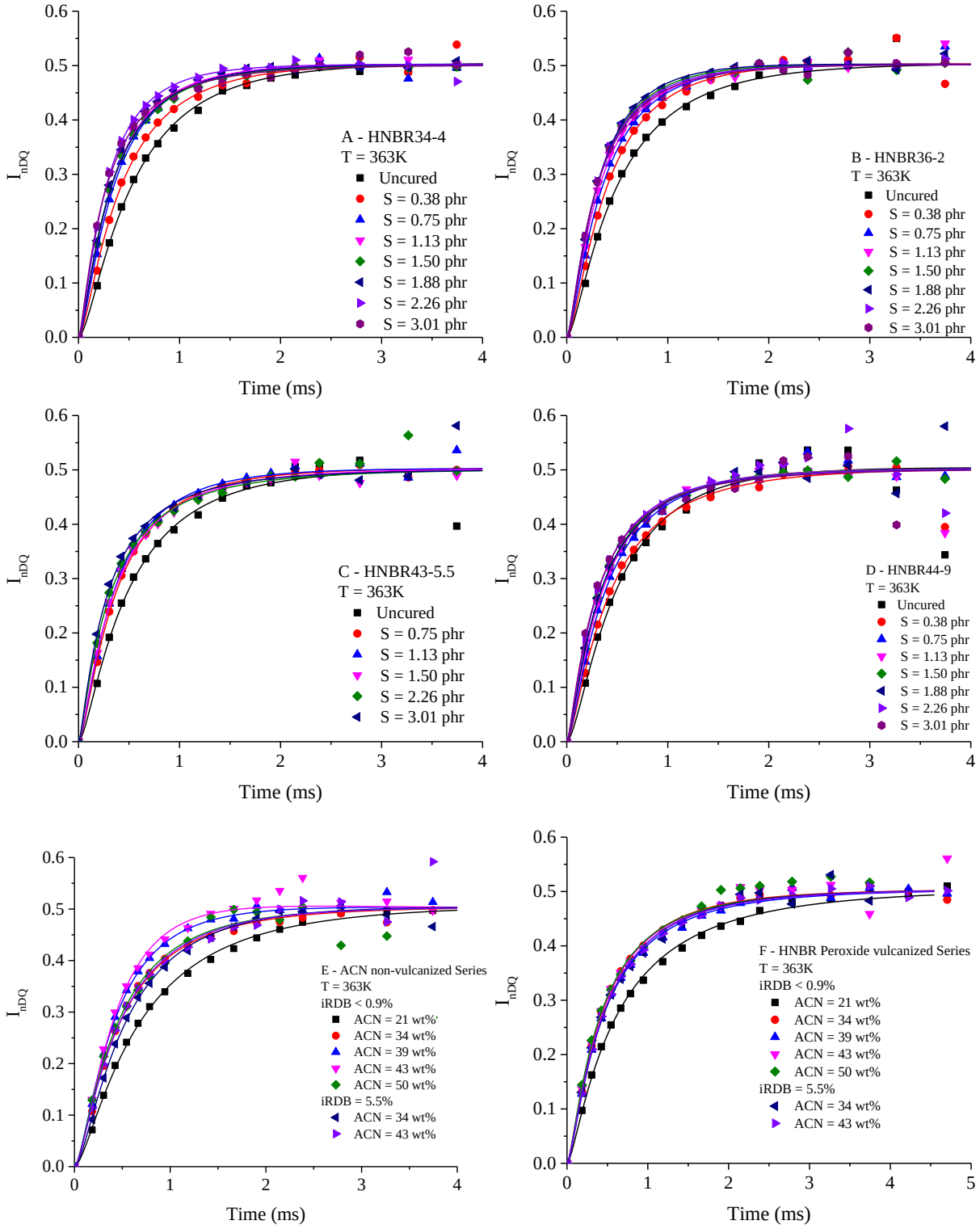

Figure A19 Fitting (solid lines) of the normalized double quantum signals I_{nDQ} (symbols) for the sulfur vulcanized samples with ACN content of 34 (A), 36 (B), 43 (C) and 44 (D) wt% and for the samples with different ACN content, non-vulcanized (E) and peroxide vulcanized (F).

References

1. Hurley, P.E., 1981. History of natural rubber. *Journal of Macromolecular Science—Chemistry*, *5*(7), pp.1279-1287.
2. Jones, K.P. and Allen, P.W., 1992. Historical development of the world rubber industry. *Natural rubber: Biology, cultivation and technology*, pp.1-25.
3. Morton, M., 1981. History of synthetic rubber. *Journal of Macromolecular Science—Chemistry*, *15*(7), pp.1289-1302.
4. Chenier, P.J. and Chenier, P.J., 2002. Elastomers. *Survey of Industrial Chemistry*, pp.329-344. Shanks, R.A. and Kong, I., 2013.
5. General purpose elastomers: structure, chemistry, physics and performance. *Advances in Elastomers I: Blends and Interpenetrating Networks*, pp.11-45.
6. Ponnamma, D., Jose Chirayil, C., Sadasivuni, K.K., Somasekharan, L., Yaragalla, S., Abraham, J. and Thomas, S., 2013. Special purpose elastomers: synthesis, structure-property relationship, compounding, processing and applications. *Advances in Elastomers I: Blends and Interpenetrating Networks*, pp.47-82.
7. Treolar, L.R.G., 2005, III Edition. The physics of rubber elasticity.
8. Anthony, R.L., Caston, R.H. and Guth, E., 1942. Equations of state for natural and synthetic rubber-like materials. I. Unaccelerated natural soft rubber. *The Journal of Physical Chemistry*, *46*(8), pp.826-840.
9. Christensen, R.G. and Hoeve, C.A.J., 1970. Comparison between theoretical and experimental values of the volume changes accompanying rubber extension. *Journal of Polymer Science Part A-1: Polymer Chemistry*, *8*(6), pp.1503-1512.
10. Wood, L.A. and Roth, F.L., 1944. Stress-temperature relations in a pure-gum vulcanizate of natural rubber. *Journal of Applied Physics*,*15*(11), pp.781-789.
11. Allen, G., Bianchi, U. and Price, C., 1963. Thermodynamics of elasticity of natural rubber. *Transactions of the Faraday Society*, *59*, pp.2493-2502.
12. Flory, P., 1961. Thermodynamic relations for high elastic materials. *Transactions of the Faraday Society*, *57*, pp.829-838.
13. Gee, G., 1966. The present status of the theory of rubber elasticity. *Polymer*, *7*(8), pp.373-385.
14. Shen, M., Hall, W.F. and Dewames, R.E., 1968. Molecular theories of rubber-like elasticity and polymer viscoelasticity. *Journal of Macromolecular Science—Reviews in Macromolecular Chemistry*, *2*(2), pp.183-224.
15. Dušek, K. and Prins, W., 2006. Structure and elasticity of non-crystalline polymer networks. In *Fortschritte der Hochpolymeren-Forschung* (pp. 1-102). Berlin, Heidelberg: Springer Berlin Heidelberg.
16. Treolar, L.R.G., 1974. The elasticity and related properties of rubbers. *Rubber Chemistry and Technology*, *47*(3), pp.625-696.
17. Mark, J.E., 1973. Thermoelastic properties of rubberlike networks and their thermodynamic and molecular interpretation. *Rubber Chemistry and Technology*, *46*(3), pp.593-618.
18. Shen, M. and Croucher, M., 1975. Contribution of internal energy to the elasticity of rubberlike materials. *Journal of Macromolecular Science—Reviews in Macromolecular Chemistry*, *12*(2), pp.287-329.
19. Mark, J.E., 1976. Thermoelastic results on rubberlike networks and their bearing on the foundations of elasticity theory. *Journal of Polymer Science: Macromolecular Reviews*, *11*(1), pp.135-159.
20. Ferry, J.D., 1980. *Viscoelastic properties of polymers*. John Wiley & Sons.
21. Langley, N.R., 1968. Elastically effective strand density in polymer networks. *Macromolecules*, *1*(4), pp.348-352.

22. Labana, S.S., 1977. Chemistry and properties of crosslinked polymers. In *ACS Symposium on Chemistry and Properties of Crosslinked Polymers (1976: San Francisco)*. Academic Press.
23. Tobolsky, A.V. and Callinan, T.D., 1960. Properties and structure of polymers. *Journal of The Electrochemical Society*, *107*(10), p.243C.
24. Smith Jr, K.J., 1976. Crystallization of networks under stress. *Polymer Engineering & Science*, *16*(3), pp.168-175.
25. Laghmach, R., Candau, N., Chazeau, L., Munch, E. and Biben, T., 2015. Phase field modelling of strain induced crystal growth in an elastic matrix. *The Journal of chemical physics*, *142*(24).
26. Gros, A., Huneau, B., Verron, E. and Tosaka, M., 2019. A physically-based model for strain-induced crystallization in natural rubber. Part I: Life cycle of a crystallite. *Journal of the Mechanics and Physics of Solids*, *125*, pp.164-177.
27. J.P. Flory, Thermodynamics of crystallization in high polymers. I. Crystallization induced by stretching, J. Chem. Phys. 15 (1947) 397–408.
28. A.N. Gent, Crystallization and the relaxation of stress in stretched natural rubber vulcanizates, Trans. Faraday Soc. 50 (1954) 521–533.
29. B. Huneau, Strain-induced crystallization of natural rubber: a review of X-ray diffraction investigations, Rubber Chem. Technol. 84 (2011) 425–452.
30. M. Tosaka, S. Kohjiya, S. Murakami, S. Poompradub, Y. Ikeda, S. Toki, I. Sics, B. S. Hsiao, Effect of network-chain length on strain-induced crystallization of NR and IR vulcanizates, Rubber Chem. Technol. 77 (2004) 711–723.
31. M. Tosaka, S. Murakami, S. Poompradub, S. Kohjiya, Orientation and crystallization of natural rubber network as revealed by WAXD using synchrotron radiation, Macromolecules 37 (2004) 3299–3309.
32. M. Tosaka, Strain-induced crystallization of crosslinked natural rubber as revealed by X-ray diffraction using synchrotron radiation, Polym. J. (Tokyo, Jpn.) 39 (2007) 1207–1220.
33. M. Tosaka, S. Kohjiya, Y. Ikeda, S. Toki, B.S. Hsiao, Molecular orientation and stress relaxation during strain-induced crystallization of vulcanized natural rubber, Polym. J. (Tokyo, Jpn.) 42 (2010) 474–481.
34. S. Toki, I. Sics, B.S. Hsiao, S. Murakami, M. Tosaka, S. Poompradub, S. Kohjiya, Y. Ikeda, Structural developments in synthetic rubbers during uniaxial deformation by in situ synchrotron X-ray diffraction, J. Polym. Sci., Part B: Polym. Phys. 42 (2004) 956–964.
35. S. Toki, I. Sics, S. Ran, L. Liu, B.S. Hsiao, S. Murakami, K. Senoo, S. Kohjiya, New insights into structural development in natural rubber during uniaxial deformation by in situ synchrotron X-ray diffraction, Macromolecules 35 (2002) 6578–6584.
36. S. Murakami, K. Senoo, S. Toki, S. Kohjiya, Structural development of natural rubber during uniaxial stretching by in situ wide angle X-ray diffraction using a synchrotron radiation, Polymer 43 (2002) 2117–2120.
37. M. Tosaka, A route for the thermodynamic description of strain-induced crystallization in sulfur-cured natural rubber, Macromolecules 42 (2009) 6166–6174.
38. S. Trabelsi, P.-A. Albouy, J. Rault, Crystallization and melting processes in vulcanized stretched natural rubber, Macromolecules 36 (2003) 7624–7639.
39. P.A. Albouy, G. Guillier, D. Petermann, A. Vieyres, O. Sanseau, P. Sotta, A stroboscopic X-ray apparatus for the study of the kinetics of strain-induced crystallization in natural rubber, Polymer 53 (2012) 3313–3324.
40. P.A. Albouy, P. Sotta, Draw ratio at the onset of strain-induced crystallization in cross-linked natural rubber, Macromolecules 53 (2020) 992–1000.

41. P. Sotta, P.A. Albouy, Strain-induced crystallization in natural rubber: Flory's theory revisited, Macromolecules 53 (2020) 3097–3109.
42. J. Rault, J. Marchal, P. Judeinstein, P.-A. Albouy, Stress-induced crystallization and reinforcement in filled natural rubbers: 2H NMR study, Macromolecules 39 (2006) 8356–8368.
43. P.-A. Albouy, A. Vieyres, R. P´erez-Aparicio, O. Sans´eau, P. Sotta, The impact of strain-induced crystallization on strain during mechanical cycling of cross-linked natural rubber, Polymer 55 (2014) 4022–4031.
44. A. Vieyres, R. P´erez-Aparicio, P.-A. Albouy, O. Sanseau, K. Saalw¨achter, D.R. Long, P. Sotta, Sulfur-cured natural rubber elastomer networks: correlating cross-link density, chain orientation, and mechanical response by combined techniques, Macromolecules 46 (2013) 889–899.
45. J.-M. Chenal, L. Chazeau, L. Guy, Y. Bomal, C. Gauthier, Molecular weight between physical entanglements in natural rubber: a critical parameter during strain-induced crystallization, Polymer 48 (2007) 1042–1046.
46. J.-M. Chenal, C. Gauthier, L. Chazeau, L. Guy, Y. Bomal, Parameters governing strain induced crystallization in filled natural rubber, Polymer 48 (2007) 6893–6901.
47. Y. Ikeda, Y. Yasuda, K. Hijikata, M. Tosaka, S. Kohjiya, Comparative study on strain-induced crystallization behavior of peroxide cross-linked and sulfur cross-linked natural rubber, Macromolecules 41 (2008) 5876–5884.
48. N. Candau, R. Laghmach, L. Chazeau, J.-M. Chenal, C. Gauthier, T. Biben, E. Munch, Strain-induced crystallization of natural rubber and cross-link densities heterogeneities, Macromolecules 47 (2014) 5815–5824.
49. J.L. Valentín, P. Psadas, A. Fern´andez-Torres, M.A. Malmierca, L. Gonz´ales, W. Chass´e, K. Saalw¨achter, Inhomogeneities and chain dynamics in diene rubbers vulcanized with different cure systems, Macromolecules 43 (2010) 4210–4222.
50. G.R. Mitchell, A wide-angle X-ray study of the development of molecular orientation in crosslinked natural rubber, Polymer 25 (1984) 1562–1572.
51. Brydson, J.A., 1978. The chemistry of rubber. *Applied Science, London*.
52. Blow, C.M. and Loo, C.T., 1975. Influence of cure system concentration on crosslink structure in SBR sulphur vulcanizates. *Polymer*,*16*(3), pp.205-208.
53. Blokh, G.A., 1968. *Organic accelerators in the vulcanization of rubber*. Israel Program for Scientific Translations.
54. Donnet, J.B. and Voet, A., 1976. Carbon black: physics, chemistry, and elastomer reinforcement.
55. Mark, J.E., Erman, B. and Roland, M. eds., 2013.*The science and technology of rubber*. Academic press.
56. Ponnamma, D., Jose Chirayil, C., Sadasivuni, K.K., Somasekharan, L., Yaragalla, S., Abraham, J. and Thomas, S., 2013. Special purpose elastomers: synthesis, structure-property relationship, compounding, processing and applications. *Advances in Elastomers I: Blends and Interpenetrating Networks*, pp.47-82.
57. Datta, S., 2004. Special-purpose elastomers. *Brendan Rodgers. Rubber compounding: Chemistry and Applications. Marcel Dekker Inc, New York*, pp.105-132.
58. Wrana, C., Reinartz, K. and Winkelbach, H.R., 2001. Therban®–the high performance elastomer for the new millennium. *Macromolecular materials and engineering*, *286*(11), pp.657-662.
59. Grassie, N. and Heaney, A., 1975. Thermal degradation of copolymers of butadiene and acrylonitrile. *Rubber Chemistry and Technology*, *48*(4), pp.678-691.
60. Milner, P.W., 1987. Advances in Nitrile Rubber (NBR). In *Developments in Rubber Technology—4* (pp. 57-85). Dordrecht: Springer Netherlands.
61. Parent, J.S., McManus, N.T. and Rempel, G.L., 1996. RhCl (PPh3) 3 and RhH (PPh3) 4 catalyzed hydrogenation of acrylonitrile− butadiene copolymers. *Industrial & engineering chemistry research*, *35*(12), pp.4417-4423.

62. Wang, H., Yang, L. and Rempel, G.L., 2013. Homogeneous hydrogenation art of nitrile butadiene rubber: a review. *Polymer Reviews*, *53*(2), pp.192-239.
63. Wang, H., Yang, L. and Rempel, G.L., 2013. Homogeneous hydrogenation art of nitrile butadiene rubber: a review. *Polymer Reviews*, *53*(2), pp.192-239
64. Kobatake, T., Kodama, K., Hayashi, S. and Yoshioka, A., 1997. Improvement of low-temperature flexibility of hydrogenated nitrile—butadiene rubber. *Rubber chemistry and technology*, *70*(5), pp.839-854.
65. Alcock, B., Olafsen, K., Huse, J. and Grytten, F., 2018. The low temperature crystallization of hydrogenated nitrile butadiene rubber (HNBR). *Polymer Testing*, *66*, pp.228-234.
66. Schawe, J.E. and Wrana, C., 2020. Competition between structural relaxation and crystallization in the glass transition range of random copolymers. *Polymers*, *12*(8), p.1778.
67. Hodge, I.M., 1995. Physical aging in polymer glasses. *Science*, *267*(5206), pp.1945-1947.
68. Stillinger, F.H., 1995. A topographic view of supercooled liquids and glass formation. *Science*, *267*(5206), pp.1935-1939.
69. Hodge, I.M. and Huvard, G.S., 1983. Effects of annealing and prior history on enthalpy relaxation in glassy polymers. 3. Experimental and modeling studies of polystyrene. *Macromolecules*, *16*(3), pp.371-375.
70. Zhang, X., Wu, J., Xu, Z., Yue, D., Wu, S., Yan, S., Lu, Y. and Zhang, L., 2021. Comparative study on the molecular chain orientation and strain-induced crystallization behaviors of HNBR with different acrylonitrile content under uniaxial stretching. *Polymer*, *219*, p.123520.
71. Hodge, I.M., 1995. Physical aging in polymer glasses. *Science*, *267*(5206), pp.1945-1947.
72. Stillinger, F.H., 1995. A topographic view of supercooled liquids and glass formation. *Science*, *267*(5206), pp.1935-1939.
73. Flory, P.J. and Rehner Jr, J., 1943. Statistical mechanics of cross-linked polymer networks II. Swelling. *The journal of chemical physics*, *11*(11), pp.521-526.
74. Quesada-Pérez, M., Maroto-Centeno, J.A., Forcada, J. and Hidalgo-Alvarez, R., 2011. Gel swelling theories: the classical formalism and recent approaches. *Soft Matter*, *7*(22), pp.10536-10547.
75. Valentín, J.L., Carretero-González, J., Mora-Barrantes, I., Chassé, W. and Saalwachter, K., 2008. Uncertainties in the determination of cross-link density by equilibrium swelling experiments in natural rubber. *Macromolecules*, *41*(13), pp.4717-4729.
76. Sanprasert, P., Sombatsompop, N., Sae-oui, P. and Sirisinha, C., 2014. Cotton fibers reinforcement of HNBR: Control of fiber alignment and its influence on properties of HNBR vulcanizates. *Journal of Applied Polymer Science*, *131*(22).
77. Smitthipong, W., Nardin, M., Schultz, J. and Suchiva, K., 2007. Adhesion and self-adhesion of rubbers, crosslinked by electron beam irradiation. *International journal of adhesion and adhesives*, *27*(5), pp.352-357.
78. Chan, J.C. ed., 2011. *Solid state NMR* (Vol. 306). Springer Science & Business Media.
79. Kitayama, T. and Hatada, K., 2013. *NMR spectroscopy of polymers*. Springer Science & Business Media.
80. Abragam, A., 1961. *The principles of nuclear magnetism* (No. 32). Oxford university press.
81. Mauri, M., Mauri, L., Causin, V. and Simonutti, R., 2011. A method based on time domain nuclear magnetic resonance for the forensic differentiation of latex gloves. *Analytical methods*, *3*(8), pp.1802-1809.
82. Mauri, M., Dibbanti, M.K., Calzavara, M., Mauri, L., Simonutti, R. and Causin, V., 2013. Time domain nuclear magnetic resonance: a key complementary technique for the forensic differentiation of foam traces. *Analytical Methods*, *5*(17), pp.4336-4344.

83. Saalwächter, K., 2007. Proton multiple-quantum NMR for the study of chain dynamics and structural constraints in polymeric soft materials. *Progress in Nuclear Magnetic Resonance Spectroscopy*, *51*(1), pp.1-35.
84. Schmidt-Rohr, K. and Spiess, H.W., 1994. *Multidimensional solid-state NMR and polymers*. Academic Press.
85. Carr, H.Y. and Purcell, E.M., 1954. Effects of diffusion on free precession in nuclear magnetic resonance experiments. *Physical review*, *94*(3), p.630.
86. Baum, J. and Pines, A., 1986. NMR studies of clustering in solids. *Journal of the American Chemical Society*, *108*(24), pp.7447-7454.
87. Saalwächter, K., 2012. Microstructure and molecular dynamics of elastomers as studied by advanced low-resolution nuclear magnetic resonance methods. *Rubber chemistry and technology*, *85*(3), pp.350-386.
88. Ok, J.H., Spencer, R.G.S., Bennett, A.E. and Griffin, R.G., 1992. Homonuclear correlation spectroscopy in rotating solids. *Chemical physics letters*, *197*(4-5), pp.389-395.
89. Breiland, W.G., Harris, C.B. and Pines, A., 1973. Optically detected electron spin echoes and free precession in molecular excited states. *Physical Review Letters*, *30*(5), p.158.
90. Warren, W.S., Weitekamp, D.P. and Pines, A., 1980. Theory of selective excitation of multiple-quantum transitions. *The Journal of Chemical Physics*, *73*(5), pp.2084-2099.
91. Cohen-Addad, J.P., 1974. Effect of the anisotropic chain motion in molten polymers: The solidlike contribution of the nonzero average dipolar coupling to NMR signals. Theoretical description. *The Journal of Chemical Physics*, *60*(6), pp.2440-2453.
92. Valentín, J.L., Carretero-González, J., Mora-Barrantes, I., Chassé, W. and Saalwachter, K., 2008. Uncertainties in the determination of cross-link density by equilibrium swelling experiments in natural rubber. *Macromolecules*, *41*(13), pp.4717-4729.
93. Syed, I.H., Stratmann, P., Hempel, G., Klüppel, M. and Saalwächter, K., 2016. Entanglements, defects, and inhomogeneities in nitrile butadiene rubbers: Macroscopic versus microscopic properties. *Macromolecules*, *49*(23), pp.9004-9016.
94. Saalwächter, K., Ziegler, P., Spyckerelle, O., Haidar, B., Vidal, A. and Sommer, J.U., 2003. H 1 multiple-quantum nuclear magnetic resonance investigations of molecular order distributions in poly (dimethylsiloxane) networks: Evidence for a linear mixing law in bimodal systems. *The Journal of chemical physics*, *119*(6), pp.3468-3482.
95. Weese, J., 1992. A reliable and fast method for the solution of Fredhol integral equations of the first kind based on Tikhonov regularization. *Computer physics communications*, *69*(1), pp.99-111.
96. Weese, J., 1993. A regularization method for nonlinear ill-posed problems. *Computer Physics Communications*, *77*(3), pp.429-440.
97. Papon, A., Saalwächter, K., Schäler, K., Guy, L., Lequeux, F. and Montes, H., 2011. Low-field NMR investigations of nanocomposites: polymer dynamics and network effects. *Macromolecules*, *44*(4), pp.913-922.
98. Knipe, J.M., Sirrine, J., Sawvel, A.M., Mason, H.E., Lewicki, J.P., Sun, Y., Glascoe, E.A. and Sharma, H.N., 2019. In Situ Curing Kinetics of Moisture-Reactive Acetoxysiloxane Sealants. *Industrial & Engineering Chemistry Research*, *58*(37), pp.17266-17276.
99. Genix, A.C., Bocharova, V., Carroll, B., Lehmann, M., Saito, T., Krueger, S., He, L., Dieudonné-George, P., Sokolov, A.P. and Oberdisse, J., 2019. Understanding the static interfacial polymer layer by exploring the dispersion states of nanocomposites. *ACS applied materials & interfaces*, *11*(19), pp.17863-17872.
100. Böttcher, C.J.F. and Bordewijk, P., 1978. Theory of electric polarization. Vol. II (1978).

101. Runt, J.P. and Fitzgerald, J.J., 1997. Dielectric Spectroscopy of Polymeric Materials, American Chem. *Soc., Washington, DC*.
102. Ngai, K.L., 2011. *Relaxation and diffusion in complex systems*. Springer Science & Business Media.
103. Richert, R. and Blumen, A., 1994. Disordered systems and relaxation. In *Disorder Effects on Relaxational Processes: Glasses, Polymers, Proteins* (pp. 1-7). Berlin, Heidelberg: Springer Berlin Heidelberg.
104. Havriliak, S. and Negami, S., 1966. A complex plane analysis of α-dispersions in some polymer systems. In *Journal of Polymer Science Part C: Polymer Symposia* (Vol. 14, No. 1, pp. 99-117). New York: Wiley Subscription Services, Inc., A Wiley Company.
105. Havriliak, S. and Negami, S., 1967. A complex plane representation of dielectric and mechanical relaxation processes in some polymers. *Polymer*, *8*, pp.161-210.
106. Kremer, F. and Schönhals, A. eds., 2002. *Broadband dielectric spectroscopy*. Springer Science & Business Media.
107. Drzeżdżon, J., Jacewicz, D., Sielicka, A. and Chmurzyński, L., 2019. Characterization of polymers based on differential scanning calorimetry based techniques. *TrAC Trends in Analytical Chemistry*, *110*, pp.51-56.
108. Müller, A.J. and Michell, R.M., 2016. Differential scanning calorimetry of polymers. *Polymer Morphology: Principles, Characterization, and Processing*, pp.72-99.
109. Roe, R.J., 2000. Methods of X-ray and neutron scattering in polymer science.
110. https://www.esrf.fr/computing/scientific/FIT2D/
111. Mitchell, G.R. and Windle, A.H., 1982. Conformational analysis of oriented non-crystalline polymers using wide angle X-ray scattering. *Colloid and Polymer Science*, *260*, pp.754-761.
112. Deas, H.D., 1952. The diffraction of X-rays by a random assemblage of molecules having partial alignment. *Acta Crystallographica*, *5*(4), pp.542-546.
113. Stribeck, N., 2007. *X-ray scattering of soft matter*. Springer Science & Business Media.
114. https://soft.snbl.eu/bubble/bubble.html
115. Rubinstein, M., 2007. Polymer physics/Michael Rubinstein and Ralph H. Colby.
116. Saville, B.A. and Watson, A.A., 1967. Structural characterization of sulfur-vulcanized rubber networks. *Rubber chemistry and technology*, *40*(1), pp.100-148.
117. Schimmel, K.H. and Heinrich, G., 1991. The influence of the molecular weight distribution of network chains on the mechanical properties of polymer networks. *Colloid and Polymer Science*, *269*, pp.1003-1012.
118. Flory, P.J., 1985. Molecular theory of rubber elasticity. *Polymer journal*, *17*(1), pp.1-12.
119. Gent, A.N. and Zhang, L.Q., 2001. Strain-induced crystallization and strength of elastomers. I. cis-1, 4-polybutadiene. *Journal of Polymer Science Part B: Polymer Physics*, *39*(7), pp.811-817.
120. Toki, S., Hsiao, B.S., Amnuaypornsri, S. and Sakdapipanich, J., 2009. New insights into the relationship between network structure and strain-induced crystallization in un-vulcanized and vulcanized natural rubber by synchrotron X-ray diffraction. *Polymer*, *50*(9), pp.2142-2148.
121. Zhao, F., Bi, W. and Zhao, S., 2011. Influence of crosslink density on mechanical properties of natural rubber vulcanizates. *Journal of Macromolecular Science, Part B*, *50*(7), pp.1460-1469.
122. Gee, G., 1947. Tensile strengths of pure gum natural rubber compounds. *Journal of Polymer Science*, *2*(5), pp.451-462.
123. Morrell, S.H. and Stern, J., 1953. Crystallization and tensile strength of vulcanized natural rubber compounds. *Rubber Chemistry and Technology*, *26*(1), pp.17-24.

124. Braun, D., Haufe, A., Leiß, D. and Hellmann, G.P., 1992. Strain-induced crystallisation and miscibility behaviour of hydrogenated nitrile rubbers. *Die Angewandte Makromolekulare Chemie*, *202*(1), pp.143-15

125. Osaka, N., Kato, M. and Saito, H., 2013. Mechanical properties and network structure of phenol resin crosslinked hydrogenated acrylonitrile-butadiene rubber. *Journal of Applied Polymer Science*, *129*(6), pp.3396-3403.

126. Nobbs, J.H. and Bower, D.I., 1978. Orientation averages for drawn rubber networks. *Polymer*, *19*(9), pp.1100-1103.

127. Flory, P.J., 1946. Effects of molecular structure on physical properties of butyl rubber. *Rubber Chemistry and Technology*, *19*(3), pp.552-598.

128. Le Cam, J.B., 2017. Energy storage due to strain-induced crystallization in natural rubber: The physical origin of the mechanical hysteresis. *Polymer*, *127*, pp.166-173.

129. Albouy, P.A. and Sotta, P., 2017. Strain-induced crystallization in natural rubber. *Polymer crystallization II: from chain microstructure to processing*, pp.167-205.